HIGH SPEED ELECTRICAL POWER TAKEOFF FOR OSCILLATING WATER COLUMNS

NEIL HODGINS

Doctor of Philosophy (PhD)

The University of Edinburgh

2010

ABSTRACT

This thesis describes research into electrical power takeoff mechanisms for Oscillating Water Column (OWC) wave energy devices. The OWC application is studied and possible alternatives to the existing Induction Generator (IG) are identified. The Permanent Magnet Generator (PMG) is found to be the most promising. Results showed that the IG could almost match the output of the PMG if it could be operated significantly above its rated capacity. This improvement would require only limited changes to the overall OWC system. The ability to operate overloaded is determined by the losses and cooling of the IG. The losses in a suitable IG were measured in tests at Nottingham University. Steady state measurements were made of the cooling ability of the OWC airflow at the LIMPET wave power plant operated by Wavegen (the sponsor company) on Islay. Thermal modelling combining the loss and cooling measurements allowed the maximum capacity of the induction generator in an OWC to be found. A simplified model that accurately represents this system is proposed for use in system design and generator control.

DECLARATION

I hereby declare that this thesis has been composed by myself, that the work is my own and has not been submitted for any other degree or professional qualification.

Neil Hodgins May 2010

ACKNOWLEDGEMENTS

This work would not have been possible without the advice and guidance of my supervisors: Dr Markus Mueller and Dr Kenneth Tease. Both have taken time out of busy private and professional lives to make this work possible. Markus kept me moving on through the project, providing advice, expertise, resources and confidence. Ken gave me an exceptional background to the wave energy component of this thesis and spent crucial extra time gathering results in the most miserable and difficult conditions. My second supervisor John Chick provided timely advice during the writing of this thesis.

This work was funded as an Engineering and Physical Sciences Research Council CASE award. The industrial partner in this award was Voith Hydro Wavegen, a negotiation made possible by Graeme Mackie and Dr John Jeffrey.

Wavegen's funding of this work and provision of unique test equipment allowed a practical, measurement based approach to be used, for which I am profoundly grateful. The onsite work was only possible with the help of Janet Lees, Freek As and Dr Tom Heath. Douglas Carmichael at the University of Edinburgh provided sage advice on electrical measurement and invaluable technical help. Dr Keith Bradley and Dr Zhang He of the University of Nottingham provided valuable expertise in the accurate measurement of losses required for my modelling work. Dr David Staton of Motor Design Ltd. answered many difficult thermal modelling questions and made a great deal of thermal modelling information available to me.

Over the course of this project, I have had my writing checked and corrected and my perspective maintained by a wonderful group of people. Most notably Alicia Whissel, David Hughes Hallett, Katherine Murphy, Kirsty Smith, Fraser Hughes, Sarah Caraher and Kate Mitchell.

Finally, this work is mainly due to the patience, understanding and support of my parents, Audrey and Eric Hodgins.

TABLE OF CONTENTS

LIST OF FIGURES

LIST OF TABLES

NOMENCLATURE

Symbol	Quantity	Unit
μ	Viscosity	kg/sm
μ_o	Permeability of Free Space	N/A^2
μrec	Recoil Permeability of Magnet	N/A^2
κ	electric loading	A/m
θ	Core loss factor	W/kg
α	Angle of Attack	°
A,B,C,D	Constants	
a_i	Wire Inner Diameter	m
Ak	Copper resistivity constant	
b	Fin thickness	m
B	Flux Density	T
Brem	Remnant flux density of Magnet	T
C	Thermal Capacitance	J/C
C_D	Coefficient of drag	
C_p	Specific heat capacity	
$C_{subscript}$	Cost	£/$/E
D	Diameter	m
D_h	Hydraulic Diameter	m
E	EMF	V
f	electrical frequency	Hz
F	Force	N
$f_{carrier}$	PWM carrier frequency	Hz
G	Humidity constant	
g_e	Effectuve Airgap Thickness	M
H_a	Airgap mmf gradient	A/M
H_c	Coercivity of magnet	A/m
I	Current	A
I	Current	A
I_r	Rotor Current	A
I_s	Stator Current	A
k	general constant	
K_{ew}	Proportion of winding in endwinding	
k_p	Wire Packing Factor	
L	Length	M
L_s	Stator Core Length	m
M	Number of Phases	
M_c	Core mass	kg
N	Rotational Speed	RPM
N	no of turns/conductors	

n_{coil}	No of turns per coil	
Nu	Nusselt number	
P	Power	W
Pbc	Brush Contact Loss	W
P_{bf}	Brush Friction Loss	W
P_{br}	Brush Resistance	W
P_{bw}	Brush Windage	W
P_{cl}	Core loss	W
P_{cu}	Copper loss	W
P_{cur}	Rotor copper loss	W
P_{cus}	Stator copper loss	W
P_e	Eddy current loss	W
P_{ele}	Electrical Power	W
P_{fw}	Friction and Windage	W
P_h	Hysteresis loss	W
P_{hm}	Harmonic loss	W
P_m	Mechanical power without input voltage	W
P	Pole Pairs	
P_r	Mechanical power to drive with voltage	W
P_r	Prandlt Number	
P_{rr}	Mechanical power in reverse rotation	W
P_{slr}	High frequency stray load loss	W
P_{sls}	Stray load loss	W
Q	Heat Flow	W
Q		
Q_{ew}	Endwinding loss	W
Q_{new}	Non-endwinding loss	W
r	radius	M
R	Electrical resistance	Ω
R_e	Reynolds number	
R^t_{eff}	Effective thermal resistance	C/W
R^t	Thermal resistance	C/W
S	slip	RPM
T	Temperature	C
T	Temperature	C
T_a	Ambient temperature	C
T_g	Generator exterior temperature	C
T_m	Thickness of maget	M
T_{rise}	Temperature rise	C
U	Linear Velocity of Surface	m/s
V	Voltage	V
V_{local}	Local velocity of air	m/s
V_{mean}	Mean velocity of air	m/s

W_r	shaft speed	Radians/s
X	general constant	
X	Molar Fraction of Water Vapour	
Y	General constant	
Δ	Core material desnity	kg/m^3
Δw	Change of work (switched reluctance machine)	J
E	Constant of proportionality for eddy current loss	
E	Emissivity	
Λ	Stator Flux	
P	Density of Air	kg/m^3
σ_{hot}	Hot Resistivity of Copper	Ω/C
Σ	Coil Spread	
Σ	Stefan Boltzmann constant	
T	Torque	Nm
T	Thermal time constant	S
Φ	Relative Humidity	

1

OWC REQUIREMENTS AND ENVIRONMENT

1.1 Renewable energy in context

Climate change, specifically a rise in global temperature relative to pre-industrial temperatures, is a cause for concern worldwide. The Intergovernmental Panel on Climate Change states [1] that it is very likely this temperature rise is due to a human influenced increase in greenhouse gas concentrations. It goes on to present measurements of an annual average 2.8mm sea level rise between 1993 and 2003 caused by melting ice and thermal expansion, that can be attributed to climate change. A sea level rise of 0.18 to 0.59m is predicted for 2090-2099 relative to 1980-1999 levels. The UK Department for Trade and Industry's 2003 Energy White Paper [2] suggests that an extra 80 million people, mostly living in countries least equipped to deal with such problems, will be exposed to flood risk. A lower bound for the damage cost of carbon emissions is set in the white paper as £35 per tonne of carbon emitted. This figure does not include catastrophic climate events, such as reversal of the Gulf Stream, or social effects such as famine and mass migration. With both the population of the world and average level of industrialisation increasing it is probable that more energy will be consumed worldwide. Therefore the means of supplying this energy without greenhouse gas emissions will be essential in the future.

Renewable energy generation offers a solution by harnessing natural resources on a scale not previously possible. By definition, renewable energy is sustainable and when used sensibly, has the potential to considerably reduce global carbon dioxide emissions. Renewable energy is generated locally, generally within the country of consumption, and does not suffer from security of supply issues that threaten other fuel sources. With rising demand and falling production, it is expected that the UK will be importing 75% of its primary energy needs by 2020 [3]. Renewable energy also provides new industry and new jobs. A report on employment in the German renewable energy industry (primarily wind) indicates a 164% increase in employment as the share of primary energy production from renewable energy increases from 3.6% to 21.5% [4].

The UK, Scotland in particular, has considerable renewable energy resources. The wind resource is estimated at over 50TWh/y [5] onshore and considerably more offshore. An estimate of more than 50TWh/y of wave energy and 36TWh/y of tidal energy in UK waters was published by the House of Commons Science and Technology Committee in 2001 [6]. In 2006 4.6TWh of hydroelectric energy was generated [7]. The electrical demand of the UK in 2006 was 350TWh [7]. To encourage the utilisation of this resource national targets were set of 10% renewable energy generation by 2010 [8] and a more ambitious Scottish target of 50% in 2020.

Current growth in renewable energy generation has been concentrated in the wind power sector. The installed wind generation capacity of the UK has risen from 1353MW in 2004 [9] to 3287.9MW in 2008. For obvious economic reasons it is advisable to run the electricity supply system from as many cost competitive sources as possible, thus it is anticipated that the renewable energy sector will diversify as it grows. One resource identified as a possibility for a large future source of energy is wave power.

Wave power is mainly generated by the differential solar heating of the Earth’s surface [10]. As an air mass is heated, it changes in pressure, and these pressure differences cause winds to blow down the pressure gradient. Over a large body of water, the friction between the water’s surface and the wind causes energy to be transferred from the wind onto the water [11]. This energy is transferred across the water surface in the form of a surface wave. Waves are also generated by seismic events and gravity (tides) [12]. The effective surface wave seen at a point is a superposition of all the incident waves at that point at that time. The waves can travel long distances in deep water with minimal loss of energy [10]. The height, and therefore the energy of a wave is determined by the wind speed, the wind fetch (the distance over which the wind blows), the wind duration and the water depth. The height of a wave for a constant wind speed reaches a maximum, where the sea is considered to have “developed” [12]. Around 71% of the Earth’s surface is covered in water and thus develops waves. Wave energy developers are particularly interested in areas close to an inhabited land mass that face into the prevailing wind across an ocean. This is because here, the waves will be fully developed and thus as energetic as possible. As a wave travels into shallower water, the wave loses energy to friction with the ocean bottom so less energy can be extracted close to land. Figure 1 shows how the resource increases (in the UK) away from the shore. The location of a wave power device is a balance between incident wave energy, device cost and device accessibility. For a test plant, accessibility is paramount while energy generation is less important, hence the onshore location of many current installations.

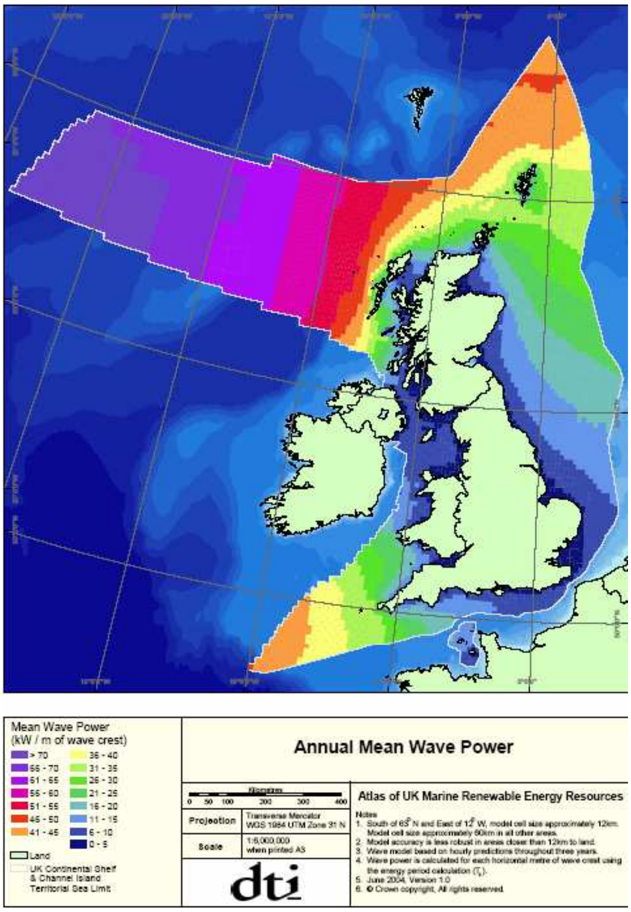

Figure 1: UK Wave Resource [13]

1.2 Study of wave power

The power available in water waves has been of interest for over two hundred years. A patent was granted in France for a simple wave energy device using a float and lever reacting against an inertial body or fixed point in 1799 [14]. Since then many more patents have been granted. Most famously Yoshio Masuda, a retired naval officer, patented an “ocean wave electric generator” in 1965 and went on to produce wave powered navigational buoys [14]. This was the first practical implementation of wave power.

Since then work has been undertaken in several universities around the world. Mathematical models of the motion of waves and the reaction of bodies to waves were developed and compared to results produced in sophisticated wave tanks. In Scotland, Edinburgh University conducted research on the Duck device as well as other wave energy converters [15]. The Cockrell raft and Lanchester Sea Clam were also developed in the UK [16]. Despite considerable study, it took an international energy crisis to begin the journey from small scale prototypes in wavetanks to full scale devices in the ocean.

1.3 Industrial scale wave power

Industrial-scale wave power was first seriously considered as an alternative source of energy in response to the oil crises in the 1970s [14]. An ambitious assessment of the cost of energy from a 2GW wave power station was undertaken in the UK from 1974-1983 [15]. However, the cost of energy was found to be unattractive. Most marine energy research took place at small scale until the 1990s. The exceptions to this were Norway who built a tapered channel shoreline device and a 500kW Oscillating Water Column (henceforth OWC, operational principle detailed later) in 1985 [17] (destroyed in 1988) and Japan who also experimented with several different large scale OWCs.

The 90s saw a number of Oscillating Water Column devices installed around the world. In 1991 a 150kW OWC was commissioned in Trivandrum, India [18]. A small prototype OWC was installed by Queen's University of Belfast on Islay in 1991. In the same year a near-shore OWC known as Osprey was deployed off Dounreay but suffered structural failure before it could be installed[18]. Japan tested a floating OWC known as the mighty whale in 1998 and a 400kW rated shoreline OWC known as PICO was installed in the Azores[18]. The follow up to the Islay OWC was a large wave research facility and 500kW rated power plant known as LIMPET, installed in 2000 by Wavegen in partnership with Queen's University of Belfast [18].

A multitude of non-OWC device types have been tested at model scale by universities and wave power companies since the 70's. Only the McCabe Wave Pump was tested at close to full scale prototype scale before the year 2000 [19]. Since then a number of different operational principles have been tested at large scale and there has been no sign of design convergence. The Archimedes Wave Swing prototype was successfully operated in 2004 [20]. In the same year the prototype Pelamis P750 device was towtested and installed at EMEC in Scotland [21]. Soon after, Pelamis' constructors Ocean Power Delivery (now Pelamis Wave Power) announced a contract for the world's first wave farm in Portugal comprising three Pelamis devices. Ocean Power Technology also deployed their 40kW power buoy for the US Navy in 2004 [22], Energetech deployed a nearshore OWC with wave focussing arms out of Port Kembla, Australia in 2005 [23]. Meanwhile, Wavegen began testing a full scale prototype turbine for breakwater OWC installations. Wavebob, a self reacting buoy became Ireland's first wave power plant in 2007[24]. A second generation of devices is now appearing from successful prototype builders: Pelamis Wave Power have contracts for large scale developments in Scotland; Oceanlinx have ocean tested a large scale model of a floating device and Wavegen has completed OWC turbines for deployment in the Mutriku breakwater in Spain [25], enhanced the original LIMPET OWC with a new turbine and are developing another breakwater at Siadar on the Scottish island of Lewis [26].

The OWC has a considerable track record in wave power. It makes up the majority of all large scale prototypes tested so far and commercial wave power facilities are being constructed. Considering the harshness of the ocean environment there is wisdom in deploying a tried and tested technology. Wavegen, a wave power company based in Inverness, are world leaders in OWC wave power plants. They own and operate the LIMPET installation; delivered the PICO power plant's turbine, have installed a new 100kW turbine on LIMPET, and are refining a turnkey 18.5kW turbine installation suitable for harbour walls. The LIMPET OWC has accrued over 35,000 hours of operation over eight years and data is continuously being gathered. This allows numerical models to be calibrated against practical measurements, enhancing future installations. Hence this study was carried out on the OWC wave power converter in partnership with Wavegen.

As considerable academic and industrial research has, and continues to be focused on wave power, and individual companies converge on a marketable "product", research is becoming more specific. Ways are being found to enhance the production of a device, reduce its cost, or both. Wavegen has expertise in bathymetry, resource prediction and interaction and turbine design, thus most significant research in those areas is already under way. The conversion of turbine kinetic energy into grid frequency electrical energy has received less attention as it lies outside of the core difficulties of building a wave energy converter. However, it merits attention due to the considerable differences between a conventionally operated electrical generator and that in an OWC wave power application.

1.4 Practical wave power

1.4.1 Variability

Wave energy is cyclical in the short term and variable in the long term. Each wave has a trough and a crest so any energy extraction tied directly to the motion of a wave will have maxima and minima within one cycle. For shoreline devices the height of the tide will affect performance on a regular cycle. Otherwise the wave power input is determined by the weather systems offshore. This results in considerable variation across short time periods (less than an hour) as well as daily and monthly variations. There is also a considerable difference between winter and summer wave power inputs as can be seen in figure 2.

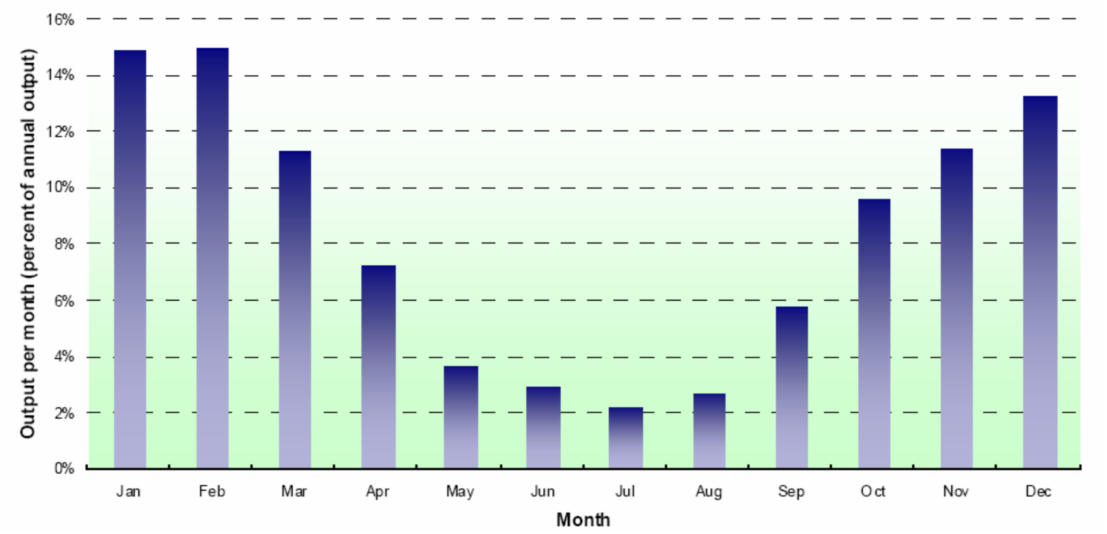

Figure 2: Monthly wave resource (as a percentage of annual total) for sites in North East, North West and South West Regions of the UK [27]

Annually there is a considerable variation of power, illustrated in figure 3. These variations have implications on the design of a wave energy converter. A compromise must be obtained between device rating and capital cost. The penalties for over-sizing include wasted capital and lower overall efficiency. An undersized device will not be able to handle the rarer but powerful sea states where maximum revenue could be generated.

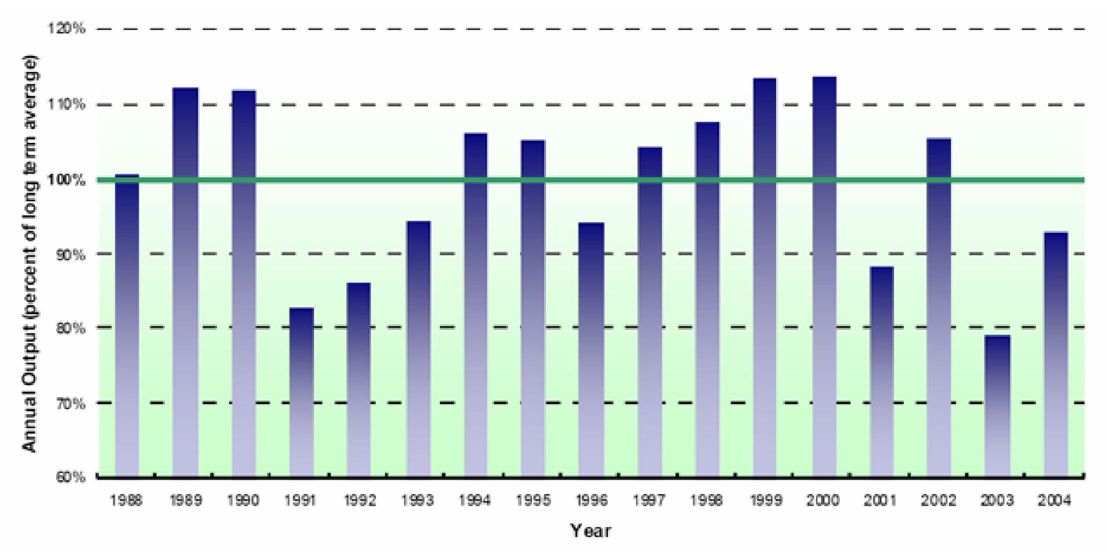

Figure 3: Variation of Annual Wave Resource (as a percentage of 16 year average) in the UK measured in North East, North West and South West Regions by Carbon Trust [27]

A wave energy converter must be designed in such a way that it can survive the largest expected storm it is economically feasible to survive. Although these conditions occur only rarely, their influence on availability (the proportion of time the converter is in a condition to run) can be significant. For the power takeoff system, a worst case scenario must be considered, which the system should be able to survive. The design of the wave energy converter type determines the worst case scenario.

1.5 The oscillating water column

The OWC method of wave energy conversion can be likened to a gearbox. The function of an OWC is to translate high force but low velocity movement of a given distance of wave crest into a more suitable motion for power conversion. This power conversion is accomplished by an electrical generator. The power output of an electrical generator generally follows equation 1 from [28].

$$P = k\overline{B}AD^2L_sN \tag{1}$$

Where k is a constant determined by machine type and winding

$\overline{B}$ is the mean airgap flux density
A is the specific electric loading
D is the diameter of the stator bore
L_s is the stator core length
N is the shaft speed of the generator

It can be seen that the power output increases directly with the shaft speed. Electric loading and airgap flux density have physical limits, so power output for a given shaft speed increases with the square of generator diameter and directly with core length. Increasing these dimensions requires additional material and raises the cost of the generator. Thus a low speed, high power output generator will be large in size and more expensive than one for a higher shaft speed. Hence the ideal motion for cheap power conversion is high speed. The OWC is designed to allow the use of off-the-shelf products. This is part of the reason for early adoption of the OWC before cheaper power converters allowed the simplified conversion of bi-directional low frequency high current power into mains frequency power. The use of off-the-shelf generators produced a robust solution while allowing design effort to concentrate on optimising the hydrodynamic and aerodynamic performance of the device.

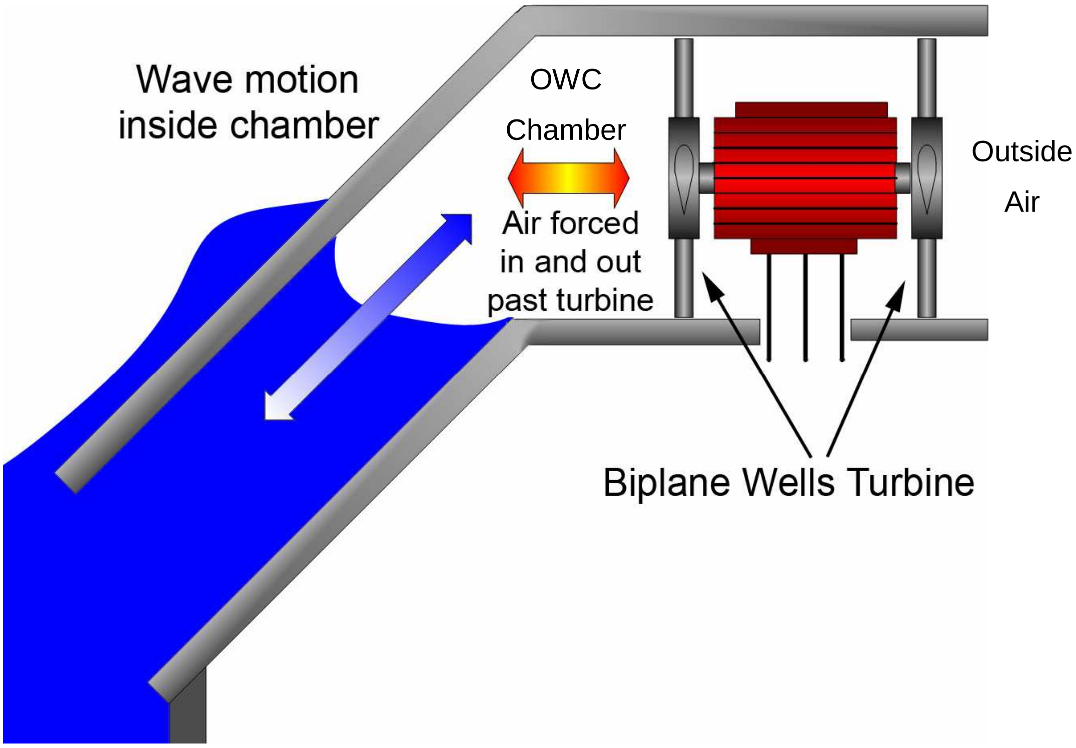

Figure 4: Principle of operation of OWC

The operating principle of the OWC is shown in figure 4. The water surface is used as a piston to compress and decompress air within a chamber. This chamber is then allowed to exchange air with the atmosphere via an outlet past a turbine. The compression of air inside the OWC chamber leads to air being forced out to the atmosphere past the turbine. The decompression of the chamber results in air being drawn back into the chamber. Each wave cycle has an exhalation and inhalation part and the airflow seen by the turbine changes direction. The turbine used in this application is the Wells turbine.

1.5.1 The Wells turbine

The Wells turbine has a number of features that make it well suited for the OWC power conversion application. Chief amongst these is its ability to rectify the bi-directional airflow into uni-directional torque. The turbine is made up of symmetric airfoil sections radiating from a central hub.

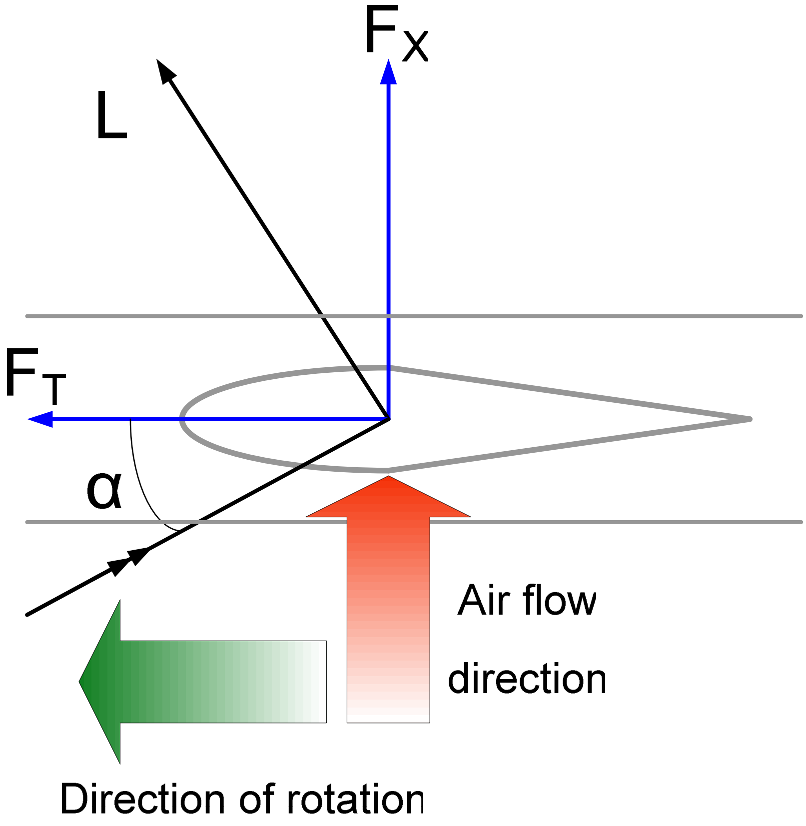

Figure 5: Wells turbine principle

As the air passes the airfoils, it creates a lift force (L in figure 5) at right angles to the angle of attack (α) seen by the incoming air. The angle of attack is given by the speed of the incoming airflow relative to the tangential speed of the turbine rotor. This speed is given by the rotational speed of the generator and the radius of the turbine blade. The resulting lift force can be decomposed into an axial force (F_X) component at right angles to the plane of rotation and a torque force (F_T). It is the torque force that is converted into power by the generator.

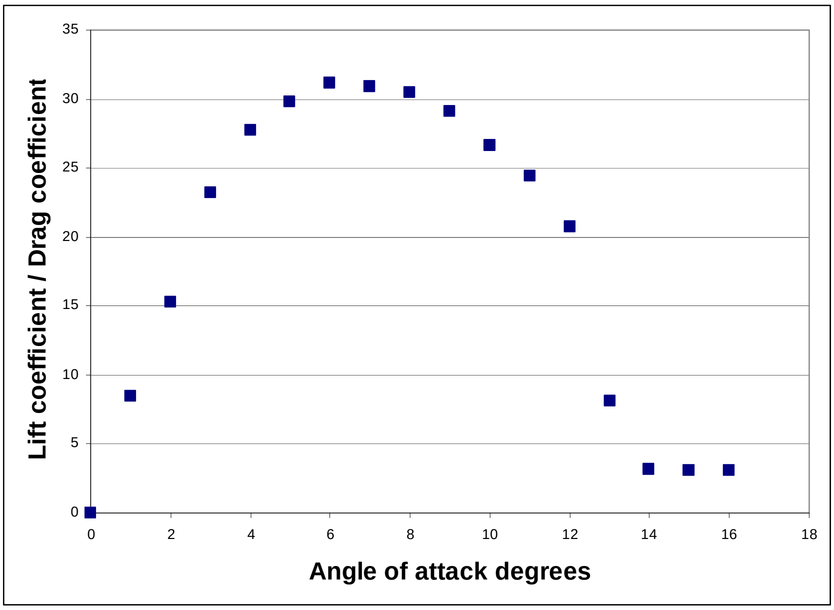

Figure 6: Ratio of lift coefficient to drag coefficient at changing angle of attack for symmetrical airfoil

The Wells turbine is an aerofoil system and as such has optimum performance at a given angle of attack which drops away as shown in figure 6 as flow separates and stall occurs. Best performance can be achieved by selecting a rotational speed which maintains the optimum angle of attack. For the turbine size considered within this thesis, this is a speed range from 1000 to 3900RPM [29]. A variable pitch Wells turbine has been proposed as an alternative; however despite laboratory testing [30], no full scale device has been deployed. Extensive wind tunnel testing of different turbine configurations gave a number of performance enhancements that have been realised at commercial scale. PICO uses stator vanes to enhance the flow of air onto the Wells turbine rotor. LIMPET's original turbine used two generators to give two rows of contra-rotating blades allowing power to be taken from induced swirl. The smaller 18.5kW turbine tested on LIMPET (shown in figure 7) uses two rows of co-rotating blades on a single generator. The only modern OWC not to use the Wells turbine is the Energetech (now Oceanlinx) device which uses a Dennis-Auld variable pitch turbine.

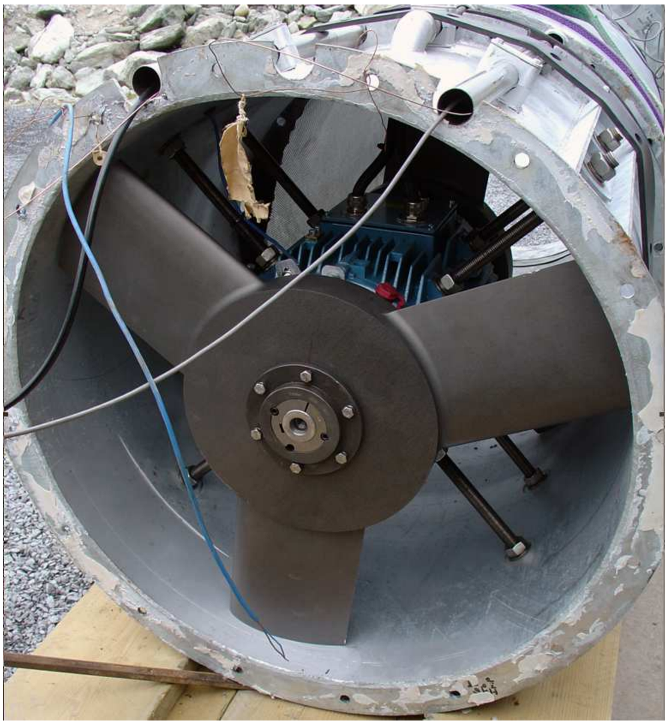

Figure 7: Three bladed turbine rotor in 18.5kW turbine turbogeneration unit

The Wells turbine design is unusually robust as the blades are of significant thickness and low (for a turbine) rotational speed. This is a particular advantage in the wave power application.

1.5.2 The overall system

An OWC can be considered as a dynamic system. The driving force is given by the incident waves. There is a spring effect due to the displacement of the water surface from its notional equilibrium, an inertia effect from the mass of moving water, and a damping effect due to power take off and parasitic effects. This is useful when understanding how the system works in general but it can be difficult to define the properties of the mass, spring and dampers [31] when matching real data.

In this system, the action of the power take off can affect the power seen by the device. If the motion of the water surface is constrained then energy is reflected rather than absorbed. Hence the correct operation of the power take off system is necessary for maximum power conversion from the wave to the air. The primary variable in determining the damping of a pre-existing turbine is the turbine rotational speed.

1.6 The electrical power conversion system

Design of this outlet and the turbine can allow the power take-off to take place close to the mains frequency rotational speed of a generator. A direct connected machine was used with limited success in the Trivandrum project in India before being replaced with a controlled machine [18]. However current systems use a power converter to allow for variation in turbine speed and thus control of the damping parameter. Regardless of the conversion system details, the output must meet all regulations for connection to the grid.

There are physical constraints on the size of the electrical conversion system. The turbine has an optimum shape. Ease of construction and minimization of power train length suggests the power conversion equipment is best located within the turbine. This means it cannot have a larger diameter greater than the turbine hub. If the conversion system is located between the blade rows on a bi-plane Wells turbine then there is also a length constraint.

The power output of the wave energy converter is determined by the incident waves which are a consequence of weather patterns. Hence the power flow through the system is variable. As noted in section 1.4.1 the power conversion system should be able to convert energy efficiently in the range of economically viable conditions. This is considerably different to a conventional power station which would be designed to run close to an optimum efficiency point.

The power take off should be robust enough to withstand a harsh operational environment with minimum maintenance. Difficulties in access to a wave power plant and in undertaking onsite work can extend downtime and incur large equipment and manpower costs. These costs have significant effects on the cost of energy from a wave power plant.

Within these constraints there are a number of solutions that can be considered. The choice of the correct conversion solution will maximise energy conversion, minimise costs and thus reduce the cost of energy from a wave power plant. This study considers the ideal conversion solution for OWCs and in particular Wavegen’s breakwater solution. The smaller size and continuing development of the system make it an attractive opportunity for practical work, thus enhancing a theoretical study.

1.7 Mechanical considerations

1.7.1 Mounting

The current arrangement of Wells turbine puts the electrical power take off system between the rotors of a biplane turbine as shown in figure 8.

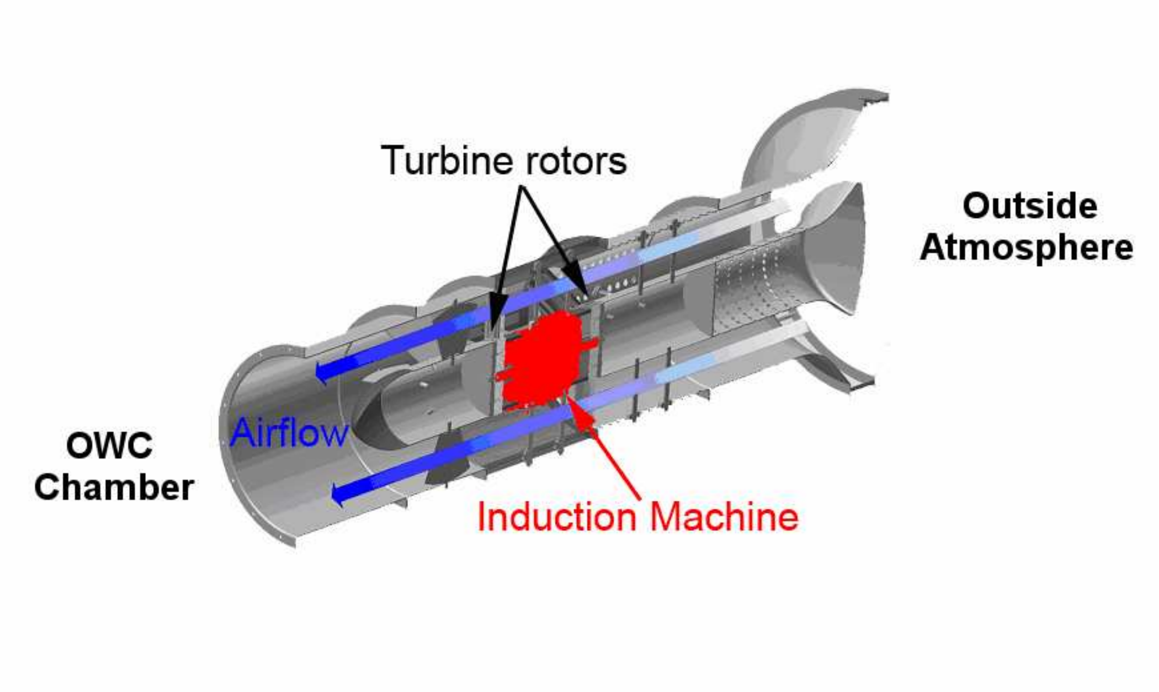

Figure 8: Location of the generator highlighted in red, OWC airflow shown in blue on the inhale part of the cycle

This is a beneficial arrangement as the lengths of all shafts are minimized, the generator cooling is improved and the turbo generation unit is a single easily handled unit. This is an important consideration where maintenance and replacement may have to occur in difficult circumstances. Figure 9 shows the turbo generation unit being installed.

Figure 9: Installation of prototype Wells turbo generation unit at LIMPET on Islay

The in-hub mounting determines the maximum diameter of any electrical power takeoff unit as no more than the hub diameter of the turbine. If a smaller diameter is required then the machine may have to be shrouded to improve the aerodynamics of the system and a different cooling mechanism may be necessary.

The frame of an electrical machine protects the internal components from the operating environment and transmits the reaction to the rotor torque to its mounting. In the case of the OWC application, a totally enclosed generator has been chosen. A ventilated machine would ingest the harmful atmosphere present in the turbine duct and become corroded or damaged internally. Hence the frame of the machine provides the final step in the heat path to the environment. Standard frames feature fins on the generator casing to enhance heat transfer.

The turbine is housed within a turbine hall (figure 10) with the control power electronics and grid connection equipment set at a distance from the seafront in a separate control room (figure 11).

Figure 10: Turbine halls connected to OWC chamber

Figure 11: Control room (foreground)

1.7.2 Operation and Maintenance

Maintenance of any wave energy device is difficult by virtue of its working environment. It is also expensive and may result in the plant being inoperable while it is being carried out. Any electrical power takeoff system must be capable of operation with minimum maintenance which can be performed at annual or longer intervals. Ideally the required maintenance period of the electrical generator would be the same or longer than the next part of the system requiring regular maintenance.

Systems requiring regular visual inspections to minimize the risk of an unscheduled shutdown would be unsuitable for this application unless the performance benefits outweigh the significant expense involved.

If another part of the turbo generation system were to fail, the ideal power takeoff system would remain undamaged and not cause any additional damage. Loss of the grid connection is a common occurrence on sites such as Islay [32], so the generator must be able to cope with such a situation.

Generators may have other advantages (not considered above) in certain situations and for certain applications. The ability to blackstart, to start without a grid connection, is not necessary for a "bulk power" OWC project, but may be essential for certain applications. These will be noted for the particular generator type .

1.8 Thesis aim

This thesis considers the hypothesis that the OWC represents a unique application for a rotating electrical machine. The application is unique, not only in the manner of power input, but also in the working environment. There is an opportunity to improve the power take off by selecting the most appropriate type of generator and considering its operation in this specific environment.

While considerable interest has been focused on hydrodynamics, moorings and turbine design for the OWC, the electrical power takeoff system has been relatively neglected. This work aims to show that improvements can be made to this system and identify where they would be most cost effective.

This work aims to present an analysis of appropriate, practical electrical power takeoff options for an 18.5kW rated breakwater turbine of the kind being tested on Islay and to be installed at Muktriku by Wavegen. It is intended that the work from this thesis will be extended and adapted by Wavegen engineers working on future OWC installations.

1.9 Thesis layout

The next chapter of this thesis introduces the components and the main loss mechanisms within electrical machines. This leads into the discussion of suitable generator types in the following chapter. The Permanent Magnet Generator (PMG) is found to be a possible replacement for the Induction Machine (IM) in current use. The preliminary design of a PMG for an 18.5kW OWC is presented in the following chapter and it is compared to the existing IM. A decision was made to study how the OWC environment changed the heat transfer from the generator in use and how this affected the generator rating. Extension of the rating of the existing generator is suggested to be almost as effective as a new generator type. This decision was made because the opportunity to carry out repeatable tests on this application presented itself and the some of the results are applicable to any generator in this environment. This measurement was made using an induction generator, whose losses had to be known in some detail. The heat transfer mechanisms within and without the generator are identified and then measured in the next chapter. From these measurements a model of the induction generator within the OWC environment is proposed. This model is discussed and the conclusions of this thesis and further work that could be undertaken is presented. The chapter titles and progression are shown in figure 12.

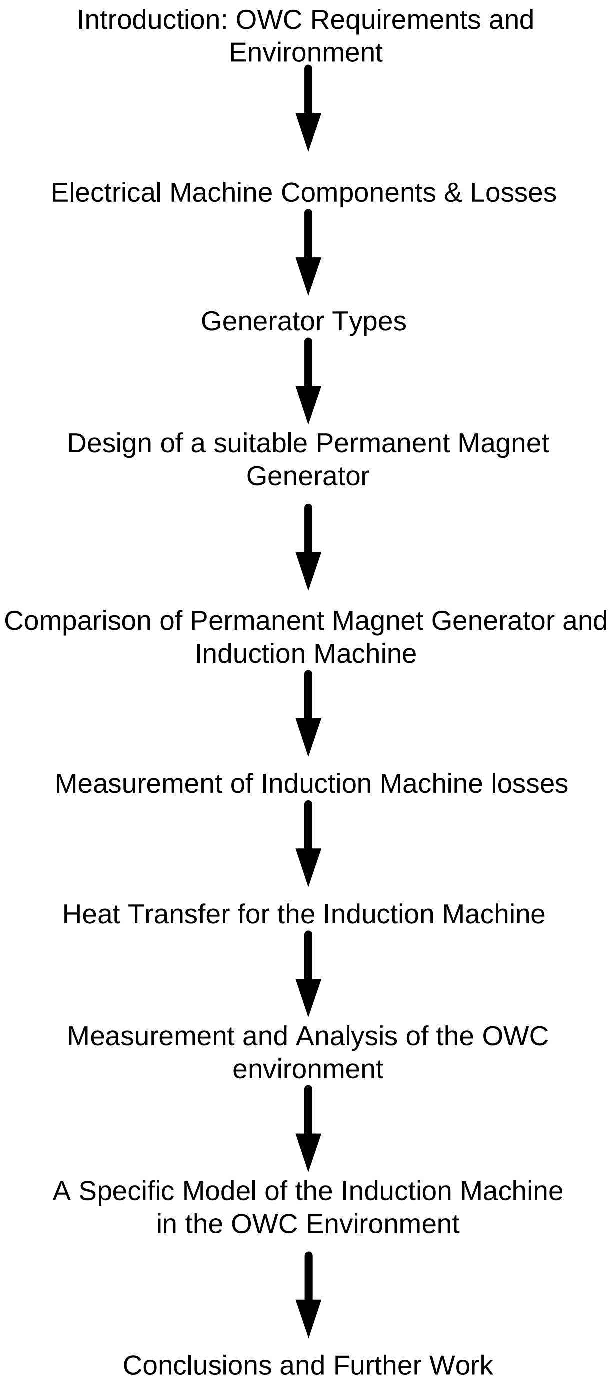

Figure 12: Chapter titles and layout of thesis

2

ELECTRICAL MACHINE COMPONENTS & LOSSES

2.1 Outline

This chapter provides a brief description of the main components of an electrical machine and the main losses in a machine. This is not intended to be an introduction to the electromagnetics, makeup and operation of electrical machines, several textbooks including “Electric Machinery Fundamentals” [33] provide this.

2.2 Components

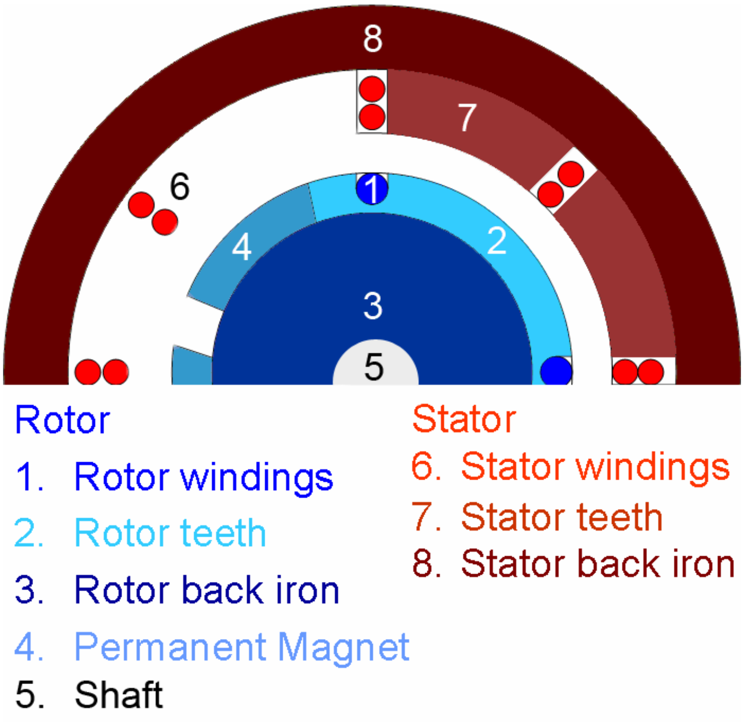

Figure 13: Axial cross section of electromagnetic components in typical locations for a radial machine. This shows all common components and is not an actual machine type.

Figure 13 shows the radial location of components within an electrical generator. All common components in electrical machines are shown for illustration. These components are described below.

2.2.1 Windings

The windings are typically composed of either strands of copper wire or copper bars surrounded by electrical insulation. At each end of the generator, past the end of the rotor is the endwinding, shown in figure 14. This is where the windings are routed around the circumference of the machine and back past the rotor or out to terminals. The pattern used in winding the machine depends on the machine type. In general a significant amount of the winding is made up by the endwinding. The working environment of the endwinding may differ substantially to the winding in core slots and it is of a relatively complex shape.

Figure 14: Endwinding and winding entering slots in an induction machine

The winding and endwinding of a machine are often the most temperature sensitive components. The insulation has a lifespan given by electrical, thermal and physical factors. If all other factors are held constant, this lifespan reduces rapidly with an increase in temperature [34]. This is due to the acceleration of chemical processes that eventually lead to the failure (usually mechanical then electrical [34]) of the insulation material. The IEEE Std 1-2000 [34] notes that although there are mechanical, electrical and environmental factors influencing insulation service life, thermal evaluation continues to be a useful test.

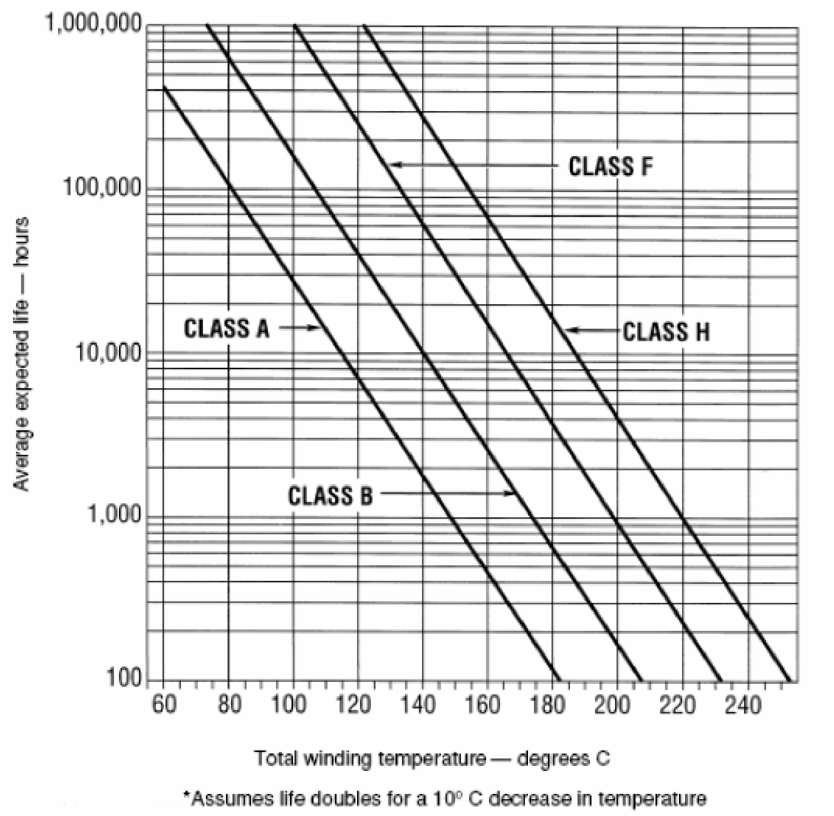

Figure 15: Expected insulation lifespan for different insulation classes plotted against temperature [35]

The degredation of insulation with temperature is approximated by the Arrhenius chemical rate equation. This assumes only a single chemical process and failure mode but is often valid in practice[34]. The lifetime at a given absolute temperature is given by equation 2 [36], some typical temperature/lifespan relationships are plotted in figure 15.

$$L_T = e^{((b/T)-a)} \tag{2}$$

Where b, a are constants for the insulation in use

T is the absolute temperature of the insulation in Kelvin

Roberts [36] states that the main criterion for motor protection is that the stator endwinding temperatures stay within agreed limits.

Where a machine has rotor conductors, they may be constructed in the same manner as the stator winding (generally where the rotor conductors are brought out to terminals) or by making a copper or aluminium cage. The cage lies in the core slots and is short circuited at each end by an endring. A cage rotor with aluminium endrings is shown in figure 16, the conductors are just beneath the surface of the core laminations. A cage rotor is generally simpler to construct than a winding and more robust. Thermal issues may occur in the rotor upon direct online generator startup where large rotor currents can be generated, however the generators in this thesis are started by a power converter. The shape of the rotor bars determines the starting and running characteristics of the generator. In some designs they may be entirely enclosed within the rotor core.

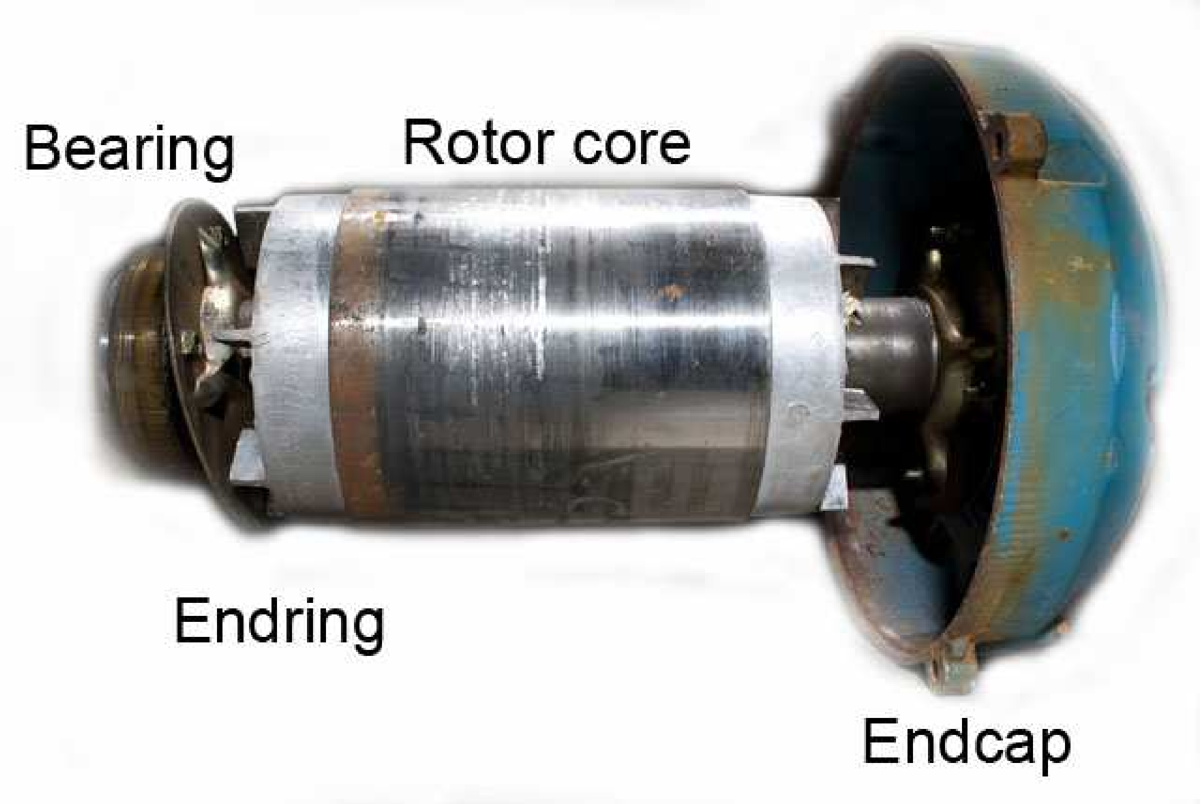

Figure 16: Induction machine rotor showing damage on core laminations, aluminimum endrings with cooling stirrers on both ends, exposed bearing on left and endcap on right

2.2.2 Core

The core sections are also known as the ‘iron’. It is made up of thin sheets of magnetic material (laminations) insulated from one another to reduce eddy currents normal to the flux path through the core. The machining involved in the production of the core can affect its performance. The insulation between laminations can be accidentally shorted or the magnetic properties of the material altered detrimentally and this is difficult to account for theoretically [37]. The core supports the windings where they are present and the stator core is fitted to the frame while the rotor core is fitted to the shaft.

2.2.3 Permanent Magnets

Permanent magnets can be constructed from a wide variety of materials and the choice of magnet type depends on the design of the electrical generator. Typically magnets are relatively expensive, mechanically and thermally sensitive and this must be taken into account when the generator is designed. The mounting of magnets is relatively simple when they are mounted in slots and more complex when surface mounted. This can complicate the production of a uniform airgap. The fitting of magnets can also contribute to the cost of a generator as permanent magnets are difficult to handle. This is more of a problem associated with large slow speed generators where construction is complicated by size.

2.3 Power converter control

Control of electrical machines by power electronics may be accomplished in different ways. Most common is frequency control, where the machine stator sees an applied frequency rather than the fixed frequency of the grid connection. The control mechanism is necessary in order to match the speed of the turbine to the incoming air, allowing optimum power takeoff. This system has a considerable cost associated with it and ways to reduce this cost are noted where the generator type allows. The losses inside the control mechanism are not considered in this thesis unless the machine choice influences them significantly.

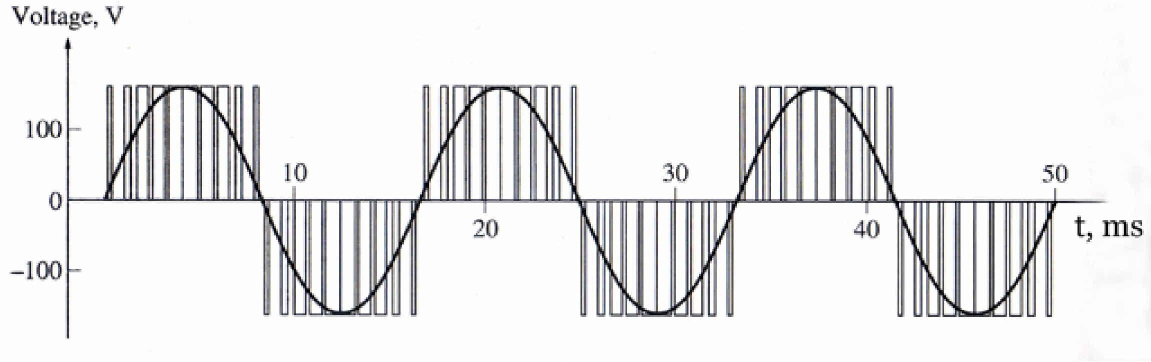

Figure 17: Pulse Width Modulation voltage waveform approximating a sinusoidal waveform [33]

Frequency control is typically accomplished by converting mains AC into DC then converting it back into variable frequency AC. The switching to make the variable frequency AC approximates a sine-wave by varying the amount of time the positive DC voltage is connected for, this is known as Pulse Width Modulation (PWM). The voltage waveform for a single phase and target sinusoidal waveform for this technique are shown in figure 17. This technique only approximates a sine wave and the difference creates high frequency harmonics. These harmonics cause additional losses, detailed in section 2.12.5.

2.4 Efficiency

The design of the electrical machine will determine its efficiency. This is the proportion of power output for a given power input commonly given as a percentage. The difference between input and output is known as the loss. Power is lost in several different ways and the quantity of power lost is determined by different factors for each. The factors determining loss and the methods for measuring the loss are described below.

2.4.1 Copper loss

The copper loss is a resistance heating loss, thus it is calculated (where a direct measurement of the current is possible) from equation 3.

$$P_{cu} = I^2 R \tag{3}$$

As the stator/rotor windings heat up, their resistance increases [37] and this feedback effect must be taken into account. The stator winding resistance can be measured directly, as can a wound rotor resistance. For a squirrel cage generator, rotor resistance losses are found by adding the core losses to the stator resistance losses and the stator output power [38]. For a slip ring supplied rotor, the brush-contact losses can be found from this measurement and the direct measurement of rotor resistance. For an induction machine rotor:

$$P_{cur} = (\mathrm{P}_{\mathrm{out}} + P_{cus} + P_{cl})s \tag{4}$$

Where P_{cur} is the rotor copper loss.

P_{out} is the electrical power output from the generator

P_{cus} is the stator copper loss

P_{cl} is the core loss

2.4.2 Friction and windage loss

The friction and windage loss is the loss of power to friction in the machine bearings and windage (aerodynamic drag) on the shaft and rotor. Thus it is proportional to shaft speed (bearing loss) and the cube of shaft speed (drag).

$$P_{fw} = fn(\omega_R^3, \omega_R) \tag{5}$$

Where ω_R is the shaft speed

It is found by plotting power input (no load) against voltage for multiple voltages (all at rated frequency). This forms a curve similar to figure 18. The curve is extrapolated to the zero voltage intercept. At zero voltage there can be no core loss thus only the friction and windage loss is present. For a wound rotor machine, brush friction loss will also be present.

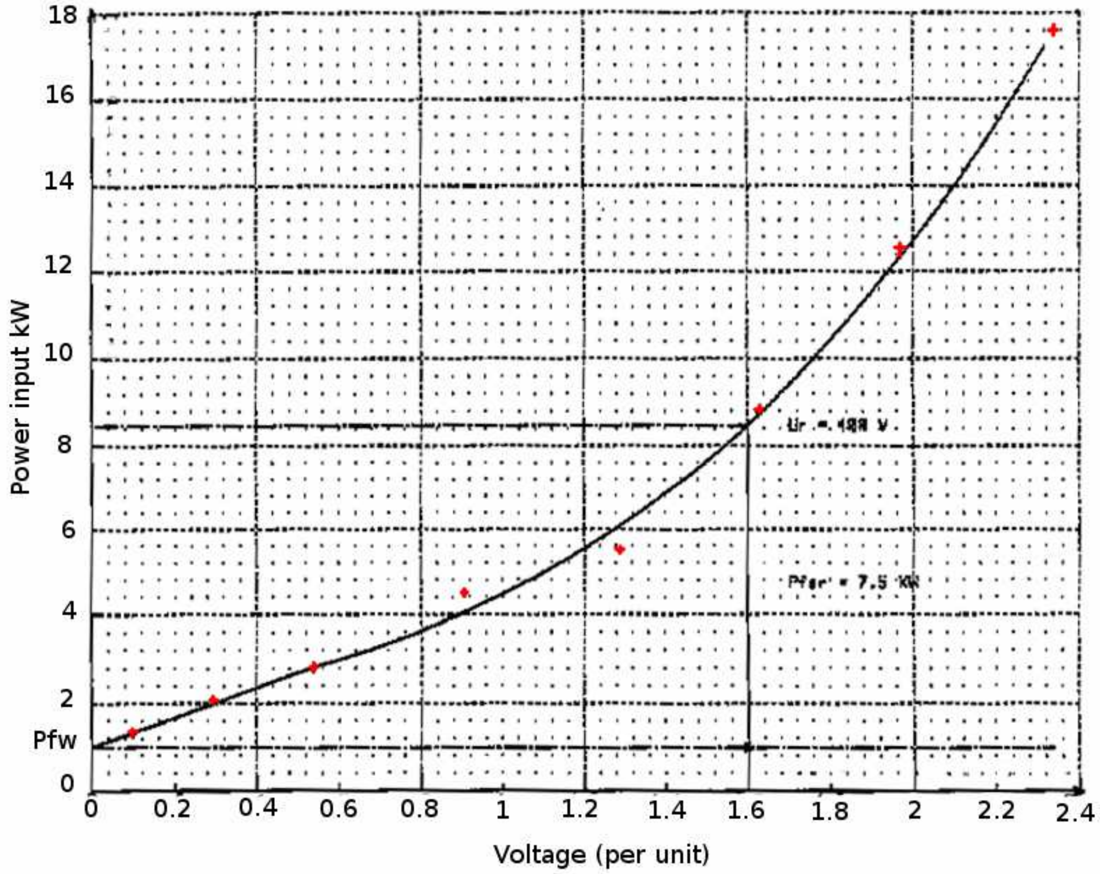

Figure 18: Power input (kW) against voltage (Per Unit) from Alstom [39]

2.4.3 Core loss

The core loss is made up of eddy current and hysteresis losses. These losses respond differently to the frequency of excitation (hence two frequency terms in equation 6) so are addressed separately.

$$P_{cl} = fn(f, f^2, B_m^2) \tag{6}$$

Where Pcl is the core loss

f is the frequency of magnetisation

Bm is the peak flux density in the material

Hysteresis is the loss of energy in the magnetisation, and demagnetisation of the core material. Thus it is proportional to the volume of material, applied flux density and the number of magnetisation/demagnetisation cycles per second [40]:

$$P_h = \eta \frac{M_c}{\delta} f B_m^x \tag{7}$$

Where P_h is the hysteresis loss

M_c is the mass of the core,

δ is the density of the core material

η is a constant of proportionality characteristic of the core material

x is a value around 1.7 to >2.0 dependent on the material used

Eddy current loss is the resistance heating loss from currents induced in the core material. Langsdorf [41] derives equation 8:

$$P_e = \varepsilon \frac{M}{\delta} f^2 B_m^2 t^2 \tag{8}$$

Where ε is an experimentally determined constant of proportionality that is inversely proportional to resistivity.

Note that the core losses are proportional to frequency to the power of x (hysteresis) and frequency squared (eddy current) respectively. The system under consideration may be inverter driven, and thus frequency can vary considerably. Thus the variation in core loss with frequency must be taken into account.

The sum of eddy current and hysteresis losses can be written as:

$$P_{cl} = k_e f^2 B_m^2 + k_h f B_m^x \qquad (9)$$

Where k_e, k_h and x are unknowns that represent the variation of eddy and hysteresis losses in the machine constructed. These coefficients are found by making measurements at three different frequencies and flux densities [38]. Alternatively k_e and k_h can be found from material properties and an additional scaling term introduced to take into account the change in properties due to machining of the material.

In a machine with teeth, the flux density will be greater in the teeth compared to the main core and should be accounted for separately in design calculations.

2.4.3.1 Variation with load

Mueller *et al* [42] have produced measurements to show that the total core loss also increases with load. Tests on an induction machine show that 50hz loss decreases while the high frequency loss increases. The high frequency losses are caused by pulsation in stator and rotor teeth. Although actually a core loss, important literature (such as the IEEE standard [38]) places these losses with the stray load loss. Hence the Brook Crompton performance calculations for an 18.5kW machine [43] show that the iron loss decreases and the stray load loss increases. This can be seen in figures 19 and 20.

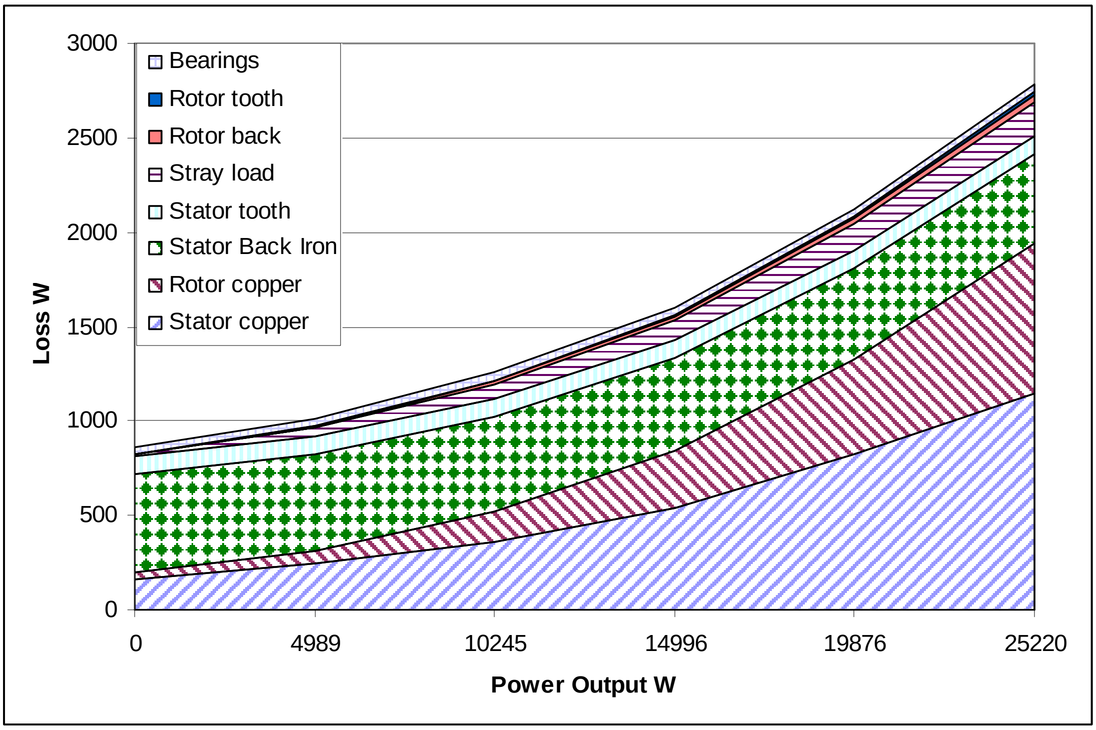

Figure 19: Change of losses for 18.5kW induction machine plotted from [43]

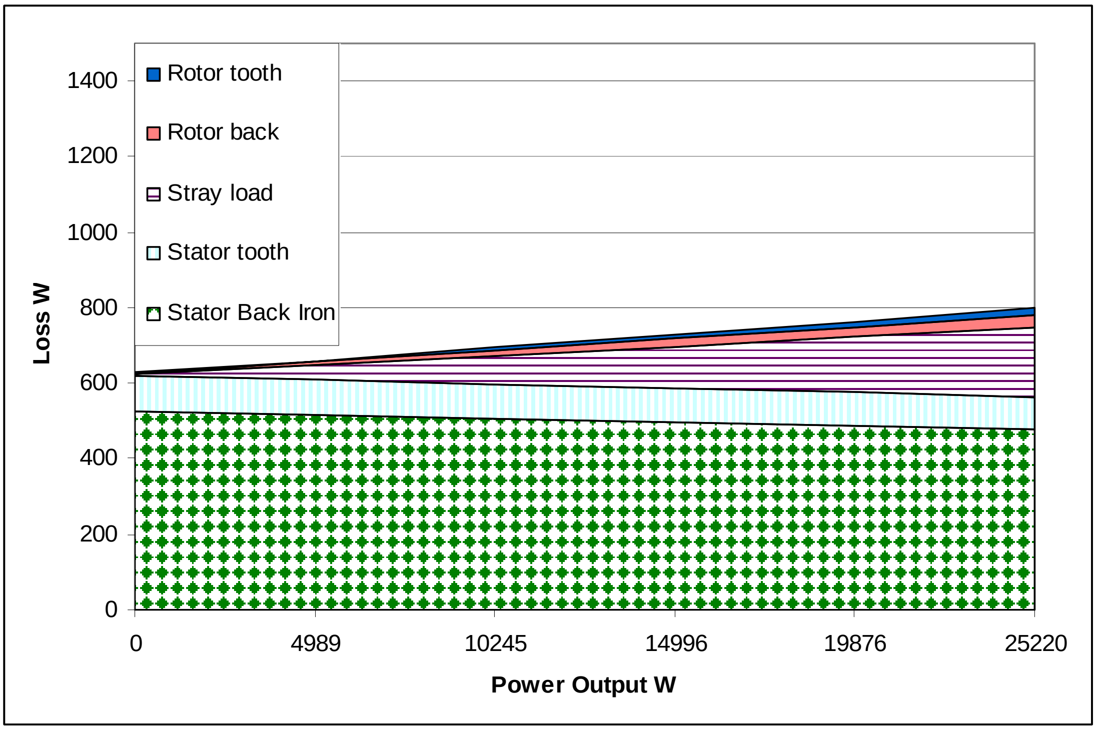

Figure 20: Change of core losses for 18.5kw induction machine plotted from [43]

The fundamental frequency stator core losses can be measured from an induction machine no-load power input. The rotor resistance loss in this case is negligible. The stator copper and friction/windage losses are subtracted from the input power, what remains is the stator core loss.

$$\text{Stator Core Loss} = \text{No Load Input Power} - \text{Stator Copper Loss} - (\text{Friction} + \text{Windage}) \tag{10}$$

2.4.3.2 Magnet Eddy Current loss

A permanent magnet generator may have eddy currents induced in the rotor magnets. Rare earth magnets have a relatively high electrical conductivity and can become demagnetised by this effect[44]. This loss can vary from negligible to significant depending on the stator layout [45]. The high order stator mmf harmonics rotate at a different speed to the rotor and will induce currents. Where stator slots are present the magnetic field in the magnets will alter and an eddy current will be induced. For these losses to be calculated the stator harmonics must be calculated, the analytical equations presented by Toda et al. [45] can then be used.

2.4.4 Harmonic loss

If a power electronic converter (inverter) is used to control the generator, an additional loss within the generator will be induced. A recent study of these losses was carried out by Green *et al* [46] using practical measurement and finite element analyses. Simulation results for a 2.1kW induction machine are shown in figure 18. Note the increase in stator and rotor iron losses. There is a power loss labelled as the inverter loss which is the loss within the inverter itself. This thesis does not consider inverter internal losses and the inverter loss referred to henceforth is the additional loss induced within the machine due to a non-sinusoidal supply. In figure 21 this is demonstrated as a considerable increase in stator and rotor iron losses. In the 2.1kW machine the difference in losses is 30W or 1.4% of the full load output power. There is an increase in copper losses but this is relatively small.

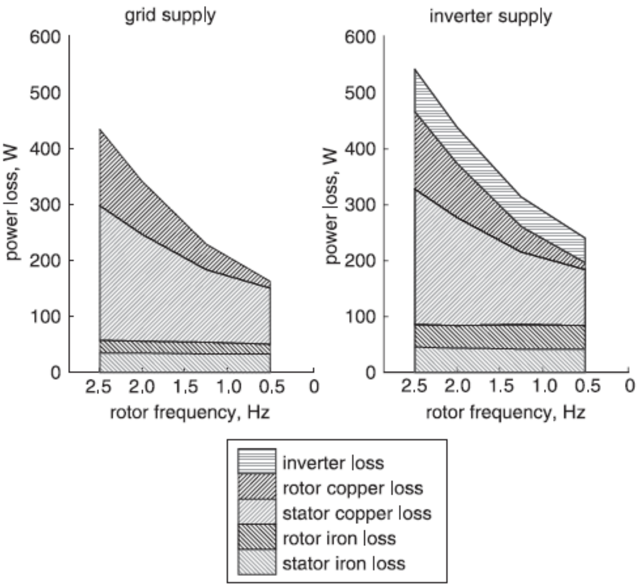

Figure 21: Variation of losses with rotor frequency with (left) and without variable frequency supply from Green *et al* [46]

2.4.5 Stray load loss

The stray load loss is a group of losses that are present in the machine, but not included in other loss categories and are hard to define and measure despite considerable study [47]. It is suggested the stray load losses are the differences between the theoretical and practical machine: "the core, windings and constructional features interact with main and leakage fluxes to produce a complex array of losses, some of which are voltage dependent and some are load or current dependent." [47]. Manufacturing imperfections and high frequency tooth pulsation losses will also be placed in this category [37].

Different standards are used when accounting for the stray load loss in an induction machine. IEEE 112 [38] provides for measurement or assumption. The JEC standard neglects stray load losses and the IEC standard introduces a fixed allowance for them [47]. A review by Slaets *et al.* [48] shows a considerable difference between similarly rated machines (greater than 1%). Sousa *et al.* [49] give the stator stray loss as:

$$P_{s\ln} = k_{\mathrm{sln}}\left[\frac{k_n}{f_n} + k_e\right]V_{\mathrm{sln}}^2 \tag{11}$$

Where V_{sln} is the voltage across the stator leakage inductance

K_{sln} is the stray load loss constant

The IEEE standard 112 [38] suggests two measurement methods for the stray load loss. The indirect method states that the stray load loss can be taken as the difference between the measured losses and the losses that can be accounted for by the copper, core, friction and windage losses. This is the method used in this thesis. Direct measurements are possible with methods that vary from machine type to machine type. Sufficient accuracy was obtained from the indirect measurement in chapter 6 so no direct measurement of stray losses was made.

2.5 Application of theory

The next chapter presents the suitable machine types and the principles of operation required to understand their advantages and disadvantages in this application.

3

GENERATOR TYPES

This chapter lists the generators suitable for use in Wells Turbine OWCs. The induction generator (used by Wavegen at present) is described first along with the doubly fed induction generator used by the PICO OWC. Synchronous machines are introduced, with and without permanent magnets providing the rotor field. The switched reluctance and other machine types are also considered.

3.1 Cage rotor Induction Machines

The induction machine is currently the most commonly used industrial electrical machine [50]. It consists of stator windings laid in slots and a cage rotor. The rotor is thus not directly connected to any external supply. Both stator and rotor generate rotating magnetic fields at the supply frequency and if the shaft speed differs from the field speed (also known as synchronous speed), currents are induced in the rotor bars and torque is generated. This torque will act to minimise the rotor currents by restoring shaft speed to field speed. The equivalent circuit of one phase of an induction machine is shown in figure 22. R1 is the stator resistance, X1 the stator leakage reactance, Rc is the loss in the stator core, Xm is the magnetising reactance, R2 is the rotor resistance, X2 is rotor leakage and R2 is the rotor resistance. E1 is the stator primary EMF, induced rotor EMF is represented by E_R.

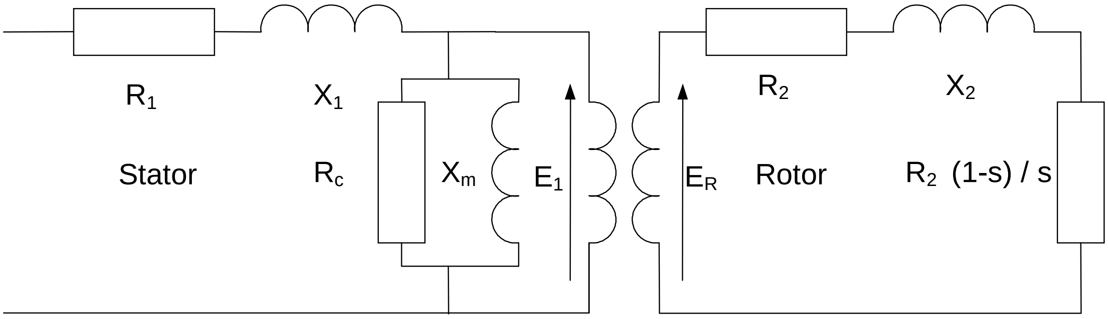

Figure 22: Equivalent per-phase circuit of cage induction machine [51]

When the rotor is below synchronous speed an accelerating torque is developed and the machine acts as a motor, above synchronous speed the machine acts as a generator. The ratio of the difference between shaft and synchronous speeds to the synchronous speed is known as the slip.

$$s = \frac{N_s - N_r}{N_s} \tag{12}$$

Where N_s is the stator field speed

N_r is the rotor or shaft rotational speed

Slip controls the torque as seen in figure 23, current draw and thus power output of the induction machine.

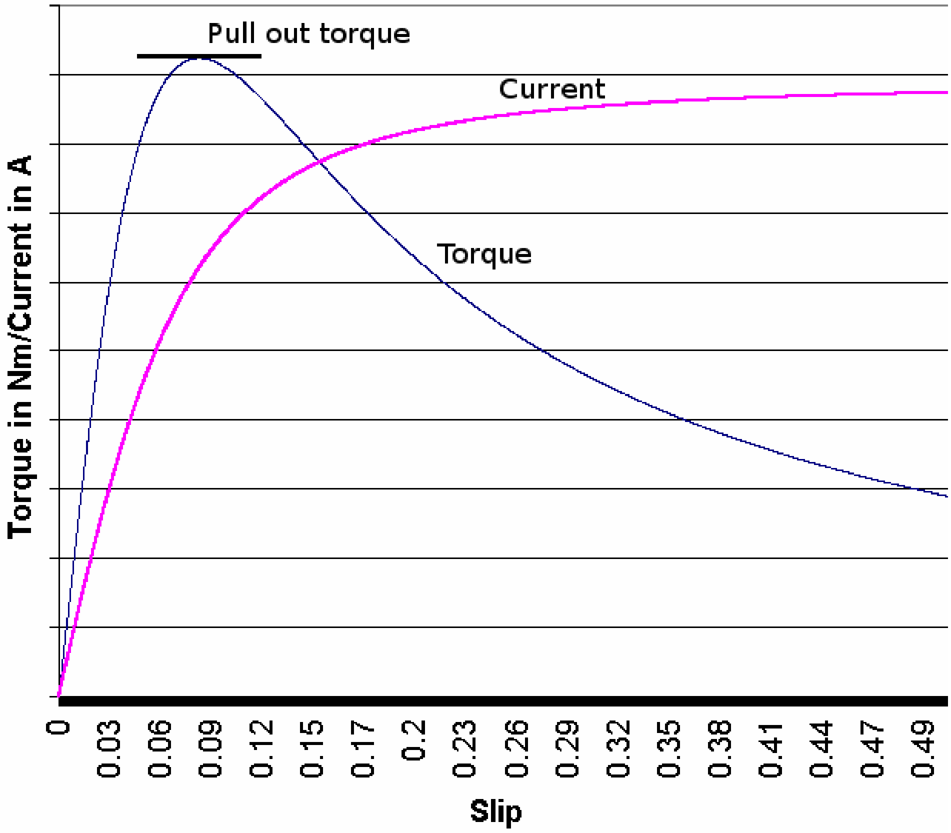

Figure 23: Per unit slip against torque and current for an induction machine

The machine rotor speed can vary over a narrow range with a fixed supply speed. Past a given slip torque reduces with increasing slip and a dangerous breakaway situation is obtained. A 150kW induction generator was used in an OWC application with a direct grid connection in Trivandrum, India, however it was designed specifically to have a wider than normal operating speed range [52]. This generator was later replaced with a Doubly Fed Induction Generator [53].

The induction generator, or the doubly fed induction generator, have been used on all recent industrial scale OWC installations and most wave energy converters in general. They have the advantages of being robust, simple and relatively cheap. The only wearing part on a cage rotor induction machine is the bearings although the stator insulation has a lifespan. This reduces failure rates and maintenance requirements. The efficiency of an induction generator is given by subtracting the loss mechanisms present from the power input. The loss mechanisms are identified in equation 13.

$$P_{out} = P_{in} - (P_{cu} + P_{fw} + P_{cl} + P_{hm} + P_{sl}) \tag{13}$$

Where P_{in} is the mechanical power input

P_{cu} is the copper loss

P_{fw} is the friction and windage loss

P_{cl} is the core loss

P_{hm} is the harmonic loss

P_{sl} is the stray load loss

3.2 Doubly Fed Induction Generator

The Doubly Fed Induction Generator (DFIG) is popular in the wind industry [18] and has also been employed on wave power plants, notably the PICO[54] and Trivandrum OWCs [53]. The DFIG has a wound rotor, which allows the rotor phase circuits to be brought out to external terminals via slip rings. The rotor winding currents can then be controlled, either by switching resistors, such as in the Trivandrum machine [53] or by a power converter, such as the PICO plant [54]. This arrangement is illustrated in figure 24.

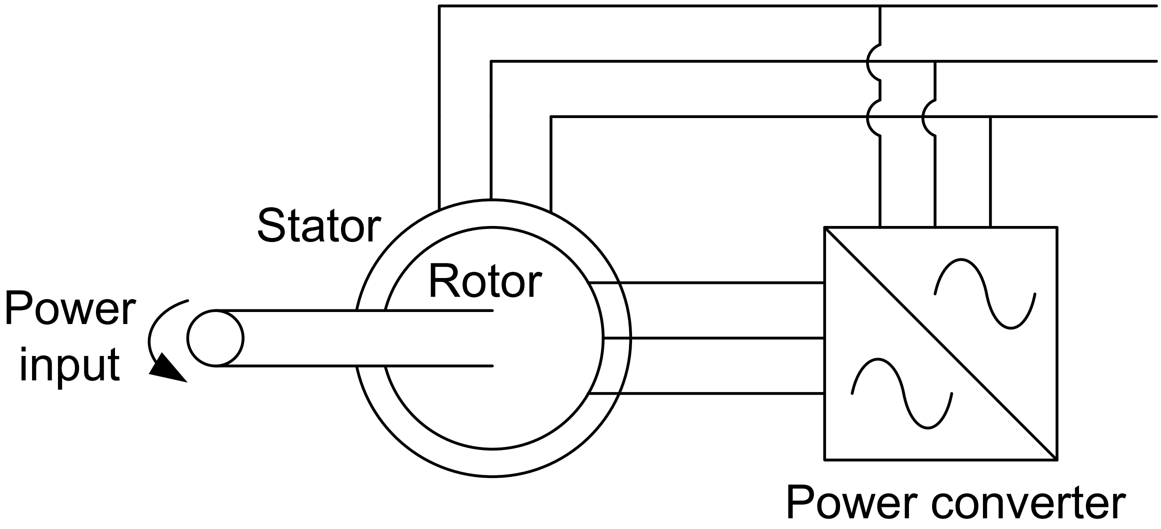

Figure 24: Doubly fed induction generator with power converter on rotor

This system has the advantage of reducing the size (and thus cost) of the power converter for a given machine rating. However, the speed range possible around the synchronous generator speed is the ratio of the rotor power converter rating to the full machine rating [55]. If the required speed range is less than zero to twice synchronous speed then a smaller power converter can be used. This will reduce the losses and the cost of the power electronics.

A wound rotor induction machine of a given rating will be more expensive than a squirrel cage type, especially in the case of a brushless DFIG. The brushes which provide an electrical connection to the machine slip rings present a failure risk and a maintenance requirement. These brushes cause losses in addition to those in a standard induction machine. There is a friction loss proportional to rotor speed and a loss due to brush resistance proportional to rotor current [37].

$$P_{out} = P_{in} - (P_{cu} + P_{fw} + P_{cl} + P_{h} + P_{sl} + P_{bw} + P_{br}) \quad (14)$$

Where P_{bw} is the brush friction loss
P_{br} is the brush resistance loss

For smaller generators, such as that used in the 18.5kW rated turbine, the reduction in converter rating may not bring a proportionate reduction in cost. Assembly and ancillary components can make up a significant portion of the cost of a converter system at relatively small scale. A quote from Control Techniques [56] gives the assembled cost of an inverter as double that of an unassembled kit. Hence the savings found at this scale will be limited. At larger scales, the relative cost of the power electronics may increase and the reduction in cost would be more significant.

3.3 Brushless Doubly Fed Generator

A machine with two stator windings of different pole numbers acting on the same rotor is known as the brushless doubly fed machine (BDFM). The BDFM allows a fractionally rated speed controller on one winding to control the power output of the other winding, achieving a similar reduction in converter size to the DFIG without the disadvantage of slip rings. The BDFM is a low speed machine, a 2 pole / 6 pole machine has a “natural” speed of 750RPM [57], suitable for larger OWC installations. The BDFM has the advantage of operating as a grid connected induction machine should the converter develop a fault [58], however the Wells turbine could stall or “break away” if operated in this condition. The BDFM will require 25% more active mass for the same output as a conventional induction machine [59] and this will reduce the benefit of a smaller converter. Considering this and the limited advantage of a smaller converter at relatively small scale, the BDFM is not particularly suited to this application.

3.4 Synchronous Generators

Synchronous generators differ from induction generators because the rotor field is stationary. The field is created by feeding DC current into the rotor windings. This forces the slip to zero as there must be no difference between stator field speed and shaft speed for a stationary rotor field. Hence the operating torque of a synchronous generator is only produced at synchronous speed. The rotor excitation requires a supply through slip rings or a rotor mounted permanent magnet generator. The excitation may be adjusted and the power factor of the machine altered. Accurate speed control may be achieved using a converter, however synchronous machines can be subject to loss of synchronism under transient conditions [51].

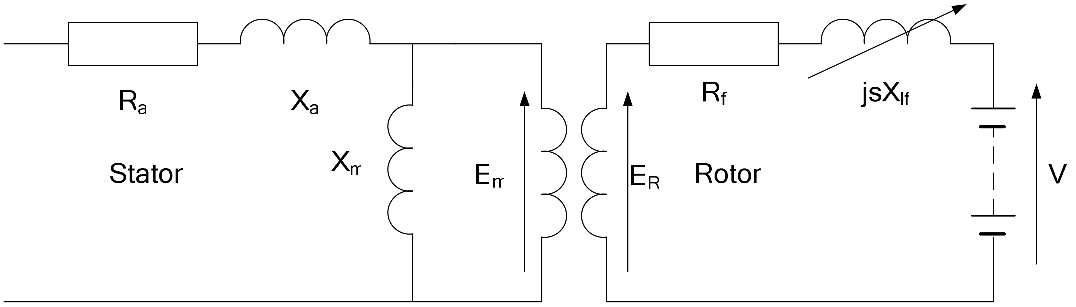

Figure 25: Equivalent circuit of a synchronous generator [51]

Figure 25 shows the steady state equivalent circuit of a synchronous machine, the AC supply to the armature (stator windings) on left and the DC input to the field winding (rotor winding) on right. The armature circuit remains the same regardless of how the excitation is provided to the field circuit. The field wound synchronous machine has stator and rotor windings and hence copper losses. An AC field is present in the stator core so there are stator core losses. There are also rotor core losses but these are negligible relative to the stator loss if a laminated rotor core is used [60]. The synchronous machine has brushes touching slip rings or a brushless system and consequently has a similar set of rotor supply losses to the DFIG.

The losses in a DFIG are given by equation 15:

$$P_{out} = P_{in} - (P_{cu} + P_{fw} + P_{cl} + P_{h} + P_{sl} + P_{bf} + P_{bc}) \tag{15}$$

Where P_{cu} is the copper loss
P_{fw} is the friction and windage loss
P_{cl} is the core loss
P_{h} is the harmonic loss
P_{sl} is the stray load loss
P_{bf} is the brush friction loss
P_{bc} is the brush contact loss

3.5 Synchronous Permanent Magnet Generators

A permanent magnet synchronous generator (PMG) has its rotor excitation supplied by the magnet, thus no slip rings or DC excitation source are necessary. A cross section is shown in figure 26. The stator can be the same as that for a synchronous generator or induction machine. They are becoming increasingly popular where a wide speed range is necessary. In addition they can provide greater torque for a given frame size than an induction machine and have greater efficiency. A typical permanent magnet machine has peak efficiency at relatively low load and efficiency changes little with increase or decrease in loading. While a wound coil has a limit on its electric loading imposed by its insulation temperature rating, a permanent magnet can produce an electric loading that is orders of magnitude greater. Equation 16 relates the coercitivity of a magnet to the current and turns required to achieve the same effect.

$$H_c T_m = nI \tag{16}$$

Where H_c is the coercivity of the magnetic material
T_m is the thickness of the magnet
n is the number of turns
I is the current

A 6mm thick Neodymium Iron Boron magnet with a Coercivity of 955kAm^{-1} would require 5730 amp turns to achieve a similar magnetomotive force. Achieving this combination in the same volume as a permanent magnet is impractical.

The PMG is subject to a cogging torque due to the interaction of permanent magnets and stator teeth. This can be rendered insignificant by skewing the stator and other measures [61]. This type of machine is normally used as a variable speed motor supplied by a controlled voltage and frequency [61].

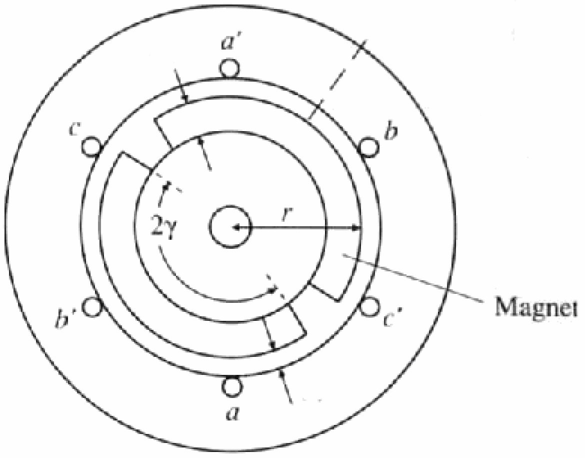

Figure 26: Two pole permanent magnet synchronous machine [40]

For the OWC application both radial flux and axial flux machine types can be considered. The axial flux machine has disc rotors of a similar diameter to the stator and flux passes along the length of the machine between them. An example of a north-north (referring to the relative alignment of magnets) machine is shown in figure 26. At 50kW or less a study conducted in [62] suggests that the axial flux type produces a greater torque per unit volume than the radial type. Also, as the windings of an axial flux machine can be placed into the airgap without stator slots, this eliminates tooth pulsation losses. However finite element analysis conducted in [63] shows that the magnetic loading of the machine will increase if stator slots are used. Electric and magnetic loading have equal contributions to the power output so the benefit of slots must be compared to the cost of slots and tooth pulsation losses [63]. Without slots retention of windings is made more complicated and may result in a larger airgap, decreasing the magnetic performance of the machine.

The power output is given by equation 30 noting that as with the synchronous generator there are no rotor core losses. An additional eddy current loss can be induced in the magnets due to the interaction of the higher stator harmonics and relatively conductive magnet material [64].

$$P_{out} = P_{in} - (P_{cu} + P_{fw} + P_{cl} + P_h + P_{sl} + P_{me}) \tag{17}$$

Where P_{me} is the magnet eddy current loss

3.6 The Switched Reluctance Generator

This is a special kind of salient pole synchronous machine that can produce torque without rotor excitation. The stator is made up of concentrated coil windings while the rotor is has poles but no coils. Coils on opposite poles are connected in series. Torque is developed by the tendency for the magnetic circuit to adopt a configuration of minimum reluctance, with the rotor core poles in line with the stator poles. The torque direction is independent of current flow.

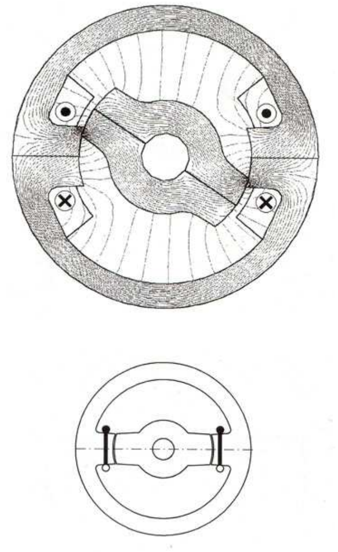

Figure 27: Two pole switched reluctance machine in unaligned position with flux paths (top) and aligned (bottom) [65]

Positive torque is produced when current flows in the phase winding as the inductance of the phase winding is increasing (The rotor pole and stator tooth are overlapping). The rate of rise of current is high in the unaligned position (Figure 27). When the rotor poles overlap with the excited stator teeth the inductance rises and the current is maintained constant with the aid of a chopping regulator. In this region, shear forces are generated that attempt to align the members. If the phase current was maintained as the poles become aligned the magnetic forces will try to close the airgap, and a negative torque will be induced if the current is maintained when inductance is reducing.

$$T = \frac{(\delta W' q N_{\gamma})}{2\pi} \tag{18}$$

The torque (equation 18) is calculated in terms of the co-energy W' (ΔWc in figure 28), the area enclosed by the operating trajectory in the flux linkage and current axes. The non-uniform torque generation creates a torque ripple and acoustic noise. This can be reduced by increasing the rotor poles, but this increases the switching frequency and thus the core losses.

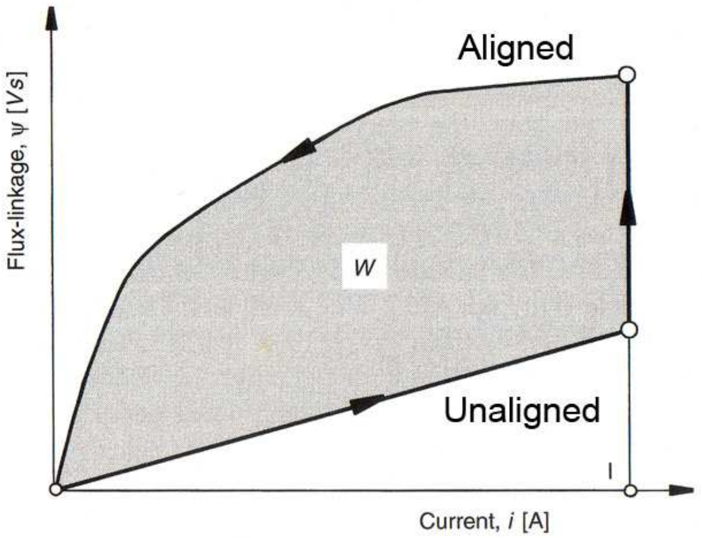

Figure 28: Co-energy, W in an ideal excitation cycle [65]

$$P_{out} = P_{in} - (P_{cu} + P_{fw} + P_{cl} + P_h + P_{sl}) \tag{19}$$

3.7 Other machine types

Specialist electrical machine types exist to fulfil exceptional requirements such as high force density, fault tolerance or low weight. However the OWC application is suitable for standard machine types and an exotic machine type is not necessary.

Other wave energy converters, notably Pelamis [66], use hydraulic power takeoff systems. A hydraulic system would allow accumulators to be used as energy storage, smoothing the power output from the system and providing a fixed speed output, eliminating the need for a power converter. However this would considerably complicate the power takeoff system, increasing maintenance requirements and adding losses in addition to the generator losses. Considering this, it is very unlikely that a performance advantage could be obtained by using hydraulics.

3.8 Discussion

Table 1 shows the loss mechanisms displayed by the electrical machine types discussed above. Machines with fewer loss mechanisms, particularly fewer no-load loss mechanisms, are more likely to have good part load efficiency and thus will tend to be better suited to an application with a broad range of input powers. The extent to which full load efficiency should be compromised for part load efficiency will depend on the input powers, which depend on the prevailing wave climate at the OWC installation. The effect of different efficiency curve shapes is explored by numerical simulation in chapter 5.

Table 1: Comparison of generator type and loss mechanisms, where a loss mechanism is present, it is highlighted in red

Generator Type	Induction Machine	Doubly Fed Induction Generator	Synchronous Machine	Switched Reluctance Machine	Permanent Magnet Generator
Harmonic Loss	🟥	🟥	🟥	🟥	🟥
Stray Load Loss	🟥	🟥	🟥	🟥	🟥
Friction & Windage	🟥	🟥	🟥	🟥	🟥
Stator Copper Loss	🟥	🟥	🟥	🟥	🟥
Stator Core Loss	🟥	🟥	🟥	🟥	🟥
Rotor Copper Loss	🟥	🟥	🟥		
Rotor Core Loss	🟥	🟥	🟥	🟥	
Brush Losses		🟥	🟥		
Magnet Eddy Current Loss					🟥

The doubly fed induction generator brings limited cost savings in the inverter at this scale while costing more due to the wound rotor of the generator. It also incurs brush losses in addition to the losses of a standard induction generator and the brushes introduce an additional maintenance requirement. The synchronous machine requires a DC excitation current to be supplied to the rotor and also has brushes. The switched reluctance machine is mechanically robust however a new power converter would be necessary to provide suitable switching. This decreases the amount of off-the-shelf components in the system, complicating repair and increasing the risk of implementation. The permanent magnet generator can be used with the existing control system, has no brushgear or excitation requirement. While eddy currents are induced in the rotor magnets, there are no rotor copper or core losses. This suggests that the permanent magnet generator is the best alternative to the induction machine for the OWC wave power application.

The next chapter describes the outline design of a set of permanent magnet generators specifically for the OWC application. Design choices are made and a model of the generator is created using a series of equations. This model predicts the performance of a generator at different power outputs and shaft speeds. These predictions are used to compare the permanent magnet design to the existing induction generator in chapter 5.

4

DESIGN OF A PERMANENT MAGNET GENERATOR FOR AN 18.5KW OWC APPLICATION

4.1 Introduction

A qualitative analysis of losses in the preceding chapter shows the Permanent Magnet (PM) generator to have the fewest loss mechanisms of the examined machine types. A quantitative assessment of the PM generators benefit in an OWC wave energy device is necessary to determine the advantage of changing generator type. This is only possible if the characteristics of such a generator are known. For this purpose a series of generators are designed using the theory in this chapter and outlined in the next chapter. This design begins with the discussion of the four main decisions defining the generator layout, next a series of more detailed decisions are made and the design equations are set out. An estimate of generator performance can be made from the design equations and this is used for comparison in chapter 5.

4.2 Permanent magnet generator design choices

A PM generator is designed to generate a realistic performance curve for further simulation work. There are four main choices that define the design of a PM generator[67]:

1. Airgap orientation, radial or axial
2. Stator type, longitudinal or transverse
3. Magnet location, surface or buried
4. Slotted or slotless stator

The choices will be made with the aim of maximising efficiency, reducing absolute losses and increasing maximum rating while creating a suitable machine.

4.2.1 Radial or axial airgap

The axial flux machine typically has two rotors to balance attractive forces across the airgap[62]. Each rotor is the full diameter of the machine thus the axial flux machine has a higher tip speed than a radial flux machine. The difference in windage between a double sided axial flux machine and a radial flux machine can be assessed by deriving the formula for power loss due to drag on a spinning cylinder starting from equation 33.

Peripheral drag on a rotating cylinder is given by equation 20 from [64]

$$P_{Dp} = C_f \rho \pi \omega^3 r^4 L \tag{20}$$

Where C_f is the drag coefficient of the cylinder
ρ is the density of the fluid in the airgap
ω is the angular velocity of the cylinder
r is the radius of the generator
L is the axial length of the generator

Drag on the face of a cylinder of external radius r and internal radius ri is given by equation 21 from [64]

$$P_{Df} = C_f \rho \pi \omega^3 (r - r_i)^5 \tag{21}$$

An axial flux machine rotor is composed of two cylinders each with diameter D and length L. The length to diameter ratio is taken from a prototype built at Durham University by Bumby & Spooner [67]. The second prototype axial flux machine detailed in [64] was rated at 29.5kW at 3000rpm (neglecting windage) and had a length to diameter ratio of 1:34. A radial flux machine rotor is composed of only one cylinder with volume identical to that of the axial flux machine's two rotors. This radial flux machine is assumed to have a length to diameter ratio of 1.5:1. Work by Sahin [64] gives the axial flux machine a torque density of 2.5 (2 pole) or 4 (4 pole) times that of the radial flux machine. Equation 22 gives the rotor radius of an axial machine relative to that of a radial machine of identical volume.

$$R_{radial} = 0.46 R_{axial} \qquad \text{2 pole} \tag{22}$$

$$R_{radial} = 0.54 R_{axial} \qquad \text{4 pole}$$

The full derivation is given as appendix i to this thesis. Equation 23 provides the result. Assuming the drag coefficients are equal it is estimated that the axial flux generator will generate between 18 and 40 times more drag than an equivalent radial flux generator.

$$P_{\mathrm{Da}} = 40\,\mathrm{P}_{\mathrm{Dr}} \qquad \text{2 pole} \qquad (23)$$

$$P_{\mathrm{Da}} = 18\,\mathrm{P}_{\mathrm{Dr}} \qquad \text{4 pole}$$

In order to generate power, the Wells turbine must be kept at operating speed between pulses of power input. Hence the windage of the generator is a no load loss in this application. It can be seen that a radial flux topology has lower windage losses than a comparable axial flux topology and thus the generators considered later in this thesis are of the radial flux type.

4.2.2 Longitudinal or transverse stator

The stator conductors can be laid out either along the length of the machine core (longitudinal) or in rings circumferentially around the machine core (transverse). These layouts are illustrated in figures 29 & 30.

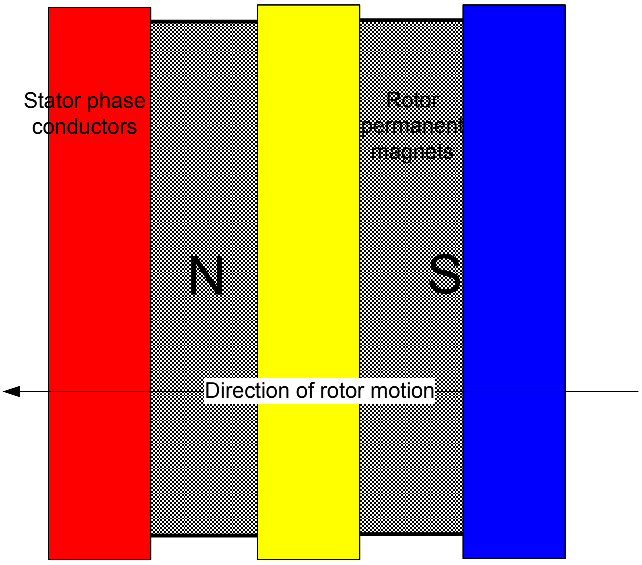

Figure 29: Relative conductor alignment and rotor motion in a longitudinal machine

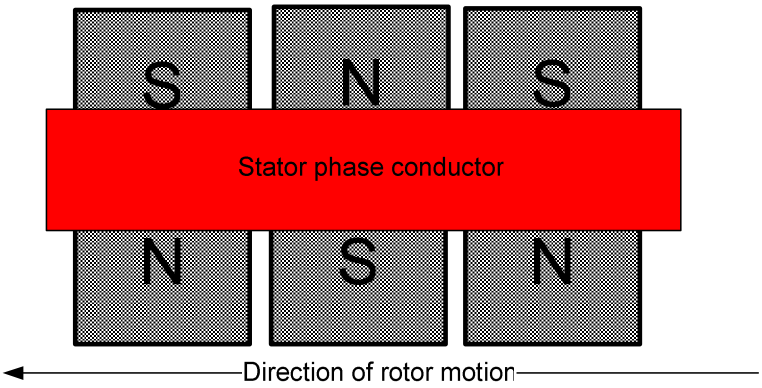

Figure 30: Relative conductor alignment and rotor motion in a transverse machine

Transverse flux PM (TFPM) machines are considered to have much higher force densities than conventional PM machines [68]. However due to the very large leakage fluxes they have a poor power factor [68]. Therefore the converter rating must be larger than the rated power output of the machine. If a longitudinal machine can be fitted into the turbine hub, it will be cheaper to specify a converter for and thus better suited to this application.

4.2.3 Surface mounted or flux concentrating (buried) magnets

The permanent magnets on the rotor can either be placed in the airgap or in the rotor core. If the magnets are placed within the rotor core, design of the core allows flux from the magnets to be concentrated. Locating magnets in the core also facilitates their retention.

The layout and flux paths of a surface mounted PM machine is shown in figure 31, adapted from Dubois [69]. Equation 24 is given by the application of Ampere's law around the illustrated path. The reluctance of the iron is assumed to be negligible.

$$\oint hdl = 2H_m t_m + 2H_a(t_a + c) = NI = 0 \tag{24}$$

Where t_m, t_a and c are defined in figure 31.

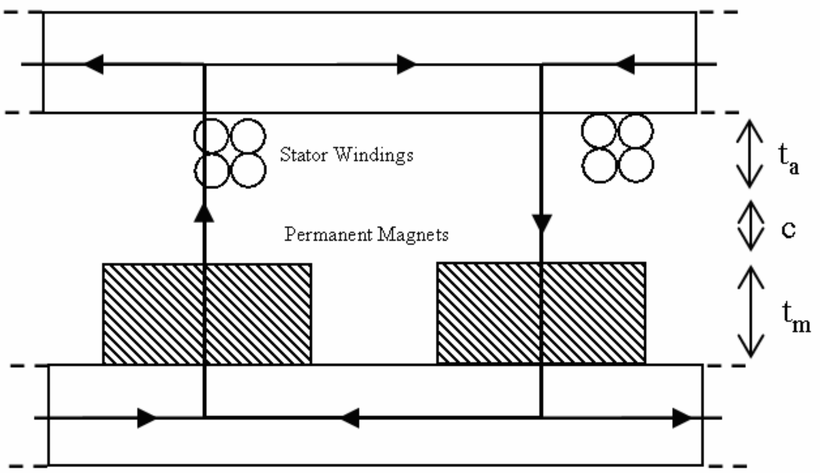

Figure 31: Layout and flux path of a surface mounted permanent magnet machine

The magneto motive force (mmf) gradient of the magnet is given by equation 25:

$$H_m = \frac{B_{gap} - B_{rem}}{\mu_o \mu_r} \tag{25}$$

Where B_{rem} is the remnant flux density of the magnet

B_{gap} is the airgap flux density

μ_o is the relative permeability of free space

μ_r is the recoil permeability of the magnet

H_m is the magnetomotive force gradient of the magnet

The flux generated by the magnet must flow through the airgap.

$$B_{gap} = \mu_0 H_a \tag{26}$$

Where H_a is the magnetomotive force gradient in the air

Substituting (25) and (26) into (24) gives equation 27 for flux density

$$B_{gap} = \frac{B_{rem} t_m}{t_m + \mu_r (t_a + c)} \tag{27}$$

Where t_m is the thickness of the magnet

The term on the bottom of equation 27 can be rearranged into an "effective" airgap of thickness given by equation 28.

$$g_{eff} = \frac{t_m}{\mu_r} + t_a + c \tag{28}$$

Thus the airgap flux density with surface mounted magnets is given by equation 29. It can be seen that the chosen magnet must have a remnant flux density greater than the desired airgap flux density.

$$B_{gap} = \frac{B_{rem}}{\mu_{rec}} . \frac{t_m}{g_{eff}} \tag{29}$$

The airgap flux density of a generator with flux concentration (magnets set into rotor as in figure 33) is given by equation 30. In this case pole face width, magnet height and thickness can be set so as to obtain useful airgap flux values from magnets with a low remnant flux density. This means that low cost ferrite magnets can be used [69]. The cost saving in the magnets must be set against the additional cost of the flux concentrating steel and the more complex shape of the rotor.

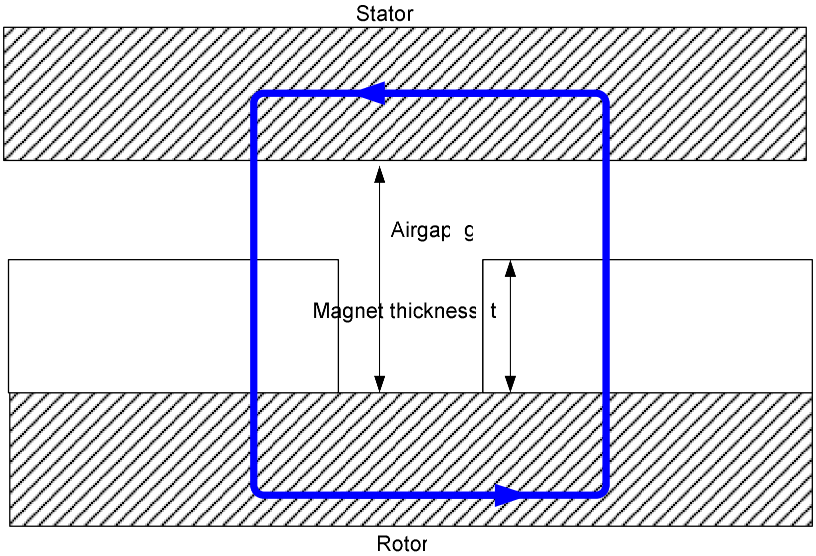

Figure 32: Permanent Magnet machine with surface mounted magnets [69], flux path marked in blue

$$B_{gap} = \frac{B_{rem}}{w/h + 2\mu_{rec}(t_{mag} + t_a + c)/t_m} \tag{30}$$

Where w, h and t_m are shown in figure 33.

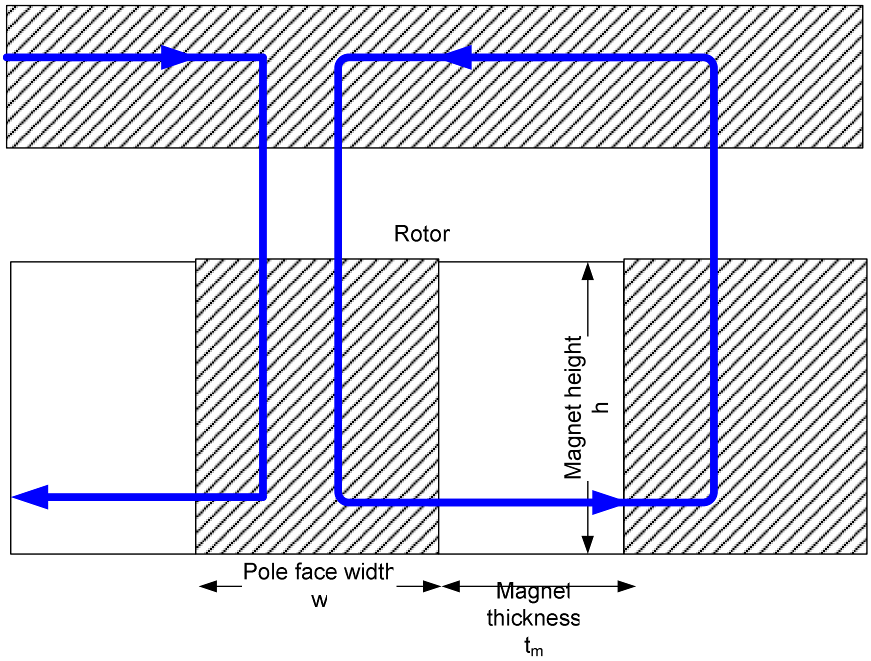

Figure 33: Permanent Magnet machine with flux concentrating magnets [69]

Dubois [69] argues that the cost of ferrite magnets is 1/10th that of a rare earth magnet (this will change with the market for such magnets) however 12 times more magnet will be required bringing no advantages in mass or cost reduction. Hence rare earth magnets are chosen for the PM generators. If the relative cost of permanent magnets changes significantly then this design decision may have to be revisited.

4.2.4 Slotted or slotless stator

The stator conductors may reside in “teeth” or slots which carry magnetic flux and support the conductors. This is advantageous as the airgap is reduced by the conductor height (the conductors are now in the magnetic circuit, not the airgap) allowing a higher airgap flux density for a given magnet thickness as the magnetic circuit has lower reluctance. Thus a machine of a given rating can be smaller. The slots also aid retention of the windings, the retention system in a slotless machine will also increase the airgap of the generator. However the slots are subject to high frequency pulsation losses. Mueller[42] measured this loss as 2% full load power at no load and 3.6% at full load for a 4 pole 37kW induction machine. Considering only the stator losses from that measurement (suitable for a PM machine) the loss is 1.2% at no load and 1.7% at full load.

A slotless stator has lower iron losses as the tooth pulsation losses are removed. It also has the advantage of improved cooling if the airgap air can be forced past the winding, Bumby [67] notes that an exposed winding could dissipate heat better than an enclosed one. However, for the wave energy converter application this advantage is reduced as the machine must be totally enclosed to prevent ingress of salt or water. In a slotless machine there is an increase in copper loss due to magnetic flux inducing eddy currents in the stator winding [67].

The choice between a slotted and slotless stator is between an increase in fixed iron losses or an increase in copper loss coupled with a less powerful machine for a given size. As the machine maximum dimensions are determined by turbine aerodynamics, it may not be possible to achieve the required rating with a slotless machine in smaller turbines.

4.2.5 Magnet design

The choice of a surface mounted topology requires a magnet with a high remnant flux density. The magnets used in the design of PM generators in this thesis are neodymium iron boron (NeFeB).

4.2.6 Stator design

4.2.6.1 Slots per pole per phase

At a given supply frequency the tooth eddy current losses increase with slots per pole per phase. To achieve a reasonably sinusoidal induced EMF, a minimum of two slots are necessary [70].

4.2.6.2 Slot closure

For stator slots the narrower the slot opening, the greater the maximum airgap flux density for a given amount of magnet. However totally closed slots increase the leakage flux and thus the iron losses [70].

4.2.6.3 Pole number

As the pole number increases, the length of end turn is reduced and the resistance per active length of coil is reduced. The stator yoke thickness is also decreased, allowing the rotor to be made larger for a given frame size and increasing torque. The optimum number of poles differs depending on the application and is limited by the number of stator slots in smaller machines.

Mi [70] compared 2, 4, 6 & 12 pole machines at 1800rpm and found that the 2 pole machine has the lowest efficiency and torque. The largest increase in torque and efficiency was between 2 and 4 poles. Experimental work presented by Mi [70] uses a 4 pole induction machine stator with a PM rotor. This work shows a considerable increase in efficiency, power output and power factor and a reduction in losses.

The choice of pole number will be made by modelling different machines using data from an OWC numerical simulation.

4.3 Detailed design equations

The Permanent Magnet machine was modelled using a series of design equations. This meant that different designs could be easily modelled. The inputs into the design equations are outlined in table 2:

Table 2: Design equation variables

Quantity	Symbol	Unit
Speed	ω	*rad/s*
Resistivity	σ	Ωm
Magnet width/pitch	α	-
Magnet recoil permeability	μ_r	
Wire diameter (inner)	a_i	m
Copper conductor area	A_{cu}	m^2
Flux density	B	T
Running Clearance	c	m
Taped conductor diameter	d_t	m
Pole number	P	-
Radius	r	m
Surface heat transfer coefficient	H	w/m^2
Stator core thickness	h_{sy}	m
1st harmonic spread factor	$k1$	-
Wire packing factor	k_p	-
Electric loading	κ	A/m
Axial length	L	m
Turns per coil	n_{coil}	-
Number of Layers	N_L	-
Wire insulation thickness	t_{oi},t_{ci}	m
Radial thickness of armature	t_a	m
Radial thickness of magnet	t_m	m
Winding temperature	T_w	C
Ambient temperature	T_{amb}	C
Circumferential width	w	m
Number of wires per conductor	W	-
Core loss factor	θ	W/m^3

4.3.1 Initial Design Decisions

The following parameters were set at the beginning of the design process:

- The maximum outer diameter is set by the dimensions of the Wells turbine. For the 18.5kW turbine the maximum diameter is 320mm.
- The speed is determined by the air flow rate through the turbine and for the purposes of this design a nominal speed of 3000rpm has been assumed. This is the nominal speed of the induction machine that is currently used.
- An aspect ratio of 1.8:1 length:diameter was chosen as appropriate for this machine to fit within the required dimensions.
- A running clearance of 2mm was deemed appropriate for the manufacture of a machine of this size.
- The harmonic spread factors were taken from work done on prototype slotless axial flux permanent magnet machines by Bumby [67]. As were initial wire and insulation thicknesses.
- The maximum winding temperature was set at 155°C suitable for class F insulation. The external ambient temperature was set to 40°C for comparative purposes (this is the temperature at which other generator data was available). A measurement of ambient temperature in the small turbine duct in summer in the proposed location would be a more suitable value.
- The surface heat transfer coefficient was set at 50 $W/m^2/K$ suitable for forced convection from the airflow past the machine[71].
- A magnet thickness of 5mm was chosen (except where noted) as this gave the appropriate power output at 3000 rpm.
- The maximum stator flux density was 1.2 T to avoid saturation of the stator core material.

4.3.2 Design equations for a slotless machine

The design equations are based on work by Bumby[67] and are included in this thesis for completeness.

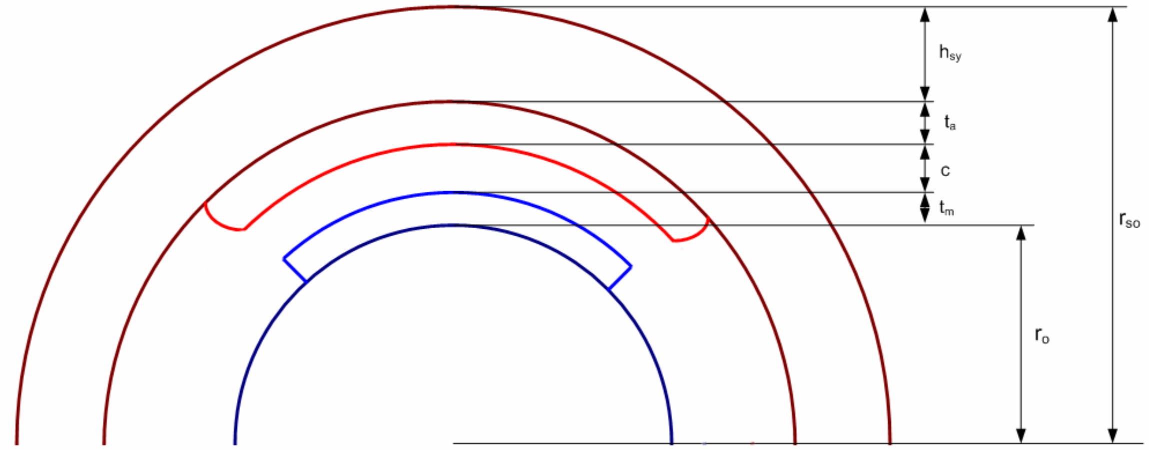

Figure 34: Dimensions of radial flux generator

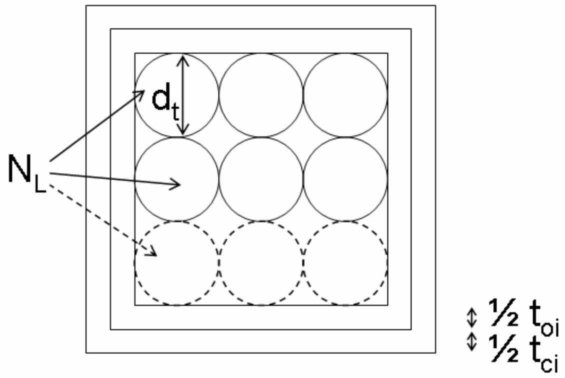

Figure 35: Components of winding height

The total winding thickness, t_a in figure 34, is calculated from equation 31.

$$t_a = d_t N_L + t_{oi} + t_{ci} \tag{31}$$

Where d_t is the diameter of the taped conductor as illustrated in figure 35.

N_L is the number of layers of conductors

t_{oi} is the winding outer insulation thickness

t_{ci} is the winding inner insulation thickness

The airgap flux density is given by equation 32:

$$\hat{B}_g = \frac{B_{rem} t_m}{\mu_r \left(\frac{t_m}{\mu_r} + c + t_a\right)} \tag{32}$$

Where $\hat{B}_g$ is the peak airgap flux density

B_{rem} is the remnant flux density of the magnet

μ_r is the recoil permeability of the magnet

The magnetic flux per pole is given by equation 33, assuming that the airgap flux density is sinusoidal in shape. Bumby [67] states that this is a better assumption than trapezoidal flux density for a slotless surface magnet machine.

$$\hat{\varphi}_{p/p} = \frac{\hat{B}_g L_r \pi (r_0 + t_m)\alpha}{\sqrt{2}P} \tag{33}$$

Where P is the number of pole pairs

α is the ratio of magnet width to pole pitch

L_r is the axial length of the rotor magnet

The generated EMF per phase is given by:

$$EMF = \sqrt{2}\pi f k_1 P n_{coil} \hat{\varphi}_{p/p} \tag{34}$$

Where f is given by equation 35

k_1 accounts for the spread of the coil.

$$f = \frac{\omega P}{2\pi} \tag{35}$$

The stator yoke thickness is the thickness that will maintain an acceptable level of stator flux density (non-saturating) for a given airgap flux density. It is calculated from:

$$h_{sy} = \frac{\phi_{p/p}}{2B_{sy\max}L_s} \tag{36}$$

Where h_{sy} is the stator yoke thickness

$B_{sy\,\max}$ is the maximum acceptable stator flux density

L_s is the stator length

The outer radius of the machine core can then be determined from:

$$r_o = r_i + t_{mag} + c + t_a + h_{sy} \tag{37}$$

This is a design constraint for the machine as it cannot exceed the radius of the turbine hub. This limits the external radius of the machine (including frame) to 161.5mm.

The mass of the core is calculated from the geometry of the machine in equation 38:

$$M_{core} = \rho_{core}(r_{so}^2 - r_{si}^2)\pi L_s \tag{38}$$

Where ρ_{core} is the density of the core material.

r_{so} is the stator outer radius

r_{si} is the stator inner radius

Bumby [67] uses a curve fitted to published data to produce an accurate equation for the core hysteresis loss for a slotless machine. This should provide a more accurate estimate than the modified Steinmetz formula from [72] as it is based on relevant measured data. The results from both equations differ by a maximum of 20% for a 4 pole 3000rpm machine. The loss is calculated by scaling a core loss factor measured at an electrical frequency of 50Hz and core flux density 1.5T to the frequency and flux density of operation. The equation for this scaling is:

$$P_{iron} = \theta\left(\frac{f}{50}\right)^{1.32}\left(\frac{B_{sy}}{1.5}\right)^{1.97} M_{core} \tag{39}$$

Where θ is the loss factor of the core material

The eddy current loss in a slotless machine winding occurs in the stator windings and is estimated by:

$$P_{eddy} = \frac{1}{32}\left(2\pi B_{sy} a_i\right)^2 \frac{2n_{coil}W}{\sigma_{hot}} L_s \left(\frac{\pi a_i^{\,2}}{4}\right) \tag{40}$$

Where P_{eddy} is the eddy loss

a_i is the coil wire diameter

n_{coil} is the number of turns per coil

W is the number of wires per conductor

σ_{hot} is the conductor resistivity at operating temperature

The turn length is required to calculate the coil resistance and is calculated as:

$$L_{turn} = 2L_s + 2\tau_c \tag{41}$$

Where τ_c is the coil pitch

The coil resistance allows the calculation of the heating effect of a given current, thus the rating of the machine. It is calculated as:

$$R_{coil} = \frac{n_{coil} L_{turn} \sigma_{hot}}{A_{cu}} \tag{42}$$

Where A_{cu} is the conductor area in the winding

The maximum acceptable copper loss is given by subtracting the non-copper losses from the ability of the machine to dissipate heat. This is a crude analysis to establish the maximum rating of the machine.

$$P_{cu\max} = 2\pi R_{so} L_s H(T_{\max} - T_{amb}) - P_{eddy} - P_{iron} \tag{43}$$

Hence the maximum current that can be passed through a winding is:

$$I_{\max} = \sqrt{P_{cu\max} / R_{coil}} \tag{44}$$

The electric loading of the machine is given by:

$$\kappa = \frac{I_{rated} n_{coil} * \text{ number of coils}}{\pi L_s} \tag{45}$$

The armature reaction is given by:

$$B_{ai(pk)} = \frac{\sqrt{2}\kappa\tau_{pm}\mu_0 k_1}{\pi(\frac{t_m}{\mu_r} + c + t_a)} \tag{46}$$

The value of armature reactance X_d:

$$X_d = \frac{B_{ai}}{B_{gap}} * \frac{V_{base}}{I_{base}} \tag{47}$$

Where V_{base} is the fundamental EMF per phase

I_{base} is the rated coil current

The hot coil resistance is given by:

$$R_{coilhot} = \frac{R_{coil} * \text{number of coils}}{3} \tag{48}$$

The load resistance is calculated by vector subtracting the armature reactance from the machine impedance and subtracting the hot coil resistance.

$$R_{load} = \sqrt{\left(\frac{EMF}{I_{\max}}\right)^2 - X_d^2} - R_{coilhot} \tag{49}$$

The maximum power output of the machine can therefore be calculated as the load resistance is known:

$$P_{\max} = 3 I_{coil}^2 R_{load} \tag{50}$$

4.3.3 Magnet Eddy Current loss

It is noted by Zhu et al. that rotor eddy current loss (in the magnets) is relatively small compared to stator copper and iron losses [73]. It could overheat the magnets if rotor heat dissipation is relatively poor. The rotor heat dissipation depends on the exact rotor design as does the eddy current loss itself. Magnet retention method can play a significant part in the eddy current loss [73] and has not been dealt with in the design so far. The harmonics that induce the loss depend on the stator slot design [45] and it is noted in the next section the choice of whether to have slots or not is not answered yet. The loss also depends on rotor speed, the power converter used and stator current [73]. As this relatively small loss acting not directly on the most temperature sensitive machine component that is difficult to quantify with any certainty and will almost certainly change in a detailed design it is neglected at this stage. It is noted however that this renders the PM machine losses optimistic when compared with a measured induction machine.

4.3.4 Core loss in slotted machine

The slotted machine case is more complex than the slotless as additional loss mechanisms are present. A simplistic analysis is presented here in lieu of measured data. The more complex loss mechanisms mentioned in section 4.2.4 are ignored. Instead the losses for the additional stator components are approximated using the modified Steinmetz formula (equation 51) from [72] which only includes the fundamental frequency eddy current and hysteresis losses.

$$P_{fe} = k_{addloss}\left[k_{hysteel}\left(\frac{f}{50}\right) + k_{eddysteel}\left(\frac{f}{50}\right)^2\right]\left[m_{st}\left(\frac{B_{st}}{1.5}\right)^2 + m_{sy}\left(\frac{B_{sy}}{1.5}\right)^2\right] \tag{51}$$

Where $k_{hysteel}$ is the loss per kg of the magnetic steel due to hysteresis losses

$k_{eddysteel}$ is the loss per kg of the magnetic steel due to eddy current losses

$k_{addloss}$ is the additional loss scale factor due to machining of the magnetic steel

m_{st} is the mass of the stator teeth

m_{sy} is the mass of the stator yoke or back iron

B_{st} is the flux density in the stator teeth given by equation 52

$$B_{st} = B_{gap}(1 + \frac{w_{teeth}}{2\pi r_{si}}) \tag{52}$$

Where w_{teeth} is the circumferential width of the stator teeth

r_{si} is the inner radius of the stator

4 pole slotted and slotless machines of identical power output were designed using equations 31 to 50. The slotted machine is unoptimised and intended for comparison at this stage. At 3000rpm the slotless machine had no load losses of 242W and the slotted machine of 303W. The efficiency curves of both machine types are compared in figure 36. The slotless machine is more efficient at part load, due to lower no load losses, however the difference is negligible near full load.

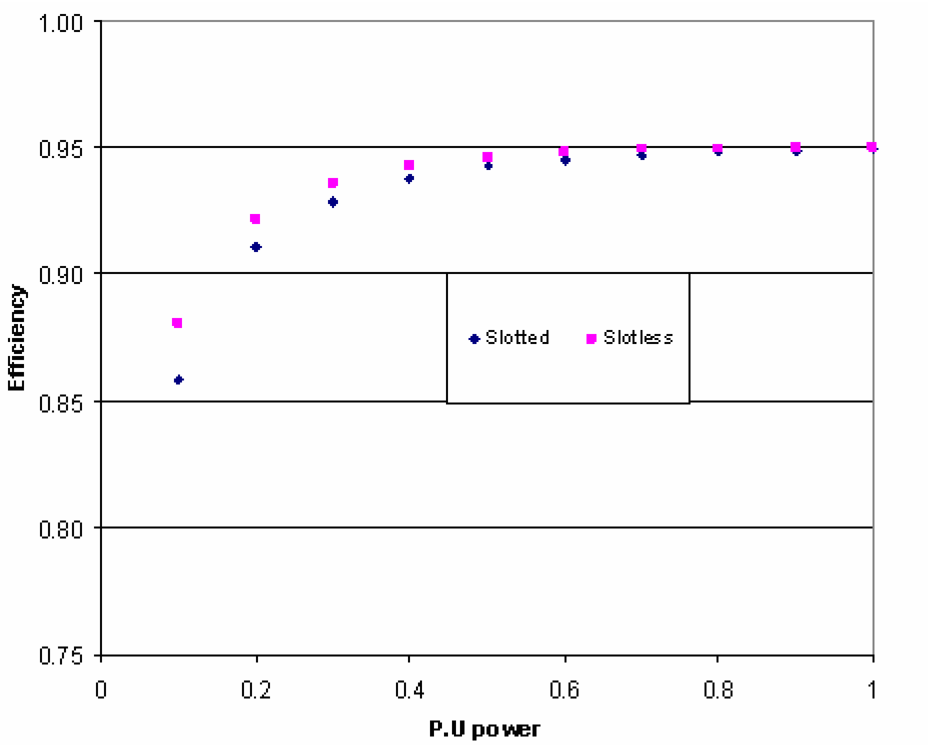

Figure 36: Calculated Efficiency vs P.U power with 22kW base of slotted and slotless machine

The machine costs are compared using the following materials costs from [69] set out in table 3:

Table 3: Materials costs for Permanent Magnet machine

C_{cu}	6	Euro/kg
C_{pm}	40	Euro/kg
C_{fe}	6	Euro/kg

Table 4 gives the costs for each machine type:

Table 4: Cost breakdown of slotted and slotless machine

	Slotless	Slotted
Copper cost	37	37
PM cost	231	65
Fe cost	992	1313
Total	**1260**	**1414**

It can be seen that the reduction in permanent magnet cost for the slotted machine is outweighed in this case by the increased iron cost. The overall costs are very similar and the uncertainty in the cost and performance analysis is sufficient to say they are equal for the purposes of the comparison chapter. The iron losses in a slotless machine are more accurately determined by analytic methods so the comparison work will be conducted with a slotless machine. The relative similarity between the estimated machine performance means that if the slotless machine is feasible, the slotted machine will be too. The choice between the two could then be made in the detailed design when considering the practicality of a radial slotless design and where finite element electromagnetic and structural analyses would make the difference between the two generators clear.

4.4 Application of theory

A radial flux, longitudinal stator surface permanent magnet generator has been chosen. The pole number of this generator is explored by the provision of 2, 4 and 6 pole designs. The choice between slotted and slotless generators has been deferred at this point because the outline analysis used in this chapter gives similar performance and cost. Constraints and more detailed design decisions have been presented. A short summary of the resulting machines machine designs is given in the next chapter and the full details comprise appendix ii of this thesis.

The next chapter compares the induction generator to the permanent magnet generator. In order to make a suitable comparison they are compared over the range of speeds and powers that will occur while in service. At first an efficiency curve taken from Bumby [67] is used to make a general comparison. Then a range of PMG designs, developed using the theory and choices in this chapter, are compared to the induction generator using a numerical model provided by Wavegen. The model allows the power converted by each generator type over a year to be calculated and compared and a quantitative comparison to be made.

5

COMPARISON OF PERMANENT MAGNET AND INDUCTION GENERATORS

5.1 General Comparison

A time domain numerical model of an OWC wave power installation has been developed by Wavegen using measured data from their Islay installation combined with wave tank and aerodynamic testing. This model has been adapted for this project to investigate the effects of changing the generator type on the performance and annual output of an installation. In order to develop the model, measurements were made of the waves present at a proposed installation of the 18.5kW turbine. This data is then used to produce representative seas, which are tested using scale collector models in Wavegen's Inverness wave tank. The wave tank tests produce pressure data at different damping levels, from which the pressures at optimum damping are found and scaled using Froude scaling to provide data for a full scale device. Each pressure against time trace is representative of a proportion of a typical year. The annual performance of a generator can be estimated from its performance in each sea state and the proportion of the year that sea is valid for. The generator model need not be complex, an equation showing the variation of efficiency with shaft power and shaft speed is all that is necessary.

In addition to the full time domain model, a simple filter model was created which allows the complications of turbine aerodynamics and control to be bypassed. This circumvents the most intensive calculations and allows more time to be spent on optimisation and analysis of the generator types. The full model and the filter model are compared in the next section of this chapter and the limitations of this model are discussed.

A frequency domain model of the OWC system has been created by Wavegen and used to produce predictions of the annual average shaft powers and turbine speeds at any deployment location. An annual average power is not directly useful for assessing the performance of a generator as it does not provide the spread of power inputs. This spread can be given by the pressure data where the simple filter model is adapted to match its annual average with that given by the predicted data. This is only practical with the simpler model as the additional complexity in the time domain model makes matching both annual average power and turbine speeds difficult.

5.1.1 Comparison of simulation methods

Within certain limitations the performance of the OWC system can be approximated by using a numerical filter to provide a relationship between the input pressure data and the turbine shaft power. A simple filter model and the complete model were run on identical seas at three different annual averages for a range of generator types. The complete model takes into account the performance of the entire system including turbine overspeed, stall, control strategy and generator maximum speed and overload limitations. Results are presented in figures 37, 38 & 39. The annual average powers quoted are turbine shaft powers. The 100% efficient is the turbine shaft power converted to electrical power by a 18.5kW rated, 100% efficient generator allowed a 25% overload.

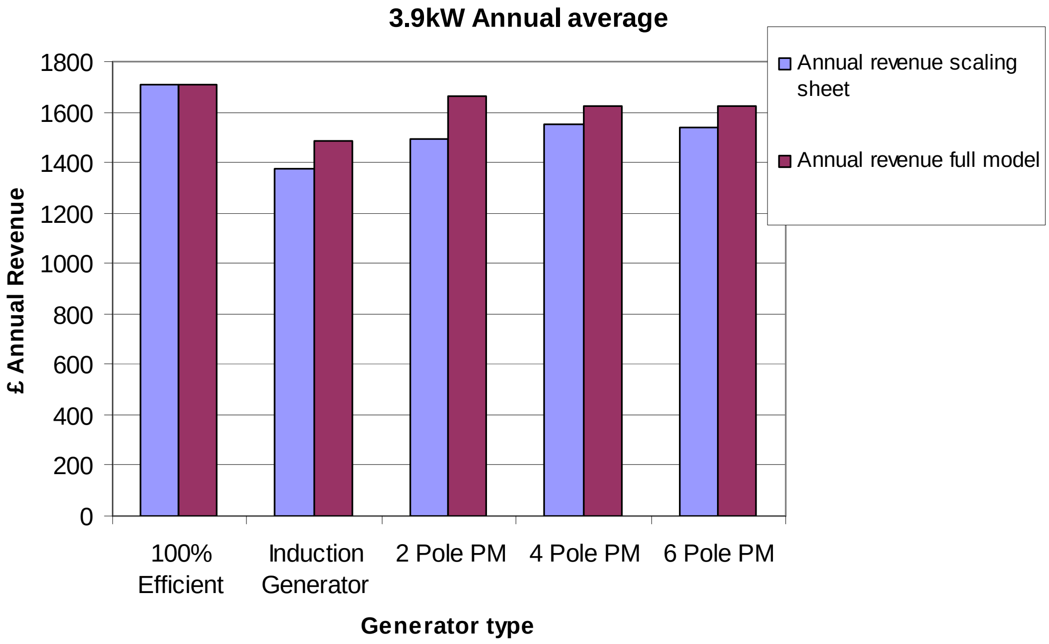

Figure 37: Comparison of turbine numerical simulation results for 18.5kW rated generators at a low annual average shaft power

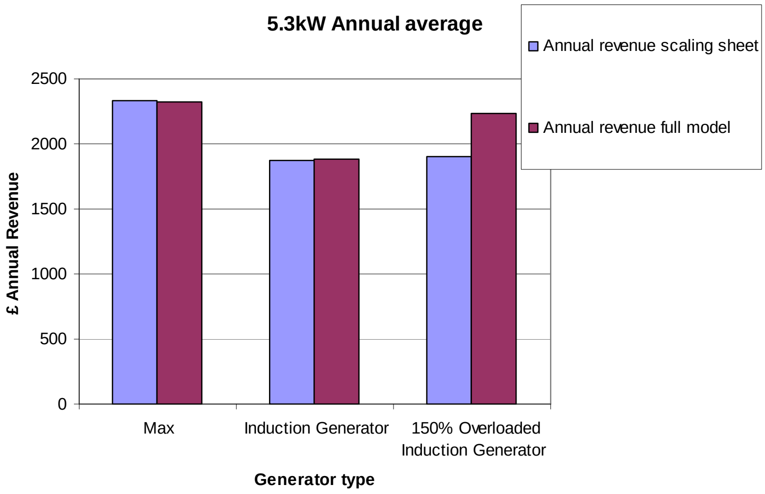

Figure 38: Comparison of turbine numerical simulation results for 18.5kW generators at medium annual average shaft power

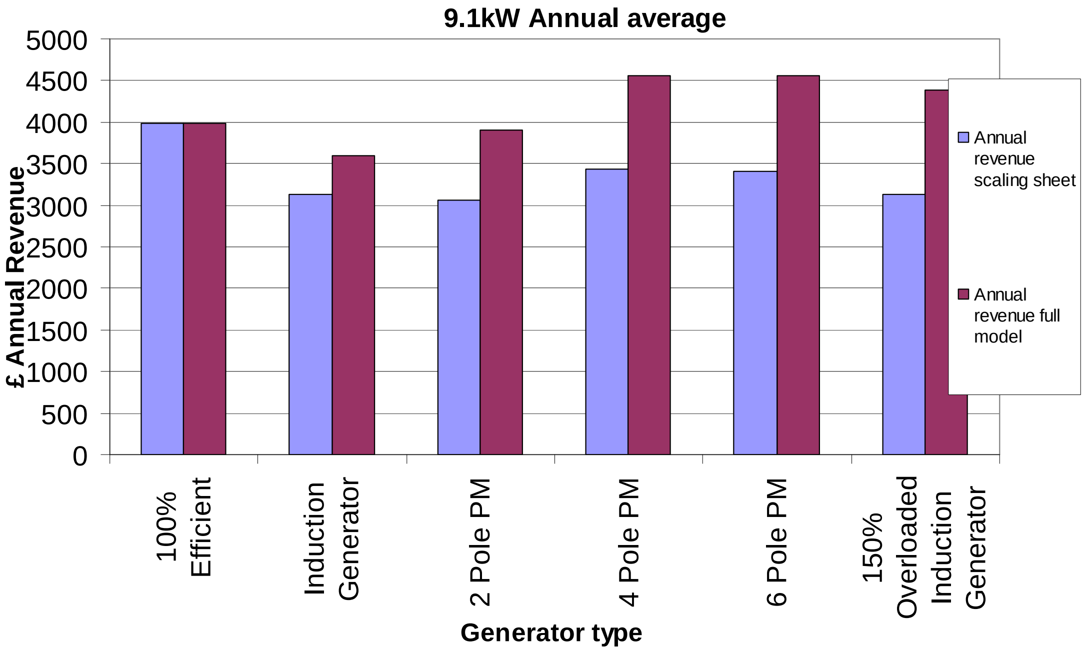

Figure 39: Comparison of turbine numerical simulation results for 18.5kW generators at high annual average shaft power

The differences between the simulations are relatively small at the low and medium powers. The difference between 150% overload results for the 5.3kW annual averages is that the higher rating suits the control strategy for the full turbine simulation. This means it can absorb more power. This is not taken into account in the simpler simulation. At 9.1kW, the turbine acts less like a linear filter. Consequently stall and overspeed effects are encountered. Here the turbine rotational speed is critical to performance. The ability of the higher rated machines to restrain overspeed and absorb additional power is not correctly reflected in the scaling sheet.

For lower annual average powers the results from the scaling sheet are very close to those from the full simulation. For powers where overspeed and stall are significant issues, it cannot simulate the turbine performance. Hence it is only used for the 6.08kW annual average turbine power which cannot be accurately replicated using the complete model.

5.2 Detailed Comparison

The design equations detailed in chapter 4 are used to create a numerical model of a permanent magnet generator. The detailed model inputs and outcomes are included as appendix ii to this thesis. The efficiency results of the design equations for 3 different speeds and 10 different per unit loads can be represented by equations 53 & 54 with appropriate constants. The total loss is the sum of the fixed and variable losses. These losses were subtracted from the mechanical power to the generator.

$$\begin{aligned} Fixed &= A\omega - B \\ Variable &= C\omega(P/P_{rated})^2 + D\omega(P/P_{rated}) \end{aligned} \qquad (53),(54)$$

Where A, B, C & D are coefficients for the trend of efficiency across the load/speed range. Fixed losses represent the losses invariant with load, variable losses represent the losses that change with load. The friction and windage loss was not modelled in the equations in section 4.3 and was neglected. The comparison induction generator has a friction and windage loss of 92W at 3000 RPM , around 1/20th of full load loss for the lowest loss generator. These equations were added to the numerical models of a Wells turbine and thus could be compared to an induction machine in service. The efficiency surface generated by applying this equation to a 4 pole permanent magnet generator is shown in figure 40.

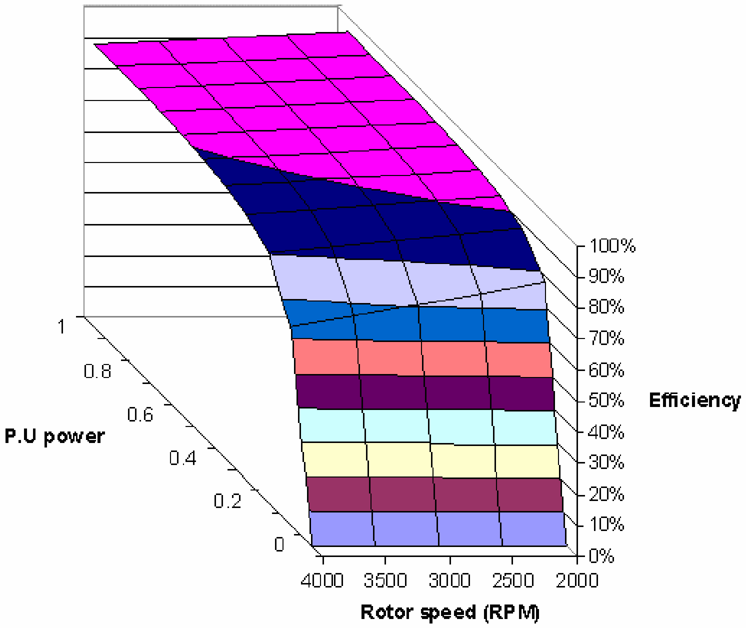

Figure 40: Efficiency of 22.7kW 4 pole permanent magnet generator against Per Unit power and rotor speed in RPM

5.3 Efficiency curve comparison

A comparison of the efficiency of various slotless permanent magnet generators to a comparable induction machine is given in figures 41 to 44. This comparison is made at a single speed, 3000 rpm, for all of the generators except the LIMPET generator which is compared at 1200 rpm. The induction machine data is taken from the current generator’s type test certificate [74] and converter induced losses have been included. These losses are not included for the slotless permanent magnet generator as their magnitude is difficult to quantify. Due to the neglect of friction and windage and converter induced harmonics the comparisons here will be slightly biased towards the permanent magnet generator. An estimate of 92W for friction and windage and 50W for converter harmonics leads to around 142W additional loss in the induction generator. These losses are strongly affected by generator rating, speed, rotor design, bearing choice and other factors. Using the induction machine loss a maximum error of 7% in the calculated full load losses of the most efficient generator would be found. The loss calculations at this preliminary design stage provide only best estimates of efficiency and are not calibrated to measurements on a directly comparable machine, hence a 7% error in the estimation is accepted. Measured data from LeRoy Somers shows that in a conventional induction generator the difference between sinusoidal and converter supply efficiencies (caused by additional losses in the generator) depends on load level and to a lesser extent on machine rating [75]. An estimate of this loss will be made for the permanent magnet generator if its advantage over the induction machine proves to be marginal. A similar converter can be used for both induction machines and permanent magnet machines so no losses inside the converter are factored into this comparison.

5.3.1 2 Pole Permanent Magnet generator

The slotless 2 pole PM generator has the lowest fixed losses of any generator investigated. A lack of slots and low electrical frequency minimise the iron losses. At 3000rpm, 210W of core losses are predicted. Its rating (15.5kW) is lower than the 18.5kW specified for the small breakwater turbine and this has been taken into account in the simulations.

Table 5: Dimension summary for 2 pole permanent magnet generator

Electrical frequency	F	50	Hz
Rated current	I	*34*	A
Terminal volts	V	*150*	V
Terminal power	P	*15300*	W
Stator outer diameter	D_o	*0.34*	m
Stator length	L_s	*0.33*	m
Magnet thickness	t_{mag}	*6.00E-003*	m
Current Density	J	*3960*	A/m

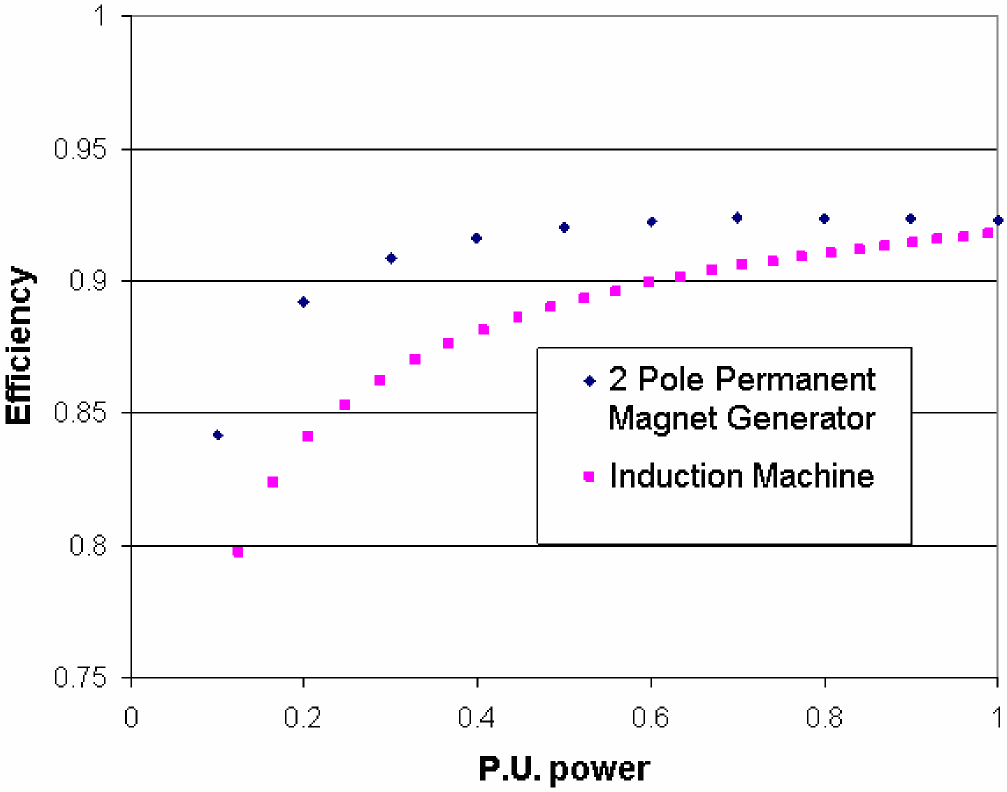

Figure 41: Efficiency vs PU load of base 15.3kW at 3000 RPM

5.3.2 4 Pole Permanent Magnet generator

Mi [70] suggests that a 4 pole machine will be better at loads near full load than a comparable 2 pole machine as it represents a better balance of copper loss to core loss. At 3000rpm, 270W of core losses are calculated.

Table 6: Dimension summary for 4 pole permanent magnet generator

Electrical frequency	F	100	Hz
Rated current	I	23	A
Terminal volts	V	330	V
Terminal power	P	22700	W
Stator outer diameter	D_o	0.28	m
Stator length	L_s	0.40	m
Magnet thickness	T_{mag}	5.00E-003	m
Electric loading	A	4400	A/m

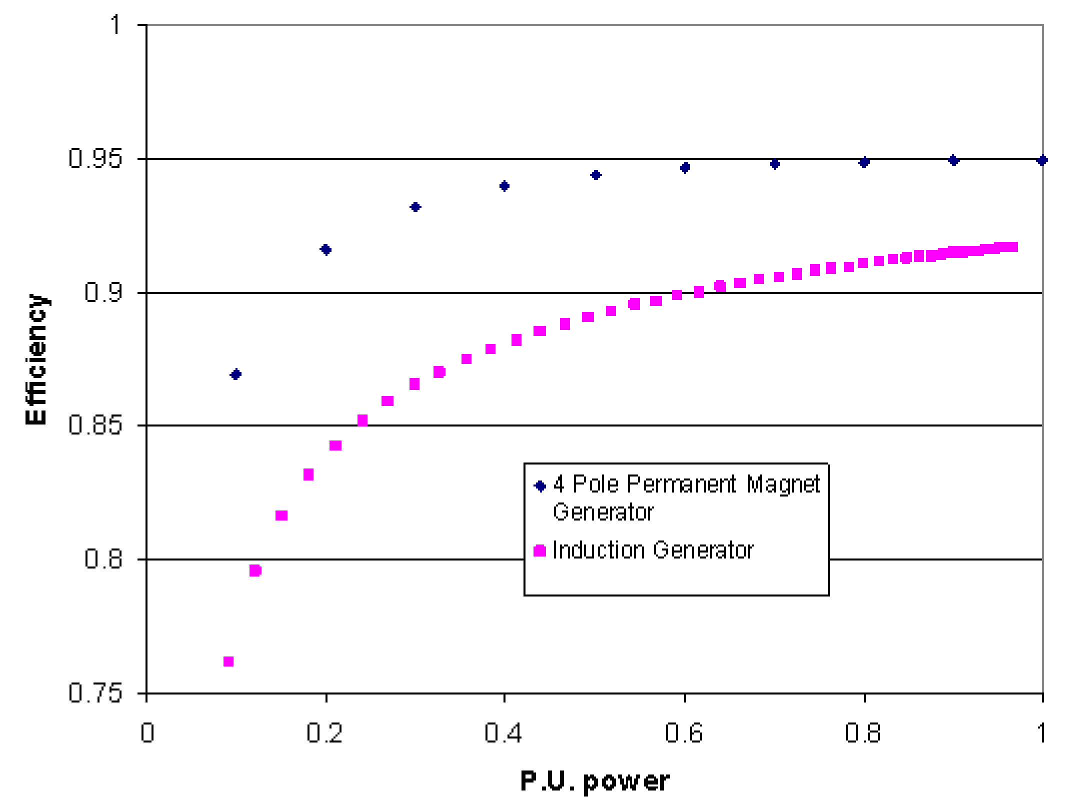

Figure 42: Efficiency against per unit power with 22.7kW base at 3000rpm

5.3.3 6 Pole Permanent Magnet Generator

A 6 pole machine was considered to increase the full load efficiency of the generator in powerful seas. It reduces the full load copper loss significantly at the expense of 320W of no-load losses.

Table 7: Dimension summary for 6 pole permanent magnet generator

Electrical frequency	f	150	Hz
Rated current	I	17	A
Terminal volts	V	430	V
Terminal power	P	22600	W
Stator outer diameter	D_o	0.27	m
Stator length	L_s	0.40	m
Magnet thickness	t_{mag}	4.00E-003	m
Electric loading	A	5000	A/m

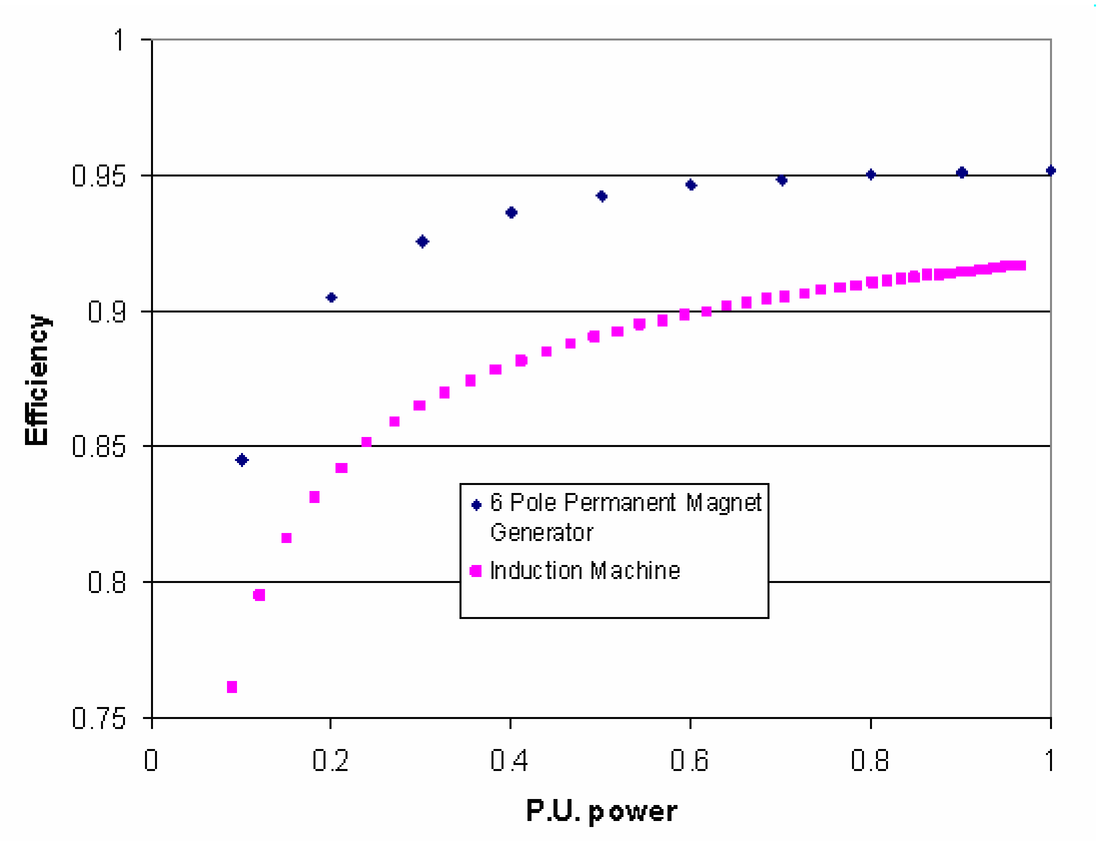

Figure 43: Efficiency against per unit power with 22.6kW base at 3000rpm

5.3.4 LIMPET Permanent Magnet Generator

This 6 pole machine was designed for comparison with the LIMPET induction generator. Hence it is rated at 250kW and 1200rpm.

Table 8: Dimension summary for LIMPET 6 Pole permanent magnet generator

Electrical frequency	f	60	Hz
Rated current	I	90	A
Terminal volts	V	950	V
Terminal power	P	253000	W
Stator outer diameter	D_o	0.80	m
Stator length	L_s	1.05	m
Magnet thickness	t_{mag}	6.00E-003	m
Electric loading	A	9800	A/m

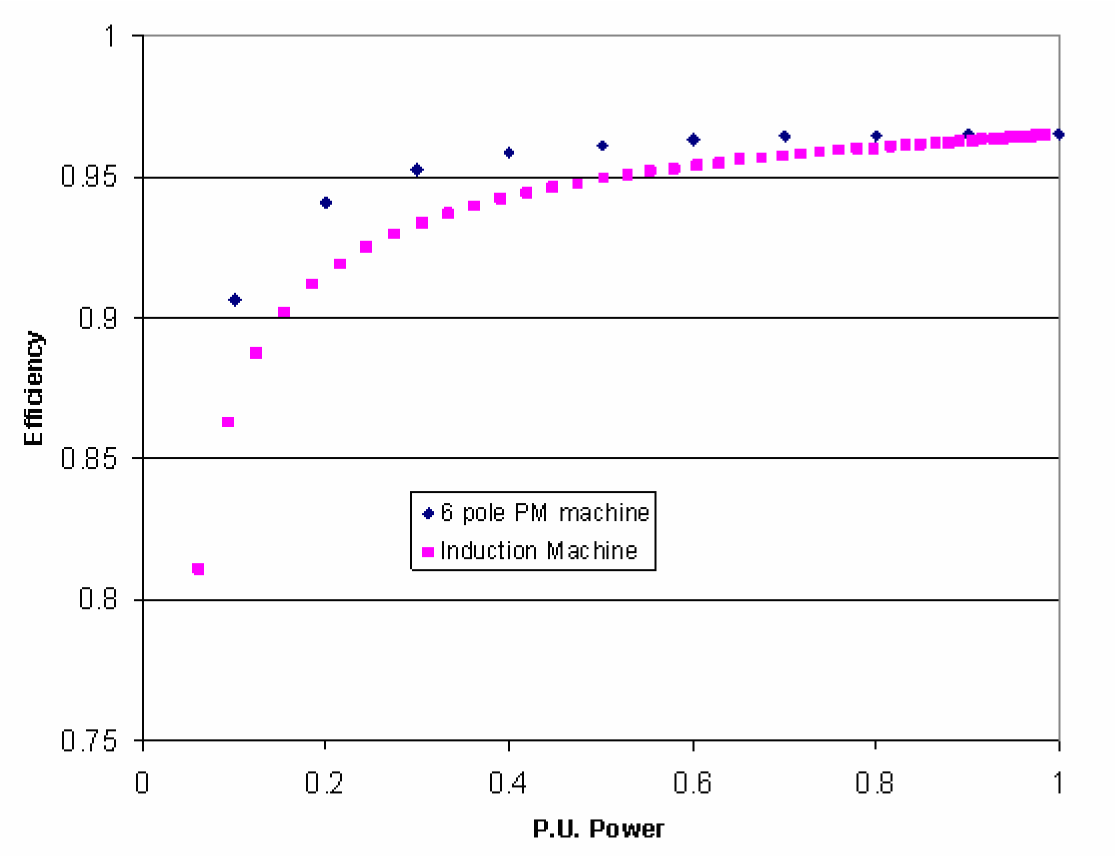

Figure 44: Efficiency against per unit power with a 250kW base

5.4 Modelling performance in an OWC

The variation of efficiency with speed and loading of the generators identified above were included in a numerical model of an OWC wells turbine and subjected to appropriate sea states. The OWC model was written as a C program by Wavegen, its main configuration panel is shown in figure 45. Wave data, in the form of a pressure trace, is read in and used to predict the power in the turbine duct. The efficiency of the turbine is found for the given flow rate, turbine speed and blade configuration and the power onto the turbine rotor can be found. The turbine rotor power can either accelerate the turbine or be taken off as generated power. The generator power is decided according to the control strategy of the OWC, allowing the turbine speed to be controlled. The generated powers over all sea states are summed and the annual average output is found.

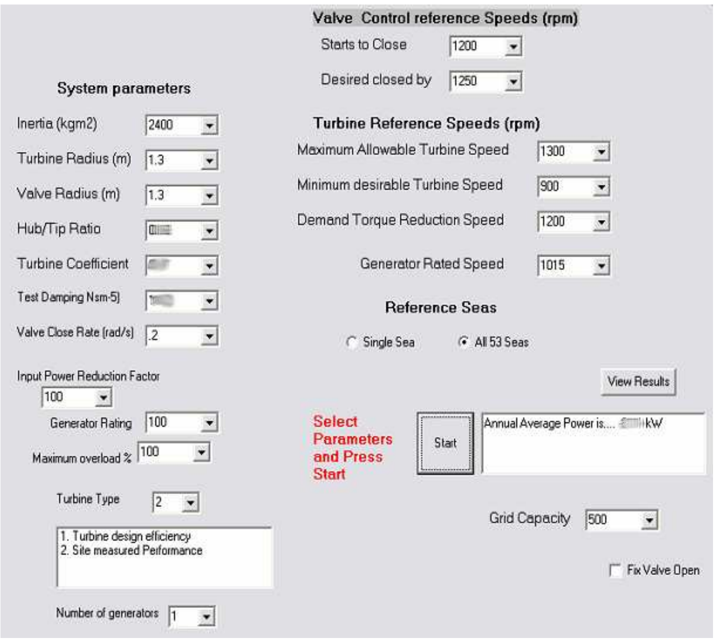

System parameters

Inertia (kgm2) 2400
Turbine Radius (m) 1.3
Valve Radius (m) 1.3
Hub/Tip Ratio [redacted]
Turbine Coefficient [redacted]
Test Damping Nsm-5] [redacted]
Valve Close Rate (rad/s) .2
Input Power Reduction Factor 100
Generator Rating 100
Maximum overload % 100
Turbine Type 2

1. Turbine design efficiency
2. Site measured Performance

Number of generators 1

Valve Control reference Speeds (rpm)

Starts to Close 1200
Desired closed by 1250

Turbine Reference Speeds (rpm)

Maximum Allowable Turbine Speed 1300
Minimum desirable Turbine Speed 900
Demand Torque Reduction Speed 1200
Generator Rated Speed 1015

Reference Seas

○ Single Sea ● All 53 Seas

Select Parameters and Press Start

Annual Average Power is.... [redacted] kW

Grid Capacity 500

☐ Fix Valve Open

Figure 45: Front panel of OWC model configured for 250kW tests. Some data deliberately blurred for confidentiality reasons.

The annual averages quoted in this section are the power present on the turbine hub, not the power in the incident wave. The generators were allowed to exceed their ratings by 25% with the exception of the overloaded induction machine which was permitted a 50% increase in rating. The availability of the device is assumed to be 100%.

5.5 Mutriku 3.2kW annual average

Data recorded from wave tank tests of a model of the Mutriku breakwater was used to evaluate the suitability of upgrading the generator to a permanent magnet type. Figure 46 shows the annual average power output of each machine type and table 9 shows the energy extracted by the generator over a year. A 100% efficient 18.5kW generator allowed a 25% overload is included as 'perfect' for reference. The output of an induction generator allowed a 50% overload is also included.

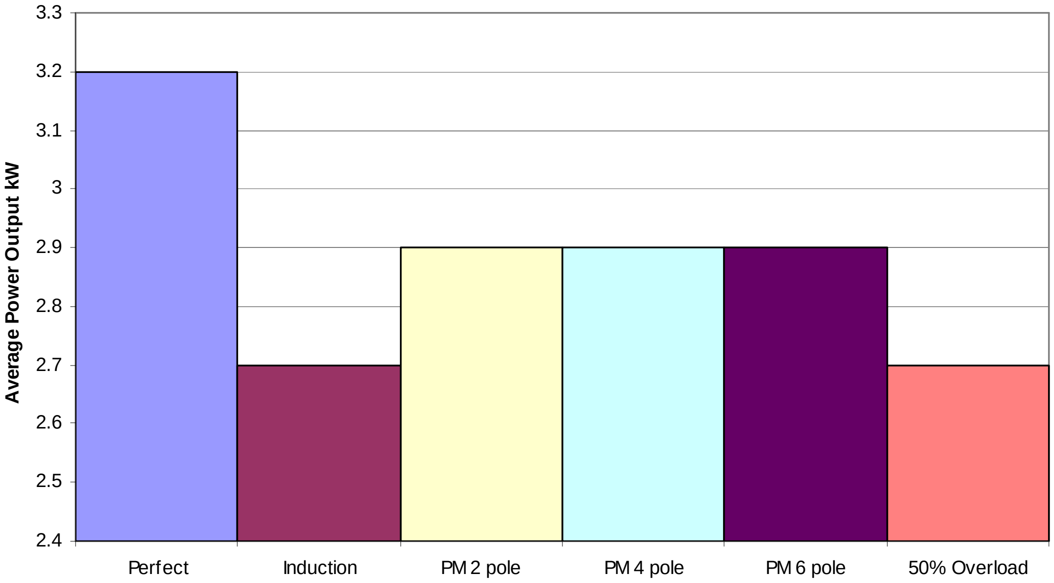

Figure 46: Calculated annual average power output for operation in 3.2kW sea state. Graphed from 2.4kW upwards to highlight differences in performance

Table 9: Value comparison of 18.5kW generators for Mutriku installation

Generator	Output (kWh)	Loss (kWh)	Improvement over Induction Generator (kWh)	Improvement over Induction Generator (%)
Perfect	28000	0	4380	18
Induction	24000	4000	0	0
PM 2 pole	25000	3000	1000	4
PM 4 pole	25000	3000	1000	4
PM 6 pole	25000	3000	1000	4
50% Overload	24000	4000	0	0

5.6 Mutriku 6.34kW annual average

This annual average was generated by Wavegen and was simulated using the simple filter model as opposed to the complete numerical model. This allowed the Wavegen data to be better matched. Figure 47 shows the annual average power output of each machine type and table 10 shows the revenue created by the generator over a year.

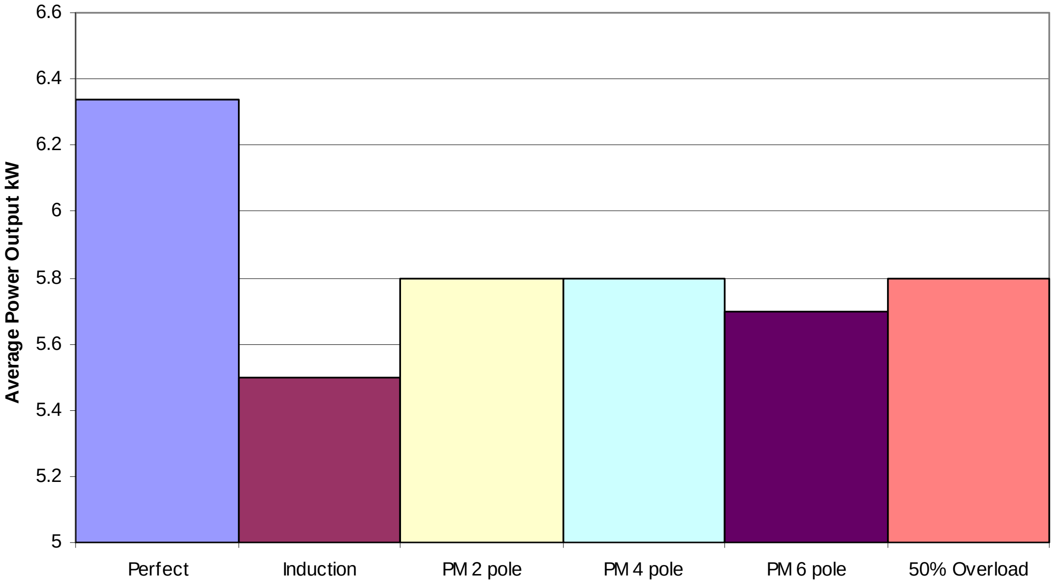

Figure 47: Calculated annual average power output for operation in 6.34kW sea state

Table 10: Value comparison of 18.5kW generators for Mutriku installation

Generator	Output	Loss	Improvement over Induction Generator (kWh)	Improvement over Induction Generator (%)
Perfect	56000	0	8000	16
Induction	48000	8000	0	0
PM 2 pole	51000	5000	3000	6
PM 4 pole	51000	5000	3000	6
PM 6 pole	50000	6000	2000	4
50% Overload	51000	5000	3000	6

5.7 Mutriku 9.1kW annual average

Three seas were chosen from the Mutriku seas and given equal annual weighting. This allows the performance of the generators in higher energy sea states to be simulated. The generators can exceed the perfect conversion result as their ratings are greater than 18.5kW and enable the OWC to accept more energy from the sea.

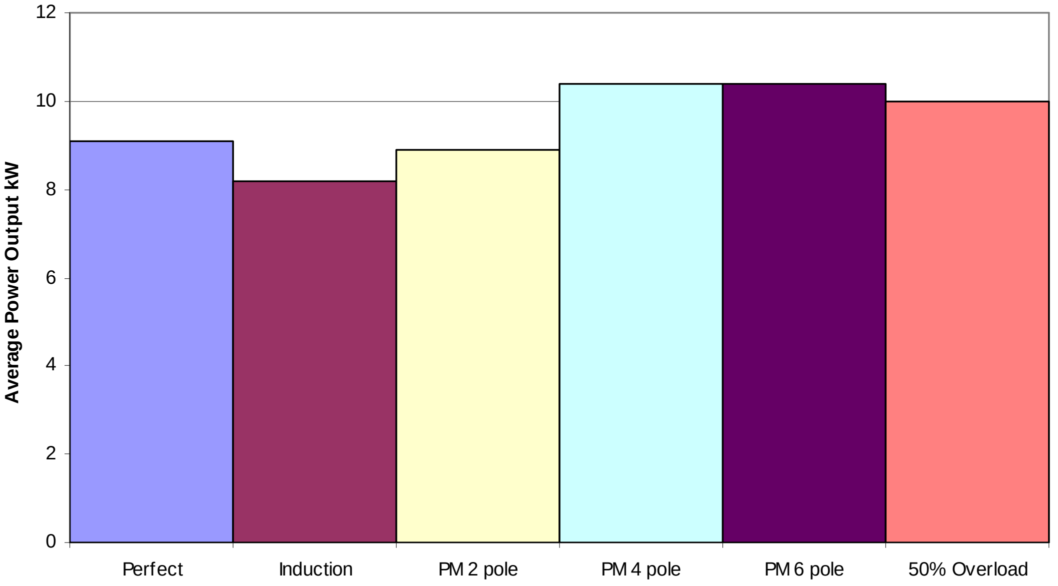

Figure 48: Calculated annual average power output for operation in 9.1kW sea state

Table 11: Value comparison of 18.5kW generators for Mutriku installation

Generator	Output	Loss	Improvement over Induction Generator (kWh)	Improvement over Induction Generator (%)
Perfect	79700	0	7880	10
Induction	71800	27156	0	0
PM 2 pole	78000	21024	6100	8
PM 4 pole	91100	7884	19000	24
PM 6 pole	91100	7884	19000	24
50% Overload	87600	11388	16000	21

The 4 and 6 pole PM generators as well as the 50% overloaded induction generator allow the turbine to run faster without overspeed issues. This reduces the damping and the OWC accepts more energy. Hence they obtain significantly more revenue than a smaller 100% efficient machine. If the 4 and 6 pole generators were permitted a 50% overload they were predicted to only make 4% extra revenue as they are already more capable than the 18.5kW machine.

5.8 LIMPET 123kW annual average

The LIMPET data set was divided into a less energetic 123kW section and a more energetic 145kW section. This allowed the turbine demand speed for each to be optimised separately in order to improve power extraction.

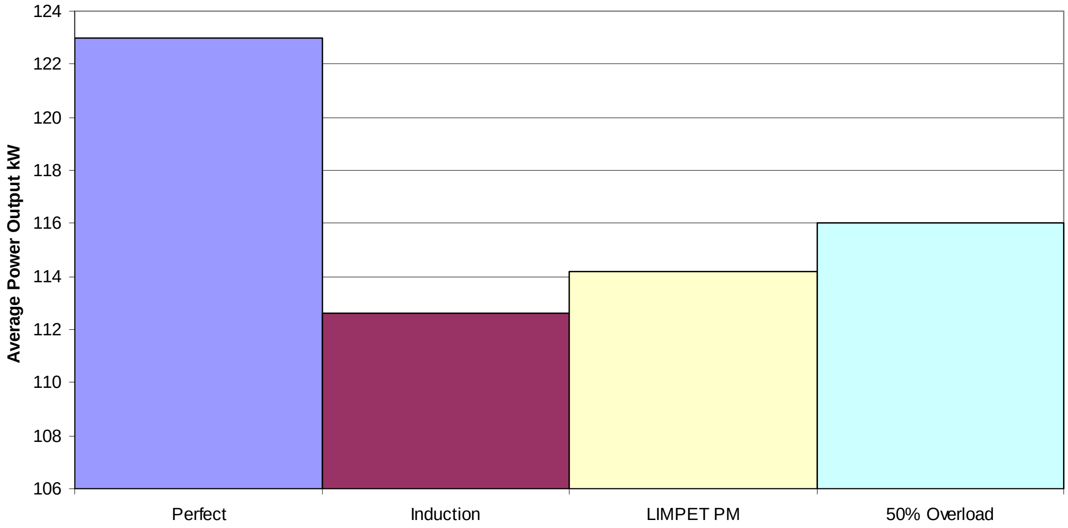

Figure 49: Calculated annual average power output for operation in 123kW sea state

Table 12: Value comparison of generators with 250kW rating for LIMPET installation

Generator	Output	Loss	Improvement over Induction Generator (kWh)	Improvement over Induction Generator (%)
Perfect	1077000	0	91100	9
Induction	986000	91104	0	0
LIMPET PM	1000000	77088	14000	1
50% Overload Induction	1016000	61320	29800	3

5.8.1 LIMPET 145kW annual average

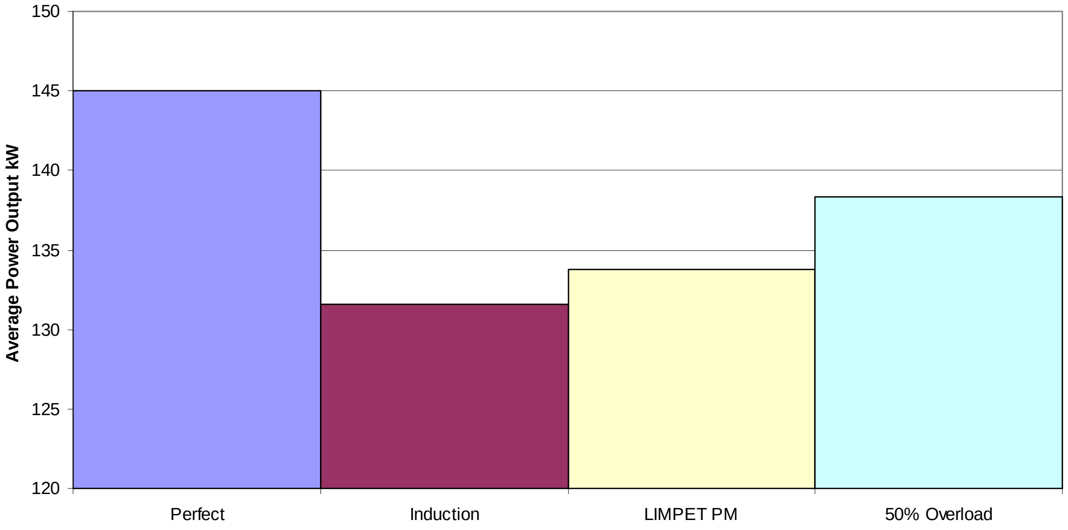

Figure 50: Calculated annual average power output for operation in 145kW sea state

Table 13: Value comparison of generators with 250kW rating for LIMPET installation

Generator	Output	Loss	Improvement over Induction Generator (kWh)	Improvement over Induction Generator (%)
Perfect	1270200	0	117384	10
Induction	1152816	117384	0	0
LIMPET PM	1172088	98112	19272	2
50% Overload	1211508	58692	58692	5

5.9 Costs

The minimum materials cost of a PM generator was assessed from the design equations by multiplying the mass of materials by the costs in table 3 (chapter 4) from Dubois [69]. This was compared to an induction generator which has the same stator and rotor iron but twice the amount of copper as the PM generator. The cost of materials decreases as the pole count increases for a given rating. The increase in number of magnets is offset by the decrease in required magnet thickness. This means less volume of magnet is required, lowering costs. The comparative costs are shown in table 14. It should be noted that in quotes for a 110kW generator obtained by Wavegen [76] the PM generator was marginally cheaper.

Table 14: Minimum materials cost of generators. Absolute and relative to a comparable induction machine

Generator	Cost	% of induction machine cost
2 Pole	1037.16	118%
4 Pole	844.2	118%
6 Pole	739.68	113%
LIMPET	17388.51	106%

5.10 Analysis

The modelled permanent magnet generators appear more efficient than a similarly rated induction machine up to full load at the power ratings simulated. This is due to reduced iron losses and no requirement for excitation current.

The low available power in the 3.2kW annual average sets a low cap on the amount of extra energy generated. In this situation the best PM generator makes 7% more energy annually than the induction machine. A PM generator with a 6.08kW annual average makes at best 6% more energy annually, although it does not take into account the feedback between the generated and input power. The results for a 9.1kW annual average, shown in table 15, the best PM generators produce 27% greater revenue than the induction generator. The overloading induction machine makes 82% of this additional revenue without incurring additional cost and risk. At a cost of energy of 5p/kWh the annual revenues in table 15 are obtained.

Table 15: Value of annual generation at 5p/kWh for 18.5kW generators in 9.1kW annual average Mutriku seas

Generator		Value	Value of improvement
Perfect	£	3985.8	394.2
Induction	£	3591.6	0
PM 2 pole	£	3898.2	306.6
PM 4 pole	£	4555.2	963.6
PM 6 pole	£	4555.2	963.6
50% Overload	£	4380	788.4

The PM generator is predicted to produce more revenue annually than the induction generator. However the neglected losses (PM eddy current, friction and windage) in the PM generator will reduce this advantage and an optimised induction generator could also close the gap predicted by the modelling here. For a low volume production run with a novel machine the design and manufacturing costs could be a large part of the total cost of the generator. This would mean that the calculated materials costs in table 14 would be a poor prediction of the generator cost. If a large amount of OWCs were to be installed with this annual average then it is possible that mass production advantages could be realised and significant additional revenue created.

The LIMPET seas simulated are extremely energetic and there is little energy to be had at part load hence the PM generator in this environment has a limited advantage. The overloading induction machine is better suited here as it can capture additional energy unavailable to the other generators.

There is additional risk associated with a PM generator as an induction machine is less likely to damage itself if forced to over-speed. This is an important consideration for operation in harsh conditions on a less stable grid. Additional safeguards would have to be put in place to prevent the PM generator damaging itself if it is disconnected from the grid and the turbine is not stopped. This will increase the total cost of the PM generator system. If a rise in the value of a renewably generated kWh or a significant reduction in the cost of magnet material were to take place, this analysis would need to be revisited. In an off-grid or black start situation a permanent magnet generator would be the logical choice as it does not require external excitation.

In the simulated wave climates 9.1kW and above, it can be seen that significant increases in revenue can be achieved by allowing another 25% overload on the induction machine. The result for 6.08kW is based on the filter model and does not take into account the ability of a more powerful machine to run in more extreme wave climates without danger of overspeed. Long term overloading may cause over temperature in the machine which will damage the winding insulation. This damage can reduce the lifespan of the machine. However, in the OWC application the cooling airflow is potentially more effective than allowed for when the machine is rated. The power input is also intermittent which will allow the machine to cool between waves. The efficiency drop from full load to 125% load is measured at 0.5% for a Brook Crompton induction machine [74]. The efficiency of a suitable induction generator at 150% load is unknown, however this overload should be achievable even for short periods of time. Alger [77] states that breakdown torque for this class of machine should be 200% full load, the LeRoy Somer quote [76] for an 110kW induction generator states that it can supply 150% maximum torque for a limited time.

The opportunity existed, due to this work being carried out with Wavegen, to carry out measurements of the environment in a working OWC and a steady state test rig with a production Wells-turbogeneration system attached. This measurement would allow the cooling of any generator in this environment to be estimated. This course of action was judged to be applicable to the existing system in the short term and allow further work on dedicated generator design to be informed. An assessment of the maximum overload of an induction machine in the OWC environment would maximise power absorption and reduce the amount of time the turbine valve is used to limit the power input to the turbine. It could also have ramifications for the design of future generators, either reducing capital cost or increasing the overload further. If a smaller generator could be used for a given system, it would be cheaper and have better part load efficiency than a larger generator. Such a generator would then overload to the desired maximum rating of the system.

The environmental measurements are presented in chapter 8, the supporting theory in chapter 7. The next chapter concerns the quantification and location of losses in the existing induction generator. By measuring the temperature of the generator in the OWC, and knowing the losses with sufficient accuracy, the cooling effect of the environment can be found and an accurate thermal model for this application created.

6

MEASUREMENT OF INDUCTION MACHINE LOSSES

6.1 Introduction

The maximum rating of an induction machine is determined by the temperature of the hottest part of the insulation, which is determined by the machines ability to dissipate heat. This heat dissipation is measured by knowing the heat generated in the machine (from losses) and the temperature of different components of the machine. Where direct temperature measurements were impractical the MotorCAD thermal modelling package was used to relate the temperature of those components to the measured temperatures. The heat generated in the machine is found by careful measurement of the machine losses across the range of shaft speeds and terminal powers measured. This chapter outlines in detail the tests used for this purpose. Three separate measurements were made of machine losses in three different operational states. Measurements were made operating at 3000rpm as a motor and generator and at 4000rpm as a generator. The highest loading achieved with the test equipment was 150% of rated load. In addition the stator winding temperature measurement, later used in OWC thermal measurements, is compared to a resistance temperature measurement method.

6.2 Standards for loss measurement

The current British standard for determination of induction machine efficiency from tests is EN 60034-2-1:2007 [78] which is identical to IEC 60034-2-1:2007. This is the standard used for the loss measurement tests. During these tests, data complying with IEEE standard 112-B 2004 [38] was generated. The relevant test methods and data analysis from the IEC standard are presented here for completeness.

EN 60034-2-1:2007 details test methods, allowing both direct and indirect measurement of losses. Direct measurement is a comparison of input and output power whereas indirect measurement requires two identical machines connected back to back. A single induction machine, identical to that studied in an OWC later in this thesis, was purchased from Brook Crompton and shipped to Nottingham University for testing. Nottingham University have a dedicated machine test facility which can measure the electrical power and mechanical power of a machine operating either as a motor or generator.

What follows is a summary of the relevant portions of the test standard, presented here for completeness.

6.2.1 Losses

The standard separates induction machine losses into constant losses, load losses and additional load losses. Constant losses are taken to be the iron loss plus friction and windage losses. Load losses are losses due to current flowing through stator and rotor resistances. Additional load loss is attributed to the stray load loss.

6.2.2 Tests

All quantities mentioned in section 6.3 are RMS quantities excluding temperatures.

The standard lists several options for testing an induction machine. The total loss in this case is obtained directly from comparing the power input to the power output. As the loss distribution is essential to further work, the loss components are also determined. The winding temperature during a test can be obtained from direct measurement or measurement of the change in winding resistance. As a direct measurement of winding temperature is to be used to measure thermal resistance later in this thesis, a winding resistance measurement was taken to check the accuracy of the thermocouples in the endwinding.

6.2.2.1 Accuracy

The IEEE standard [38], requires all instrumentation to be calibrated within 12 months of the test and show errors of less than 0.2% of the instruments full scale for the tests described below.

6.2.2.2 No load test

The no load test was conducted for 3000 and 4000rpm at rated voltage and frequency. Losses were recorded when the power input varied less than 3% between measurements made at 30 minute intervals. The core loss, friction and windage were measured from seven tests made at voltages varying from 125% to 20% of rated voltage.

6.2.2.3 Load Curve test

The generator was loaded to a maximum of 150% of its rated load and then at descending loads such that two measurements were made above rated load and three below. Six data points were recorded for each test in rapid succession to minimize the winding temperature change.

6.3 Loss determination from test data

6.3.1 Friction and Windage, Iron loss

The loss data for appropriate no load tests are plotted with winding resistance losses subtracted. A trend is found for the remaining loss against voltage squared. Which when extrapolated gives the friction and windage loss as its zero intercept. With this offset removed, the iron loss can be found. Owing to the small quantities involved relative to the full scale of the instruments the error here is relatively large, estimated at 3.4%.

6.3.1.1 Stator copper loss

The stator copper loss is found from equation 55.

$$P_s = 1.5 * I^2 R_* \tag{55}$$

Where R_* is the resistance between two motor terminals at the test temperature. This is found from equation 56 from the IEEE standard [38]

$$R_* = R_a \frac{t_* + k_1}{t_a + k_1} \tag{56}$$

Where R_a is the measured resistance between two motor terminals at t_a

t_a is the temperature at which a resistance measurement was made

t_* is the recorded test temperature

k_1 is $\frac{1}{\text{Temperature coefficient of resistance}}$ which is 235 for copper [38]

The maximum expected error in stator current measurement is 0.1A, assuming the full range resistance is double the measured resistance, then a maximum error of 0.0014Ω is obtained. For full load at 3000 RPM this gives a +/-0.6% error.

6.3.2 Rotor copper loss

The rotor copper loss is found from equation 57.

$$P_r = (P_{in} - P_s - P_{fe}) * s \tag{57}$$

It is corrected to the reference temperature in equation 58:

$$P_{r\theta} = (P_{in} - P_{s\theta} - P_{fe}) * s_\theta \tag{58}$$

The slip is temperature corrected as it is directly related to the rotor resistance [38] using equation 59:

$$s_\theta = s_t \frac{t_\theta + k_1}{t_t + k_1} \tag{59}$$

The calculation of slip is responsible for the majority of the error in rotor copper loss estimation. If the instruments used are up to the IEEE standard then a 5.4% error is possible.

6.3.3 Stray load loss

The stray load is found by subtracting all of the above losses from the measured loss:

$$P_{stray} = P_{in} - P_{out} - P_s - P_r - P_{fe} - P_{fw} \tag{60}$$

The measurements of stray load loss are then smoothed by assuming a variation with load torque given in equation 61:

$$P_{stray} = B\tau^2 + C \tag{61}$$

Where τ is the load torque, B and C are constants found from linear regression of the data points. Since stray load has been determined from all of the other measurements it has an error of 14% at full load, 3000RPM. This error becomes relatively large at low power outputs (91% at 25% power output) but this is small in absolute terms as the stray load is less than 20W.

6.4 Loss measurement equipment

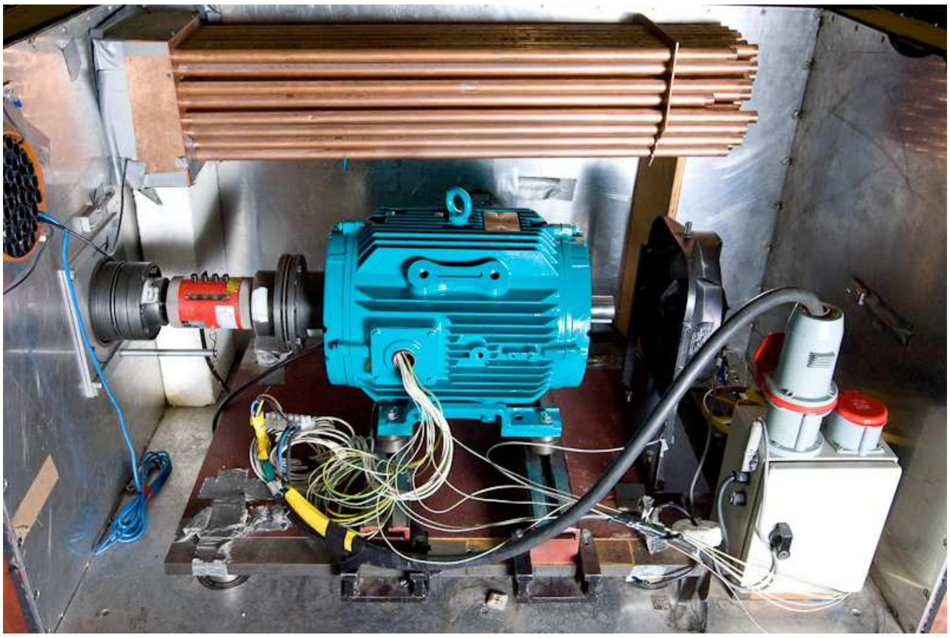

Figure 51: Induction Machine in Calorimetric test rig at Nottingham University

The tests were performed on a Brook Crompton induction machine identical to the generator in the Wavegen 18.5kW turbine. The sole difference was a foot mounting instead of the original generator's strut mounting, to ease installation into the test rig. Stator winding thermocouples identical to those used later in this thesis were present in the stator windings. The machine was delivered to Nottingham University for tests in their electrical machines laboratory. Tests were performed by Mr Zhang He in the calorimetric test rig (Figure 51) without its lid in place. No calorimetric measurements were made as sufficient accuracy could be gained when the rig was operated according to the standard described above.

The test machine was coupled to a load machine by a torque measurement device. Cooling was provided by a separate fan unit as the generator does not require a shaft mounted fan in service. The electrical power was measured by a PM3000 power analyser. A measurement of stator winding temperature was then made by shutting the machine down and measuring the stator winding resistance. During the tests a constant record was made of thermocouple measured stator winding temperature and a series of thermal images of the generator exterior were made.

6.5 Analysis of test data

6.5.1 Fixed losses

Table 16: Friction and windage for different operation modes

	Friction & Windage W
Motor 3000rpm	187
Generator 3000rpm	186
Generator 4000rpm	264

Table 16 shows the friction and windage losses found from no-load test data. The two data points available, along with the zero intercept, do not follow the expected cube relationship. A linear regression is found to be more accurate. From the available data the friction and windage loss can be estimated by:

$$P_{f\&w} = 0.068RPM \tag{62}$$

The core loss is plotted in figure 52. It reduces with power output and rotor speed. The stator voltage is held constant and the speed increased, therefore the stator flux is decreased in accordance with equation 63 from [79].

$$V = \omega_e \lambda_s \tag{63}$$

Where ω_e is the speed of rotation of the stator magnetic field
λ_s is the stator flux linkage

The hysteresis loss (introduced in 2.10.3) is given by equation 64. The decrease in stator flux (and therefore stator flux density) will result in a reduction of hysteresis loss. Eddy current loss will remain constant as the frequency increases at the same rate as stator flux decreases.

$$P_h = \eta \frac{M_c}{\delta} f B_m^x \tag{64}$$

Where x is a value around 1.7 to >2.0 dependent on the material used.

The approximation for core loss obtained by linear regression is:

$$P_{core} = P_{elec}(kW) * (-0.0001 * RPM - 0.5) + (400 - 0.05 * RPM) \tag{65}$$

The error due to this approximation is 1.3%, which added to the measurement uncertainty gives a 4.7% relative error. MotorCAD simulations show that this gives a 0.8% change in stator end-winding temperature at full load and 1.2% change at 25% load.

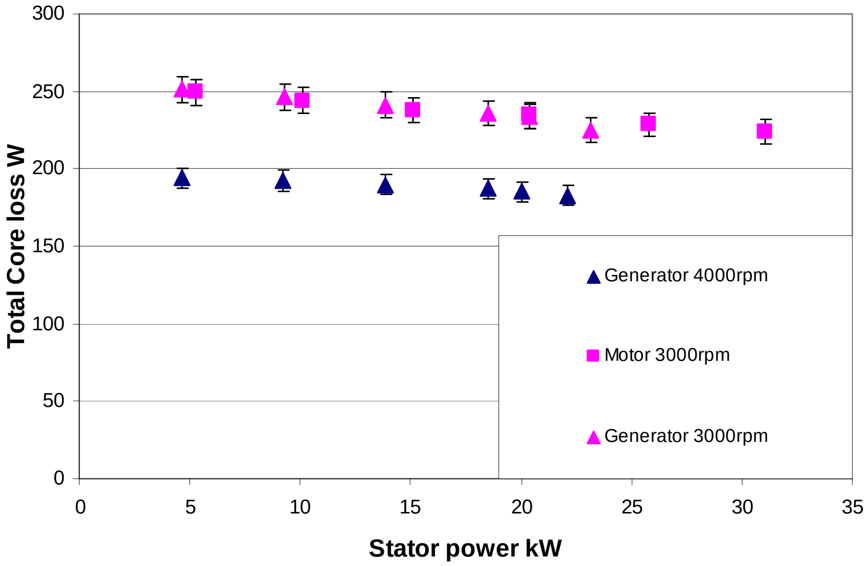

Figure 52: Core loss plotted against stator current

6.5.2 Stator copper loss

The stator endwinding was the hottest part of the winding in all the simulations carried out. This is due to its poorer cooling, increasing its resistance and thus losses. Without temperature effects, the ratio of stator loss allocated to the endwinding winding is 0.47. The temperature difference was measured in motorCAD and the alteration in loss location is illustrated in figure 53. The trend for this change is given as equation 66.

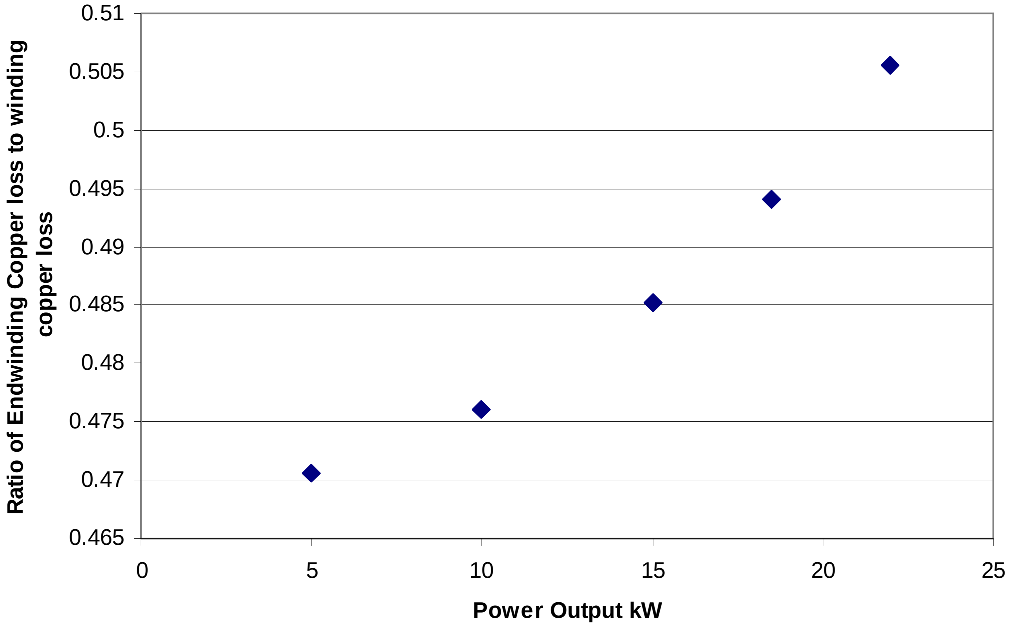

Figure 53: Ratio of copper loss in Endwinding compared to winding changing due to increase in resistivity

$$\frac{P_{ew}}{P_s} = 0.00008 P_{elec}(kW)^2 - 0.0002 P_{elec}(kW) + 0.47 \qquad (66)$$

The stator copper loss can be approximated by equation 67. This equation was found from quadratic regression of the measured values against electrical power output at the two test speeds. A linear regression was used to find the variation of the quadratic coefficients with speed.

$$P_s = (1.98 - 0.00016 * RPM)(P_{elec}(kW))^2 + (222 - 0.05 * RPM) \qquad (67)$$

The maximum error arising from this approximation when compared to measured data is 2.2%. The measurement error brings this to 2.8%.

6.5.3 Rotor copper loss

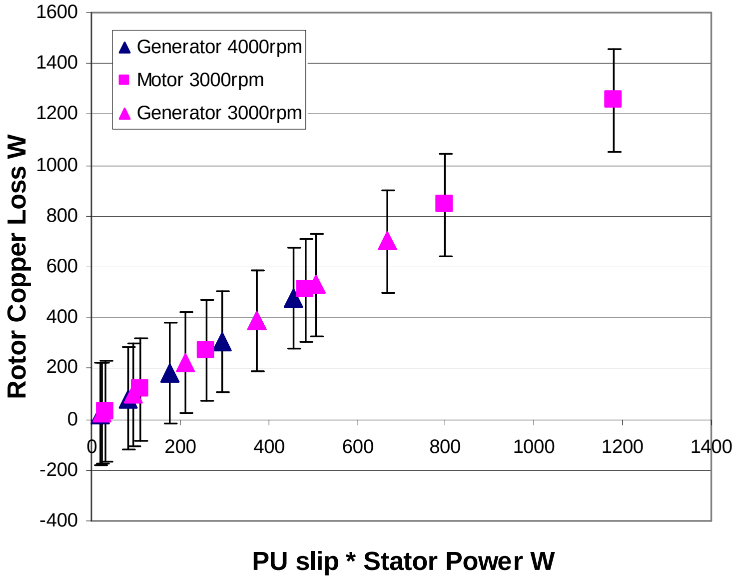

Figure 54: Variation of Rotor Copper loss with stator power multiplied by per unit slip

Figure 54 shows the rotor copper loss is plotted against the power into (for motor) or out of (for generator) the stator multiplied by the per unit slip. The rotor loss can thus be found from equation 68 with electrical power measured in kW.

$$P_r = 1060 * s * P_{elec}(kW) \tag{68}$$

In a model such as Wavegen's wave to wire model, the induction machine slip may be inconvenient to calculate so the rotor copper losses are found from equation 69. This equation was found in a similar way to equation 67.

$$P_r = (2.576 - 0.00037RPM)P_{kw}^2 - (14.6 - 0.002856RPM)P_{kw} + (64.7 - 0.01318RPM) \tag{69}$$

Equation 69 has errors of up to 6% as it is generalising an independent variable. Including the measurement errors this gives a maximum 11.4% error. MotorCAD modelling shows that this leads to a 1.3% error in the stator endwinding temperature at full load and 0.6% at 25% load.

6.5.4 Stray loss

The stray loss is the loss within the machine unaccounted for by the previous loss mechanisms. In the test standard used this includes the rotor core losses. Figure 55 shows there is a considerable difference in stray loss between motoring and generating. As the loss model is to be used on an induction machine acting as a generator the generator points are used to give the trend in equation 70. This trend was generated by quadratic regression of the measured datapoints.

$$P_{stray} = 0.8548 * P_{elec}(kW)^2 - 1.0471 * P_{elec}(kW) + 6.6936 \qquad (70)$$

This equation gives an average 2% error, much smaller than the 14% error in measurement. The stator endwinding temperature is sensitive to this relatively large deviation at full load, a 14% change in stray load losses can cause a 4.3% change in stator endwinding temperature. This poses a limitation on the thermal modelling because the stray load loss is the hardest to measure or predict, including when moving from machine to machine of the same rating. Measurements on 11kW induction machines carried out by Bradley [80] show a 120% difference in stray load loss value. This implies that should the manufacturer of the induction generator used change, or the generator design change, then a new set of loss measurements need to be carried out.

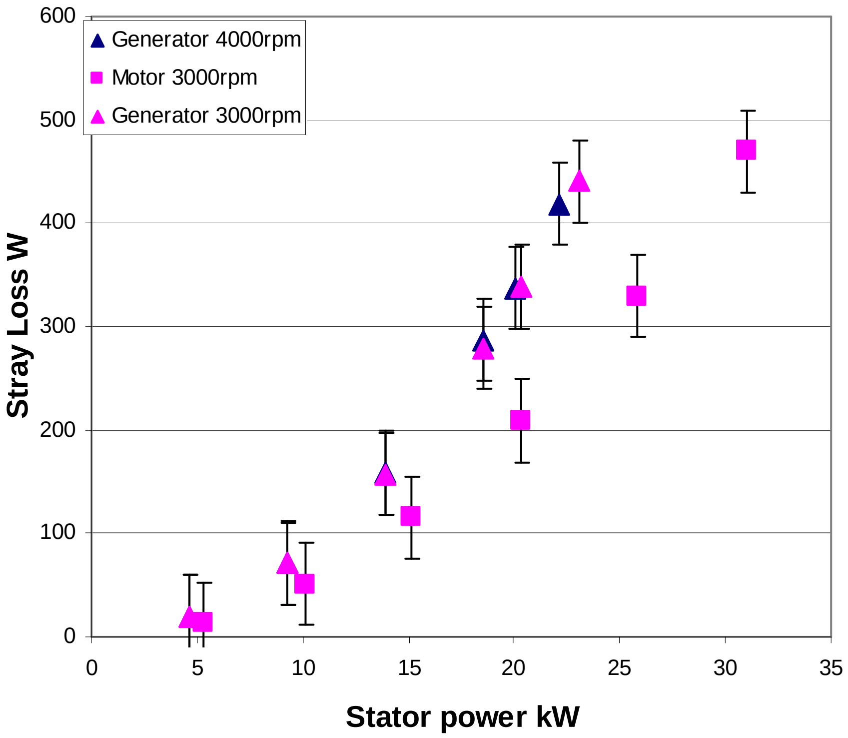

Figure 55: Variation of stray load loss with stator power

6.6 Loss model

The purpose of the loss model is to output the magnitude and location of the losses within an induction generator based on a few critical inputs. This will be used in future thermal modelling.

Inputs to the model will be either stator current or stator power, measured or estimated stator winding temperature, generator or motor operation and rotational speed. The stator and rotor copper losses and stray load are related to stator current/power. Winding temperature changes the winding resistance, affecting both copper losses. Stray load loss and to a lesser extent core loss changes whether the machine is operating as a motor or a generator. The core loss is also connected to this input but is more strongly influenced by rotational speed.

6.6.1 Location of losses

The test data alone is insufficient for accurate thermal modelling, it is necessary to know the location of each loss within the machine.

6.6.1.1 Location of copper losses

Copper losses are assumed to occur uniformly throughout the winding and are allocated by copper volume. This will lead to errors as the hottest part of the winding will have the highest resistance, and thus proportionately more losses. This error will be proportional to the difference between winding and endwinding temperature with constant of proportionality equal to the change of resistivity of copper with temperature ($3.9\text{x}10^{-3}$ per °C). If the difference in temperature between endwinding is large the model will underestimate endwinding temperature. This will be examined further in the thermal modelling chapter.

6.6.1.2 Location of core losses

The core loss at no-load will be allocated to the stator as the rotor is rotating at the same speed as the magnetic field. Hence the frequency of fundamental flux changes 'seen' by the rotor back iron is very low. The rotor core loss varies according to equation 71 from [49].

$$P_{cr} = k_h sf\phi^2 + k_e (sf)^2 \phi^2 \tag{71}$$

Where f is the stator electrical frequency. It is multiplied by the slip s in this case to get the rotor electrical frequency. The core loss measured is strictly that at no load and thus no fundamental frequency rotor core loss is observed. At higher frequencies, the effective slip is 1. Hence only high frequency rotor losses will be significant at no-load. Mueller [42]shows that the high frequency loss is significant, 327W for a 37kW machine which makes up 42% of the no load core losses. Green [46] attributes around 40% of the no-load core losses to high frequency loss (50% with inverter supply) for a 2.1kW induction generator. In the models used in this thesis 40% of the core loss is allocated to the rotor of the induction generator. This loss will occur in the rotor tooth, not the rotor core as the rotor slots are not open at the surface [42]

The effect of the exact allocation of stator and rotor iron losses is examined using the MotorCAD thermal analysis package. A 20% variation around the 40% rotor core loss allocation was allowed. This sensitivity analysis yielded a maximum 1.68% difference in stator endwinding temperature, showing that the critical generator temperature is largely insensitive to the exact allocation of core losses.

6.6.1.3 Location of stray load losses

When using the IEEE test standard, part of the stray load losses represents the increase in high frequency core losses. Mueller [42] shows a 56% increase in core loss from no-load to full load. If applied to the induction generator tested here, such an increase is well within the measured value of stray load loss. MotorCAD provides a rule of thumb split of 25% of stray load loss to the stator tooth and the remainder to rotor tooth [81]. Yamazaki [82] provides finite element analysis of the rotor of a 10hp induction machine showing that most of the stray loss is accounted for in the rotor through harmonic cage and inter-bar current losses. As with the core losses, the MotorCAD thermal model is largely insensitive to the exact allocation of stray load losses. A 20% change in allocation around 75% rotor, 25% stator gives a 1.4% change in stator endwinding temperature.

6.6.1.4 Converter Induced Harmonic Losses

The losses induced in the induction generator by the power conversion system have been introduced in section 2.10.5. The exact value of these losses depends on the inverter waveform, the design of the induction generator and any harmonic suppression present in the system. A conservative estimate of 5% is given by Boys & Miles[83] in 1994. Inverter design has improved considerably since and a figure closer to the 1.4% increase given by Green [46] is more likely, although it is measured for a very small machine. An arbitrary 2.5% loss is henceforth assumed with an error of 1.5%. This will be included as an increase in stray load losses.

6.7 Use of measurements in thermal modelling

Table 17: Summary of errors in loss measurement and the effect of the error on the stator endwinding temperature, magnitude of full load loss for 4000RPM generator

Loss	At full load	Magnitude Error	Effect Magnitude Error	Effect Location Error	
Stator Copper	479W	2.8	2.8	0	%
Rotor Copper	307W	11.4	1.3	0	%
Core	187W	4.7	1.2	1.68	%
Stray	287W	14	4.3	1.4	%

It can be seen from table 17 that the key parameter, stator endwinding temperature, is relatively insensitive to errors in the magnitude and location of the losses. The stator copper loss is the exception to this, but can be estimated from the current input and the stator winding temperature. This may change if a generator with a radically different layout is used.

6.8 Summary

The magnitude and distribution of losses presented in this chapter will be used in a thermal model of an induction generator. This model is developed in the next chapter, then compared to measurements made on an OWC system in steady state. The analysis of steady state measurements uses the loss model generated in this chapter as it is impractical to perform a sufficiently accurate input/output power audit of the induction generator when in operation on an OWC. The turbine is constructed in such a way that mounting a torque transducer is impractical and estimating the power onto the turbine rotor from the flowing air will not be sufficiently accurate.

7

HEAT TRANSFER AND THE INDUCTION MACHINE

7.1 Heat transport mechanisms from generator surface

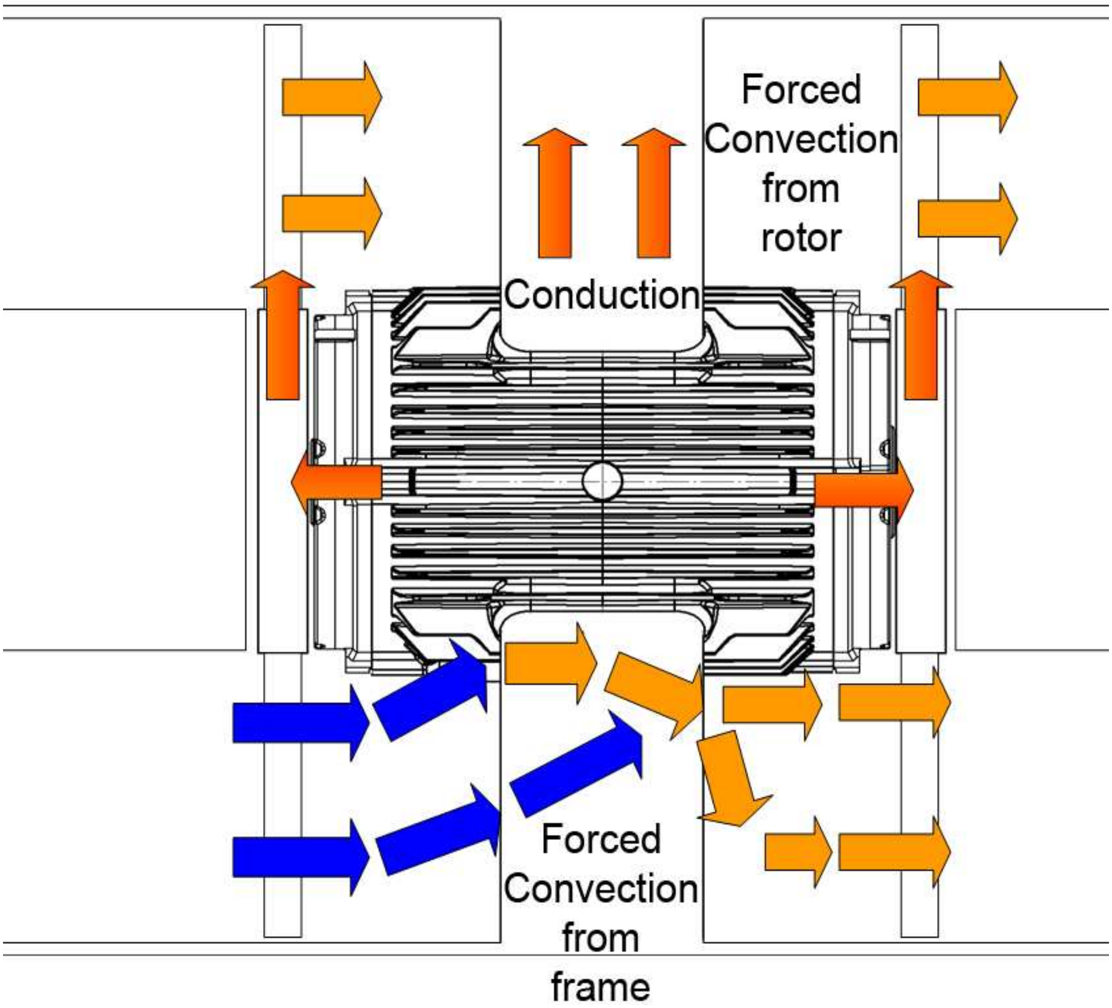

Figure 56: Main heat paths out of generator in an OWC application

The heat flow out of the generator, illustrated in figure 56, is through convection into the turbine airflow, conduction to the generator supports and turbine rotors or radiation. The generator is mounted directly in the turbine airflow and has fins to increase the surface area for convection. Where a significant external airflow provides the bulk of the cooling action, forced convection is the dominant convection mode. This heated air is then either blown out of the duct and into the turbine hall or sucked into the OWC chamber. If the OWC is not in operation and the valve is closed, this airflow will be removed and buoyancy driven (natural) convection will provide convection cooling. The supports holding the generator in place are aluminium and there are four located around the outside of the generator. Heat transferred to the strut will either be convected into the cooling air or conducted to the turbine duct. Heat conducted through the generator shaft to the turbine rotors will be force convected to the turbine air from the turbine blades.

7.2 Heat transport mechanisms inside the generator

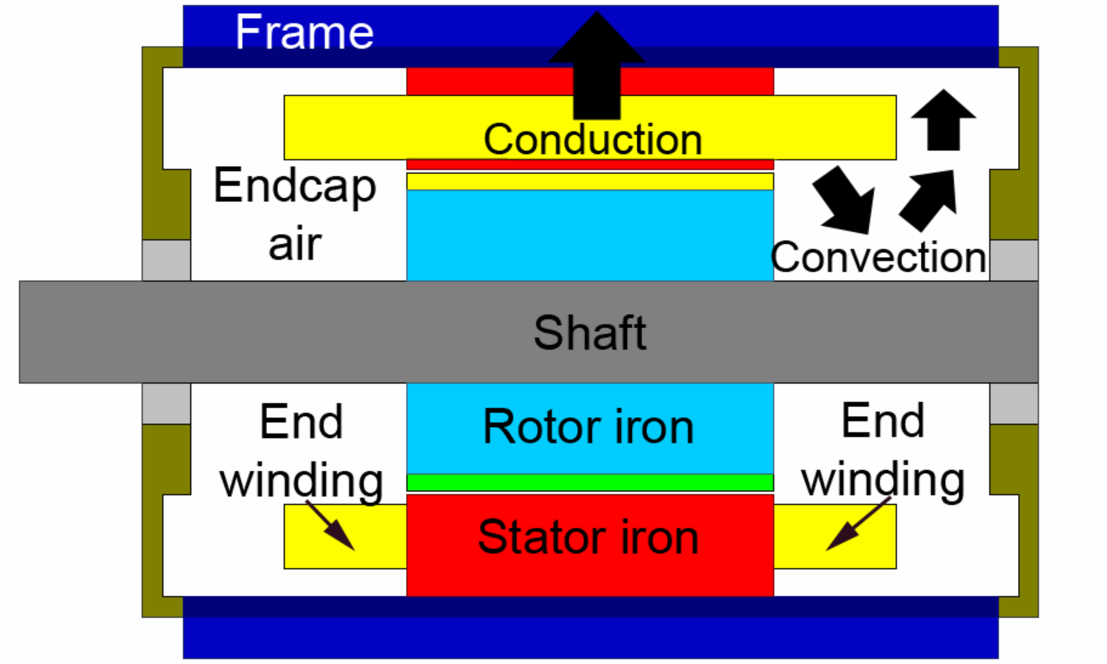

Figure 57: Main heat paths inside the induction machine adapted from MotorCAD [81]

Heat flow within the generator is either by conduction between components in good thermal contact or convection across the airgap or in the endcap air. The main heat transfer paths and components are illustrated in figure 57. Conduction heat transfer within the machine is relatively easy to compute. The endwinding, the largest heat source in the endcap has a very complex geometry making prediction of forced convection heat transfer difficult. Stirrers, primitive fans, are present on the end of the rotor to aid endcap convection.

7.3 Thermal flow

Thermal flow can be modelled in a similar way to the flow of current in electrical circuits. In this analogy, temperature corresponds to voltage; heat flow is given by current; heat sources are analogous to electrical current sources; heat capacities behave like capacitors; and thermal resistances for a given set of conditions can be modelled as electrical resistances. A thermal node is defined as a component of the machine with negligible internal thermal resistance. The rate of heat transfer is given by the difference in temperature between two nodes and the thermal resistance between those nodes.

$$Q = \frac{T_1 - T_2}{R^t} \tag{72}$$

Where Q is the heat flow in watts
T is the temperature at that node
R^t is the thermal resistance between nodes

7.3.1 Radiation heat transfer

The radiative heat flow is defined by the difference in fourth powers of the generator and its surroundings.

$$Q_r = \varepsilon \sigma A (T_g^{\,4} - T_a^{\,4}) \tag{73}$$

Where Q_r is the radiative heat flow
ε is the emissivity ratio, the ratio of the subjects radiation to that of a perfect blackbody
σ is the Stefan-Boltzmann constant, $5.67\text{x}10^{-8}$ $\text{W/m}^2\text{K}$
A is the area of the generator surface
T_g is the generator exterior temperature
T_a is the ambient temperature of the surroundings

If the generator frame reaches 36°C and the surroundings are at 10°C then if it were a black body it would radiate 72W of heat. Mellor [84] suggests an emissivity of 0.4 for a painted metal surface. This gives 29W of heat dissipation. This is not a major heat path from the machine and will be neglected in further study.

7.3.2 Conduction heat transfer

The conduction to other structures is dependant on the thermal contact between the frame or shaft and the structure. The rotors are attached to the steel shaft by a taper lock collar and are made from aluminium, the struts are attached directly to the generator frame. The conductivity of these connections is unknown although it could be improved if this was considered sufficiently advantageous. The thermal resistance of conduction through an object is given by equation 74.

$$R^t = \frac{l}{kA} \tag{74}$$

Where l is the length of the conductor
A is the area of the conductor
k is the thermal conductivity of the conductor

7.3.3 Convection heat transfer

Many accepted empirical correlations exist in the heat transfer literature to relate the heat transfer from solid to fluid during convection[85]. The thermal resistance in degrees per Watt of a solid/fluid boundary during convection is given by equation 75.

$$R^t = \frac{1}{h_c A} \tag{75}$$

Where h_c is the convective heat transfer coefficient in units of $W/m^{2\circ}C$.

This is found from the Nusselt (Nu) number by equation 76.

$$h_c = \frac{Nu.k}{L} \tag{76}$$

Where L is the characteristic length of the convection surface
k is the thermal conductivity of the fluid.

The Nusselt number can be found from correlations with the Grashof (Gr) and Prandtl (Pr) numbers for natural convection or Reynolds (Re) and Prandtl numbers for forced convection. Typical forms of the two convection correlations are given in equation 77 for natural convection and equation 93 for forced convection[35].

$$Nu = a(Gr.\mathrm{Pr})^{b} \tag{77}$$

$$Nu = a(\mathrm{Re})^{b}(\mathrm{Pr})^{c} \tag{78}$$

$$\mathrm{Re} = \frac{ul}{v} \tag{79}$$

Where a,b and c are empirical constants for the particular geometric shape being analysed.

Nu is the Nusselt number
h is the convective heat transfer coefficient
l is the characteristic length
k is the conductive heat transfer coefficient of the fluid
Re is the Reynolds number
u is the fluid velocity
v is the kinematic viscosity

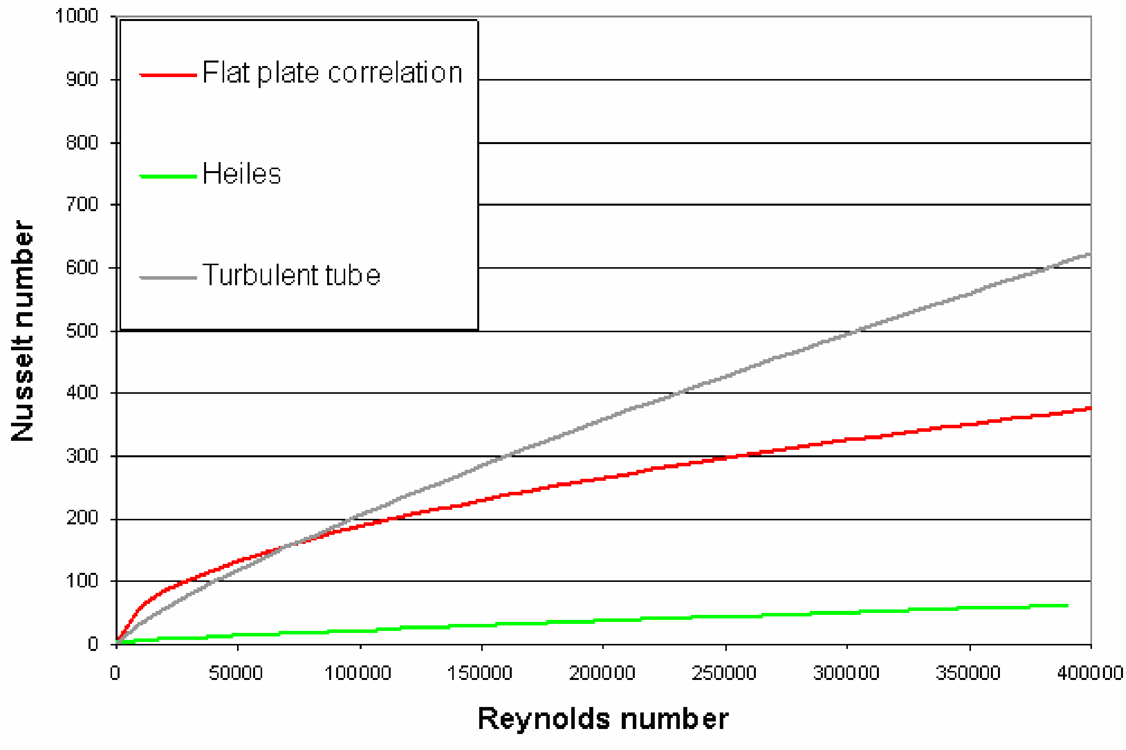

Figure 58: Correlations of Nusselt number to Reynolds number

The length used in the Reynolds number is either the fin length of the generator or the hydraulic diameter. Helies [86] also gives a dimensional correlation specifically for generator cooling which has been non-dimensionalised for comparison. The correlations detailed below are compared in figure 58.

Flow over a flat plate correlation [35]

$$Nu = 0.664(\mathrm{Re})^{0.5}(\mathrm{Pr})^{0.33} \tag{80}$$

Where Pr is the Prandtl number of the flow

Fully turbulent flow over a flat plate

$$Nu = (0.037(\mathrm{Re})^{0.8} - 871)(\mathrm{Pr})^{0.33} \tag{81}$$

The Heiles [86] correlation is given by

$$h_c = \frac{\sigma_{air} Cp_{air} DV}{(4L)}[1 - e^{-m}] \tag{82}$$

$$m = 0.1448(L^{0.946} / D^{1.16}).(k_{air} /(\sigma_{air} Cp_{air} V))^{0.214} \tag{83}$$

$$D_h = 4A_c / P_c \tag{84}$$

Where h_c is the convective heat transfer coefficient

σ_{air} is the density of air

Cp_{air} is the specific heat capacity of air

D_h is the hydraulic diameter

L is the length of a cooling fin

A_c is the channel area

P_c is the channel perimeter

V is the airflow velocity

This is non-dimensionalised by

$$Nu = h_c D_h / k_{air} \tag{85}$$

Where Nu is the nusselt number
K_{air} is the thermal conductivity of air

Turbulent flow through a circular tube is given by equation 86 from[35]:

$$Nu = 0.023\,\mathrm{Re}^{0.8}\,\mathrm{Pr}^{0.33} \tag{86}$$

The convection heat transfer from the surface depends on the fluid flow, the surface area and the temperature difference.

$$Q = hA(T_g - T_d) \tag{87}$$

Where Q is the convective heat flow
h is the heat transfer coefficient
A is the area of the generator surface
T_g is the generator exterior temperature
T_d is the mean temperature of the duct air

The cooling effect of convection from a surface is measured using the Nusselt number. This dimensionless number compares the convective cooling with the conductive cooling from the surface.

7.3.4 Properties of humid air

The OWC environment on Islay is significantly humid. The properties of dry air are altered by the presence of water vapour. An analysis of this effect is presented as appendix iii to this thesis. The change in convective heat transfer coefficient from dry to saturated air is a factor of 1.008 to 1.012 depending on flow velocity. This effect is not significant for the measurement work carried out in this thesis and is neglected henceforth.

7.4 Heat Transfer Models

7.4.1 The Critical Component

As noted in chapter 2, the stator windings are the most critical temperature in cage rotor machines of standard type operating in steady state load conditions.

7.4.2 Mellor, Roberts & Turner: lumped parameter thermal model

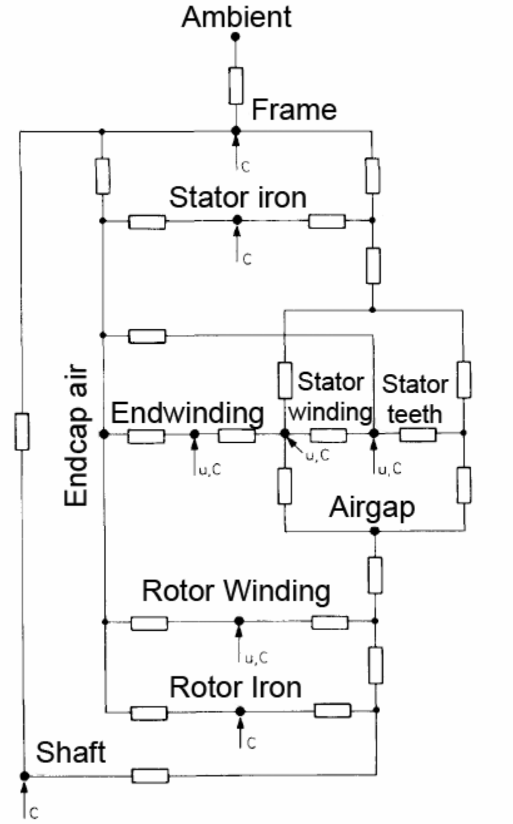

Figure 59: 11 node thermal model from [87]. C indicates thermal capacitance, U indicates heat input

The thermal model illustrated in figure 59 is a lumped parameter thermal model of an induction machine [87]. A lumped parameter model is where the properties of machine components are lumped into representative thermal components.

The heat input and storage components are simple to compute. The thermal resistances are more complex as there are many mechanisms of heat flow. Some of these, such as forced convection, are non-linear. Others depend on very specific details of machine construction and can be extremely difficult to measure.

The model described by Mellor *et al* in [87] uses a 11 node network with 23 thermal resistances. This model assumes symmetry about the shaft and a radial plane through the centre of the machine. The network was compared with results from a well instrumented 75kW induction machine and a 7% difference in the predicted stator winding temperature and 1% difference in stator endwinding temperature was found. The stator endwinding was measured to be the hottest part of the machine [87]. The sensitivity of each parameter to the major heat transfer coefficients was measured by increasing each heat transfer coefficient by 20% and observing the change in temperature. The results of this are detailed in table 18.

Table 18: Change in component temperature in °C as heat transfer coefficient is increased by 20% from [87]

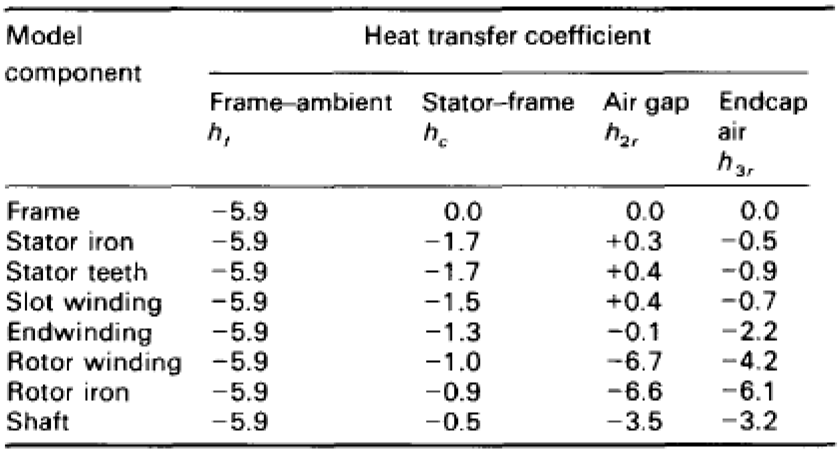

Model component	Heat transfer coefficient			
	Frame–ambient h_f	Stator–frame h_c	Air gap h_{2r}	Endcap air h_{3r}
Frame	−5.9	0.0	0.0	0.0
Stator iron	−5.9	−1.7	+0.3	−0.5
Stator teeth	−5.9	−1.7	+0.4	−0.9
Slot winding	−5.9	−1.5	+0.4	−0.7
Endwinding	−5.9	−1.3	−0.1	−2.2
Rotor winding	−5.9	−1.0	−6.7	−4.2
Rotor iron	−5.9	−0.9	−6.6	−6.1
Shaft	−5.9	−0.5	−3.5	−3.2

These results show that in this model the frame to ambient thermal resistance is the dominant parameter for the stator winding temperature. Mellor obtains this value by test, the rest of the model can be created from design drawings [87].

7.4.3 The MotorCAD model

MotorCAD is a thermal modelling package specifically intended for electrical machine design. It was created by Motor Design Ltd. to perform analytical thermal modelling on different machine types. The MotorCAD model of an induction machine has 31 nodes and 63 thermal resistances. It is laid out as in figure 60. The MotorCAD model is intended for the design of bespoke machines and so takes a large number of parameters into account.

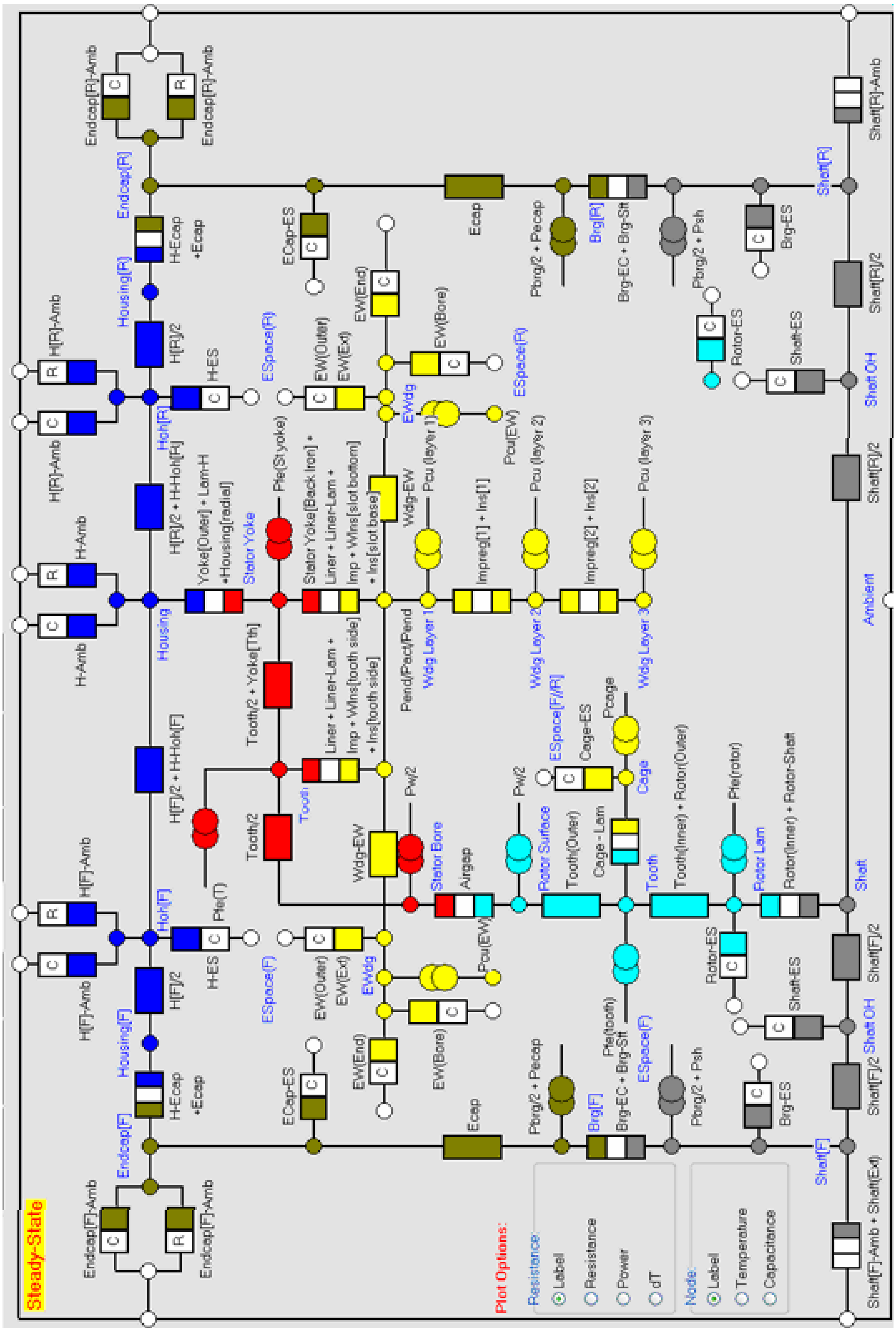

Figure 60: Motorcad thermal network for induction machine. Yellow indicates windings, red stator core, light blue rotor core, blue casing, dark green endcap and grey shaft components.

Dimensional, material and loss data are input into the model. It allows both steady state and transient temperatures to be calculated. Test data can be modified into a suitable format for the transient solver. This allows the model to be compared to real data directly and hence the model parameters calibrated to reflect the real generator.

Particular difficulty occurs when estimating the conduction properties from the stator winding to the core. The thermal properties of the impregnation can vary significantly. The same is true with the conduction from stator core to frame. In MotorCAD these parameters are modelled as a small airgap with a size that will be adjusted to yield the correct results. Mellor [87] used an equation from Shlykov [88] but found one of the motors to require a radically different value in testing. The equation and Mellor's motor coefficients are shown in figure 61. The contact pressure can be calculated from the size of the stator core and frame before the fitting process and the properties of the materials involved. Mellor [87] notes that the 5.5kW motor had its core removed for a test and was re-inserted loosely.

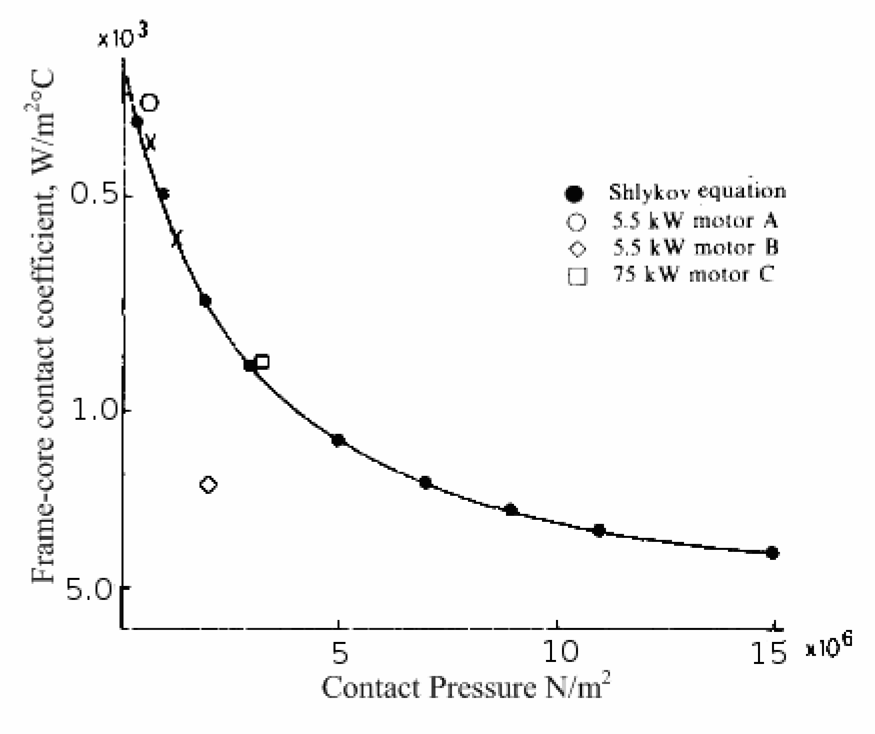

Figure 61: Contact heat transfer coefficient against contact pressure from Mellor [87]

7.4.3.1 Parameter sensitivity of MotorCAD model

The MotorCAD model of the induction machine is especially sensitive to some parameters. Boglietti [89] studied the sensitivity of the stator winding temperature to four parameters:

- Convection heat transfer coefficient from the machine surface
- “Goodness” of winding impregnation,
- Conductivity of the winding impregnation
- Interface gap between the stator housing and the core.

Boglietti carried out tests by injecting a DC current into the stator windings of instrumented induction machines. The conclusion was that the housing natural convection heat transfer coefficient was the most sensitive parameter. The DC supply prevented rotor rotation (and the shaft fan cooling) so no forced convection was taking place. If forced convection is taking place, the airspeed in the fin channels is the most important parameter as it determines the forced convection heat transfer coefficient [89], agreeing with the results for Mellor’s model [87]. The impregnation goodness is also a factor. A 80% reduction in goodness gives a 4-8% increase in winding temperature depending on motor rating. A 100% increase gives a 2-3% reduction in winding temperature. The interface gap was less important in these measurements but it is noted for a heavily loaded machine this would become important.

7.5 Calibration parameters

Some parameters can be determined with sufficient accuracy before the testing while others need to be brought into line with the real data. Dimensions and materials properties are known and do not change during testing. The actual convection heat transfer coefficient of the generator can only be estimated by empirical correlations. In the OWC application there is turbulence shed by the rotors which will increase the convective cooling from the generator surface by an increase in local velocity and mixing of air in and out of the channels between fins. MotorCAD's theoretical calibrations are for a shaft mounted fan, hence the leakage of cooling flow from the channels to the ambient is a problem. In an OWC the reverse is the case. The conduction cooling from the mounting of the generator depends on the thermal contact between the generator casing and the strut. The tests detailed here will include the measurement of generator temperatures at multiple points and thus the cooling measured and used to correct these parameters.

7.5.1 Control Techniques Thermal Model

The Control Techniques inverter used is a programmable model which contains a basic thermal model of the induction machine. The parameters used in this thermal model are accessible and will alter actions taken by the inverter when the induction machine nears its limits. The proper setting of these parameters allows an approximation of the stator winding temperature of the induction machine to be arrived at. This can be used to prevent over temperature while allowing overloading in the short term. Time constants measured on the steady state turbine test rig on Islay allow the thermal model to be calibrated correctly and the best possible output within the limits of the Control Techniques thermal model.

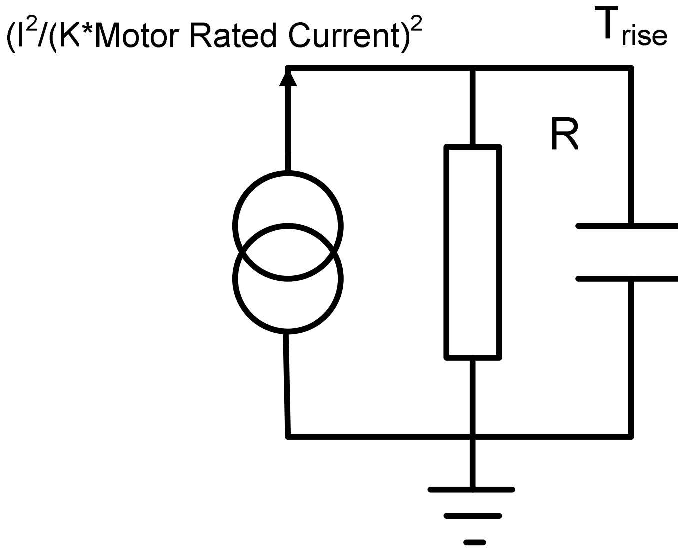

Figure 62: Thermal model used in Control Techniques inverter [79]

The Control Techniques inverter uses a basic thermal model outlined in [79] and shown in figure 62 to estimate the rise of the stator windings.

The heat input to the stator windings is given by the square of the instantaneous motor current, I, compared to the square of the motor rated current multiplied by a constant. R represents the thermal resistance between the stator windings and an external sink. C represents the heat capacity of the machine. The inverter accepts user input values of motor rated current and thermal time constant. The default value for the time constant is 89s and time constants of longer than 3000s cannot be accepted. The time constant is given by equation 89.

$$\tau = R^t C \tag{89}$$

This model predicts stator winding temperature rise as a percentage of rated temperature rise using equation 90 [92].

$$T_{rise} = [I^2/(MotorRatedCurrent)^2]*(1-e^{-t/\tau})*100\% \tag{90}$$

Where t is the time in seconds

The temperature rise is also known as the overload accumulator. When this value reaches 100% then an action is taken to prevent overheating. This may be a drive trip or a reduction of the current limit. The Control Techniques inverter also permits the reduction of thermal limits when the speed of the machine drops below certain limits (and any shaft mounted fan reduces in flow). Considering that the operational range of the 18.5kW turbine is above this region this part of the model may be neglected.

This model is the most basic possible of the induction machine, presumably for computational reasons. It does not consider ambient temperature, for a machine in a cold environment (such as an OWC operating on the west coast of Scotland in winter) this means that even at 100% temperature rise, the rated temperature has not been reached. The manual also supposes that the machines rated current will produce its limiting temperature rise. In the case of the Brook Crompton induction machine currently used by Wavegen, its measured stator temperature rise from an ambient of 20°C is 75°C, hence a stator winding temperature of 95°C is achieved [74]. However the same measurement document lists the insulation as Class F, thus limited to a 155 °C temperature less any hotspot allowance. If a 10°C hotspot allowance was to be used, a maximum rise of 125°C is possible before insulation rated limits are reached.

Hence, if this model is to be used to model the limits of the machine the maximum temperature rise should be used to generate the Motor Rated Current parameter. In the case of the Brook Crompton induction machine considered here it will be much greater than the current for which the machine is rated.

This model assumes constant values for R^t and C, assuming the user is not inputting time constant values continuously. The thermal resistance R^t will vary with flow speed over the generator casing and the “blockage effect” of other losses in the machine. The blockage effect is where losses between the stator winding and the generator surroundings increase the stator temperature (as the stator heat must flow out through the loss producing regions, consequently the stator temperature must be larger). The thermal capacitance C can be measured if R^t is known from the time constant. C could also be calculated using the specific heat capacity of the various materials used and the volume of each component, this is the method used by MotorCAD, however the internal geometry of the machine is not always accessible to the end user and the complex shapes of the intenal components require careful measurement.

If a single time constant is to be used in the OWC application it should be chosen in such a way to allow maximum power to be generated but not endanger the machine. The most pessimistic time constant is the lowest. This implies the machine will heat up quickly and cool down quickly. Assuming the thermal capacitance of the machine is constant then this will vary with R^t. The Unidrive Manual mentions the model for a constant current but does not mention the memory effect needed for an unsteady current to be measured.

7.6 Modelling for the Oscillating Water Column Environment

The models proposed by Mellor and Motor Design Ltd show that induction machines can be thermally modelled from design drawings, material properties and a few parameters that need calibration. The choice of model depends on the application, MotorCAD provides detail on the temperature of every significant component in the machine while the Control Techniques model only considers the endwinding temperature. This is because MotorCAD is intended to inform the design of new electrical machines using a desktop computer and the Control Techniques model must run in real-time on the microprocessor found in an inverter drive. The thermal model appropriate for an OWC application will be a compromise between these extremes. The MotorCAD model requires some special knowledge and measurement to use accurately and it is only necessary to know the temperature of the endwinding in this application. However changing the OWC system without changing the generator will alter some aspects of the thermal model while others remain constant. The Control Techniques model cannot take this into account and thus the thermal resistance network must be more complex.

The parameters used in thermal modelling must be measured in order to achieve accurate results. The most important of these parameters is the heat transfer from the generator surface. In the OWC environment this will be considerably different to that expected from a conventionally fan cooled generator. The airflow past the generator casing will be of variable velocity and temperature, as determined by the wave power input. Both of these parameters are needed for application-specific thermal modelling of the induction machine. If the model is to be used to predict maximum safe power output in service, the airflow must be linked to measurements made in service if it is not measured directly. To do this a series of tests must be carried out to measure the effect of the OWC environment on heat transfer from the induction generator.

8

MEASUREMENT AND ANALYSIS OF THE OWC ENVIRONMENT

8.1 Operational Measurements

The forced convection heat transfer coefficient from the generator casing has been shown by Mellor[87] to be the most important parameter for accurate thermal modelling. It is likely that the airflow in the OWC duct differs significantly from that provided by a shaft mounted fan and this will affect the heat transfer coefficient and therefore the temperature of the windings. Hence the cooling provided by this airflow must be measured, along with the range of air temperature found in an OWC duct. The duct temperature can be directly measured, however measurement of the heat transfer from the generator casing is more complex. The heat transfer coefficient can be calculated from the temperature of the casing and the airflow using the generator losses measured in chapter 6. Measurements over a range of airflow speeds and power outputs show the relationship between these parameters and heat transfer coefficient. This data can then be used in a thermal model to predict the maximum generator rating in a given situation.

8.1.1 Sensors

The 18.5kW turbine on Islay has pitot probes measuring air flow velocity and a retrofitted stator winding temperature sensor. Additional sensors mounted on the OWC device are rugged, waterproof to IP67 and securely attached. The sensors used connect to Wavegen’s data logging apparatus in order to synchronise the data measurement and allow reliable access to recorded data.

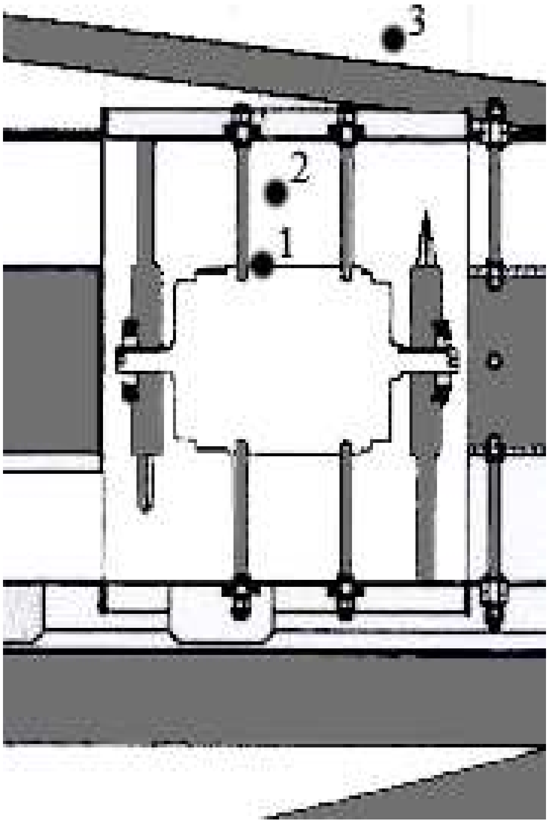

Figure 63: Location of additional temperature sensors in OWC duct

Sensor 1 in figure 63 is the frame temperature measurement. This is made by sensors bonded to the exterior of the frame and insulated from the airflow. The sensors are constructed from silicon rubber and are of the surface mounting type. The output signal is read by a dedicated distributed input/output card. The sensors are placed on the side of a fin for ease of installation. This is not as good as mounting directly to the main body of the frame and a correction must be applied to the temperature data. The sensor itself is accurate to within 0.375°C at 15°C.

Sensor 2 in figure 63 is the duct air temperature measurement. This is made by a tube inserted into the duct. The same sensor will make temperature and humidity measurements. The duct air temperature and humidity sensor is attached to the exterior of the duct and a rugged probe inserted into the airflow. The sensor used is a Vaisala 333 temperature and relative humidity probe. It is accurate to within 0.2°C at 20° C. The probe is stainless steel, 12mm in diameter and has a suitable replaceable filter on its end. The filter can be cleared with compressed air when clogged.

Sensor 3 in figure 63 is an exterior temperature sensor that is located in the outside air. The sensor produces a 4-20mA signal for interface reasons. It is accurate to within 1.2°C. An IP65 outside air temperature sensor producing a PT100 type signal was used. The exterior air sensor does not require the IP67 sealing necessary in the turbine duct as it can be located away from the harshest conditions.

8.1.2 Air flow sensors

There are two pressure based flow sensors in the inlet to the turbine. In addition five pressure sensors made measurements at selected points within the turbine duct. These sensors are used to record the air velocity through the duct for each test.

8.1.3 Electrical property measurements

The control techniques inverter measures the provided current, voltage, power factor and field speed of the induction machine. It also uses a model to estimate the machine slip.

8.1.4 Testing

The machine was rendered into a cool and isothermal state by leaving it unexcited and stationary with the valve closed for a long period of time. This allowed the temperature sensors to be checked for consistency.

To measure the ‘still air’ heat transfer coefficient the generator needs to be put into a state where the losses are known and constant. The turbine was started with the valve to the OWC chamber closed and the turbine speed was maintained at 4000RPM. The closed valve prevented OWC airflow driving the turbine and thus the load on the generator was the aerodynamic drag of the turbine rotor. Wavegen have measured this with some accuracy so the load is known and the input power can be measured. The difference between these quantities is the losses in the induction machine which must dissipated by convection and conduction from the generator casing. Measuring the ambient air and generator casing temperatures allow the heat transfer coefficient to be estimated.

8.1.5 Results

8.1.5.1 Calibration of sensors

The sensors were checked against each other after the generator was disconnected for over four hours. The valve was closed and the turbine stationary, the sea state was very calm and airflow in the duct minimal and the turbine is situated inside a dark room with thick concrete walls. Readings were taken over the course of six minutes and averaged. The offset of each sensor was changed to make it read identically to the duct temperature sensor which was factory calibrated.

Table 19: Calibration temperature measurements

Sensor	Average	New offset
Winding 1	3.35	13.24
Winding 2	6.53	10.07
Casing 1	17.45	-0.86
Casing 2	16.73	-0.13
Duct	16.59	0
Turbine hall	18.45	1.86

8.1.5.2 4000RPM with valve closed

The machine was run for 191 minutes with the valve closed at a speed of 4000rpm in early summer. The recorded temperature traces are shown in figure 64. The average power input into the machine once at speed is 3906W measured by the control techniques inverter drive. The average difference in temperature between the casing and the duct air is 3.89°C. Aerodynamic calculations by Wavegen give an estimated load of 2966W at 4000rpm and hence 940W of losses, allowing an error of 10%. This leads to an estimate of the heat transfer coefficient of between 217.5 and 266W/°C.

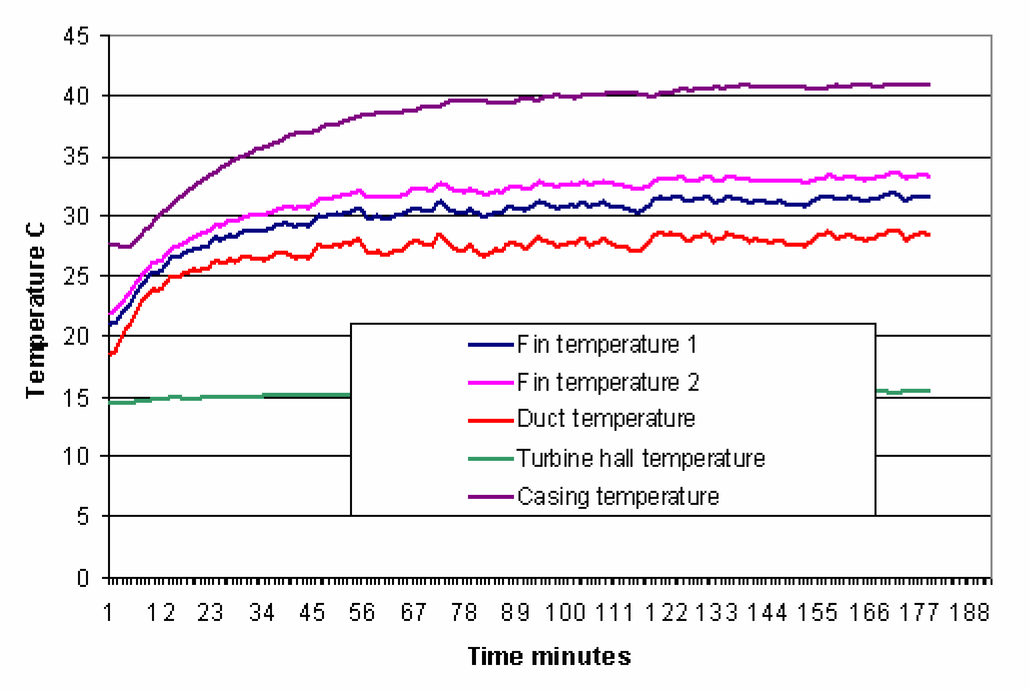

Figure 64: Temperature traces for 191 minutes on 4000RPM valve closed test

8.1.6 Short term temperature changes

A sample of wave cycles was analysed to see if the temperatures varied significantly in the short term. A typical wave cycle has an inhalation of air, a dwell and an exhalation of air. During this time the turbine will go from a local maximum of power to a minimum and back again. A minute of waves was measured while the turbine was running and the results are shown in figure 65. There are no significant short term changes in temperature although the generator power averages 7.7kW and varies between a maximum of 20kW and a minimum of 4.25kW. The thermal capacitance of the components in the induction machine is significant. MotorCAD modelling predicts the windings require 7896 J per °C temperature rise, the total stator thermal capacitance is 52640 J/°C and the total machine capacitance is 64970J/C. Ignoring all cooling flow, it would take 37.5 seconds for a uniformly distributed loss from full load to increase the machine temperature by 1C. Considering full load stator loss it would take 13.5 seconds to increase just the windings by 1C. With significant cooling in place it is unlikely that any rapid changes in temperature will occur. Hence further studies can be carried out on a minute by minute basis without reducing accuracy.

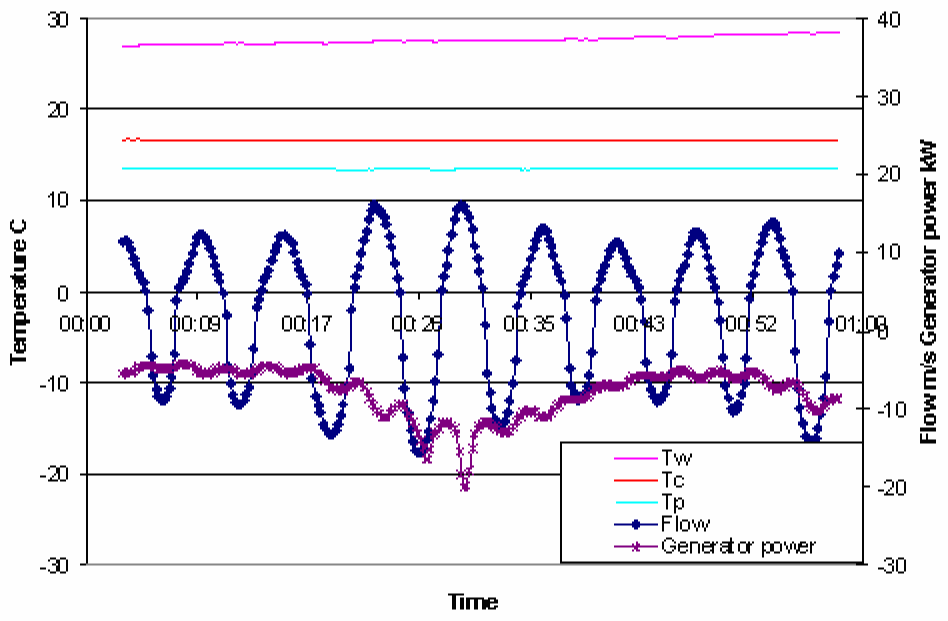

Figure 65: Temperature variation with changes in flow and generator power

8.1.7 Duct, casing and turbine hall temperature

The difference between the duct and turbine hall temperatures will be useful in predicting the cooling flux in a given turbine duct without the expensive and vulnerable duct temperature and humidity sensors. If a solid correlation was found, a cheap, well protected and easily maintained sensor could be used to calculate the rate of turbine cooling. The variables that determine the difference between the duct and turbine hall measurement in the long term are the input of heat due to generator losses, the air velocity in the duct, the volume of air enclosed within the duct and the OWC chamber temperature.

The constant speed test shows the difference between the duct and hall temperatures as the machine is accelerated and then moves into steady state. With the valve closed, the duct temperature is dominated by the generator losses and humidity. All other variables are removed or held constant. This can be seen during the deceleration phase at 18:02 and subsequent reacceleration at 18:10 in figure 66. The turbine hall temperature increases slightly during the test, an effect that can be ascribed to the generator heat output as any external heat inputs (i.e isolation) will be decreasing.

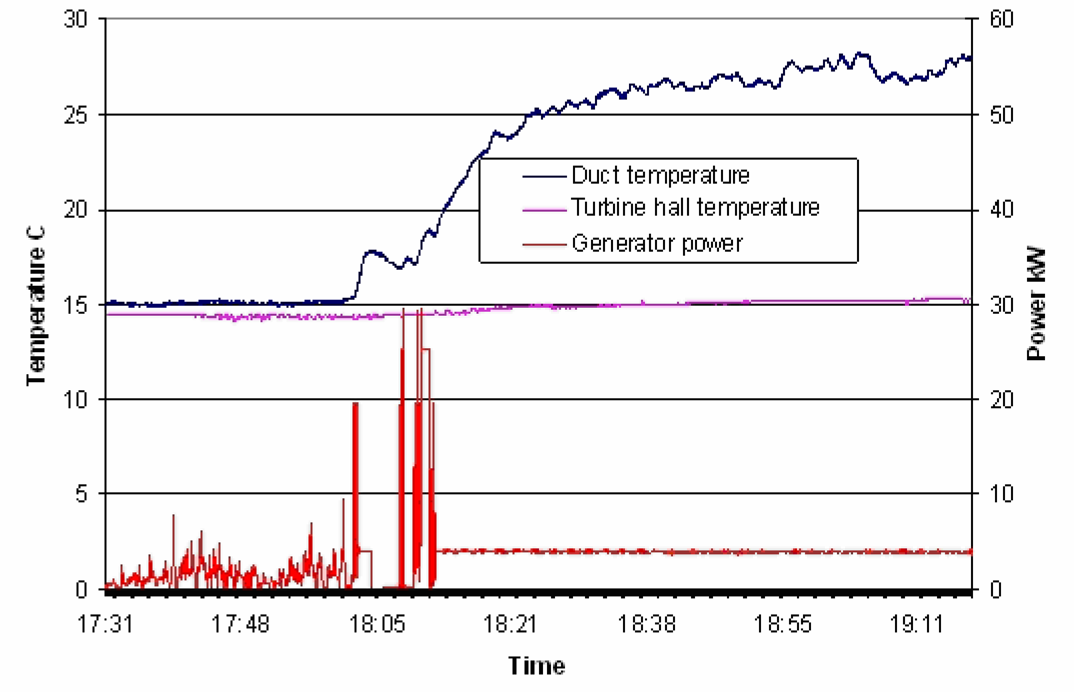

Figure 66: Duct temperature and turbine hall temperature for 983W loss in generator with valve closed

With the valve open and turbine running the duct temperature shown in figure 66 is considerably above the turbine hall temperature despite a relatively high sea state. This is also the case for the lower sea states shown in figures 67 & 68.

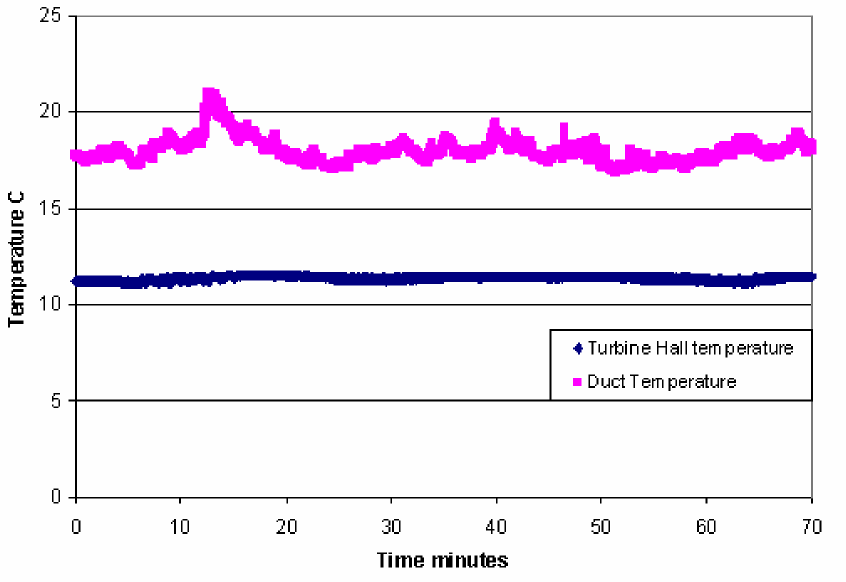

Figure 67: Duct and Turbine Hall temperatures for 11.5kW average sea state

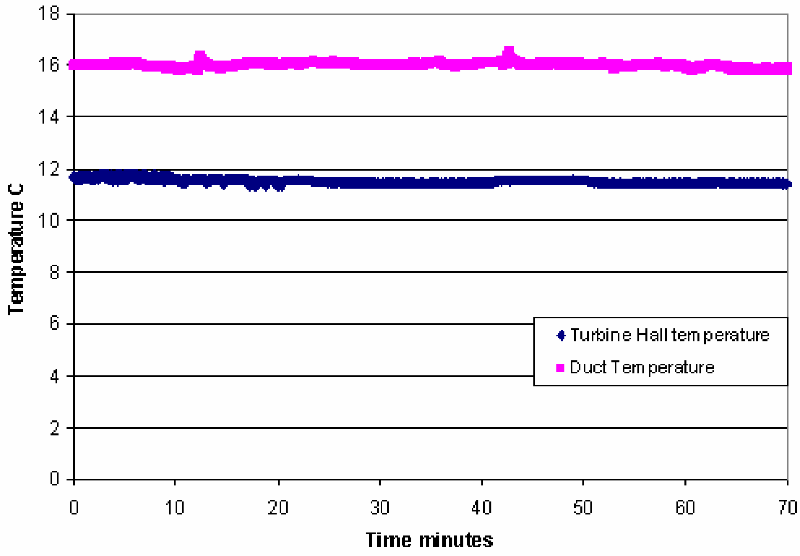

Figure 68: Duct and Turbine Hall temperature for 1kW average sea state

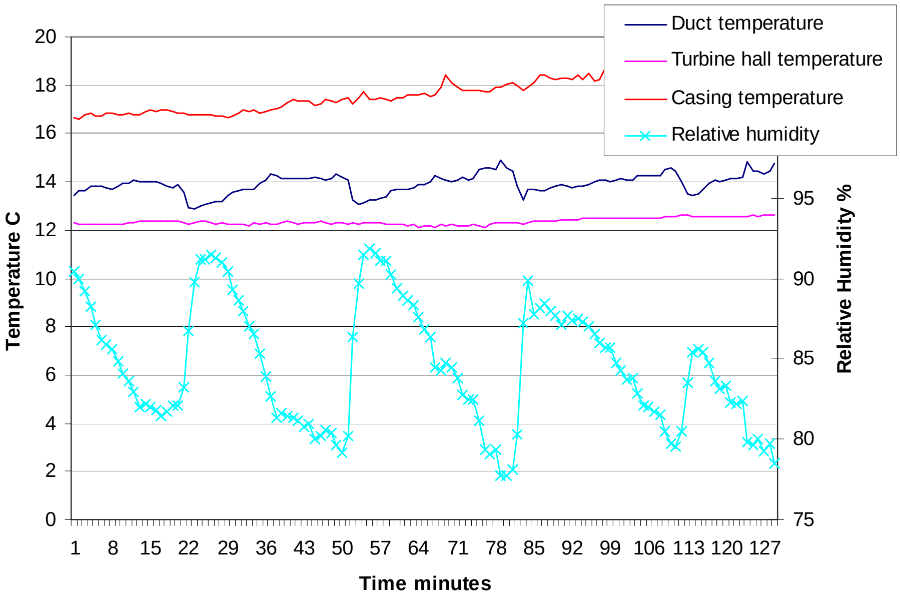

Figure 69: Duct, Turbine hall, Casing and Relative humidity for 9kW, relative humidity spikes show when cool water is sprayed into the duct

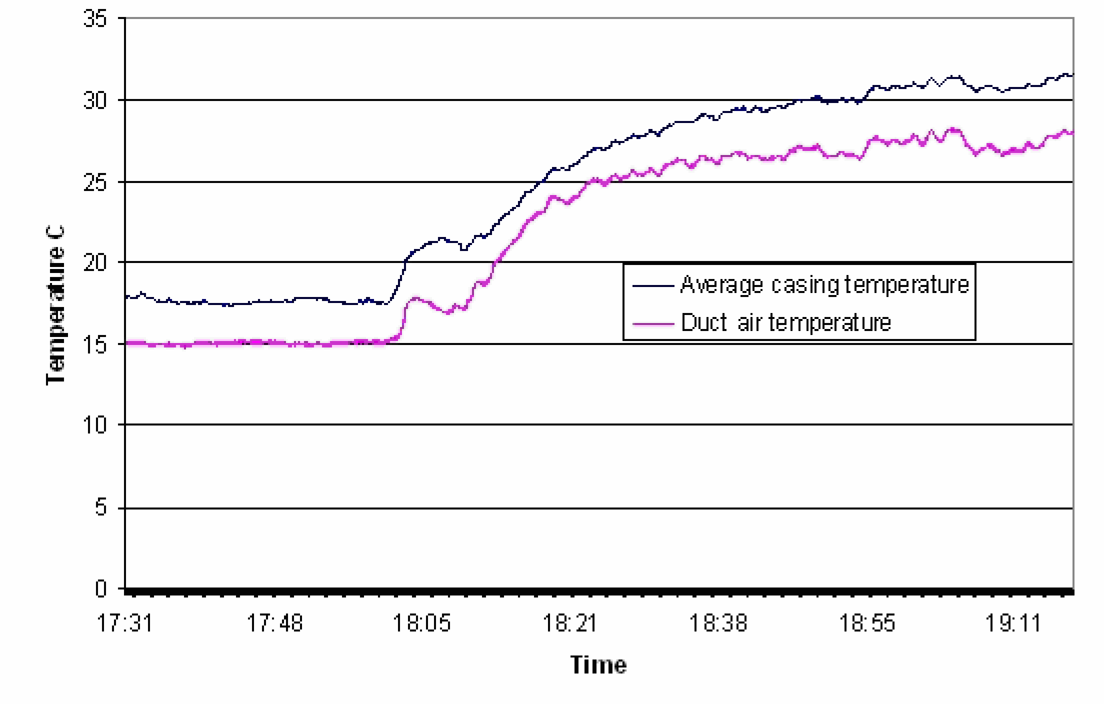

Figure 70: Duct temperature and Average casing temperature for 983W loss in generator and valve closed

In figure 69 the casing temperature and duct air temperature are considerably different as the air flow through the duct is replaced frequently. When the valve is closed and airflow limited, it can be seen (in figure 70) that the duct air temperature follows the casing temperature.

Using external temperature alone is not enough to predict the cooling air temperature or the casing temperature when the turbine valve is closed. In normal operation they remain relatively close. The most important scenario, however, is the limits of overload in a powerful sea. The average flow will be large so this may bring the duct temperature closer to the external air temperature but will also increase the influence of chamber temperature. It would be beneficial to obtain a relationship between ambient temperature readings made in the turbine hall and the duct air temperature. The duct temperature sensor is more prone to salt buildup, water ingress and mechanical damage, provides slight obstruction to airflow and is more difficult to repair whereas the turbine hall temperature sensor is inexpensive, operates in a calmer environment and can be maintained or replaced easily.

8.2 Steady state tests

To simplify the validation and calibration of a thermal model, the model can be compared to measurements made on a turbine in steady state. This is not possible in an OWC driven generator as the wave power input is significantly variable over the time taken for the generator to reach thermal steady state. Hence tests were carried out on a turbine driven by a constant airflow provided by a fan. This eliminates the thermal capacitance terms from the final measured temperatures while allowing the capacitance to be measured from the time taken to reach steady state.

8.2.1 Steady state Wells turbine test rig

Figure 71: Steady state test rig ductwork separated for sensor installation

The steady state test rig is used by Wavegen to allow the performance of Wells turbine configurations to be assessed. It consists of a duct section with dimensions similar to that used on the 18.5kW OWC Wells Turbine, shown in figure 71. It has expansion sections at inlet and the outlet to the settling chamber (shown in figure 72) which sits between the turbine and the fan. The fan sucks air through the turbine and expels it outside of the test chamber.

Figure 72: Test rig in LIMPET turbine hall. Turbine in foreground, settling chamber and fan motor in background

The turbine under test was a biplane turbine with five blades on each rotor. It had a tip diameter of 0.75m and a hub diameter of 0.32m. The generator is controlled by a Control Techniques inverter with distributed data acquisition located close to the rig. The fan speed was controlled by an Alstom inverter.

8.2.2 Induction machine temperature sensors

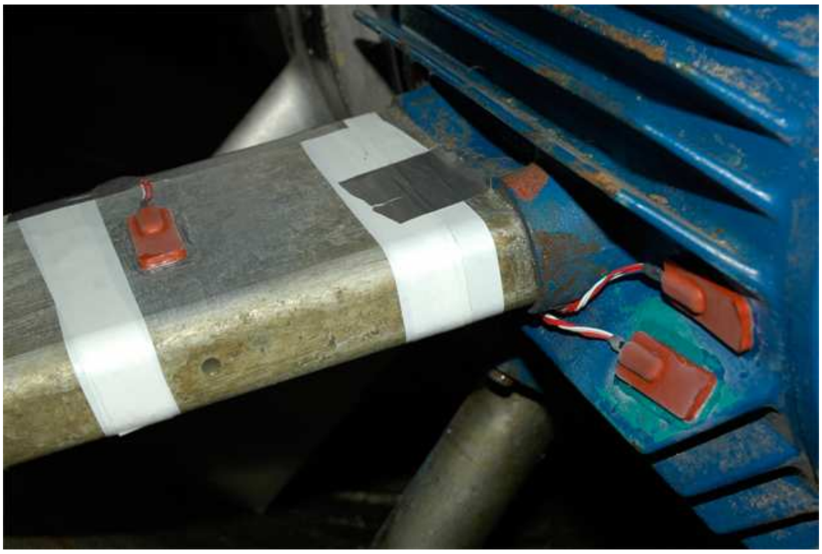

Figure 73: Mounted surface temperature measurement sensors

The machine frame temperature measurement, shown mounted in figure 73 is made by two sensors bonded to the generator casing at opposite ends. A sensor was added to the generator fin to observe the difference in fin and casing temperatures. Another sensor is mounted on the support strut to identify any conduction cooling from the strut. The sensors are constructed from silicon rubber and are of the surface mounting type. The sensor is accurate to within 0.375˚C at 15˚C.

Figure 74: Vane anemometer in turbine duct upstream of turbine blades

The duct air temperature measurement is provided by the vane anemometer inserted into the duct with an accuracy of 0.1˚C. An exterior temperature sensor that is located in the outside air that is being drawn into the turbine duct. This measures the ambient temperature. It is accurate to within +1.2˚C and – 0.2˚C.

The induction machine to be used for this test has a thermocouple buried in the stator end windings, identified as the hottest part of a force cooled machine's stator winding. This sensor was used to prevent the machine from overheating and show that the inside of the stator has reached a steady temperature. This sensor is accurate to within 2.5°C.

In addition to the pressure based sensors used in the previous tests a manually logged vane anemometer was used to record the air velocity through the duct for the steady state tests with an accuracy of 0.1m/s.

8.2.3 Steady state test method

A constant flow will be generated in the turbine duct by the test rig fan. The induction generator will absorb power from this flow at a constant rate, running at a constant speed. The airspeed, generator power output, temperature and humidity will be measured. The test will end when the stator windings are observed to have reached a steady temperature over a significant period of time.

The machine was left idle for a significant amount of time to allow all temperatures to settle close to ambient. This happened overnight between tests. IEEE 112-2004[38] specifies that temperature tests can start when all components are measured to be within 5°C of ambient. The temperature sensors were read and the rig was then started in a safe manner. The required flow was applied to the turbine with the generator operating at the test speed. The power applied to the generator was be the highest power to be applied in that round of tests. Data was collected throughout the test at 5Hz. Once the generator's stator winding sensor showed that steady state has been reached (IEEE 112-2004 [38] defines steady state as "a lower than 1°C temperature rise over 30 minutes") the next test was started. Close groups of tests allowed more load points to be tested within a day. The collection of a relatively wide spread of data was desirable over the duration of the tests so the variation of temperatures with airspeed and power input is known over the machines operating range.

Over the course of testing two different generator speeds were used: 4000 and 3000RPM. The difference in speed changes the operation of the turbine and allows another point on the flow against power graph to be recorded.

8.3 Results

8.3.1 Calibration of temperature sensors

The readings of all temperature sensors at ambient temperature with the generator approximately isothermal were collected before every test. An offset was introduced to all temperatures to bring them in line with the ambient temperature sensor for each data set. The ambient temperature sensor was checked against a certified thermometer and measured 1.86C warmer. The offsets for the tests are noted in table 20. For comparison the manually read vane anemometer ambient temperature is included.

Table 20: Temperature sensor offsets for tests in degrees Celsius

	T_a	Vane anemometer ambient	Stator	Fin	Strut	Upstream	Downstream
Test 1	8.6	X	-0.9	5.0	2.7	4.3	4.2
Test 2	5.9	5.9	-1.0	-0.6	-0.6	-0.8	-0.7
Test 3	10.7	9.7	-0.3	-0.9	-1.1	-1.1	-1.0
Test 4	10.6	10.5	-5.3	-1.2	-1.3	-1.5	-1.3

8.3.1.1 4000RPM, 19.4kW, 17.3kW, 15kW

All powers are given as the motor drive measured real power. Three power levels were tested before the turbine was shut down overnight. The test duration was four hours and twenty minutes excluding generator cooling period. The results are shown in figure 75.

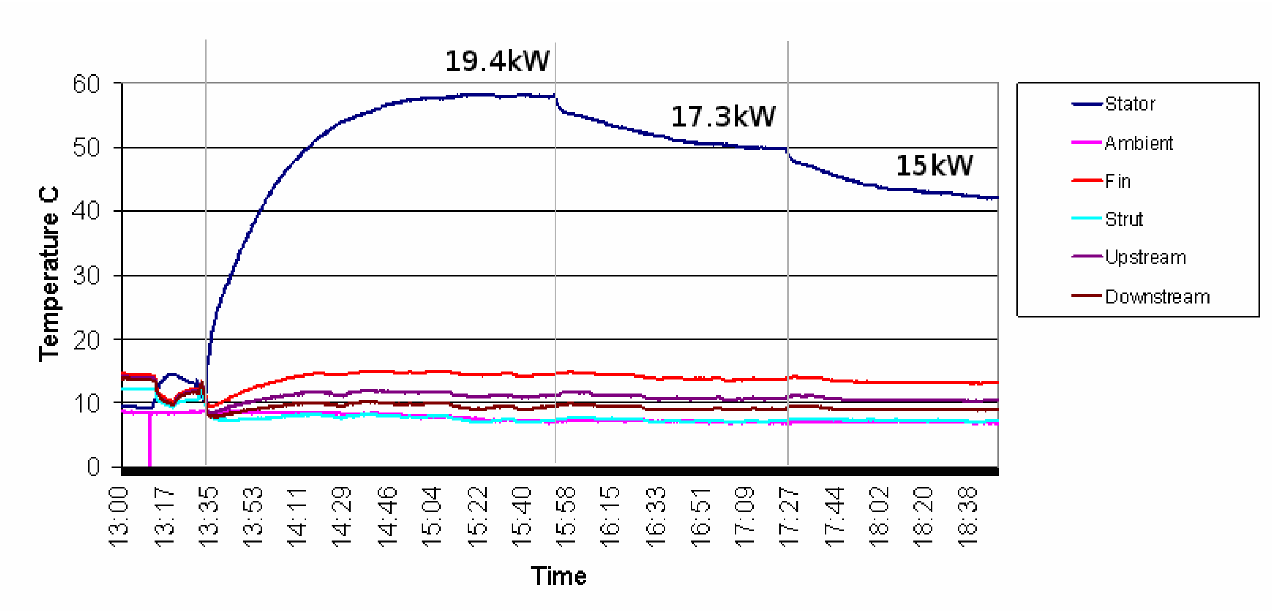

Figure 75: Temperatures recorded for three power levels at 4000rpm, 19.4kW, 17.3kW & 15kW

8.3.2 3000RPM, 20kW, 16kW, 12.5kW

Three power levels were tested. The test duration was seven hours. There was a gap in logging after the first test as essential new software was loaded to the logging machine, shown as the drop in temperature to near zero in figure 76. The recorded temperatures are shown in figure 76. The vane anemometer recorded air velocities of 12.72m/s at 20kW, 11.6m/s at 16kW and 10.6m/s at 12.5kW.

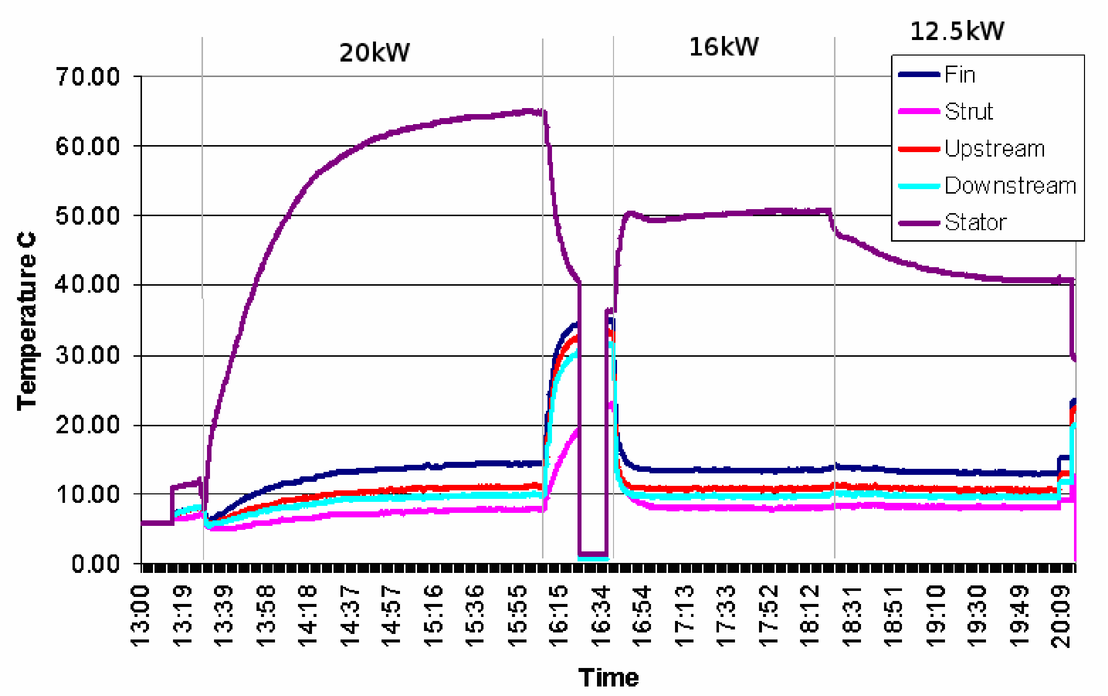

Figure 76: Temperatures recorded for three power levels at 3000rpm, 20, 16 and 12.5kW

8.3.3 4000RPM, 7.75kW, 4kW, 0kW, 20kW and 9.2kW

The turbine was left to sit overnight. Three tests, shown in figure 77, were conducted the next morning at 4000RPM at low powers. The 0kW trace was obtained by adjusting fan speed so no net real power was measured by the inverter. Once the temperature was settled for the 0kW trace, a 20kW test was begun. There is a gradient change visible in the stator temperature as the initial fan setting of 1400rpm delivered a constant power that was too great for the generators software safety mechanisms to allow.

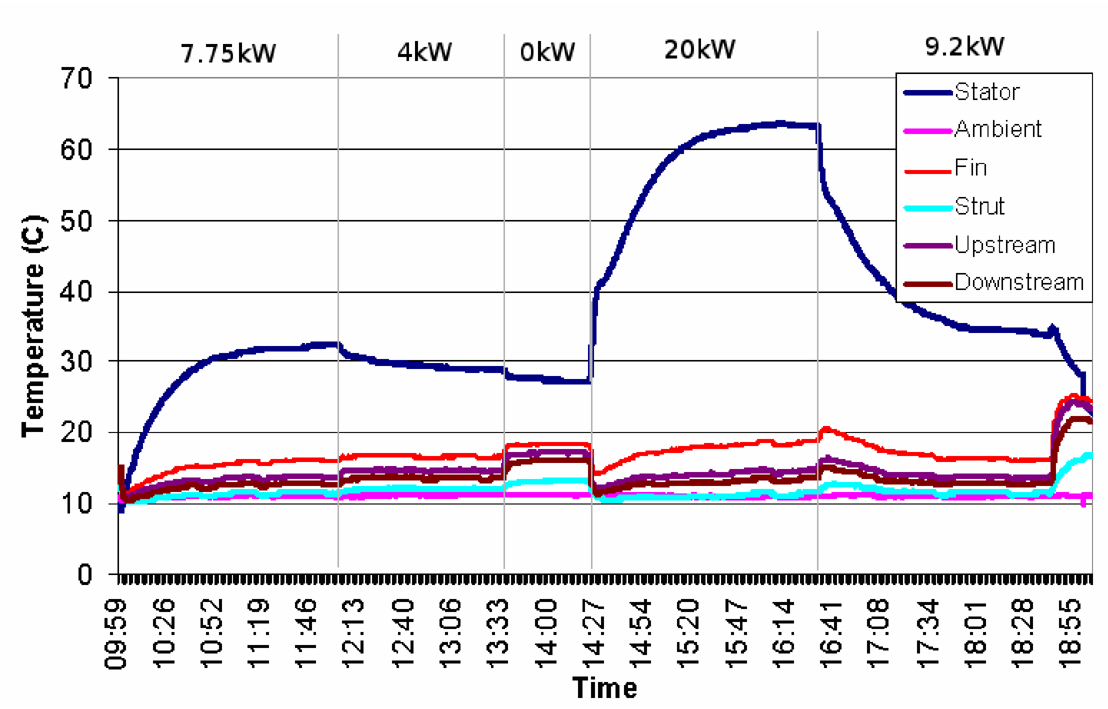

Figure 77: Temperatures recorded for five power levels at 4000RPM, 7.75kW, 4kW, 0kW, 20kW and 9.2kW

8.3.4 Stalled tests

By reducing the turbine rotor speed the angle of attack of the blades can be increased to the point where aerodynamic stall occurs. This reduces the power absorbed by the turbine rotor for a given airspeed and increases the turbulence present in the turbine duct. The turbine was run at both 2700 and 1600RPM with the test rig fan operating at full speed. It took some time to set the test up properly so a smooth curve to the first result was not observed. The stator temperature measurements exhibit notable noise due to the vibration of the turbine. It is visible from figure 78 that the noise on the stator winding measurement was greater than 1°C. The test was ended when a plateau of significant length was reached. For the 5.5kW test and air speed varied between 15.5 and 16.75m/s. During the 1.2kW test the air speed varied between 16.5 and 17.2m/s.

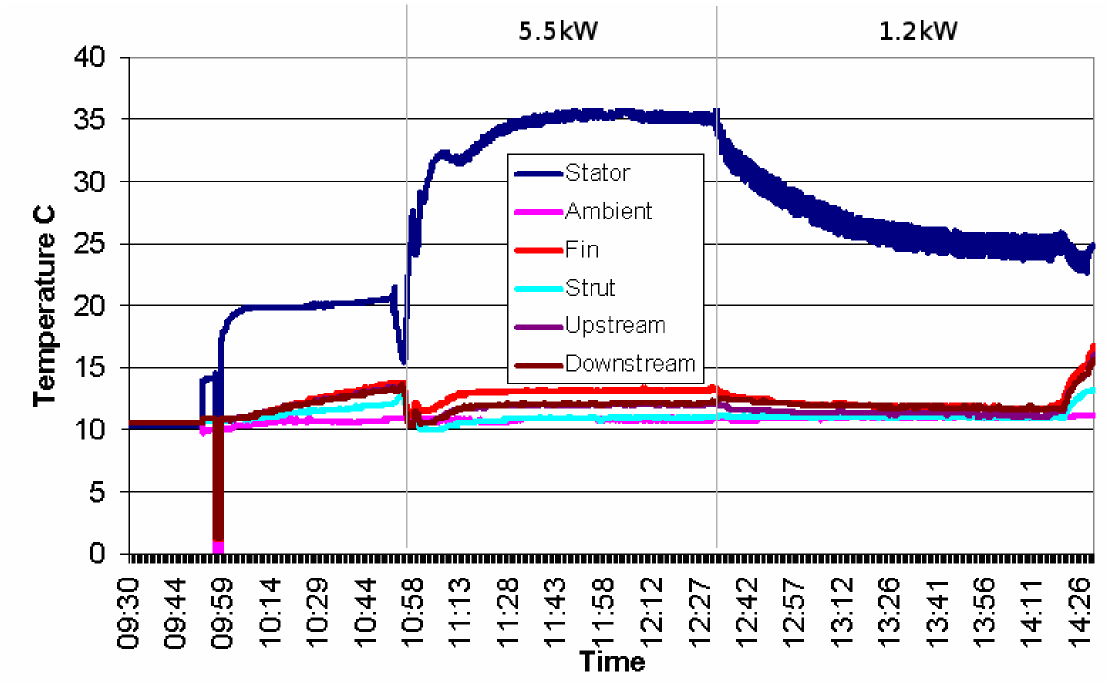

Figure 78: Temperature measurements for stalled tests at 5.5kW and 1.2kW

8.4 Analysis

8.4.1 Effective thermal resistance

The steady state stator temperature for each test was recorded, as was the current magnitude present in the machine stator. The stator copper loss was known from equation 91. The proportion of this loss in the generator endwinding is approximated by equation 92. This does not take into account the temperature difference between winding and endwinding and consequent resistance increase.

$$P_{loss} = \sqrt{3} I^2 R \tag{91}$$

$$P_{ew} = P_{loss} \frac{L_{ew}}{L_{winding}} \tag{92}$$

Where L_{ew} is the length of the endwinding
$L_{winding}$ is the length of a winding

The effective thermal resistance between the stator endwinding and generator surroundings is calculated from equation 93. The results are plotted against airspeed in figure 79 and generator power in figure 80.

$$R_{eff}^{t} = \frac{P_{ew}}{T_{stator} - T_{ambient}} \tag{93}$$

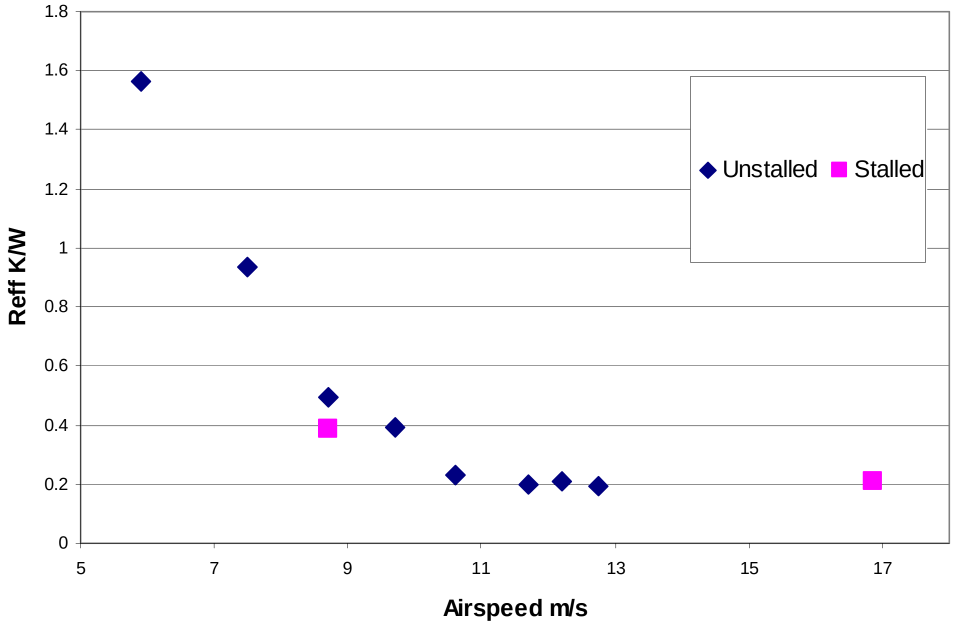

Figure 79: Effective thermal resistance plotted against airspeed for a stalled and unstalled turbine

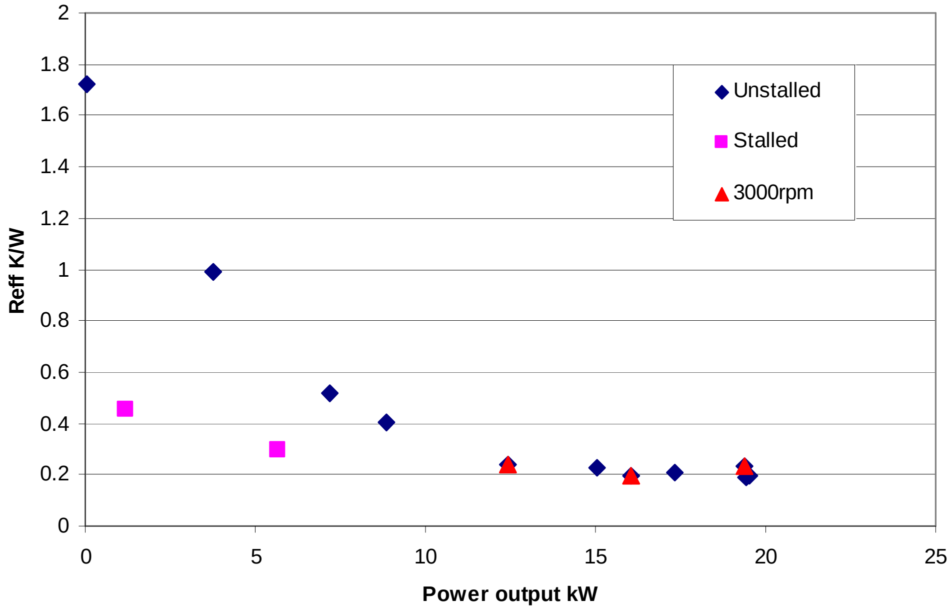

Figure 80: Effective thermal resistance plotted against generator power output for a stalled and unstalled turbine

The effective resistance reduces with both airspeed and power output to a minimum value. This suggests that either the cooling of the generator surface is no longer the dominant thermal resistance and that other fixed internal resistances govern the flow of heat.

8.4.2 Time constants

Where a complete curve was present, the time constant of the generator as it moves between stator temperatures was noted. The time constants were plotted against measured airspeed in figure 81 and generator power in figure 82.

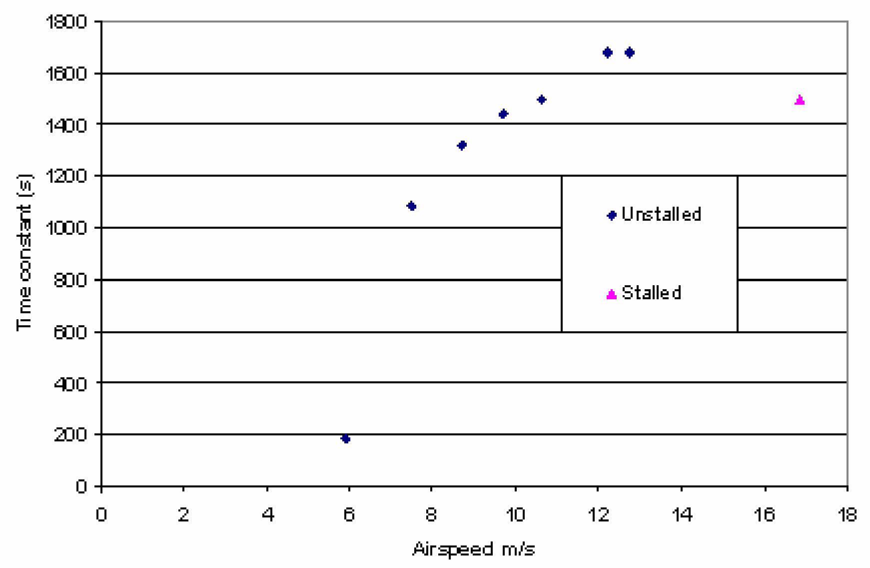

Figure 81: Generator time constant for varying airspeed

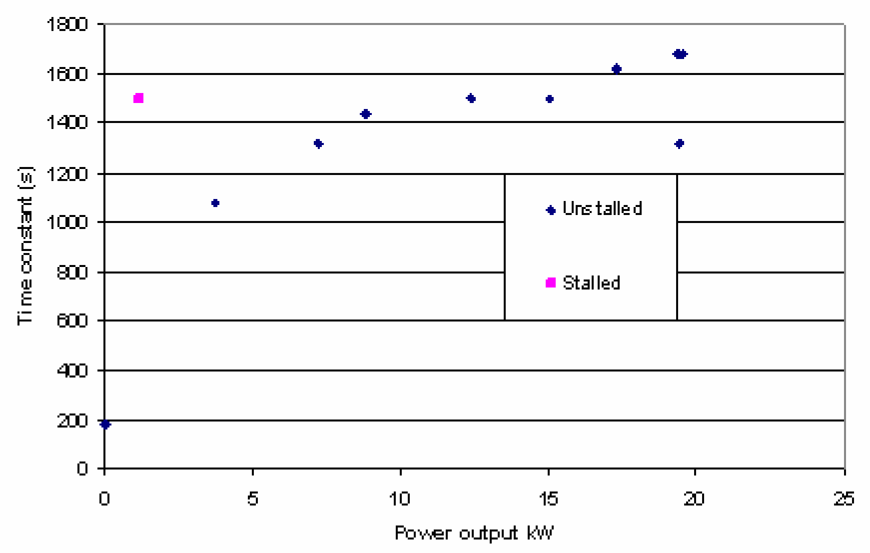

Figure 82: Generator time constant for varying generator power output

The time constant increases with both power output and airspeed. The time constant is the thermal resistance multiplied by the thermal capacitance. The effective resistance decreases as airspeed past the generator increases, it can be surmised that the thermal capacitance must increase faster than the decrease in thermal resistance. This could be explained by the relatively hot stator being better able to reject heat to other regions of the machine, hence the effective thermal capacitance being increased.

8.4.3 Effective thermal capacitance

The thermal time constant is made up of the thermal resistance and thermal capacitance. The thermal resistance changes with power output, hence care must be taken when calculating the thermal capacitance of a system moving thermally between two power outputs, including starting from cold (as different components have different thermal time constants).

The transient blockage resistance will differ from the steady state blockage resistance as the components in the generator heat and cool at different rates. The difference between this thermal circuit and an electrical circuit is that the resistance and capacitance values change with power input (and thus losses). A MotorCAD simulation of the effective thermal resistance as the generator moves from a constant 25kW to 10kW at 20m/s and 5m/s is shown in figure 83. The time constant of the 5m/s trace is 41 minutes, the 20m/s trace has a time constant of 32 minutes. It can be seen that the effective thermal resistance varies significantly over the time constant period. To aid non-steady state modelling, the thermal resistance should be split into components without memory effects such as casing convection and components with memory effects such as the effect of other losses.

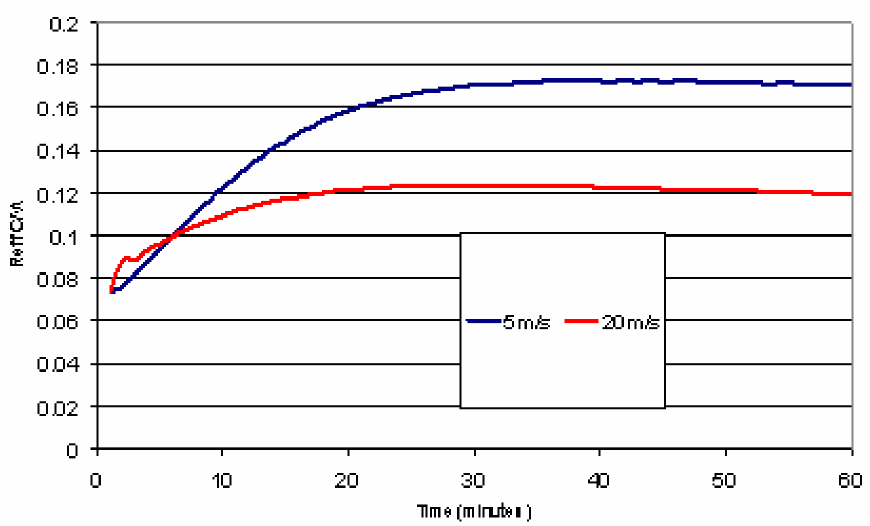

Figure 83: Variation of R^t_{eff} as generator reduces in output from 25kW to 10kW at different airspeeds.

The thermal capacitances obtained from cold start and mid run values can be seen in figures 84 & 85. The data from cold starts is limited to three tests. The 7.21kW test is in line with data from the 0kW and 4kW tests (carried out directly afterwards) however the tests closer to 20kW show differences between the cold start and mid run values. The increase in capacitance can be seen in both figures, however the effect causing this is related to generator power output, not airspeed.

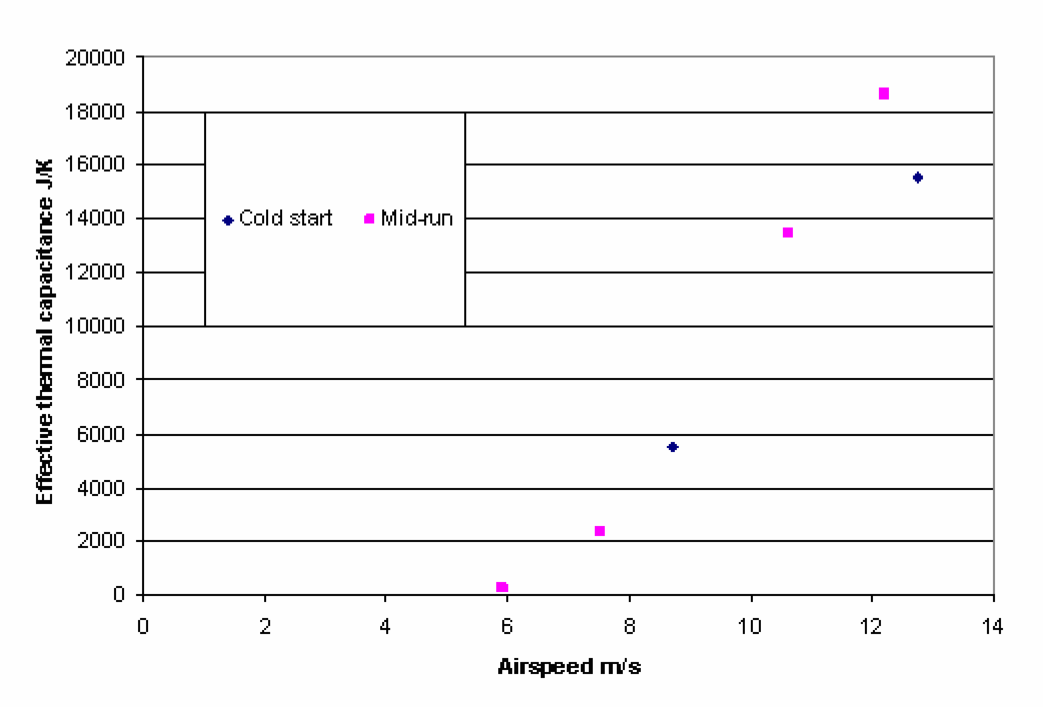

Figure 84: Thermal capacitance values for cold start and mid run tests plotted against airspeed

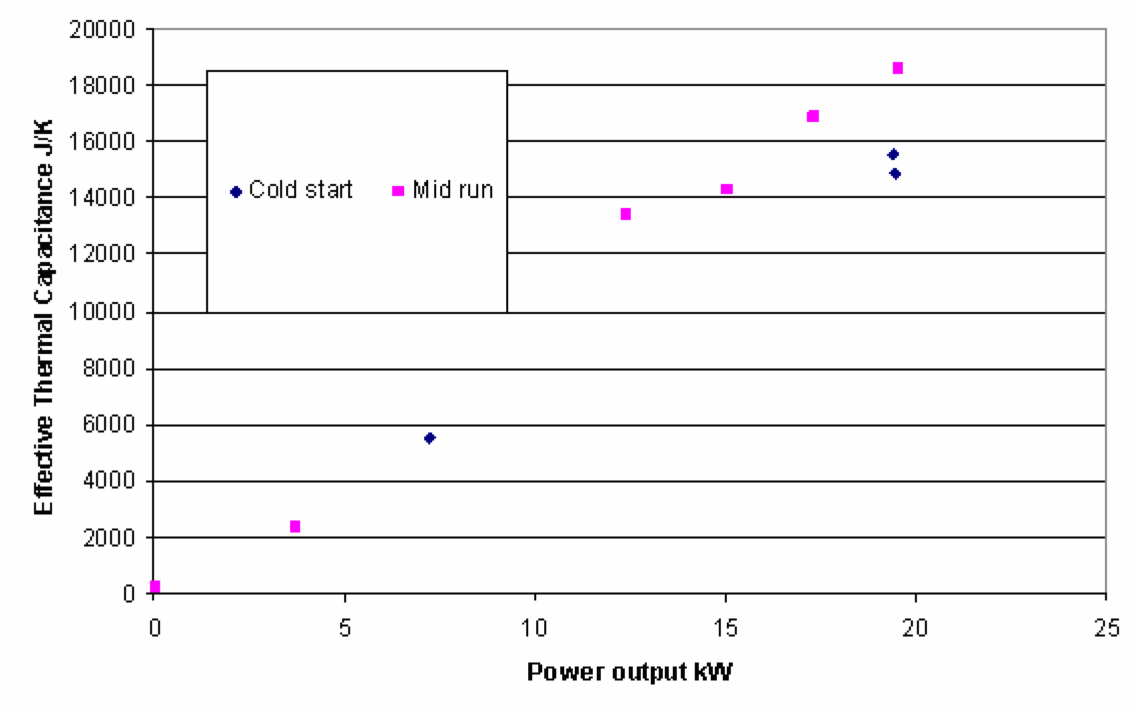

Figure 85: Thermal capacitance values for cold start and mid run tests plotted against generator power output

8.4.4 Comparison of 3000 and 4000rpm tests

The most direct comparison of flow and speed for 3000 and 4000rpm is made at around 19.5kW. At 3000rpm, 19.4kW is obtained at 12.75m/s measured airspeed. At 4000rpm, 19.5kW is obtained at 12.2 m/s airspeed. Hence at that level the flow and power are nearly identical. This is confirmed in figure 86 where the 3000rpm values plotted lie on a trend very close to the 4000rpm values. This implies that the relative differences between flow and power at these speeds in the range of tested powers and airspeeds are small.

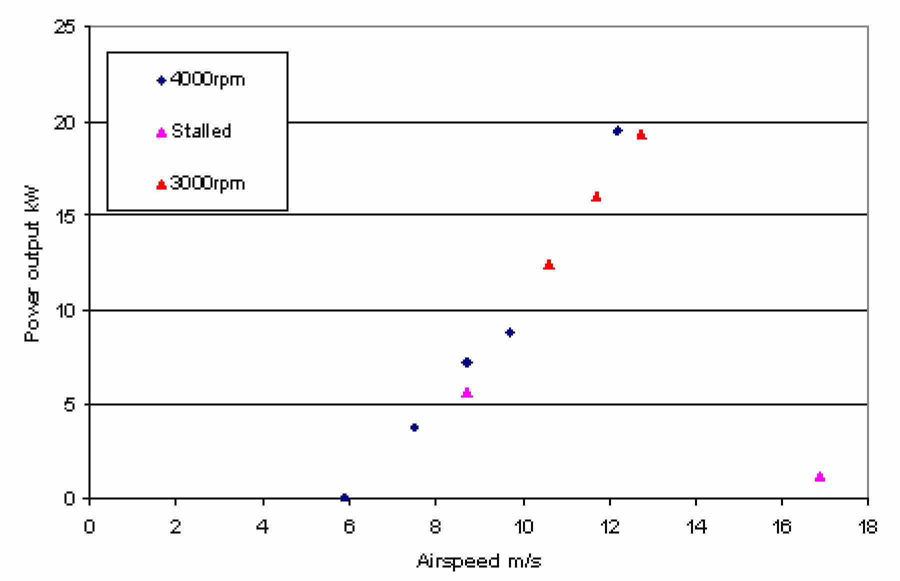

Figure 86: Power output compared with measured airspeed for different turbine speeds

8.4.5 Surface mounted sensors

The strut temperature sensor was placed to reveal any steady state temperature rise during the tests. A temperature rise could indicate heat conduction away from the generator by its support structure. In all but the first three tests a temperature rise was indicated. Figure 87 shows that the strut temperature generally decreases with airspeed but the exact relationship is lost in the scatter in the data. A decrease in temperature with airspeed would be expected if the forced convection heat transfer from the generator casing and the strut itself was removing the generator heat more efficiently.

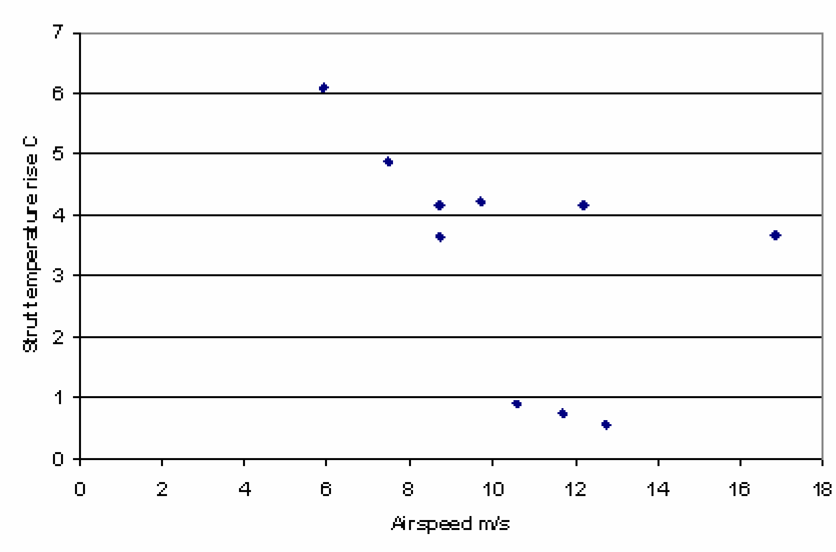

Figure 87: Strut temperature rise plotted against measured airspeed

The fin temperature sensor was installed to calibrate earlier data (also measured on the generator fin) against the generator casing temperature. An estimate of the difference between fin and casing was made from theory. The measured fin temperatures were consistently above those of generator casing sensors. The difference is proportional to airspeed and changing with turbine RPM, illustrated in figure 88.

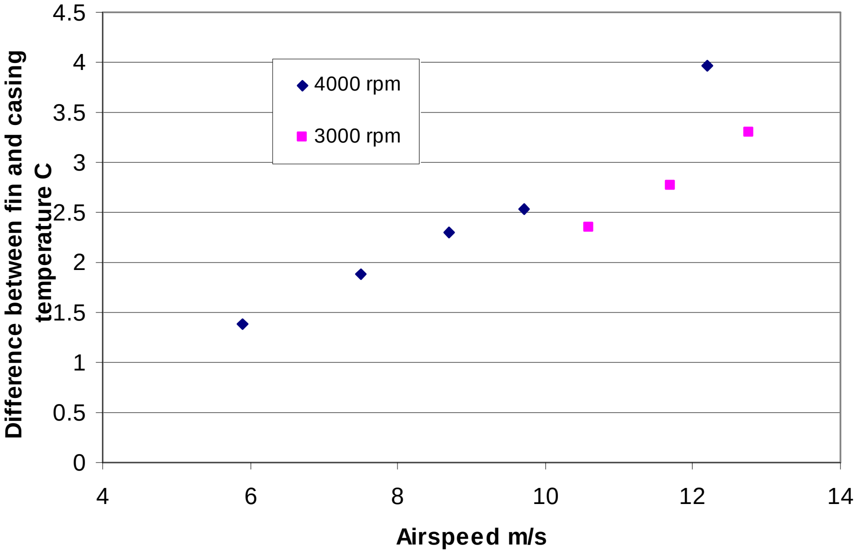

Figure 88: Relationship between airspeed and difference between fin and upstream casing temperature sensor readings

The temperature difference is attributable to fast moving turbulent airflow from the turbine rotor heating the fin or sensor. During the "soak back" (period of temperature equalisation illustrated in figure 89) after the end of a series of tests the fin is only hotter for a short period of time. The soak back is the period of equalisation in temperature that occurs when the generator is switched off and the cooling airflow is removed by closing the valve to the OWC chamber. The removal of the airflow increases the thermal resistance between the generator casing and surroundings hence the casing temperature increases rapidly while dissipating the stored heat.

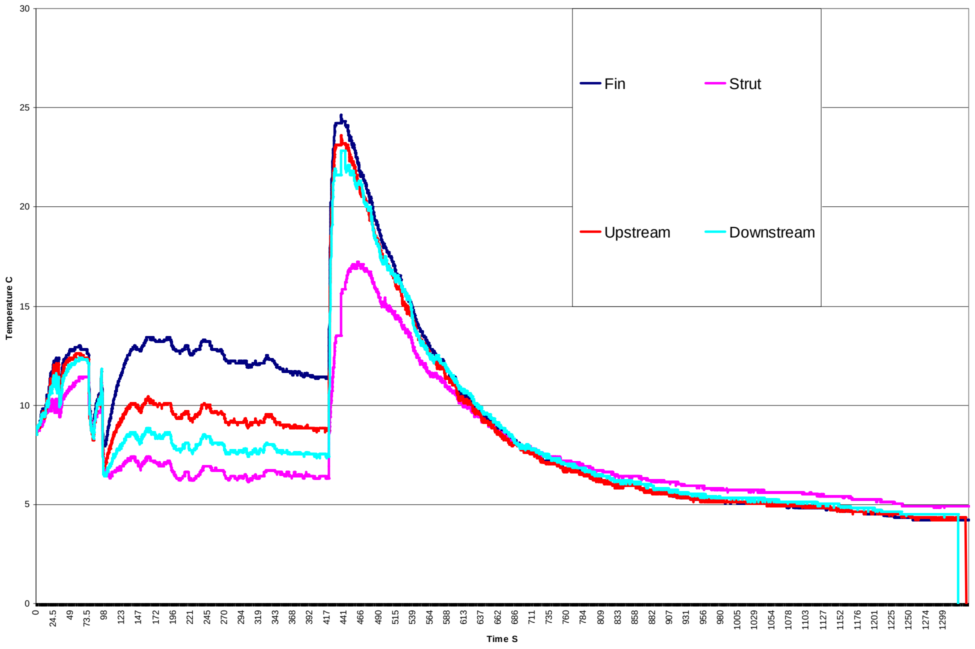

Figure 89: Surface sensor temperature spike after test end

The measured temperature rise in the generator casing sensors can be seen before the temperature spike in figure 89. The upstream generator casing sensor, close to the fin temperature sensor, was consistently hotter than the downstream sensor in all tests. In a uni-directional test rig it was expected that the downstream sensor be slightly hotter than the upstream sensor. During the tests this was only observed during stall. Excepting stall, the difference between the sensors was constant and did not change with airspeed or temperature. The difference did disappear during the soak back tests suggesting there is a similar heating effect from being immediately downstream of the turbine rotor during tests. Consequently the downstream temperature is considered to be the most accurate representation of the generator casing temperature.

8.5 Discussion

The thermal behaviour of an induction generator in an OWC was measured in operation and in steady state. The thermal time constant of the generator is sufficiently long that minute by minute data is sufficiently accurate for the tests and future modelling. The duct temperature in operation remains close to the turbine hall (ambient) temperature, further measurements with more accurate sensors could show a relationship and allow the cooling air temperature to be calculated from ambient temperature readings. A large data set would be necessary to obtain this relationship with any certainty.

Tests were carried out in steady state between 0 and 20kW or power output at 3000 and 4000RPM (stalled tests were carried out at lower speeds to induce stall). The effective thermal resistance between the endwinding and surroundings was calculated using measured data. Using this and the measured time constants for the generator, the thermal capacitance could be found. The thermal capacitance of the generator rises with power output, suggesting an increase in “utilisation” of heat capacitive components.

In the next chapter the test data will be included in a series of thermal models along with loss data from chapter 6. The thermal models are then used to predict the critical temperature of an induction generator in an OWC under certain conditions and a generalised model is presented.

9

A SPECIFIC MODEL OF THE INDUCTION MACHINE IN THE OWC ENVIRONMENT

9.1 Introduction

This chapter sets out thermal models suitable for modelling the induction machine in an OWC. Motor Design Ltd's MotorCAD model is calibrated using test data from the previous chapter and simulations are carried out to find the maximum steady state power output. The model found in Control Techniques inverters is updated with measured values of the generator time constant, however the scope of this model is limited. A more adaptable model is proposed, complex enough to be adapted to different size machines in the OWC application while consisting of relatively few components. The components that make up this model are identified and quantified for the 18.5kW turbine and an error analysis is carried out on the model.

9.2 Modelling using MotorCAD

9.2.1 MotorCAD model of 18.5kW induction machine

A model of the Brook Crompton 18.5kW induction machine was created in motorCAD from design drawings [93]. The parameters used are given as appendix iv. The radial cross section of the generator is shown in figure 90 and its axial cross section is shown in figure 91. The materials library in motor-CAD was used to provide materials data.

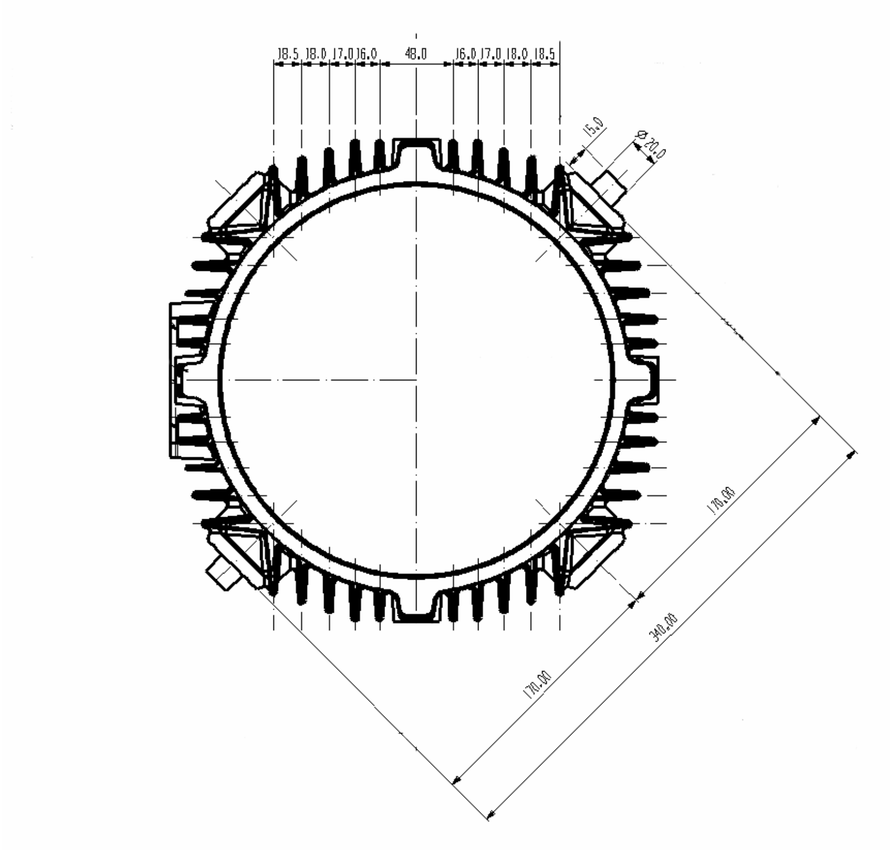

Figure 90: Radial cross section of Brook Crompton 18.5kW induction machine

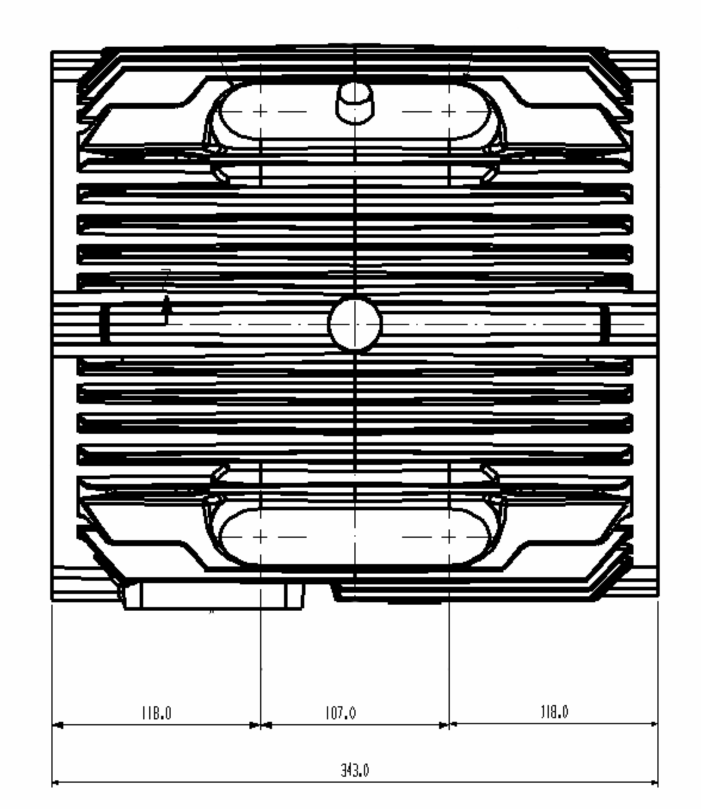

Figure 91: Axial cross section of Brook Crompton 18.5kW induction machine

9.2.2 4000rpm with valve closed

The induction machine was operated as a motor to spin the turbine at 4000rpm with the valve to the OWC chamber closed. This test was introduced in section 8.1.5.2 . The duct temperature measurements made at the time were used to provide appropriate external fluid properties for the motorCAD thermal model. With the valve closed with a calm sea, the dominant cooling path could be natural convection. The airspeed measurement system is not designed to operate in this situation and there is some leakage airflow around the valve so the actual airspeed in the duct is unknown. This section shows the calibration of the motorCAD model to the induction generator and turbine.

9.2.2.1 Natural convection

The machine was considered alone without conduction to the turbine rotors or duct structure. A simulation considering only natural convection from the generator is compared to measured data in figure 92.

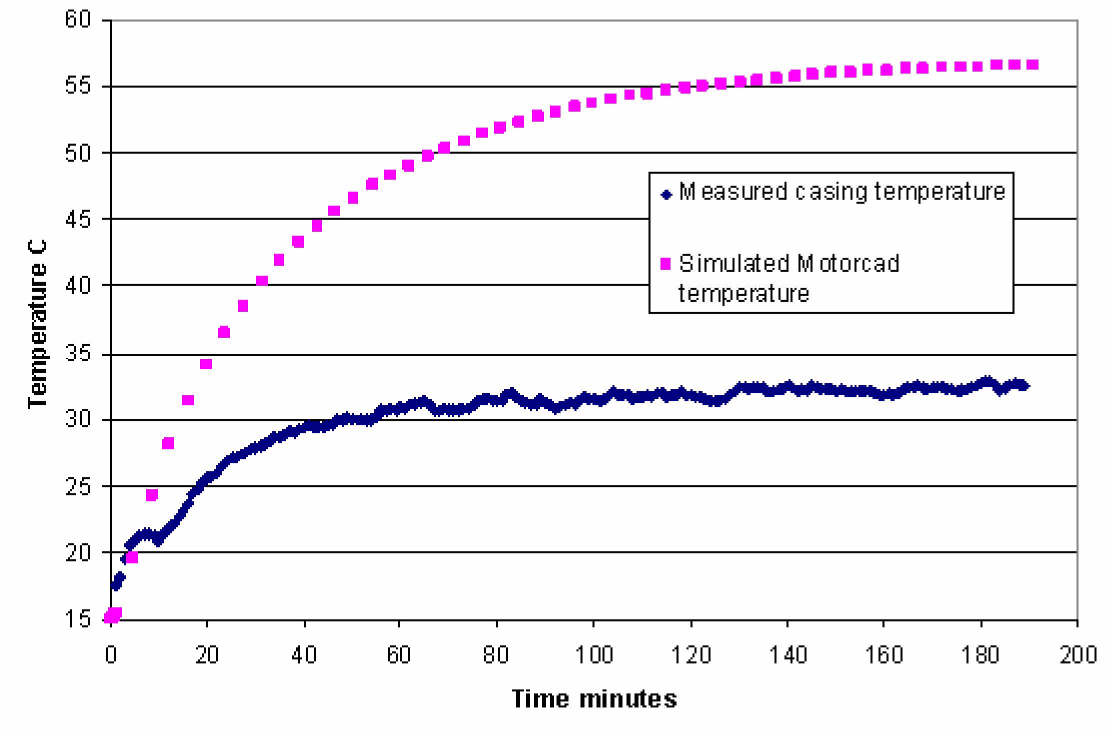

Figure 92: Comparison of measured and simulated data for 4000rpm steady state test

The difference in temperature suggests that the cooling is not being modelled correctly by considering only natural convection from the generator casing.

9.2.2.2 Natural convection with blades

The turbine blades, rotating at 4000rpm will have a significant cooling effect on the machine. Their thermal resistance will be low as they are passing through the air at speed. The thermal resistance was calculated by considering the hub and blades separately using equation 94.

$$\mathrm{Re}_D = \frac{\rho u L}{\mu} \qquad (94)$$

Where L is the width of the blade or the radius of the hub.

At 4000rpm, the blades are at an average Reynolds number of 2000 x10^3 and thus the turbulent correlations for flat plate flow apply. The rotor hub is at an average Reynolds number of 220x10^3 and the flow is transitional.

The Prandtl number is given by equation 95:

$$\Pr = \frac{C_p \mu}{k} \tag{95}$$

Where k is the thermal conductivity of air.

The relationships between Reynolds, Prandtl and Nusselt numbers for flat plate flow are given in chapter 7 of this thesis. The heat transfer coefficient is calculated from equation 96 and thermal resistance is given by 97.

$$h = \frac{Nu}{L} k \tag{96}$$

$$R^t = \frac{1}{hA} \tag{97}$$

Where A is the surface area of the hub or blades.

This value was used to replace the machine shaft to ambient value resistance in motor-CAD. An additional thermal capacitance of 15400kJ/C (calculated from rotor mass and material specific heat capacity) was added to the each end of the shaft to simulate the heat storage of the turbine rotor.

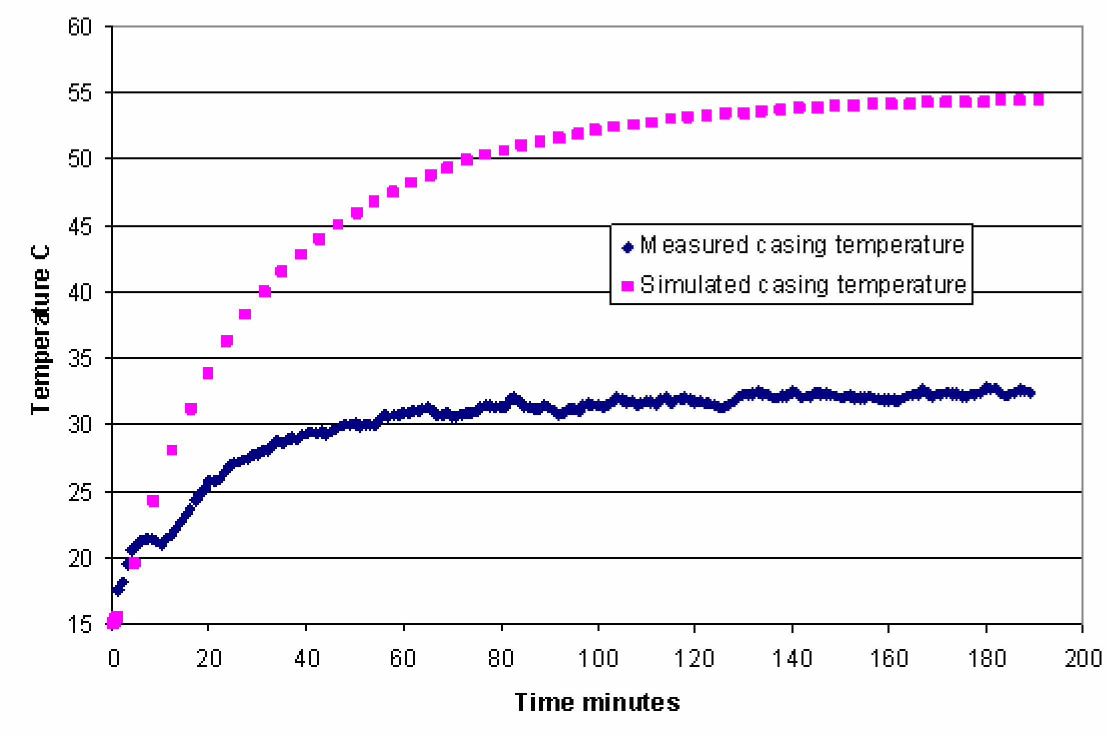

Figure 93: Comparison of measured data and Motor-CAD simulated data including turbine blade model for 4000rpm steady state test

The stator casing temperature is reduced but not brought in line with experimental measurements (see difference in figure 93). The blades provide a cooling path from the rotor, but the rotor temperatures are only slightly below the stator winding temperatures and the airgap presents a higher thermal resistance compared to the back iron so the majority of the stator heat does not cross the airgap and dissipate via the blades.

9.2.2.3 Forced convection

The turbine valve was closed for the duration of the test but there is significant leakage airflow which will have a cooling effect. The turbine rotors also disturb the air at the ends of the machine and may induce a slight airflow. With the valve closed the flow sensors in the turbine duct will not read correctly and the airflow velocity cannot be directly measured.

Motor-CAD simulates the forced cooling of the machine housing using experimentally verified correlations for open channel and flat plate flow [35]. The flow along open channels (between fins on the housing) will leak and thus may reduce cooling. This is modelled by multiplying the mean airflow by a leakage in per unit as in equation 98.

$$V_{local} = V_{mean}.Leakage \tag{98}$$

In the wells turbine application, leakage is less applicable than with a fan cooled machine. The air leaking from the cooling channels will be replaced with air of a similar speed from the bulk airflow and thus a net change in velocity will not occur. Hence the per unit leakage is set to 1.

Blocked channels and terminal boxes are taken into account using the blockage variable for that region. The total convection heat transfer coefficient is multiplied by this blockage to give the true heat transfer coefficient for that area.

$$h = h_{\max}.\frac{unblockedchannels}{totalchannels} = h_{\max}.blockage \tag{99}$$

The terminal box at the rear of the generator means the rear fins have a blockage of 0.7. The corner fins are entirely obscured by mounting lugs in the active section (axially) of the machine so have their blockage values set to 0. Figure 94 shows the inputs to the simulation for an air velocity set at 0.2m/s.

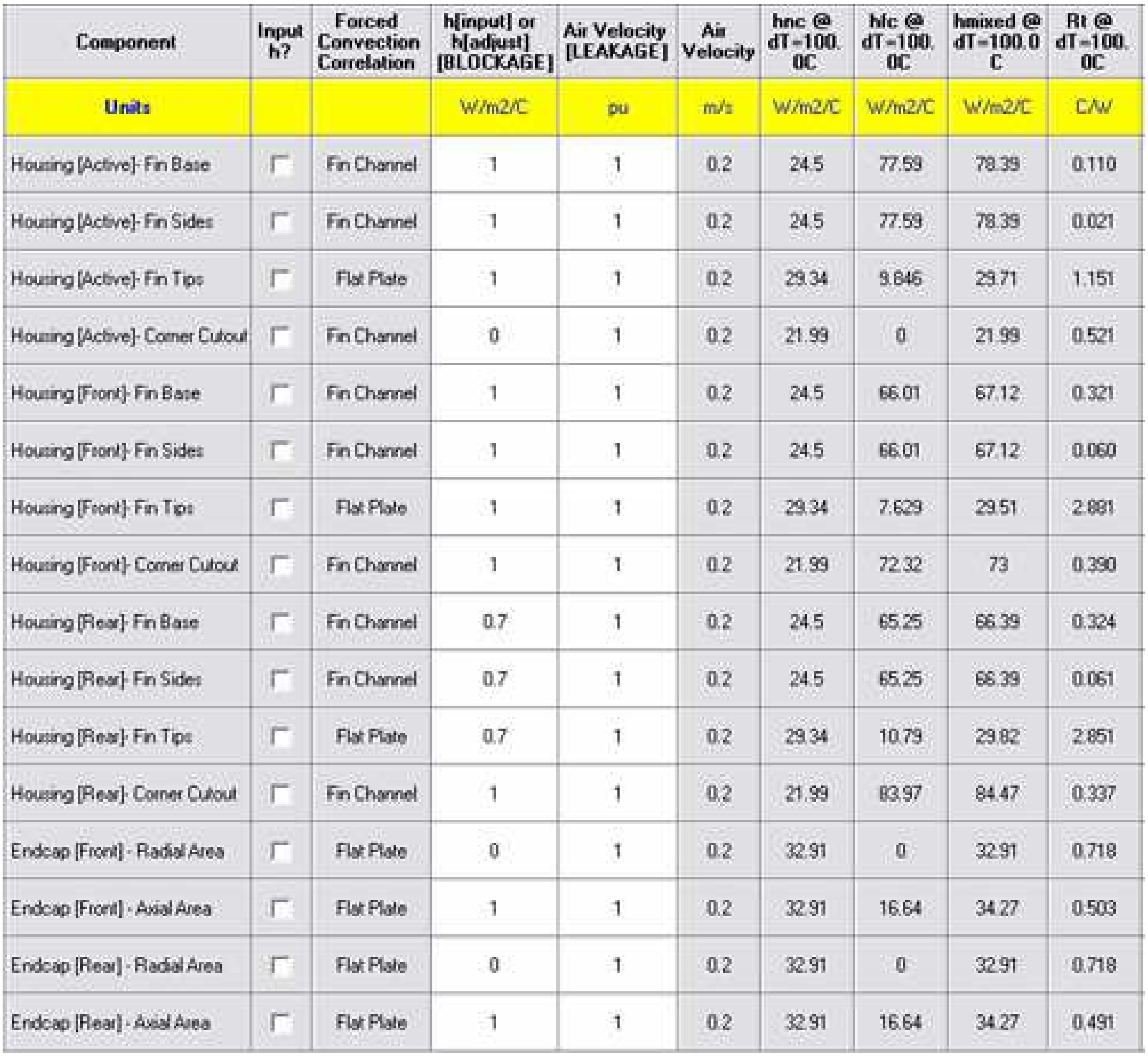

Component	Input h?	Forced Convection Correlation	h[input] or h[adjust] [BLOCKAGE]	Air Velocity [LEAKAGE]	Air Velocity	hnc @ dT=100. 0C	hfc @ dT=100. 0C	hmixed @ dT=100.0 C	Rt @ dT=100. 0C
Units			W/m2/C	pu	m/s	W/m2/C	W/m2/C	W/m2/C	C/W
Housing [Active]- Fin Base	☐	Fin Channel	1	1	0.2	24.5	77.59	78.39	0.110
Housing [Active]- Fin Sides	☐	Fin Channel	1	1	0.2	24.5	77.59	78.39	0.021
Housing [Active]- Fin Tips	☐	Flat Plate	1	1	0.2	29.34	9.846	29.71	1.151
Housing [Active]- Corner Cutout	☐	Fin Channel	0	1	0.2	21.99	0	21.99	0.521
Housing [Front]- Fin Base	☐	Fin Channel	1	1	0.2	24.5	66.01	67.12	0.321
Housing [Front]- Fin Sides	☐	Fin Channel	1	1	0.2	24.5	66.01	67.12	0.060
Housing [Front]- Fin Tips	☐	Flat Plate	1	1	0.2	29.34	7.629	29.51	2.881
Housing [Front]- Corner Cutout	☐	Fin Channel	1	1	0.2	21.99	72.32	73	0.390
Housing [Rear]- Fin Base	☐	Fin Channel	0.7	1	0.2	24.5	65.25	66.39	0.324
Housing [Rear]- Fin Sides	☐	Fin Channel	0.7	1	0.2	24.5	65.25	66.39	0.061
Housing [Rear]- Fin Tips	☐	Flat Plate	0.7	1	0.2	29.34	10.79	29.82	2.851
Housing [Rear]- Corner Cutout	☐	Fin Channel	1	1	0.2	21.99	83.97	84.47	0.337
Endcap [Front] - Radial Area	☐	Flat Plate	0	1	0.2	32.91	0	32.91	0.718
Endcap [Front] - Axial Area	☐	Flat Plate	1	1	0.2	32.91	16.64	34.27	0.503
Endcap [Rear] - Radial Area	☐	Flat Plate	0	1	0.2	32.91	0	32.91	0.718
Endcap [Rear] - Axial Area	☐	Flat Plate	1	1	0.2	32.91	16.64	34.27	0.491

Figure 94: Natural convection menu from motor-CAD

The air velocity was estimated by matching the measured and simulated generator casing temperatures. The best match is shown in figure 95. The airflow best matching the results was 0.25m/s. The model predicts a steady state temperature of 32.3̊C on the active part of the generator casing. This figure is not unreasonable for the turbine with valve closed in a low sea state.

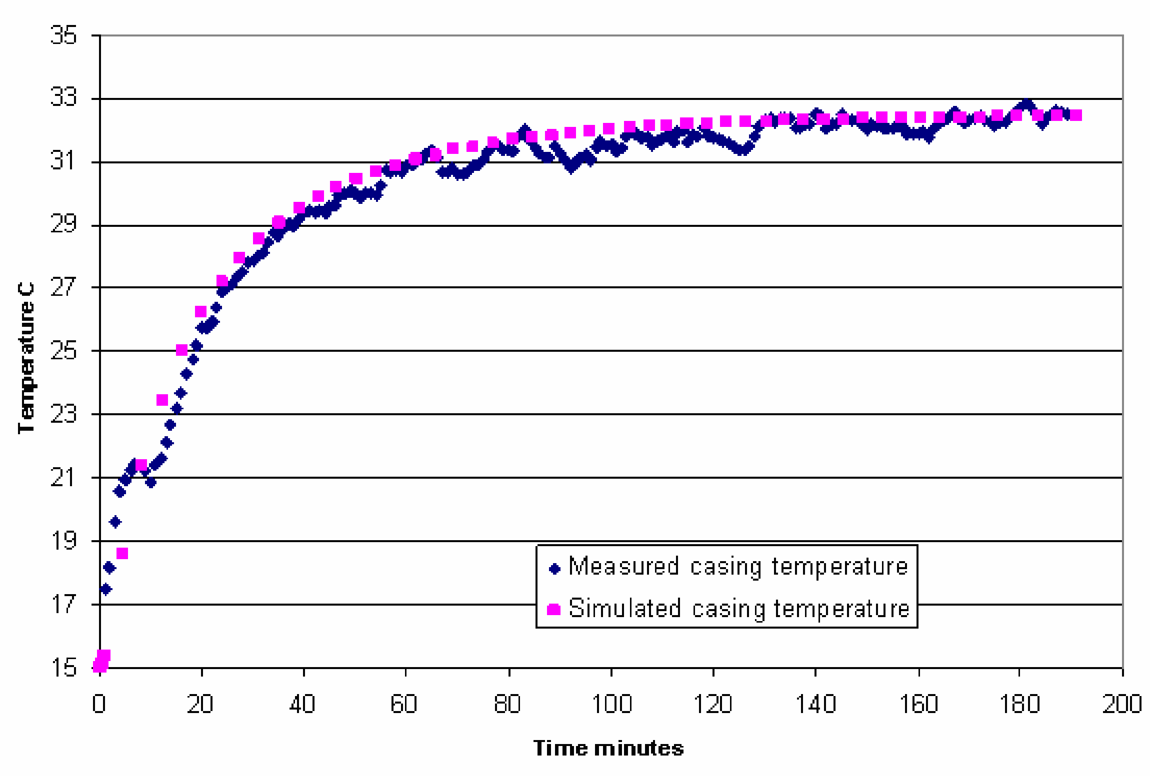

Figure 95: Comparison of measured data and Motor-CAD simulated data including blade model and 0.25m/s airflow for 4000rpm steady state test

9.2.3 Heat dissipation paths from stator windings

The heat generated in the stator windings is transferred out by conduction through the insulation to the stator core or convection from the endwindings into the endcap air.

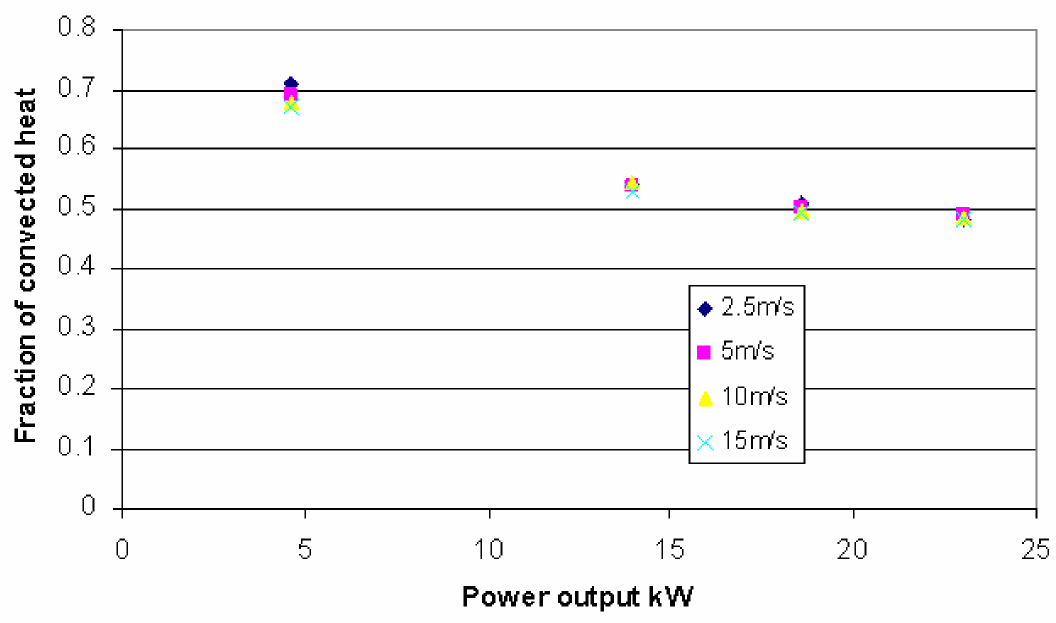

Figure 96: Fraction of stator winding heat transferred by convection to total heat transfer for increasing power output.

The change in dominant heat transfer path is illustrated in figure 96. At low powers, where iron loss is the dominant loss the winding heat mainly escapes by convection. As the copper losses become dominant more heat is transferred via conduction with equal amounts being conducted and convected at rated power. There is no change of internal thermal resistance with either power or external airspeed. Hence the change must come from the relative increase of copper losses.

9.2.4 Sinusoidal limit

Using the motorCAD model calibrated above, the maximum power that can be sustained in a series of high power waves was simulated by making the approximately sinusoidal duty cycle shown in figure 97. The airflow over the machine is varied from zero to the maximum sustainable airflow (without stall) at 4000rpm with an external temperature of 15̊C. This cycle was created in MotorCAD and repeated until steady state occured. The steady state temperature was compared to the generator winding insulation limit (class F, 155̊C) and the magnitude of the stator copper loss (and therefore power output) brings the stator winding steady state temperature close to the limit. As the winding temperature rises, the resistance of the winding increases so the losses increase. With the winding temperature feedback a maximum sustained output of 20kW RMS is predicted by this model. The peak power of this sinusoid is 34kW.

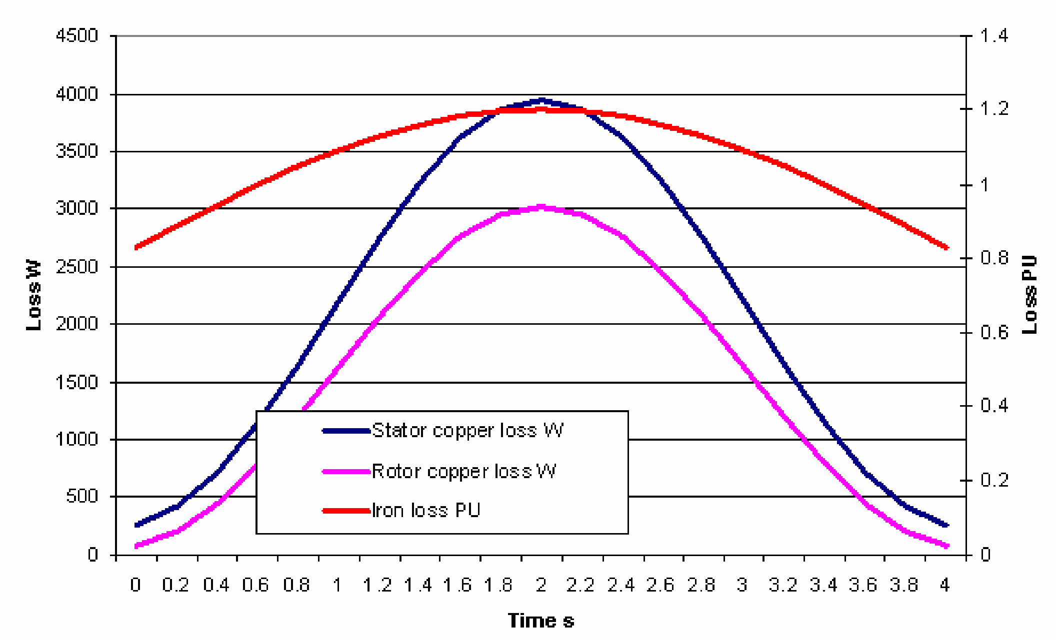

Figure 97: Loss duty cycle

9.2.5 Steady state test comparison

The MotorCAD model was used to predict the heat transfer from the generator casing for the steady state tests. The forced convection model in MotorCAD is based around a fan positioned at one end of the generator which forces air through the cooling channels with a prescribed velocity. This velocity decreases as the convecting air leaks out of the channels and into the still environment. The OWC airflow is significantly different. The flow is bi-directional, considerably turbulent and leakage will bring cool air from the flow in the duct into the fin channel. The turbulence in the flow may be particularly important: Staton [35] states that “a 20% increase in turbulence in the flow over an axial fin can result in a 50% increase in heat transfer”. Figure 98 shows the MotorCAD model when compared to the data measured from steady state tests. Also shown is the measured data with all measurement errors set to reduce the heat transfer.

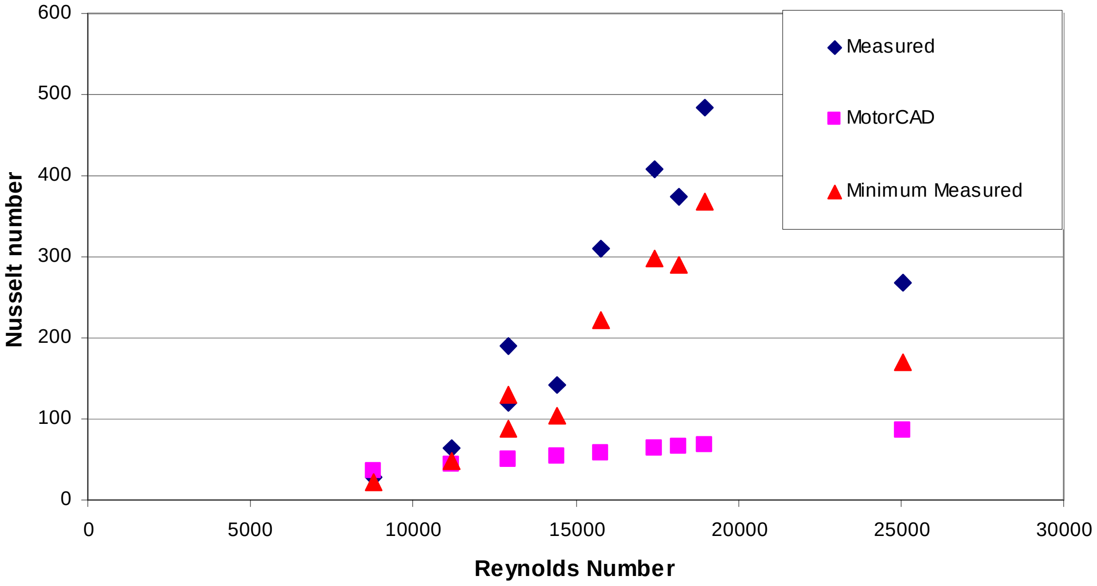

Figure 98: Comparison of measured data and MotorCAD forced convection model

It can be seen from figure 98 that MotorCAD predicts worse heat transfer than that found by measurement. Hence the sinusoidal limit test in section 9.2.4 will be a pessimistic estimate of the maximum sustainable overload. Burchell[94] began a computational fluid dynamics study into the cause of the high heat transfer as a masters project but the complexity of the problem prevented a conclusion in the time allotted.

9.2.6 Motorcad use in future modelling work

The MotorCAD model exceeds the level of complexity necessary for design work on the OWC system. Its “input data” section requires 10 pages of data in addition to the internal and external dimensions of the generator. This information is not easy to gather accurately as it requires disassembly of the generator or close co-operation with the machine manufacturer. The preceding section also shows that one of the most important parameters in machine thermal modelling is not accurately predicted for this application. This suggests that a model generated from measured data would be better suited for predicting the rating of a generator in this particular application. A simpler model would be easier to integrate into the OWC design process and be better suited to real time prediction of temperatures.

9.3 Control Techniques single node Thermal Model

The thermal model built into the Control Techniques Inverter can be adjusted in the light of the test data and motorCAD modelling. The variables available within the model are maximum temperature (in the form of maximum steady state motor rated current, called the Overload accumulator) and the thermal time constant.

The Control Techniques model is shown in operation in figure 99, steep increases in temperature are associated with pulses close to maximum power output. The inverter was using a very short time constant for safety reasons and hence the predicted changes in temperature are rapid. This is at odds with the time constants of greater than 1000 seconds measured in section 8.4.2.

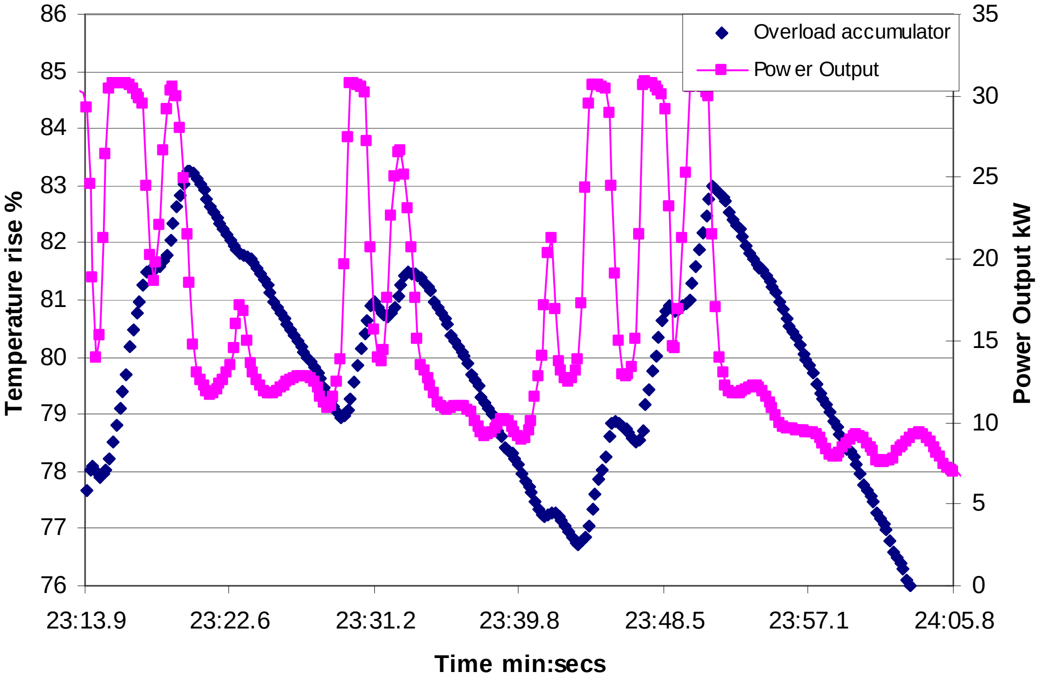

Figure 99: Control Techniques Thermal model in operation

9.3.1 Thermal time constant

The thermal time constant represents the combination of thermal resistance and capacitance properties of the induction generator (introduced as equation 89). This time constant increases with airspeed and power, noted in chapter 8, despite a decrease in thermal resistance. The time constant to be used in the Control Techniques model is that for the power at which the stator will reach maximum rated or allowed temperature. This is the reference time constant. A safety margin could be introduced by using reference time constant shorter than that for maximum acceptable temperature. The longer time constant in sustained operation at higher powers means that the reference time constant is reached and the current limited before over-temperature can occur. Lower powers will not overheat the generator.

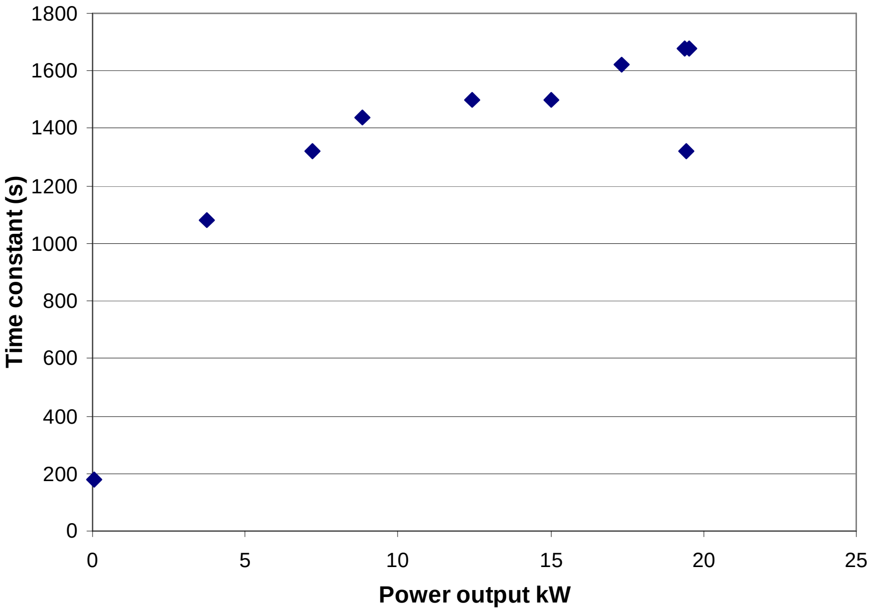

Figure 100: Variation of thermal time constant with power output during steady state tests

In the OWC application it is possible to relate the peak power to the RMS power by assuming the power input is sinusoidal, in this case, the 20kW continuous maximum test power corresponds to a 28kW sinusoidal peak power input. The measured data shown in figure 100 gives a time constant of 1680 seconds. A pessimistic time constant could be taken from the 1320 second value for 19.4kW continuous power that lies well below most of the data. It has been observed that the small turbine plateaus at 32kW during storms. For this output, using a linear fit and counting the 0kW 180 second value, a time constant of 2340 seconds is obtained. A better data fit can be achieved with a non-linear fit. However this places disproportionate importance on the single 0kW data point. It may be best to disregard it until further 0kW tests can be carried out and use a shorter, safer, time constant. Discounting the 0kW value and the 1320s/19.4kW values predicts a time constant of 2107 seconds using linear regression with a good fit ($R^2 = 0.92$). These values are valid only for a given turbine. If a considerably higher power could be obtained at a lower airspeed then the time constants could prove too long. Testing on different turbine types would produce data showing different relationships between airspeed and power. This would allow the separation of the effects dependent on each and thus a more generalised model. Such a model would allow the prediction of suitable time constants from the power to airspeed curve of the turbine.

9.3.2 Maximum temperature

The maximum stator temperature allowed by the Control Techniques model is the motor rated current multiplied by 1 or 1.05 depending on parameters selected. Three tests were conducted with currents close to the motor rated current. At 4000rpm an average temperature rise of 51̊C was recorded. At 3000rpm a temperature rise of 57̊C was recorded. This compares to the 75̊C rise recorded in the generator's type testing. The cooling present in the OWC application is much better than that used during type testing. Hence a current greater than the rated can be sustained before the rated temperature rise is reached. The temperature rise of the 4000RPM unstalled tests plotted against power output in figure 101 shows a trend which can be fitted with a polynomial equation. This fit is more representative than a linear fit as stator temperature feeds back into stator losses, so it is expected that the temperature will rise faster at higher powers. Using this fit, a stator temperature rise of 75̊C will be obtained while operating at 24.6kW (35.5A) continuously. Using a sinusoidal approximation this would give 34.8kW peak power output.

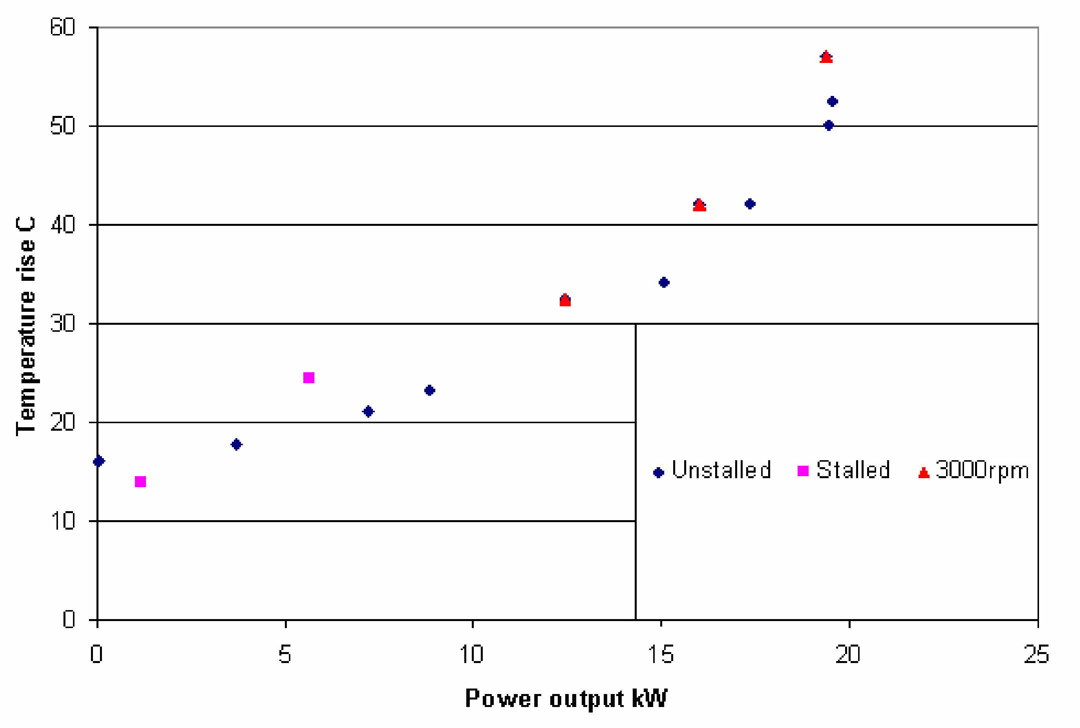

Figure 101: Stator temperature rise compared to power output.

The Control Techniques model is the most basic possible model of the induction machine, presumably for computational reasons. It does not consider variations in ambient temperature. A machine in an environment that has significant variation of temperature is either being under utilised or may exceed rated temperature rise.

9.4 Measured steady state effective thermal resistance

A thermal resistance representing the heat flow paths from the stator endwinding to the surroundings can be calculated from losses within the induction machine and both the endwinding and ambient temperatures. The thermal resistance calculated in this manner is referred to as the effective resistance. Only the endwinding heat is considered when calculating this resistance and the temperature rise due to other losses is modelled as a resistance, not a separate heat source. The variation of effective resistance with generator power output is as illustrated in figure 102.

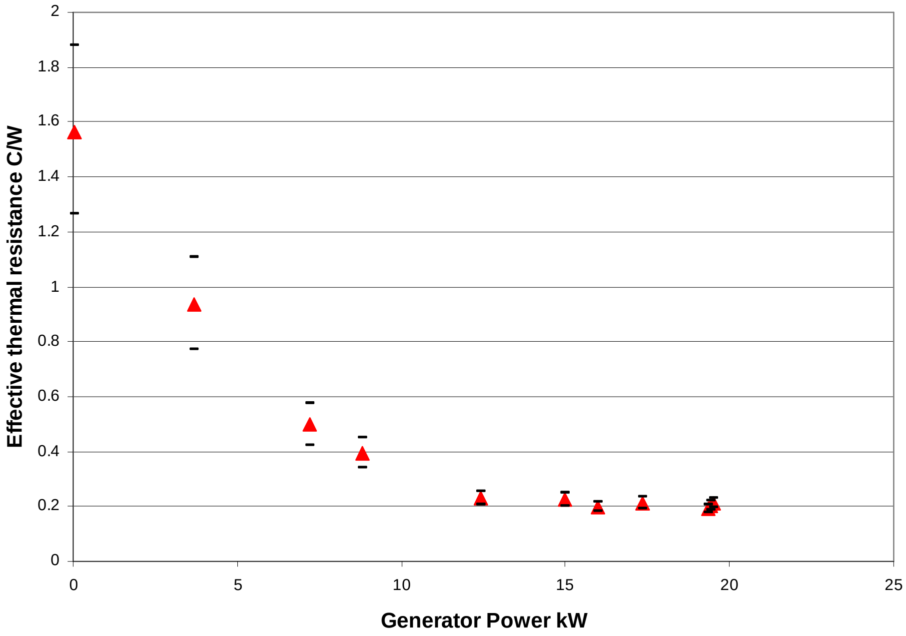

Figure 102: Variation of effective thermal resistance with power output, error bounds marked by black lines

A trend for the variation shown in figure 102 is given by:

$$R_{eff}^{t} = 0.00055(P_{kw})^2 - 0.1745(P_{kw}) + 0.1527 \qquad (100)$$

This is valid up to 12.5kW. Beyond this a constant value of 0.2 can be assumed.

If any part of the OWC turbo generation system was to change, this trend would have to be altered. The extent of this change cannot easily be predicted using this model and hence it is of limited use to future designs.

To gain further insight into the heat flow paths and to allow extension into non-steady state operation the effective resistance of the model can be expanded into identifiable elements with different characteristics using a combination of measurements and modelling.

9.5 Improved model

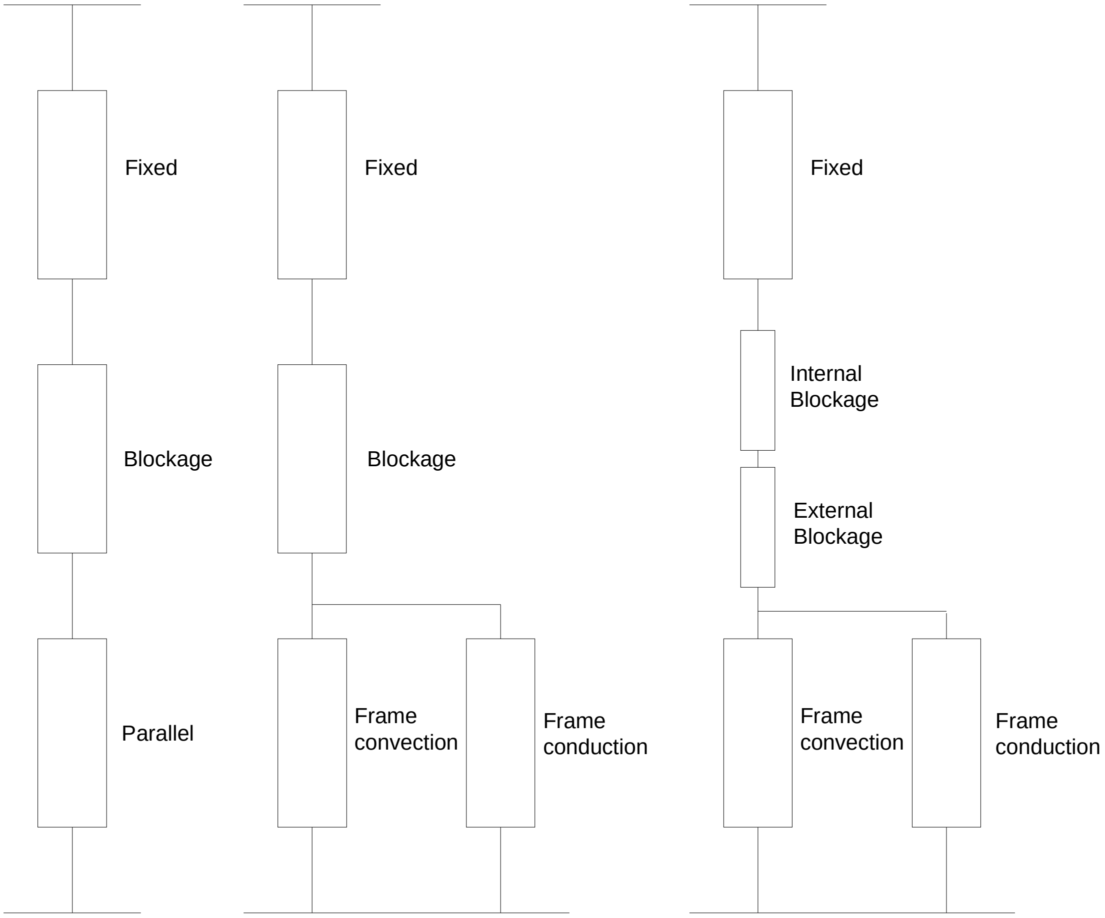

Figure 103: Resistance network of new model, center with parallel resistance split into frame and strut components, right with blockage resistance split into internal and external components

The model illustrated in figure 103 shows the flow path of heat from the stator endwinding to the generator surroundings. The expanded resistance network is made of four components that have different relationships to generator power output and airspeed.

The quantities used in the calculation of these resistances are:

Q_{ew}, the endwinding losses
Q_{new} the non-endwinding losses
Q_t the total losses
I_s the stator current
T_w is the stator winding temperature
T_{ew} is the stator endwinding temperature

The endwinding losses can be directly linked to the stator current by equation 101:

$$Q_{ew} = K_{ew} I_s^2 R_{stator} (1 + \alpha (T_{ew} - T_{cold})) \tag{101}$$

Where K_{ew} is the proportion of the winding found in the endwinding
T_{cold} is the temperature at which R_{stator} was found
R_{stator} is the cold stator electrical resistance
α is the temperature resistance coefficient of copper

The non-endwinding losses are given by equation 102:

$$Q_{new} = (1 - K_{ew}) I_s^2 R_{stator} (1 + \alpha (T_{ew} - T_{cold})) + f(P(kW)) \tag{102}$$

Where f is the sum of the trends of the rotor copper loss, stator back iron, stray load, stator tooth, rotor back iron rotor tooth losses and friction losses.

MotorCAD simulations give the following relationship between stator endwinding and stator winding temperatures:

$$T_w = -0.0074 T_{ew} + 0.9517 \tag{103}$$

9.5.1 Fixed resistance

The fixed resistance is a thermal resistance due to conduction and internal convection. It shows no significant change in value with power output or airspeed, depending on the internal geometry of the machine and material properties. MotorCAD modelling shows this to be a resistance of 0.0753 °C / W.

9.5.2 Blockage resistance

The blockage resistance is the effect of other losses in the generator increasing the stator temperature. Heat must flow from the stator endwinding into other loss generating components. Thus the stator endwinding must be at a higher temperature than these components. These losses would be modelled in a more complex model as additional current sources, but in this simplified model the only concern is the effect of these losses on stator heat flow.

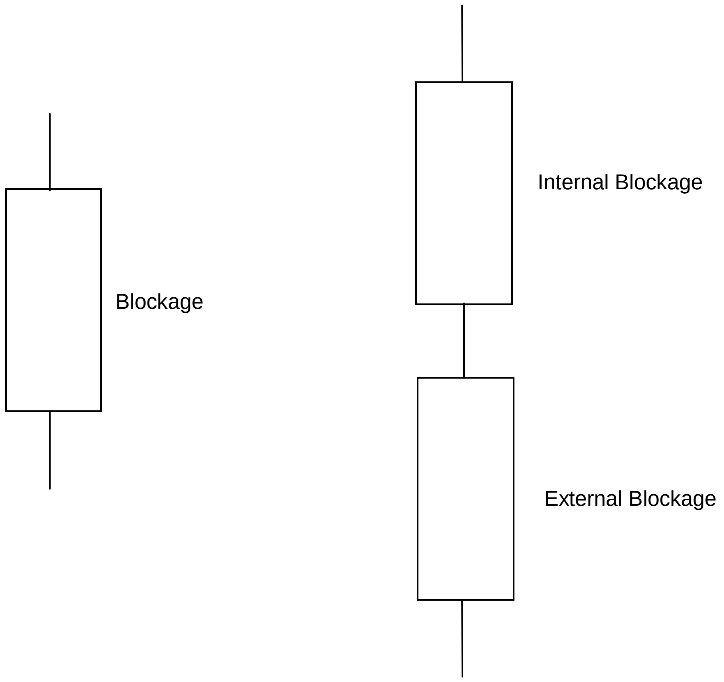

Figure 104: Expanded Blockage resistance

The blockage resistance is the sum of two series components as shown in figure 104. The internal blockage resistance represents the temperature rise in the endwinding due to the internal conduction and convection of non-endwinding losses. The external blockage is the temperature rise due to the convection of these losses from the generator casing and into the ambient air.

$$\text{internal blockage} = fn(Q_{new}, R_x^t) \tag{104}$$

Where R^t_x is the appropriate thermal resistance between the source of the loss and the generator casing at that power output. R_x changes as the losses move in the machine. Hence the fixed blockage component is found by modelling in motorCAD. The casing of the generator was modelled as having a no-resistance connection to the ambient and simulations were run with full generator losses and again with only the endwinding loss. The difference in temperature and endwinding losses give a resistance that varies as shown in figure 105.

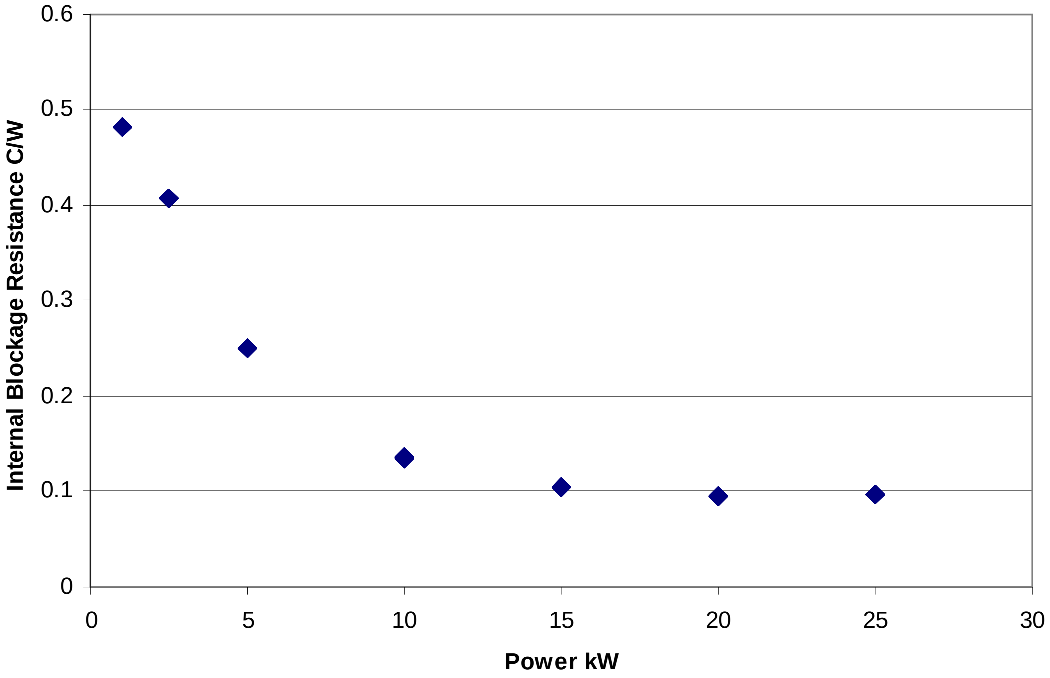

Figure 105: Variation of internal blockage resistance with power output

This variation can be estimated from equation 105 below 20kW, above this a value of 0.1 can be used.

$$R^{t}{}_{\text{internal blockage}} = -0.00006P(kW)^3 + 0.0035P(kW)^2 - 0.068P(kW) + 0.54 \tag{105}$$

The heat from the non-endwinding losses will leave the generator by the same mechanism as the endwinding losses, hence the casing blockage resistance and parallel resistance are linked.

$$\text{external blockage} = fn(Q_{new}, R^{t}{}_{p}) \tag{106}$$

Where R^t_p is the parallel resistance (detailed later)

The change in temperature due to external blockage is given by

$$DT_{\text{external blockage}} = Q_{new} R_p^t \tag{107}$$

For the single node model, the thermal resistance due to casing blockage is found by

$$R^{t}{}_{\text{external blockage}} = \frac{DT_{\text{external blockage}}}{Q_{ew}} \tag{108}$$

The total remaining thermal resistance is divided as:

$$R^{t}_{measured} - R^{t}_{fixed} - R^{t}_{\text{internal blockage}} = R^{t}_{p} + R^{t}_{\text{external blockage}} \tag{109}$$

$$R^{t}{}_{measured} - R^{t}{}_{fixed} - R^{t}{}_{\text{internal blockage}} = R^{t}_{p} + \frac{Q_{new}}{Q_{ew}} R^{t}_{p} \tag{110}$$

Hence the blockage and parallel resistance can be calculated from measured data. The external blockage is essentially the parallel resistance scaled by the ratio of endwinding to non-endwinding losses. The casing blockage resistance is plotted along with fixed blockage resistance in figure 106.

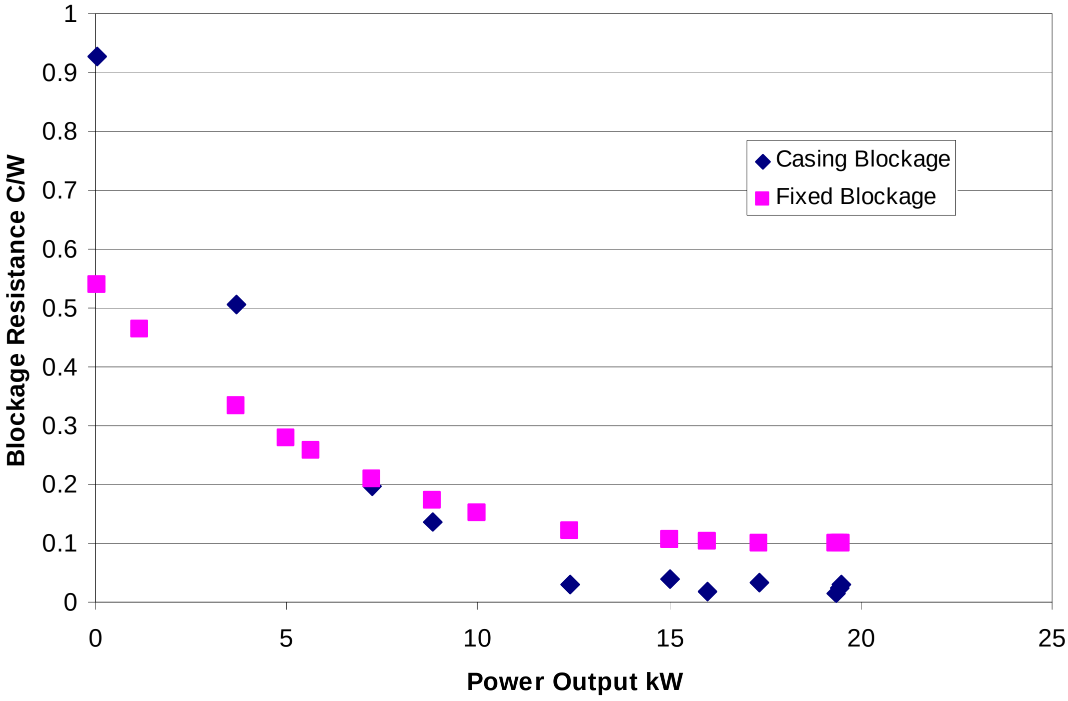

Figure 106: Components of blockage resistance

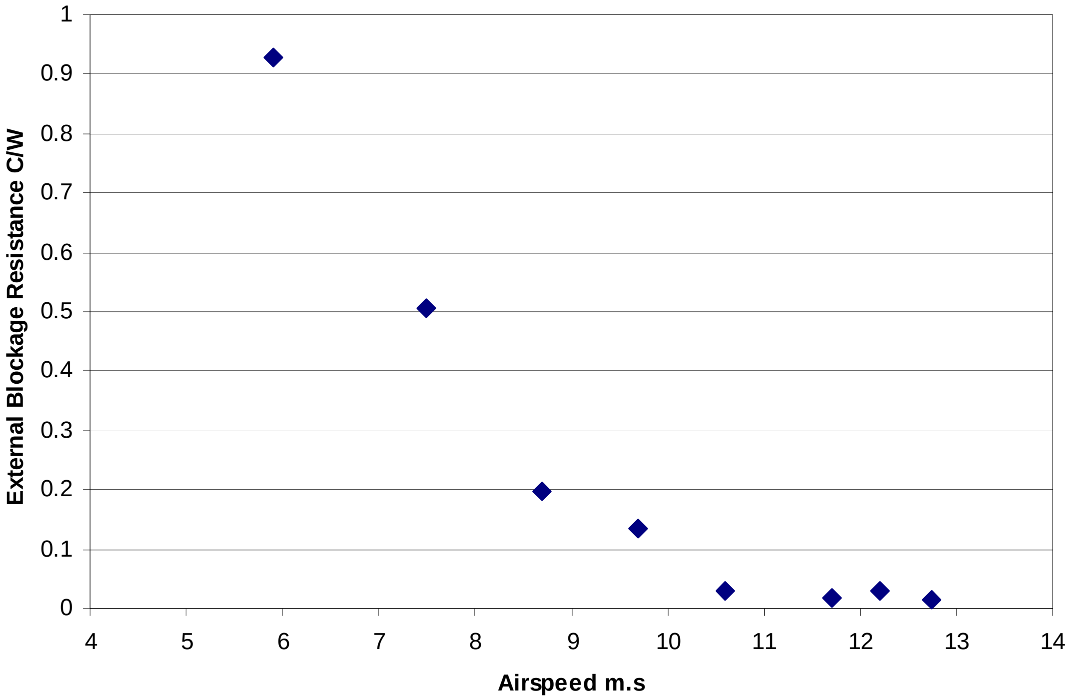

Figure 107: Variation of external blockage with airspeed

Figure 107 shows that the airspeed in the turbine duct affects the ability of the generator to dissipate heat from its surface. At high airspeeds the casing blockage resistance is negligible, at low airspeeds it is the dominant thermal resistance in this model. This variation will also be seen in the parallel resistance (as the two are effectively scaled versions of one another) and is discussed further in that context.

9.5.3 Parallel resistance

The heat transfer between the generator surface and the surrounding air is complex. The strut and casing resistances transfer heat in parallel out of the generator. Collectively they are known as the parallel resistance. The heat flow along the strut is part conduction, part convection and the heat transfer from generator casing to the strut depends on a contact resistance which has an unknown value. The convective heat transfer from the generator casing depends on the casing geometry and the behaviour of the airflow downstream of the turbine blades. Here the measured data is compared to standard non-dimensional correlations and a specific correlation is developed.

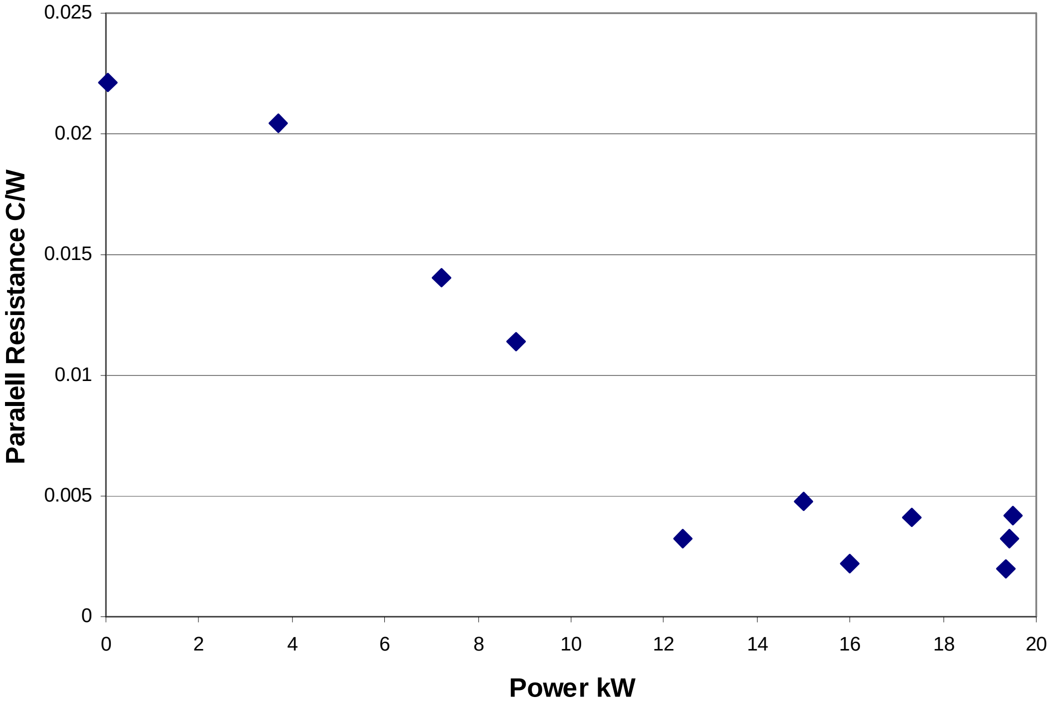

Figure 108: Variation of parallel resistance with generator power output

The variation of this parallel resistance can be seen in figure 108. There is scatter visible in the parallel resistance above 12kW, relative to the size of other thermal resistances, the variation is negligible. The value of this resistance is small relative to the other resistances appearing in the model. This is because the losses in the stator endwindings are a minor fraction of the total loss until the airspeed has considerably reduced the parallel resistance. Despite its small value it is studied further as it determines the variation of the external blockage resistance. This is carried out using the sensors mounted on the generator's casing.

9.5.3.1 Measured data from surface temperature sensors

An independent measure of the heat transfer from generator casing to the surroundings is given by the data from surface temperature sensors and the ambient temperature sensor. Temperature sensors were placed on each end of the generator casing exposed to the OWC airflow, as the test flow was uni-directional; these were called Up and Downstream relative to the generator active section. The temperature rise of the casing relative to the ambient temperature, is plotted in figure 109. Significant errors are present due to the inaccuracy of the instruments relative to the measured quantity.

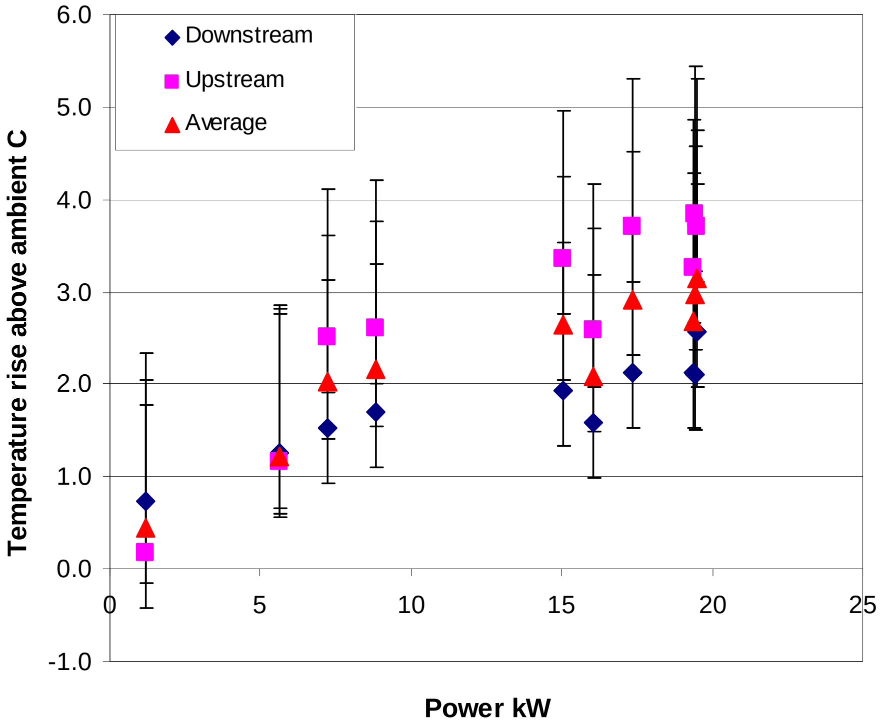

Figure 109: Temperature rise recorded by surface mounted temperature sensors

Using this measurement and the heat flow out of the generator, the surface heat transfer coefficient and thermal resistance can be calculated. This is compared (in figure 110) to the thermal resistance found by subtracting the fixed and fixed blockage resistances from the total measured resistance, giving the modelled data points.

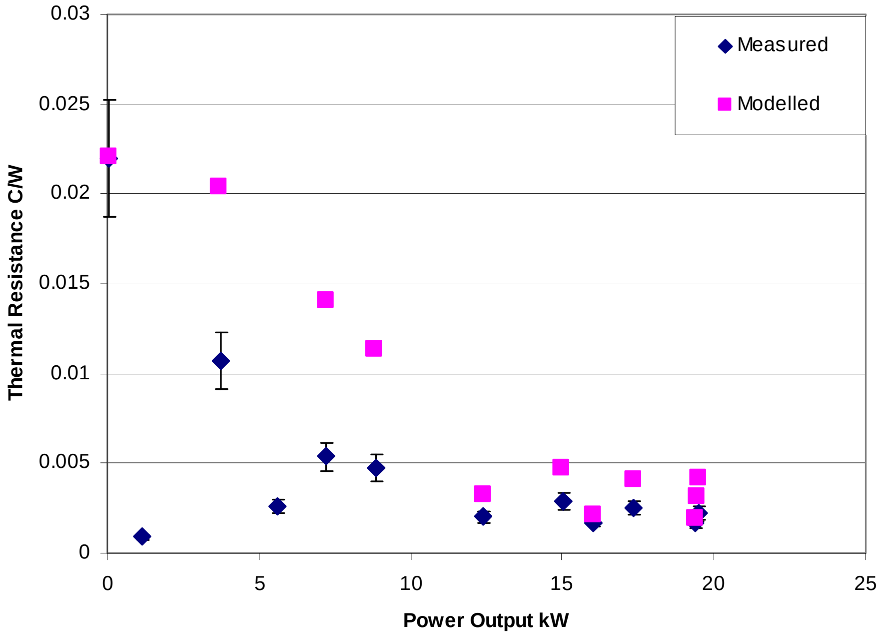

Figure 110: Comparison of modelled thermal resistance and measured thermal resistance

Although the data follows the same broad trend (except the omitted stalled data points at 5.6 and 1.1kW) there is an offset present. This could be explained by the temperature sensors being cooled below the average generator casing temperature. It is possible that the cool flow of air over the back of the sensor is affecting its measurement or the contact with the generator surface is imperfect. If a single value offset is introduced to the measured casing data the match illustrated in figure 111 is found. The value of this offset producing the best match is approximately 2.3°C, in excess of the maximum instrument error of 1.6°C. The surface measured value for the no-load test is probably incorrect as there is no corresponding increase in overall effective thermal resistance.

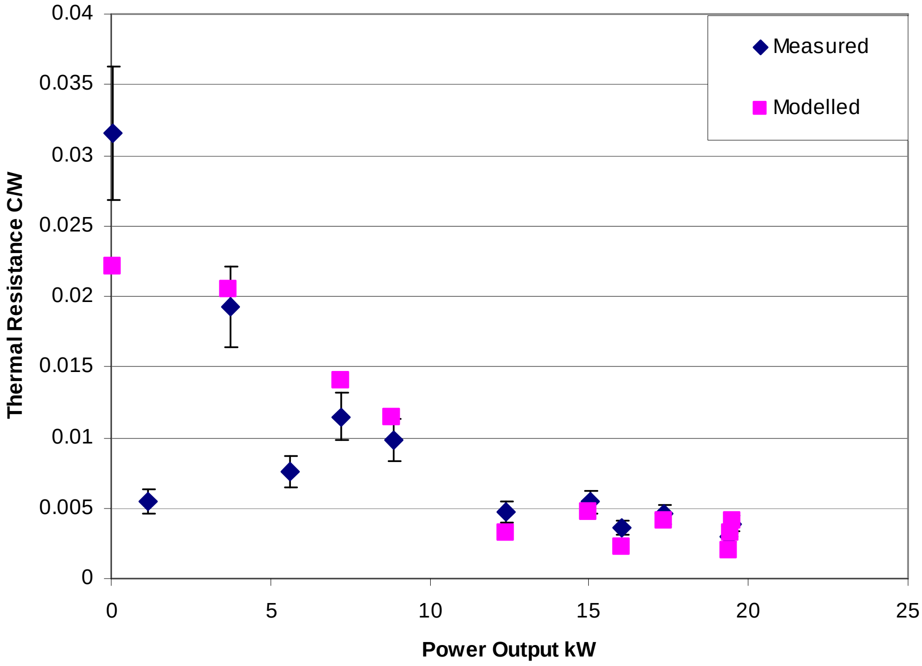

Figure 111: Comparison of modelled thermal resistance and measured thermal resistance with 2.3°C offset

Below 12.3kW the parallel resistance can be estimated using equation 111. Beyond that point it has a value of 0.0034C/W.

$$R^{t}_{parallel} = -0.002P(kW) + 0.028 \tag{111}$$

The external blockage resistance is found by scaling this formula by the ratio of non endwinding losses to endwinding losses:

$$R^{t}_{\text{external blockage}} = \frac{Q_t}{Q_{ew}}(-0.002P(kW) + 0.028) \tag{112}$$

9.5.4 Strut conduction/convection

The generator is mounted in the turbine duct using four large struts. These struts conduct heat away from the generator surface. The resistance here is the sum of two mechanisms, convection of heat away from the strut surface and conduction along the strut plus an unknown thermal resistance between casing and strut. The convection depends on the airspeed past the generator and the conduction is given by material properties and strut geometry. When the airspeed is significant, convection is calculated from the flat plate correlation in equation 12. When no air is being driven past the strut, buoyancy driven natural convection will dominate the convection heat transfer. The heat transfer coefficient for natural convection varies to a maximum of 10W/m²/C.

Every unit length can be modelled as a network of two thermal resistances, one to the ambient air via convection and the other conduction along the length of the strut, laid out as shown in figure 112. The complete strut is thus modelled as a sum of these networks.

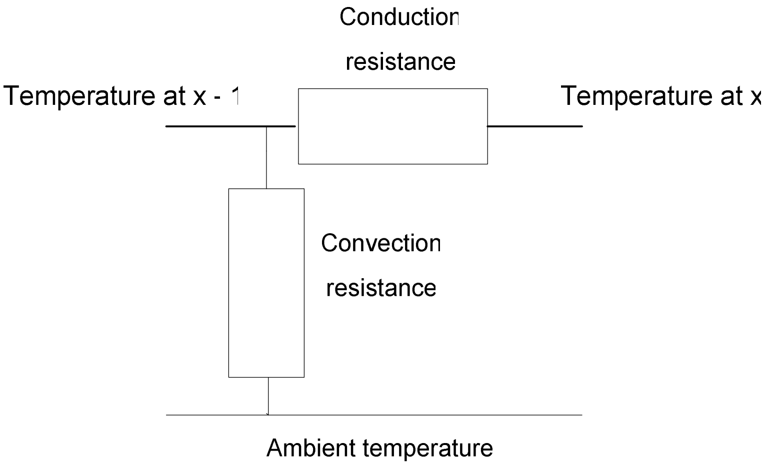

Figure 112: Strut segment thermal resistance network

There is a 6% difference in thermal resistance between maximum measured Nusselt number and minimum measured Nusselt number in the steady state tests. For operation within the range of measurements (up to 19.5kW) the strut resistance can be assumed to be fixed. If the cooling changes to natural convection, the resistance increases by a minimum of 16% and a maximum of 24%. Should all forced airflow cease the overall convection resistance must change. This condition is unlikely to occur in service as the Wells turbine windage and valve leakage has been observed to cool the generator in a forced convection dominated manner rather than by natural convection.

The smallest possible value of the strut thermal resistance is 0.028°C/W, as this is the largest value of the parallel resistance. When the strut resistance is set to this, maximum heat will be dissipated through the strut.

9.5.5 Casing resistance

The casing resistance represents convective heat transfer between the generator casing and the cooling air. This is predicted by non-dimensional correlations of Nusselt number to Reynolds number. These correlations are presented in chapter 7.

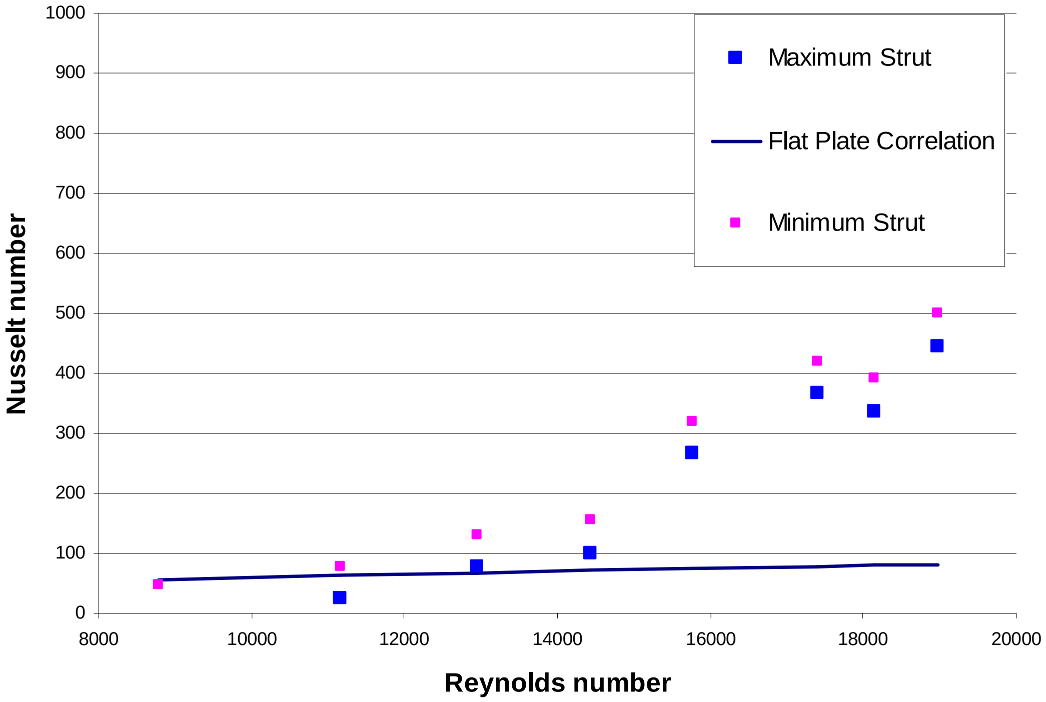

Figure 113: Nondimensionalised measured parallel resistance data against standard flat plate heat transfer correlation

If the parallel resistance was equal to the casing resistance, the "minimum strut" data points in figure 113 would give the relationship between Nusselt and Reynolds numbers. If the strut resistance, which can be approximated as fixed, is set to the minimum value compatible with modelled parallel resistance then the "maximum strut" points would be followed. Both show considerably better heat transfer at high Reynolds numbers than predicted by the non-dimensional correlations detailed above. The "minimum strut" data set falls close to the flat plate correlation at low Reynolds numbers. This would fit with the hypothesis of an airflow which is extremely turbulent between the turbine blades at high speeds, inducing considerable mixing and thus cooling the generator surface better, and calms as the airspeed in the duct is reduced. A correlation was found for the "minimum strut" heat transfer data points and is given by equation 113.

$$Nu = 1.1 * 10^{-11} \mathrm{Re}^{3.2} \mathrm{Pr}^{0.33} \tag{113}$$

Figure 114 shows that the measured results lie within the range of possible heat transfer, although the temperature difference is much lower than for normal forced convection.

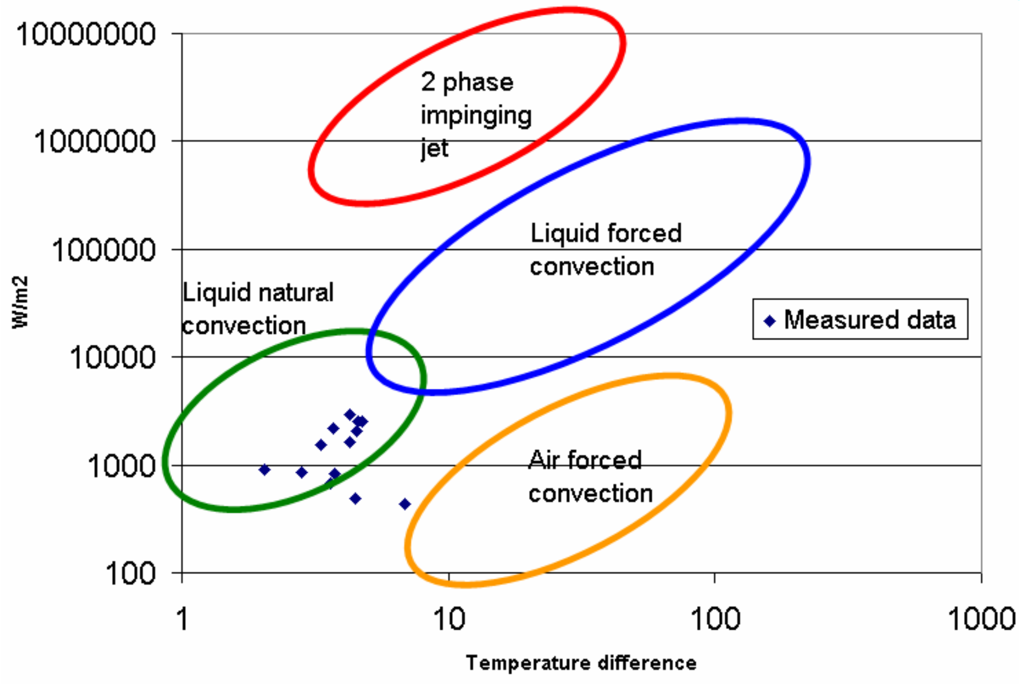

Figure 114: Heat flux compared to temperature difference for various cooling types, measured data is shown as blue dots, other data from NREL [95]

A power against airspeed velocity trend has been found for the steady state tests. It is illustrated in figure 115.

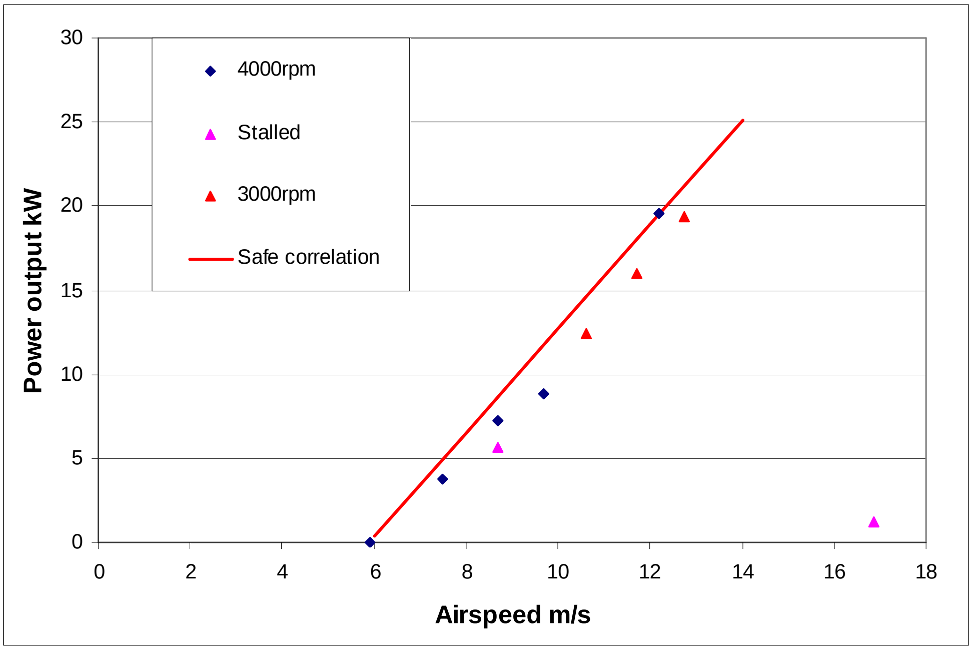

Figure 115: Generator power output and measured airspeed for steady state tests

Hence in the steady state heat transfer correlations to airspeed may be converted to correlations to generator power. If the generator stalls, the airspeed relative to the power output increases, hence the cooling is better and any inaccuracy will not lead to overheating. If the turbine were to be made more efficient, and more power was produced for a given airspeed, then the correlation would have to be changed.

Equation 114 calculates the casing heat transfer from the Nusselt number:

$$R^{t}_{case} = \frac{D_h}{k_{air} A_{case} Nu} \tag{114}$$

If a direct airspeed measurement is taken, the casing resistance can be given by equation 115.

$$R^{t}_{case} = \frac{D_h}{1.1 * 10^{-11} k_{air} A_{case} (\frac{VD_h}{v})^{3.2} \Pr^{0.33}} \tag{115}$$

Where D_h is the length of a cooling fin

k_{air} is the conductivity of air

A_{case} is the exposed casing surface area

υ is the kinematic viscosity

The safe correlation, where the least airspeed is available for a given power output, is given by equation 116 and shown in figure 115.

$$Velocity = 0.32 * P(kW) + 5.89 \tag{116}$$

Hence

$$R_{case}^{t} = \frac{L}{1.1*10^{-11} k_{air} A_{case} (\frac{0.32(P(kW)+18.22)L}{v})^{3.2} \Pr^{0.33}} \tag{117}$$

The casing resistance correlations differ from accepted non dimensional correlations and the data points lie close to, but not on a Re^N curve, which is the accepted shape of a forced convection correlation. Further steady state tests with different sensors along with better measurement of the induction generator losses would provide confirmation and a more accurate correlation.

9.6 Total resistance

The model can use either the parallel resistance which is a quadratic fit to the measured data or the casing resistance which is based on the non-dimensional correlation. The measured data and the two improved models are shown in figure 116. The parallel resistance model follows the measured data and the expanded casing resistance model is close, except around no load. There is only a single no-load data point and forcing the correlations to match that data point increases the complexity of the equations used or pulls the correlation away from the other measured data. The parallel model correlation lies within the error bounds of the effective thermal resistance measurement at no load whereas the expanded model does not.

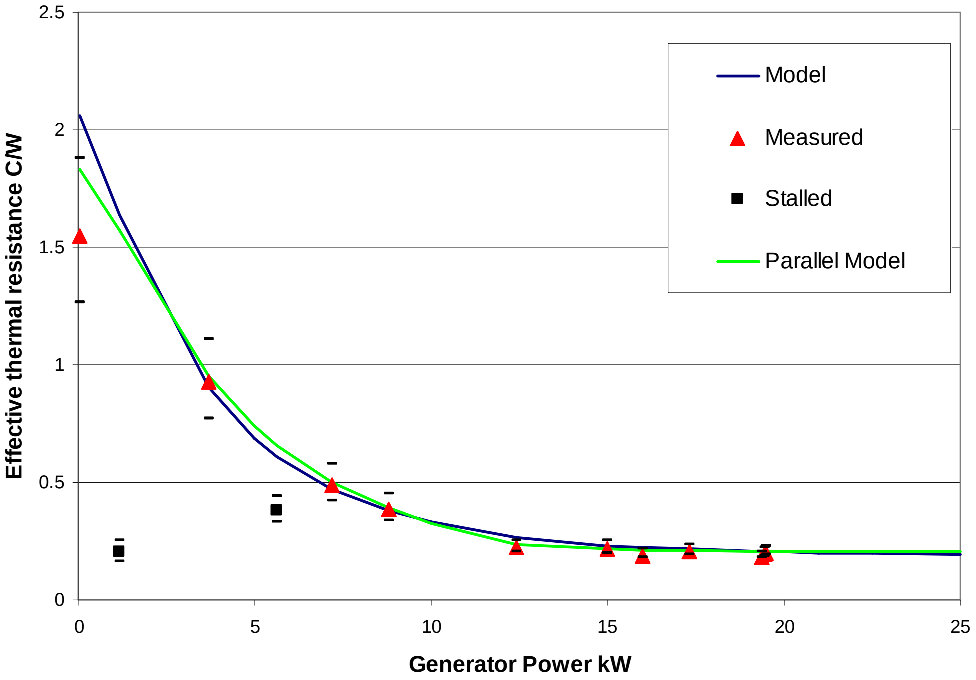

Figure 116: Comparison of measured data and model

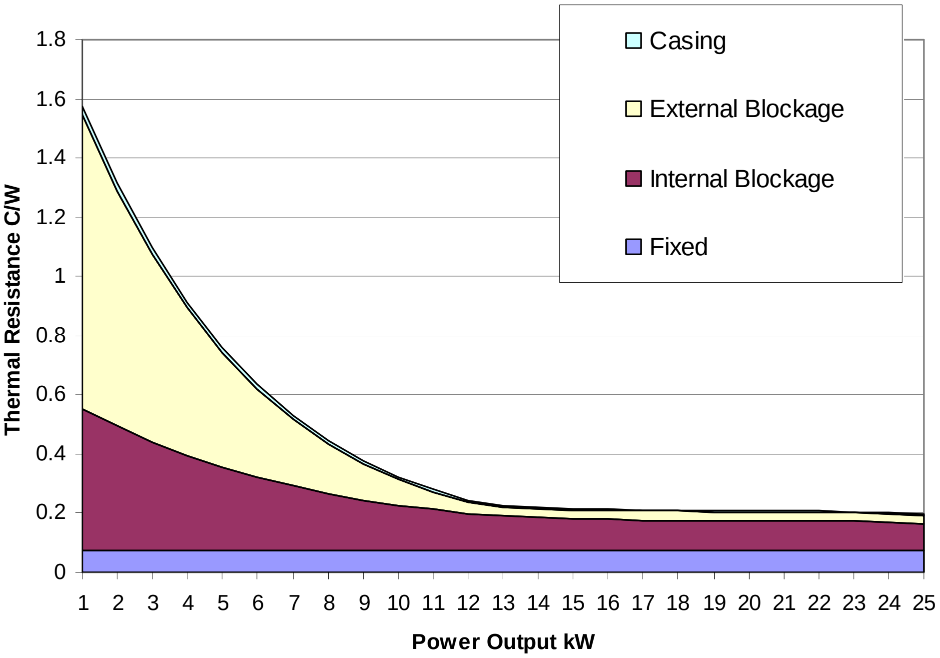

Figure 117: Calculated relative magnitude of effective resistance components of the improved model varying with generator power output

Figure 117 illustrates the predicted contribution of each resistance type as the generator power output increases. In the existing model the blockage resistances are the largest component of effective resistance at all times. Hence the non-endwinding losses are responsible for the bulk of the stator endwinding temperature rise. At full load the two largest thermal resistances are due to heat transfer processes inside the generator. Figure 118 shows that the external heat transfer processes “saturate” above airspeeds of around 10m/s and little change of thermal resistance is noted past this point. Thus in the OWC the internal heat transfer is the greatest limitation on generator rating. If this heat transfer could be enhanced then the capacity of the generator would increase proportionately.

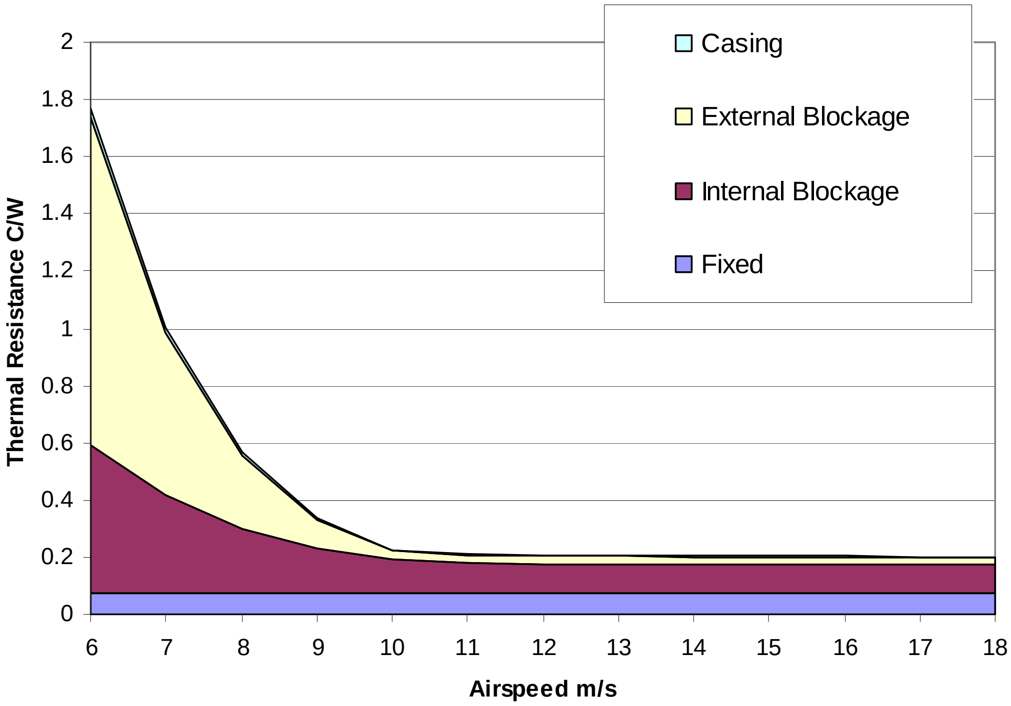

Figure 118: Calculated relative magnitude of effective resistance components varying with airspeed

Two stalled tests were carried out to provide data where the airspeed and power output had a different relationship to those in other tests. This separates out the effects that have a relationship with airspeed and the effects that have a direct relationship with output power. The effective thermal resistance was calculated using the improved model and the measured airspeed (as opposed to the airspeed/power correlation).

A value of the effective resistance, measured in 'deep' stall with airspeed 16.85m/s and power output 1.2kW, is 0.45°C/W with the model predicting 0.43°C/W. For a less stalled data point at 5.7kW and 8.7m/s, the model is not as good. A value of 0.3°C/W is measured and a value is calculated of 0.65°C/W. This value is close to the value for internal effective resistance suggesting either an error in measurement or alternatively that when the turbine is stalled the casing heat transfer is even better than predicted. Even though the measured airspeed was 8.7m/s, the turbulence present downstream of the stalled rotors created a higher speed over the generator casing. This would fit also with the extremely small casing resistance for the other stalled value. Further stalled tests would allow the reasons for this discrepancy to be found and either confirm or correct the model.

9.7 Effective capacitance

As different loads were applied to the induction generator, the temperatures being measured would change smoothly. Where a complete curve showing the change in temperature was present, the time constant of the generator as it moves between stator temperatures was found from the time taken to complete 63% of the change between starting value and final value.

The time constants derived from measured data are plotted against measured airspeed in figure 119 and generator power in figure 120.

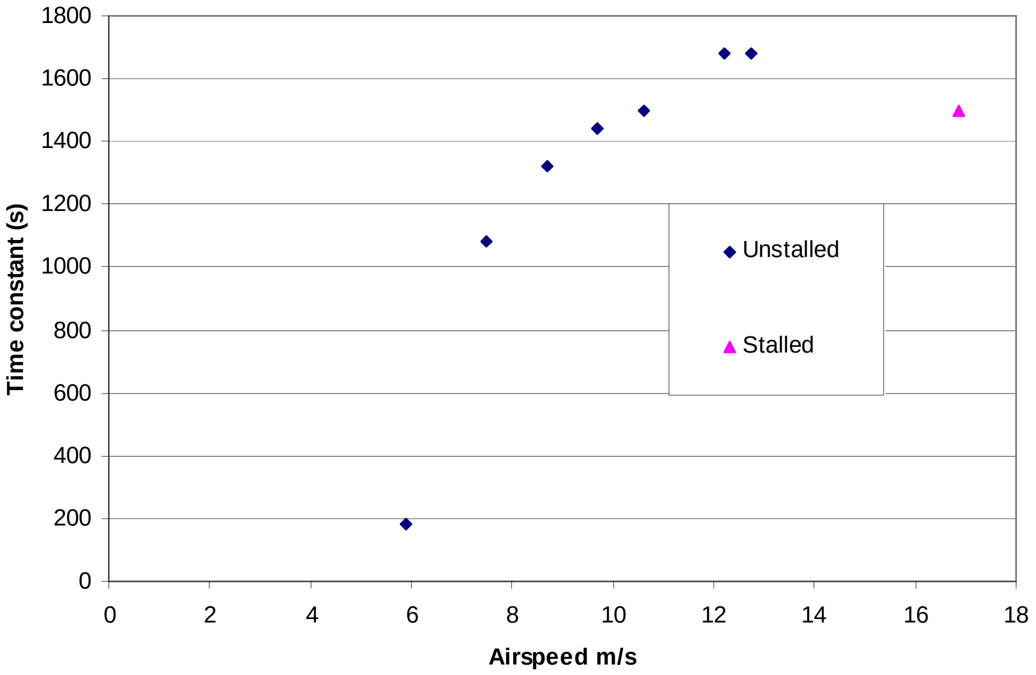

Figure 119: Generator time constant for varying airspeed

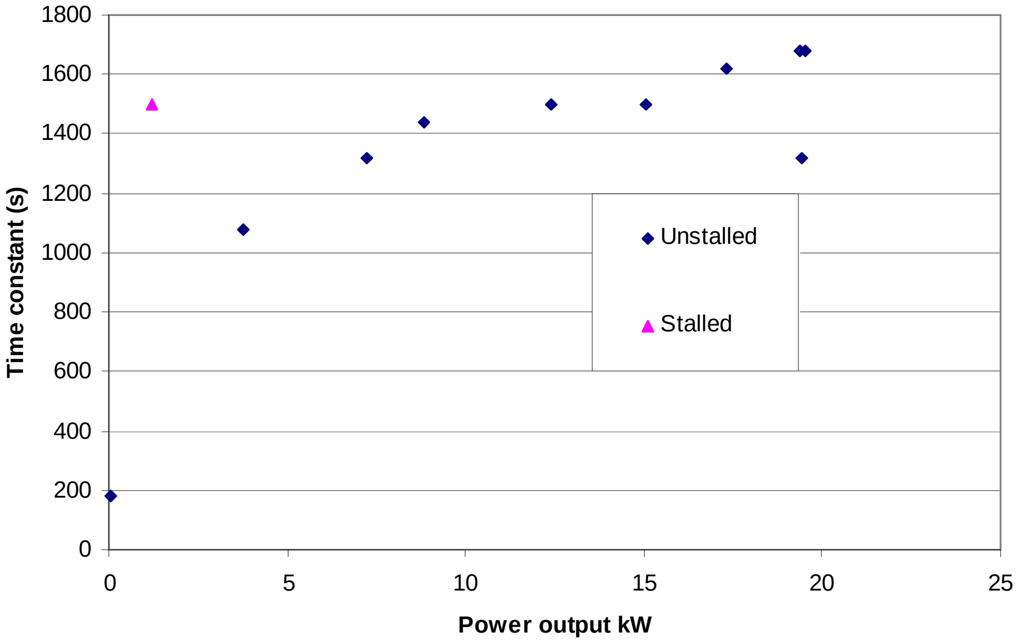

Figure 120: Generator time constant for varying generator power output

The time constant increases with both power output and airspeed. The time constant is the thermal resistance multiplied by the thermal capacitance. The effective resistance decreases as airspeed past the generator increases, it can be surmised that the thermal capacitance must increase faster than the decrease in thermal resistance. This could be explained by the relatively hot stator being better able to reject heat to other regions of the machine, hence the effective thermal capacitance being increased. This relationship would be governed by the balance of fixed losses and stator copper losses in a similar manner to the blockage resistance. The change of effective thermal capacitance is shown in figure 121.

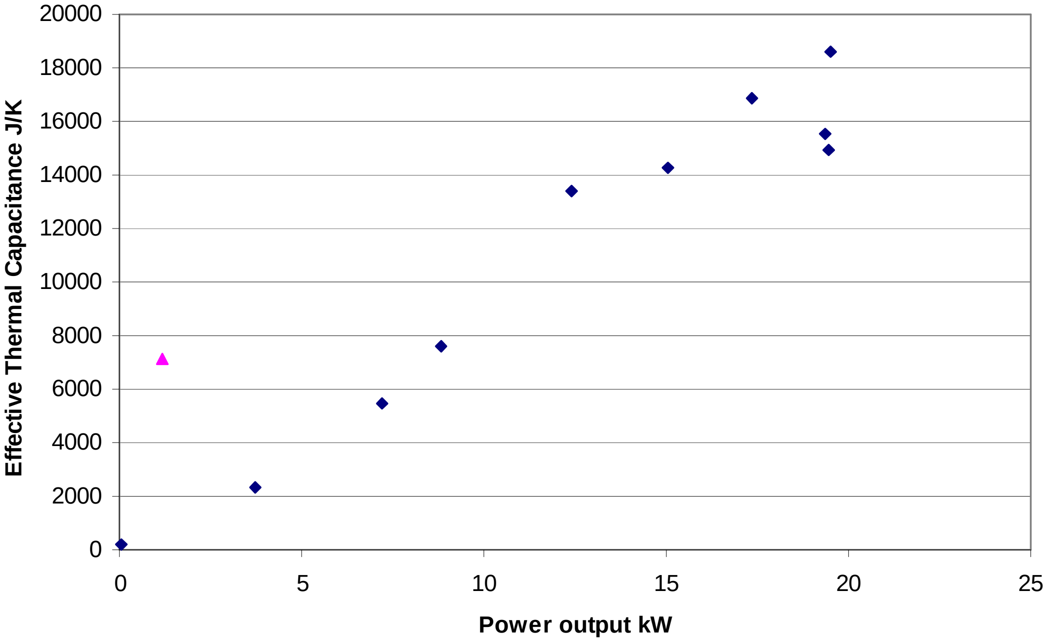

Figure 121: Change of effective thermal capacitance with power output

The change of effective thermal capacitance can be modelled with the linear fit described in equation 118.

$$Ceff = 415 * P(kW) \tag{118}$$

MotorCAD estimates a total heat capacity of 5020J/C in the endwindings. The measured data suggests this is not being fully utilized below 12kW power output. This is consistent with motorCAD's calculation that 90% of the endwinding heat capacity is in the wire insulation and impregnation.

9.8 Discussion

The complexity necessary in a thermal model depends on the application of that model. The model used by Control Techniques is adequate when the induction generator is in operation with a constant ambient temperature and uniform cooling and it is not necessary to maximise the generator's output. However, this is not the case in the OWC application, where the ambient temperature changes, the cooling is strongly correlated with airflow and the airflow is related to the generator's power output. The model used in MotorCAD is too complex for operational use and for system planning. This complexity would make it more difficult to integrate the motorCAD model into an overall system simulator than a smaller model. The data from MotorCAD would also contain detail unnecessary at the system design level, making it harder to understand the model outputs. MotorCAD's forced convection models do not represent the OWC environment accurately and would have to be altered. A model is proposed that breaks the system down into intuitive blocks depending on relationship to generator power output/losses and airspeed. The resistance values of these blocks can be illustrated simply, such as in figure 117 and the effect of any changes can be easily observed. If the airspeed/power output were to change, such as if a new turbine were to be used, but the generator was to remain the same, then the fixed resistance, internal blockage and strut conduction would remain constant. The change to cooling then could be modelled by using the relationship between airspeed and casing resistance, the external blockage also being dependent upon the casing resistance.

Once in operation, this model could be simplified to a power output/cooling relationship and used with the measurements made of thermal capacitance to prevent the generator from overheating.

The new model represents the minimum complexity needed for understanding non-steady state operation. It is possible to operate with a much simpler model, such as the Control Techniques model, but a compromise is made such that the model prevents overheating but is not necessarily accurate. This is because the airspeed and power output are observed to occasionally decouple. This occurs when the turbine does not respond to a particular pulse of air and less power is seen for a given airspeed than would be predicted using steady state modelling. This would be the focus of further work to make a non-steady state model.

It is observed that the airspeed and power output can be decoupled in operation and so these effects must be separated in the thermal network. The remaining issue is that the temperature rises that cause the blockage resistance will not change instantly as the generator power changes but will vary according to their own time constants. This complicates the prediction of blockage resistance in non-steady state. It is the copper loss and stray load loss that will have the greatest effect on the difference in overall resistance as the core loss is reasonably constant. Of these, the stray load loss occurs in areas where MotorCAD predicts the greatest thermal capacitance; hence it will pose the most problems in non-steady state modelling.

10

CONCLUSIONS AND FURTHER WORK

10.1 Achievement of thesis aim

The thesis aim, stated at the end of chapter 1 is:

"This work aims to present an analysis of appropriate, practical electrical power takeoff options for an 18.5kW rated breakwater turbine of the kind being tested on Islay and to be installed at Muktriku by Wavegen."

The initial analysis of electrical power takeoff system begins in chapter 3 with a discussion of the many possible generator types. The Permanent Magnet generator is selected as a promising alternative to the existing Induction Generator. Chapter 5 compares the Permanent Magnet and Induction Generators and finds advantages to both. This work then continues by investigating an improvement to both generators although the practical work is undertaken on the existing Induction Generator. This improvement is quantified by a thorough investigation of the OWC environment in chapter 8 and corresponding modelling work. A practical thermal model for use in OWC design and operation is detailed in chapter 9.

10.2 Discussion

Designing a power conversion system for an OWC is complicated by the variable nature of the resource. If the system is rated for the peak power produced by the device it will operate well below its capacity for most of its life. If the system is rated for the average input power, it will not be able to handle highly productive periods. Two solutions to this problem are discussed in this PhD. Firstly Permanent Magnet Generator has low fixed losses thus is able to operate efficiently over a wide range of power inputs. Hence a PMG can be specified for peak power with little compromise. Alternatively an induction generator can be allowed it to overload when the power input is beyond its rated capacity. This is possible because the generator sits in the airflow of the OWC. The speed and cooling effect of this airflow is related to the turbine power. Existing work on the thermal modelling of electrical machines, detailed in section 7.4, highlights the frame to ambient thermal resistance as the most important parameter when considering the winding temperature of a generator. Firsthand experience of the OWC application suggested that the cooling was significantly better than the norm for a totally enclosed fan cooled machine, suggesting a low frame to ambient resistance, allowing the generator to be overloaded.

These solutions were compared quantatively using a simulation of the 18.5kW rated OWC operating on Islay and Mutriku. The permanent magnet generator provides 27% more power output over a sample year (9.1kW annual average turbine power) than an induction generator only allowed to overload to 125%. However most of this increase can be matched by allowing the induction generator to overload to 150%. This would allow the power output of existing turbines to be increased (such as the 16 turbines for Mutriku [25]) without significant changes to the system. If the cost of energy were to increase or the plant had a black-start requirement, a correctly rated PM generator would be a better solution for future OWC installations.

The opportunity existed to measure the maximum safe overload of the induction generator in the 18.5kW turbine on Islay. Chapters in this thesis which consider the relationship between heat transfer coefficient and airspeed would also be applicable to the rating of a PM generator. Measuring the heat transfer from the generator would allow the maximisation of power output while avoiding damage and lifespan reduction due to overheating. The stator endwinding of a generator is subject to a proportion of the copper loss, with generally poor cooling and is made of temperature sensitive insulation, hence this is the critical component. Heat transfer from an induction generator was calculated by measuring the temperature of the generator and the losses occurring within the generator.

The loss measurements were carried out in accordance with the IEEE standard [38] at Nottingham University on a 18.5kW generator identical to that tested on Islay. The position of each loss inside the generator was found from literature and the errors in measurement and position were assessed.

Measurements of the temperature were made in the generator and the surrounding air. These measurements were made in operation and in steady state. The temperature and loss measurements were used to calculate a heat transfer coefficient from the generator surface and an "effective thermal resistance" which is given by the loss and temperature rise in the stator endwinding. Knowing this resistance, a thermal capacitance could be calculated from the observed thermal time constant.

Thermal models available from Control Techniques and MotorCAD were considered in the light of the measured data. The Control Techniques model is a single node model and can be brought into line with the measured data, however it is not designed to take into account the coupling between generator power and cooling or changes in ambient temperature. The MotorCAD model has over thirty nodes and requires accurate knowledge of the external and internal geometry of the generator to configure. It is used in this project to simulate the flow of heat within the generator. The model it uses for external convection was shown to be unsuited for predicting heat transfer to the OWC airflow, and would require alteration for this application. It would be impractical to use this detail of model while the turbine is in operation, or while designing other aspects of the system.

A simple steady state model to predict the temperatures of an OWC in operation is proposed. It consists of four thermal resistances whose values can be found from losses and modelling or from the steady state measurements. There is a single heat source driving the model, the stator endwinding heat. The inputs required to operate the model are the current flowing into the generator (from which endwinding loss can be calculated), the airspeed over the generator surface and the ambient temperature. The thermal resistances change according to the environment seen by the generator. Relationships between thermal resistance and power-output or airspeed are presented for the 18.5kW turbo-generator. This model can be adapted to other OWC generators and turbines by changing the value of the appropriate resistance.

The OWC wave energy device does not operate in steady state. The steady state model is invalid when the blockage resistance becomes inaccurate. This resistance is dependent on the temperature of non-endwinding components in the induction generator. These components retain heat and may remain above the temperature predicted by the steady state model. This will render the blockage resistance inaccurate. If the generator has been operating at low power and increases in power, it will be some time before the blockage resistance rises to meet the value predicted by the steady state model and an overprediction of stator endwinding temperature will occur. If the generator power decreases, an under prediction of the stator endwinding temperature can occur. This is not modelled in the steady state model, or measured when considering effective thermal capacitance.

More broadly, renewable power applications can put generators in environments which have different cooling properties to that normally seen by an electrical machine. There is an incentive to get the maximum out of the generator in these applications as the generator output translates directly into revenue. The work in this thesis shows that in some cases, this can be used to increase the rating of a given generator. Modern control systems make it possible to alter the rating of a generator in real time by using a temperature measurement, or model the temperature of the generator in the absence of temperature measurement. Thermal modelling of the environment during the design of the system would allow this rating increase to be estimated and the generator rated accordingly.

10.3 Contribution to knowledge

This thesis shows that a reduced loss generator type increases the output of the OWC electrical power takeoff system. This output will translate directly into increased revenue. A comparable increase can be found by operating the existing generator type beyond its nameplate capacity. This is made possible by the nature of the OWC wave energy converter. Measurements in this thesis allow the increase in capacity of the generator to be quantified for a particular turbine and generator type. Models in this thesis allow the increase in capacity to be determined from test data.

Appendicies v,vi and vii are published papers based on the work in this thesis. Another paper has been accepted by the Power Electronics, Machines and Drives conference in 2010.

10.4 Further work

The permanent magnet generator is an interesting alternative to the induction generator for the OWC wave energy converter. If a large number of OWCs were to be installed with permanent magnet generators then the net increase in revenue would become significant, prior to this point it would be worth testing the generator on a single turbine to identify any issues.

The heat transfer correlations discussed in section 9.4.5 can be further investigated using steady state computational fluid dynamics to study the airflow around the generator cooling fins. The speed of flow around these elements strongly affects the heat transfer from the generator surface. Understanding the flow in this region will allow the generator casing to be designed to take advantage of this situation and further enhance the heat transfer.

The total thermal resistance between the endwindings and the surroundings is dominated by the internal thermal resistances above 12kW. This suggests that work to increase internal heat transfer will have a considerable effect on the maximum continuous power of the generator. Measures such as heat pipes in the stator endwindings could be considered.

The results presented in this thesis were made on a single installation and over a small portion of a year. Ambient temperature measurements made over the course of a year at an installation site would be useful when using the thermal model to rate a generator. It is possible that the coolest parts of the year coincide with the most powerful seas, this should be taken into account when using the thermal model.

Further steady state tests could be conducted where the stator endwinding temperature predicted by the model was compared to a real-time measurement. This would demonstrate the operation of the model in a simple situation. Data from further testing could be used to enhance the existing heat transfer correlations.

In service testing of the thermal model could be conducted using a generator with a stator endwinding temperature sensor. The results from the model could be compared to the recorded data and the difference between steady state and actual operation noted. This would be useful when attempting the conversion of the model from a steady state model to a real-time non-steady state model.

This work shows that a customised thermal model for a renewable energy application can allow a standard generator to be operated safely beyond its normal rating. The generator in any renewable energy device must cope with a broad range of power inputs and the rating selected must be a compromise between part load efficiency and full load capacity. The ability to operate beyond normal capacity translates directly into additional revenue, an ability that can be enhanced by the operating environment. The operational environment of a renewable energy device is measured in great detail to assess the potential resource. It would, therefore, be trivial to make additional measurements for the purpose of thermal modelling. Thermal modelling is an area of ongoing study in the electrical machines field and detailed models already exist for the electrical machine designer. The combination of these models with on-site measurements allows the creation of a specific model for the device. Specific modelling is necessary as the environments faced by electrical machines in renewable energy differ from location to location as well as application to application. The low cost of thermal measurement and modelling combined with the possibility of significant additional revenue suggest that this will be an area of significant study in the near future.

REFERENCES

[1] “Climate Change 2007 The Physical Science Basis” Intergovermental Panel on Climate Change, 2007, http://www.ipcc.ch/ipccreports/ar4-wg1.htm, accessed June 2008

[2] “Energy White Paper: Our Energy Future - Creating a Low Carbon Economy” Department for Trade and Industry, February 2003, http://www.berr.gov.uk/files/file10719.pdf, accessed June 2008

[3] “UK International Priorities: The Energy Strategy” Foreign & Commonwealth Office Climate Change and Energy Group, October 2004, http://www.fco.gov.uk/Files/kfile/Energy_Report_281004,0.pdf

[4] “Renewable Energy: Employment Effects” Federal Ministry for the Environment, Nature Conservation and Nuclear Safety, Germany, June 2006, http://www.bmu.de/files/pdfs/allgemein/application/pdf/employment_effects_061211.pdf

[5] “The UK wind resource, Wind Energy Fact Sheet 8” Department of Trade and Industry (now BERR), June 2001, http://www.berr.gov.uk/files/file17789.pdf, accessed June 2008

[6] “Science and Technology – Seventh Report” House of Commons, Science and Tehcnology Committee Publications, April 2001 http://www.parliament.the-stationery-office.co.uk/pa/cm200001/cmselect/cmsctech/291/29102.htm , accessed January 2009

[7] “UK Energy in Brief” Department for business enterprise & regulatory reform, July 2007, http://www.berr.gov.uk/files/file39881.pdf, accessed June 2008

[8] “Postnote: Renewable Energy” Parliamentary Office of Science and Technology, October 2006 no.164, http://www.parliament.uk/post/pn164.pdf, accessed June 2008

[9] “World Wind Energy Review 2008” World Wind Energy Association WWEA, February 2009, http://www.wwindea.org/home/images/stories/worldwindenergyreport2008_s.pdf, accessed October 2009

[10] “Realities of Wave Technology” Heath T, Wavegen, http://www.wavegen.com/pdf/art.1727.pdf, Accessed March 2006

[11] “Ocean surface waves” Wikipedia, http://en.wikipedia.org/wiki/Ocean_surface_wave, Accessed March 2006

[12] “INTRODUCTORY OCEANOGRAPHY, *Chapter 10 - Ocean Waves”,* Knowles E, North Carolina State University, 1997, http://www4.ncsu.edu/eos/users/c/ceknowle/public/chapter10 , Accessed March 2006

[13] “Atlas of UK Marine Energy Renewable Resources” Department for Trade and Industry, June 2004, http://www.dti.gov.uk/renewables/publications/pdfs/annualmeanwavepower.pdf, accessed March 2006

[14] "Wave Energy Converters and their Impact on Power Systems" Polinder H, Scuotto M, International Conference on Future Power Systems, November 2005

[15] "An Overview of Wave Energy Technologies: Status, Performance and Costs", Thorpe T, IMECHE seminar, Wave Power: Moving towards Commercial Viability, London, November 1999

[16] "Ocean Energies Environmental, Economic and Technological aspects of alternative power sources" Charlier R, Justus J, Elsevier Oceanography Series via Google Book Search, accessed January 2009

[17] "Commercial Tapered Channel Wave Power Plants in Australia and Indonesia" Mehlum E, IEEE Ocean Engineering Society, Proceedings of Ocean Technologies and Opportunities in the Pacific for the 90's, October 1991

[18] "Oscillating Water Column Wave Energy Converter Evaluation Report", The Carbon Trust, February 2005, http://www.carbontrust.co.uk/NR/rdonlyres/8F79783B-9969-45F9-957A-BD6A662EE688/0/owc1.pdf, accessed march 2006

[19] "Ocean Energy Developments in Ireland" Sweeney E, Renewable Energy Association, Wave and Tidal Technology Symposium, Cardiff, September 2008

[20] "Feedback linearization control applied to the Archimedes Wave Swing" Valerio D, Beirao P, Sa da Costa J, IEEE Control Systems Society & IEEE Robotics and Automation Society, Mediterranean Conference on Control and Automation, Athens, July 2007

[21] "The Pelamis Prototype" Pelamis Wave Power, http://www.pelamiswave.com/content.php?id=142, accessed April 2008

[22] "Ocean Power Technologies, Project: Oahu, Hawaii" http://www.oceanpowertechnologies.com/projects.htm, accessed April 2008

[23] "Media update June 2005" Energetech, June 2005, http://www.oceanlinx.com/uploads/MediaUpdateJune2005.pdf, accessed April 2008

[24] "First Electricity from Irish Waves", Parish A, October 2007 http://www.wavebob.com/latest_news/first_electricity_from_irish_waves.php, accessed April 2008

[25] "Press release: 2nd July 2007", Wavegen, July 2007, http://www.wavegen.com/news_mutriku.htm, accessed April 2008

[26] "npower submit plans for wave power scheme", Wavegen, April 2008, http://www.wavegen.com/news_npower%20april%2008.htm, accessed April 2008

[27] "Variability of UK marine resources" Environmental Change Institute, University of Oxford, The Carbon Trust, July 2005, www.carbontrust.co.uk, accessed May 2008

[28] "Electric Machinery Volume II: AC machines" Liwschitz-Garik M, Whipple C, D. Van Nostrand, 3rd Edition, pp85, 1946

[29] "The Development of A Turbo-Generation System for Application in OWC Breakwaters" Heath T, Wavegen, September 2007, http://www.wavegen.com/EWTEC%202007%20PAPERS/tom.pdf , accessed May 2010

[30] "Dynamic Response of a Variable Pitch Wells Turbine" Tease K, http://www.wavegen.co.uk/pdf/variablepitchwellsturbine.pdf , accessed October 2009

[31] "Dynamic System Modeling of an Oscillating Water Column Wave Power Plant based on Characteristic Curves obtained by Fluid Dynamics to enhance Engineered Reliability" Arlitt R, Tease K, Starzmann R, Lees J, September 2007, www.wavegen.com, accessed May 2008

[32] "Islay Limpet Project Monitoring Final Report" Wavegen, 2002 www.wavegen.com, accessed June 2008

[33] "Electric Machinery Fundamentals" Chapman S, 4th Edition, Mc Graw-Hill

[34] "IEEE Recommended Practice – General Principles for Temperature Limits in the Rating of Electrical Equipment and for the Evaluation of Electrical Insulation" IEEE Power Engineering Society, December 2000

[35] "Thermal Analysis of Electric Motors and Generators, Training Course notes" Staton D, Motor Design Ltd, May 2007

[36] "The Application of an Induction Motor Thermal Model to Motor Protection and Other Functions" Roberts D, PhD Thesis, University of Liverpool, September 1986

[37] "Electric motor handbook" Chalmers, B.J, 1988, Butterworths, pp58,454

[38] "IEEE 112-2004 Standard Test Procedure for Polyphase Induction Motors and generators" IEEE Power Engineering Society, November 2004

[39] "Test report asynchronous motor" ALSTOM moteurs, supplied to Wavegen, 1999

[40] "Electric machines and drives" Slemon G R, 1992, Addison-Wesley, pp177-181

[41] "Theory of alternating-current machinery", Langsdorf A.S, 1955, McGraw-Hill, pp31-39

[42] "Calculation of iron losses from time-stepped finite-element models of cage induction machines" Mueller M Williamson S Flack T Atallah K Baholo B Howe D Mellor P, IEE Conference publication: 'Electrical Machines and Drives', Durham, September 1995

[43] "Design Calculation Output – Guiseley Electrical Design Program" Brook Crompton, June 2007

[44] "Eddy-Current Loss in the Rotor Magnets of Permanet-Magnet Brushless Machines Having a Fractional Number of Slots Per Pole" Ishak D, Zhu Z, Howe D, IEEE Transactions on Magnetics, Vol 41 No 9, September 2005

[45] "Rotor Eddy-Current Loss in Permanent Magnet Brushless machines" Toda H, Xia Z, Wang J, Atallah K, Howe D, IEEE Transactions of Magnetics, Vol 40 No 4, July 2004

[46] "Losses in grid and inverter supplied induction machine drives" Green T, Hernandez-Aramburo C, Smith A, IEE Proceedings Electric Power Applications, Vol 150 Issue 6, November 2003

[47] "Stray load losses in induction motors: A challenge to academia" Glew C N, IEE Power Engineering Journal, February 1998

[48] "Energy efficiency of induction machines" Slaets B, Van Roy P, Belmans R, Hameyer K, IEEE, Proceedings of The International Conference on Electrical Machines 2000, Espoo, Finland, August 2000

[49] "Loss Modelling of Converter Induction Machine System for Variable Speed Drive", Sousa G, Cleland J, Spiegel R, Chappell J, 1992, Proceedings of the 1992 International Conference on Industrial Power Electronics, Control, Instrumentation & Automation: Power Electronics and Motion Control, San Diego

[50] "Transient thermal characteristics of an induction machine rotor cage", Siymbalapitia, D.J.T, McLaren, P.G, Tavner, P.J, IEEE Transactions on Energy Conversion, Vol. 3, No. 4, page 1, 1988

[51] "Power Systems and Machines, lecture notes" Wallace A, The University of Edinburgh, 2003

[52] "Generating Electrical Power from Wave Energy, The Indian Experiment" Indiresan P, Murthy S, IEEE Aerospace Systems and Power Conditioning, Proceedings of the 24th intersociety Energy Conversion Engineering Conference, Washington, August 1989

[53] "Maximizing Power Output From A Wave Energy Plant" Jayashankar V, Udayakumar K, Karthikeyan B, Manicannan K, Venkatraman N, Ranagaprasad S, IEEE Power Engineering Society Winter Meeting, Singapore, January 2000

[54] "Stability Study of the Slip Power Recovery Generator Applied to the Sea Wave Energy Extraction" Marques G, IEEE Power Electronics Specialists Conference, Toledo Spain, June 1992

[55] "Variable-Speed Wind Power Generation Using Doubly Fed Wound Rotor Induction Machine – A Comparison with Alternative Schemes" Datta R, Ranganathan V, IEEE Transactions on Energy Conversion, Vol. 17 No 3 September 2002

[56] "Control Technqiues Quote for Edinburgh University Q203991" Donohue T, March 2008

[57] "The BDFM as a Generator in Wind Turbines" McMahon R Wan X Abdi-Jalebi E Tavner P, Roberts P Jagiela M, European Power Electronics and Drives Association, European Power Electronics- Power Electronics and Motion Control Conference, Portoroz, Slovenia, 2006

[58] "Generalised theory of the brushless doubly-fed machine. Part 1: Analysis" Williamson S, Ferreira A, Wallace A, IEE Proceedings Electrical Power Applications, Vol 144 No 2, March 1997

[59] "Performance of BDFM as generator and motor" McMahon R Roberts P Wang X Tavner P, Proceedings of IEE electric Power Applications Vol. 153 Issue 2, March 2006

[60] "Rotor Loss Estimation in Permanent Magnet Machines with Concentrated Windings" Bottauscio O, Pellegrino G, Guglielmi P, Chiampi M, Vagati A, IEEE Transactions on Magnetics Vol 42, No 10, October 2005

[61] "Reduction of Cogging Torque in Permanent Magnet Motors" Touzhu L Slemon G, IEEE Transactions on Magnetics, Vol. 24 Issue 6, November 1988

[62] "Compact Electrical Generators for Diesel Driven Generating Sets", N.L. Brown, PhD Thesis, University of Durham, 2002.

[63] "Finite element analysis and experimental test of an axial flux toroidal generator" Martin R, Bumby J, Mueller M, 2004

[64] "Design and Development of a High-Speed Axial-Flux Permanent-Magnet Machine" Sahin F, PhD Thesis, Eindhoven University of Technology, May 2001

[65] "Electronic Control of Switched Reluctance Machines" Miller T, Newnes Power Engineering Series, 2001

[66] "State of the Art Hydraulics for the Pelamis Wave Energy Converter" Henderson R, Yemm R, Ocen Power Delivery Ltd, Fluid Machinery for Wave and Tidal Energy: State of the Art and New Developments IMECHE conference, October 2005

[67] "Torus Generator. Design Build and Test of Two prototypes" Bumby JR, Spooner E, University of Durham, 2000

[68] "Power conditioning of the output from a linear vernier hybrid permanent magnet generator for use in direct drive wave energy converters" Brooking P, Mueller M, IEE Proccedings of Generation, Transmission and Distribution, Vol. 152 No. 5, September 2005

[69] "Optimised Permanent Magnet Generator Topologies for Direct Drive Wind Turbines" Dubois M, University of Delft, 2004, http://ee.its.tudelft.nl/epp/Research/Projects%20PhD/thesis_Dubois.pdf

[70] "Minimization of Iron Losses of Permanent Magnet Synchronous Machines" Mi C, Slemon G, Bonert R, Electrical Machines and Systems, 2001. ICEMS 2001. Proceedings of the Fifth International Conference on
Volume 2, 18-20 Aug. 2001 Page(s):818 - 823 vol.2

[71] "Mass and Heat transfer" Mills A, Richard D. Irwin, Boston, 1995

[72] "Principles of Electric Machines and Power Electronics. (2nd ed.)" P.C. Sen, New York: Wiley, 1997, p. 355.

[73] "Improved analytical modelling of rotor eddy current loss in brushless machines equipped with surface-mounted permanent magnets" Zhu Z, Ng K, Schofield N, Howe D, IEE Proceedings on Electrical Power Applications, Vol 141 No 6, November 2004

[74] "Type Test Certificate" Brook Crompton for 18.5kW induction generator, November 2004

[75] "EFFs_Mains vs Inverter" supplied by Virdi, P on behalf of LeRoy Somer, November 2005

[76] "AC Motor Quotation Q08 7846 2523" LeRoy Somer, via Wavegen, August 2008

[77] "The Nature of Polyphase Induction Machines" Alger P.L, p337, Chapman & Hall, 1951

[78] "BS EN 60034-2-1:2007 Rotating electrical machines – Part 2-1: Standard methods for determining losses and efficiency from tests (excluding machines for traction vehicles" British Standard, January 2008

[79] Unidrive SP Advanced User Manual" Control Techniques, July 2004

[80] "Evaluation of Stray Load Loss in Induction Motors With a Comparison of Input-Output and Calorimetric Methods" Bradley K, Cao W, Arellano-Padilla J, IEEE Transactions on Energy Conversion, Vol 21 No 3, September 2006

[81] "MotorCAD software" Motor Design Ltd

[82] "Stray Load Loss Analysis of Cage Induction Motors Considering Inter-Bar Currents Using 3-D Finite Element Method" Yamazaki K, Watanabe Y, IEEE International Conference on Electric Machines and Drives, May 2005

[83] "Empirical thermal model for inverter-driven cage induction machines" Boys J, Miles M, IEE Proceedings of Electrical Power Applications Vol. 141, No 6, November 1994

[84] "Thermal analysis of permanent magnet machines" Liu Z, Howe D, Mellor P, Jenkins M, IEE Proceedings Electric Power Applications, Vol 138, Issue 5, Sept 1991

[85] "Advances in heat transfer, Supplement 1: Laminar flow , forced convection in ducts" Shah R, London A, Academic Press London, 1978

[86] "Design and Arrangement of Cooling Fins" Heiles F, Elecktrotecknik und Maschinenbay, Vol. 69 No. 14, July 1952

[87] "Lumped parameter thermal model for electrical machines of TEFC design" Mellor P, Roberts D, Turner D, IEE Proceedings-B Vol. 138 No. 5, September 1991

[88] "Thermal Resistance of Metallic Contacts" Shlykov Y, Ganin Y, International Journal of Heat and Mass Transfer 1964

[89] "TEFC Induction Motors Thermal Models: A Parameter Sensitivity Analysis" Boglietti A, Cavagnino A, Staton D, IEEE Industrial Applications Society, 2004

[90] "Thermal Modeling of an Induction Machine Through the Association of Two Mumerical Approaches" Trigeol J, Bertin Y, Lagonotte P, IEEE Transactions on Energy Conversion Vol. 21 No. 2, June 2006

[91] "The Nature of Polyphase Induction Machines" Alger P, Chapman & Hall, 1951

[92] "Advanced User Guide, Unidrive SP" Control Techniques, Issue 8, http://www.controltechniques.com/CTcom/Default.aspx?Page=338&DocVarId=516, accessed March 2006

[93] "Design drawings 18.5kW induction machine", Brook Crompton, April 1997

[94] "CFD Modelling of an Induction Generator in an Oscillating Water Column Wave Energy Device to Assess Heat Transfer" Burchell J, MEng Mechanical Engineering with Renewable Energy Dissertation, University of Edinburgh, April 2009

[95] "Thermal Management of Power Electronics Task at NREL" Hassani V, June 2004, http://www.nrel.gov/vehiclesandfuels/powerelectronics/pdfs/program_review_6-7-04_thermal_mgmt.pdf, accessed march 2009

[96] "ITS-90 Formulations for vapour pressure, frost point temperature, dewpoint temperature and enhancement factors in the range -100 to +100 C" Hardy B, Proceedings of the Third International Symposium of Humidity and Moisture, April 1998

[97] "Thermophysical properties of humid air, models and background" M. Conde Engineering, , http://www.mrc-eng.com/ , 2005, accessed November 2006

[98] "Density of Dry Air, Water Vapor and Moist Humid Air" The Engineering Tool Box, www.engineeringtoolbox.com, 2005, accessed September 2007

[99] "Forced convection heat transfer to air/water vapour mixtures" Richards D, Florschuetz L, NASA contractor report 3769, National Aeronautics and Space Administration Scientific and Technical Information Office, 1984

APPENDICIES

i. Derivation of Radial vs Axial drag comparison

This derivation compares the drag on a “cigar shaped” radial flux machine to the drag on a two rotor “pancake” machine. The numbered equations are those found in the text. This is an approximate comparison as it makes no attempt to examine the following effects:

- Relatively close stationary surface, slot flow & drag effects
- Different flow regimes for axial and radial rotors
- Different surface properties of axial and radial rotors

The drag torque is found for the periphery of a cylinder using equation (a) from [64]:

$$\tau_D = \frac{C_f \rho \pi \omega \quad r^4 L}{2} \qquad \text{(a)}$$

Where τ_D is the drag torque
C_f is the coefficient of drag
ρ is the density of air
ω is the angular velocity of the cylinder
r is the outside radius of the cylinder
L is the axial length of the cylinder

The drag torque of a cylinder face with radius r and interior radius r_i is given by:

$$\tau_D = \frac{C_f \rho \pi \omega^2 (r^5 - r_i^5)}{2} \qquad \text{(b)}$$

Where r_i is the interior radius

$$P = \omega \tau_D \qquad \text{(c)}$$

The radial flux machine is modelled as a single cylinder of radius r_r and length l_r it has a length to radius ratio as in equation (d)

$$L_r = 3r_r \tag{d}$$

The length to diameter ratio is taken from a prototype built at Durham University by Bumby & Spooner [67]. The second prototype axial flux machine detailed in [67] was rated at 29.5kW at 3000rpm (neglecting windage) and had a length to diameter ratio of 1:34. Therefore axial flux machine rotors are modelled as two cylinders each of radius r_a and length l_a it has a length to radius ratio as in equation (e)

$$L_a = \frac{2}{34} r_a \tag{e}$$

Work by Sahin [64] gives a 2 pole axial machine 2.5 x the torque density of a radial machine for the B_{gap}/B_{stator} and 2 pole configuration. Hence the total volume of both axial flux cylinders is half that of the radial machine.

$$5\pi L_a r_a^2 = \pi L_r r_r^2 \tag{f}$$

Combining equations d, e and f:

$$\frac{10}{34} r_a^3 = 3r_r^3 \tag{g}$$

$$0.46 r_a = r_r \tag{35}$$

The drag on the cylinder of the radial machine in terms of r_a is given by:

$$P_{Dpr} = \frac{C_f \rho \pi \omega^3 (0.46 r_a)^4 (1.38) r_a}{2} \tag{i}$$

The drag on the faces of the radial machine are given in terms of r_a by:

$$P_{Dfr} = C_f \rho \pi \omega^3 (0.46 r_a)^5 \tag{j}$$

The drag on the periphery of the cylinders of the axial machine is given in terms of r_a by:

$$P_{Dpa} = \frac{2C_f \rho\pi\omega^3 r_a^{\ 5}}{34} \tag{k}$$

The drag on the faces of both cylinders of the axial machine is given in terms of r_a by:

$$P_{Dfa} = 2C_f \rho\pi\omega^3 r_a^{\ 5} \tag{l}$$

So the total drag on each machine is given by:

$$P_{Dt} = P_{Dp} + P_{Df} \tag{m}$$

Radial flux (2 pole generator):

$$P_{Dtr} = C_f \rho\pi\omega^3 \left(\frac{0.063}{2} + 0.021 \right) r_a^{\ 5} \tag{n}$$

$$P_{Dta} = C_f \rho\pi\omega^3 \left(\frac{2}{34} + 2 \right) r_a^{\ 5} \tag{o}$$

So for identical values of drag coefficient:

$$P_{Dta} = 40 P_{Dtr} \tag{36}$$

In the case of a 4 pole machine Sahin [64] gives predicts the axial flux generator will have four times the torque density of an equivalent machine. Repeating the above analysis suggests that the axial flux machine drag will larger than that of the radial machine with the relationship in equation

$$P_{Dta} = 18 P_{Dtr} \tag{36}$$

A Wells turbine in a wave energy converter must be kept at speed to accept power from an incoming wave, thus windage is a no-load loss. It can be seen that a radial flux topology has lower windage losses than a comparable axial flux topology and thus is better suited for this application.

ii. Permanent Magnet generator designs

2 Pole

General	RATING	15.35	KW
Speed	*ω*	3000	rpm
		314.1592654	rad/sec
Pole number	*p*	2	
Frequency	*f*	50	Hz
Rotor OR	*Ro*	**0.11**	m
Stator IR	*Rsi*	1.24E-001	m
Sator yoke thickness	*Tsy*	4.83E-002	m
Stator OR	*Rso*	1.72E-001	m
Outer diameter	*Dout*	3.44E-001	
Rotor L/R	*Aspect ratio*	**1.50E+000**	
Rotor axial length	*Lr*	3.300E-001	m
Stator axial length	*Ls*	0.3300	m
Rotor OD velocity	*vm*	34.55751919	m/s
Mean pole pitch	*τpm*	3.46E-001	m
Running clearance	*c*	2.00E-003	m
Number of coils		6	
Stator phase spread	*theta w*	60	mech. Degree
Coil spread	*σ*	60	elec. degree
Coil pitch	*τid*	1.29E-001	m

Stator

Wire diameter (inner)	ai	0.001	m
Wire insulation thickness		0.0001	m
Wire outer diameter	ao	0.0011	m
Number of wires per conductor	n	4	
Wire packing factor	kp	0.6	
Conductor diameter	d	0.0011	m
Taped conductor diameter		0.0044	m
Copper area/conductor	ACu	3.14159E-06	m2
Layers		1	
Insulation thickness to core		0.0006	m
Outer insulation thickness		0.0006	m
Winding thickness	ta	0.0056	m
V/turn		26.81652273	V
Peak fundamental emf/turn		26.81652273	V
Max possible turns per coil		5	
Actual/maximum turns		0.8	
Turns per coil	Ncoil	20	

Magnet

Magnet OD	*Do mag*	0.116	m
Magnet ID	*Di mag*	0.110	m
Magnet width/pitch		0.653	
Magnet thickness	*tmag*	6.00E-003	m
Magnet axial length	*Lmag*	0.330	m

Magnet mass	*Mmag*	6.61E+000	kg
Magnet Brem	*Brem*	1.21	T
Magnet recoil permeability	*μr*	1.07	
Minimum Airgap	*g*	0.01360	m
Effective airgap	*geff*	0.01321	m
Bgap	*Bgap*	0.514	T
B1 peak	*B1 pk*	0.514	T

Power output and losses

Rated current	*I*	172.4596724	A
EMF per phase	*Eph rms*	59.88229612	V (RMS)
Terminal volts	*V*	40.98321673	V
Terminal power	*P*	21203.85639	W
Torque	*T*	67.49397115	Nm
Armature joule loss	*Pjoule*	1791.743772	W
Eddy loss	*Peddy*	152.5629012	W
Iron loss	*Piron*	64.52722037	W
Total loss		2008.833893	W
Full load efficiency		91.35%	

4 Pole

	Power Output	23.05	KW
Speed	*ω*	3000	rpm
		314.1592654	rad/sec
Pole number	*p*	4	
Frequency	*f*	100	Hz
Rotor OR	*Ro*	**0.11**	m
Stator IR	*Rsi*	1.23E-001	m
Sator yoke thickness	*Tsy*	1.89E-002	m
Stator OR	*Rso*	1.42E-001	m
Outer diameter	*Dout*	2.83E-001	m
Rotor L/R	*Aspect ratio*	**1.80E+000**	
Rotor axial length	*Lr*	3.960E-001	m
Stator axial length	*Ls*	0.3960	m
Rotor OD velocity	*vm*	34.55751919	m/s
Mean pole pitch	*τpm*	1.73E-001	m
Running clearance	*c*	2.00E-003	m
Number of coils		12	
Stator phase spread	*theta w*	30	mech. Degree
Coil spread	*σ*	60	elec. degree
Coil pitch	*τid*	6.42E-002	m

Stator

Wire diameter (inner)	*ai*	1.00E-003	m
Wire insulation thickness		1.00E-004	m
Wire outer diameter	*ao*	1.10E-003	m
Number of wires per conductor	*n*	4	
Wire packing factor	*kp*	0.6	
Conductor diameter	*d*	1.10E-003	m
Taped conductor diameter	*dt*	4.40E-003	m
Copper area/conductor	*ACu*	3.142E-06	m2
Layers	*NL*	1	
Insulation thickness to core	*tci*	6.00E-004	m
Outer insulation thickness	*toi*	6.00E-004	m
Winding thickness	*ta*	5.60E-003	m
V/turn		2.89E+001	V
Peak fundamental emf/turn		28.85859726	V
Max possible turns per coil		5	
Actual/maximum turns		0.8	
Turns per coil	*Ncoil*	20	

Magnet

Magnet OD	***Ro mag***	0.115	m
Magnet ID	*Ri mag*	0.110	m
Magnet width/pitch		0.570	
Magnet thickness	*tmag*	5.00E-003	m
Magnet axial length	*Lmag*	0.396	m
Magnet mass	*Mmag*	5.77E+000	kg
Magnet Brem	*Brem*	1.21	T

Magnet recoil permeability	*μr*	1.07	
Minimum Airgap	*g*	0.01260	m
Effective airgap	*geff*	0.01227	m
Bgap	*Bgap*	0.461	T
B1 peak	*B1 pk*	0.461	T

Power output and losses

Rated current	I	23.18481449	A
EMF per phase	Eph rms	346.3031671	V (RMS)
Terminal volts	V	331.3417925	V
Terminal power	P	23046.29397	W
Torque	T	73.35863212	Nm
Armature joule loss	Pjoule	972.6511121	W
Eddy loss	Peddy	60.76126256	W
Iron loss	Piron	181.2879312	W
Total loss		1214.700306	W
Full load efficiency		0.949931965	

6 Pole

	Power Output	22.63	KW
Speed	*ω*	3000	rpm
		314.1592654	rad/sec
Pole number	*p*	6	
Frequency	*f*	150	Hz
Rotor OR	*Ro*	**0.11**	m
Stator IR	*Rsi*	1.22E-001	m
Sator yoke thickness	*Tsy*	1.09E-002	m
Stator OR	*Rso*	1.33E-001	m
Outer diameter	*Dout*	2.65E-001	m
Rotor L/R	*Aspect ratio*	**1.80E+000**	
Rotor axial length	*Lr*	3.960E-001	m
Stator axial length	*Ls*	0.3960	m
Rotor OD velocity	*vm*	34.55751919	m/s
Mean pole pitch	*τpm*	1.15E-001	m
Running clearance	*c*	2.00E-003	m
Number of coils		18	
Stator phase spread	*theta w*	20	mech. Degree
Coil spread	*σ*	60	elec. degree
Coil pitch	*τid*	4.24E-002	m
Stator			
Wire diameter (inner)	ai	0.001	m
Wire insulation thickness		0.0001	m
Wire outer diameter	ao	0.0011	m
Number of wires per conductor	n	4	
Wire packing factor	kp	0.6	
Conductor diameter	d	0.0011	m
Taped conductor diameter	dt	0.0044	m
Copper area/conductor	ACu	3.14159E-06	m2
Layers	NL	1	
Insulation thickness to core	tci	0.0006	m
Outer insulation thickness	toi	0.0006	m
Winding thickness	ta	0.0056	m
V/turn		24.98985158	V
Peak fundamental emf/turn		24.98985158	V
Max possible turns per coil		5	
Actual/maximum turns		0.8	
Turns per coil	Ncoil	20	

Magnet

Magnet OD	Ro mag	0.114	m
Magnet ID	Ri mag	0.11	m
Magnet width/pitch		0.57	
Magnet thickness	tmag	0.004	m
Magnet axial length	Lmag	0.396	m
Magnet mass	Mmag	4.617791353	kg
Magnet Brem	Brem	1.21	T

Magnet recoil permeability	μr	1.07	
Minimum Airgap	g	0.0116	m
Effective airgap	geff	0.011338318	m
Bgap	Bgap	0.398944939	T
B1 peak	B1 pk	0.398944939	T

Power output and losses

Rated current	*I*	34.23963128	A
EMF per phase	*Eph rms*	160.8991364	V (RMS)
Terminal volts	*V*	149.4660023	V
Terminal power	*P*	15352.98242	W
Torque	*T*	48.87006086	Nm
Armature joule loss	*Pjoule*	1072.498502	W
Eddy loss	*Peddy*	7.770275341	W
Iron loss (core loss)	*Piron*	202.8909368	W
Total loss		1283.159714	W
Full load efficiency		92.29%	

LIMPET 250kW

	Power Output	253.3581073	KW
Speed	ω	1200	rpm
		125.6637061	rad/sec
Pole number	p	6	
Frequency	f	60	Hz
Rotor OR	Ro	0.35	m
Stator IR	Rsi	0.376	m
Sator yoke thickness	Tsy	0.026423154	m
Stator OR	Rso	0.402423154	m
Outer diameter	Dout	0.804846308	m
Rotor L/R	Aspect ratio	1.5	
Rotor axial length	Lr	1.05	m
Stator axial length	Ls	1.05	m
Rotor OD velocity	vm	43.98229715	m/s
Mean pole pitch	τpm	0.366519143	m
Running clearance	c	0.002	m
Number of coils		18	
Stator phase spread	theta w	20	mech. Degree
Coil spread	σ	60	elec. degree
Coil pitch	τid	0.13124876	m

Stator

Wire diameter (inner)	*ai*	2.00E-003	m
Wire insulation thickness		1.00E-004	m
Wire outer diameter	*ao*	2.10E-003	m
Number of wires per conductor	*n*	8	
Wire packing factor	*kp*	0.6	
Conductor diameter	*d*	2.10E-003	m
Taped conductor diameter		1.68E-002	m
Copper area/conductor	*ACu*	2.513E-05	m2
Layers		1	
Insulation thickness to core		6.00E-004	m
Outer insulation thickness		6.00E-004	m
Winding thickness	*ta*	1.80E-002	m
V/turn		5.60E+001	V
Peak fundamental emf/turn		56.01008585	V
Max possible turns per coil		5	
Actual/maximum turns		0.8	
Turns per coil	*Ncoil*	20	

Magnet

Magnet OD	*Do mag*	0.356	m
Magnet ID	*Di mag*	0.350	m
Magnet width/pitch		0.653	
Magnet thickness	*tmag*	6.00E-003	m
Magnet axial length	*Lmag*	1.050	m
Magnet mass	*Mmag*	6.69E+001	kg

Magnet Brem	*Brem*	1.21	T
Magnet recoil permeability	*μr*	1.07	
Magnet Cost	*Cpm*	40	Euro/Kg
Minimum Airgap	*g*	0.02600	m
Effective airgap	*geff*	0.02561	m
Bgap	*Bgap*	0.265	T
B1 peak	*B1 pk*	0.265	T
Power output and losses			
Rated current	*I*	90.00796689	A
EMF per phase	*Eph rms*	1008.181545	V (RMS)
Terminal volts	*V*	938.280303	V
Terminal power	*P*	253358.1073	W
Torque	*T*	2016.159758	Nm
Armature joule loss	*Pjoule*	7055.278669	W
Eddy loss	*Peddy*	920.847589	W
Iron loss (core loss)	*Piron*	1183.362274	W
Total loss		9159.488533	W
Full load efficiency		96.51%	

iii. Effect of Humidity on Forced Convection Heat Transfer Coefficients

There is some overlap of symbols between this appendix and other sections of this thesis. P denotes partial pressure in this section, rather than power. s is an enhancement factor, f is a friction factor and X is a molar fraction. It is concluded that humidity makes little difference to the outcome of this work and consequently these symbols are used with their usual meanings elsewhere.

The OWC environment on Islay is significantly humid. This section examines the effect of this humidity on heat transfer from the generator. The properties of dry air are altered by the presence of water vapour. The magnitude of this variation is determined by the quantity of vapour present in a given mass of air. This is determined from the temperature, air pressure and the ratio of the air pressure to the saturation vapour pressure. This is the relative humidity. The air is said to be saturated when the vapour pressure of the air is equal to the saturation vapour pressure. This is 100% humidity. In this state as much vapour will be removed from a water surface as will be returned, thus the air and water are in equilibrium.

$$\varphi = \frac{p_v}{P_{vs}} \tag{p}$$

The saturation vapour pressure varies with temperature and air pressure. This variation is described by the Arden Buck equation q in kPa.

$$P_{vs} = 0.61121 e^{\left(\frac{(18.678 - t/234.5)t}{257.14 + t}\right)} \tag{q}$$

Where t is the temperature (dry bulb) in Celcius.

The mole fraction of water vapour in the mixture is given by equation r.

$$X_w = \varphi s \frac{p_{vs}}{P} \tag{r}$$

Where P is the mixture pressure
and s is the enhancement factor.

The enhancement factor is a correction for work with moist air rather than pure water vapour. It is calculated in Equation s from [96].

$$s = e^{[\alpha(1-\frac{p_{vs}}{p})+\beta(\frac{p}{p_{vs}}-1)]} \qquad (s)$$

Where

$$\alpha = \sum_{i=0}^{3} C_i t^i \qquad (t)$$

$$\beta = \sum_{i=0}^{3} B_i t^i \qquad (u)$$

With the coefficients C & B between 0 and 100C given in table 21:

Table 21: Coefficients of C and B

C0	0.000353624	B0	-1.07588
C1	2.93284E-05	B1	0.063268
C2	2.6169E-07	B2	-0.000253689
C3	8.58136E-09	B3	6.34053E-07

The mixing ratio, the mass of water vapour per kg of air is given by equation v from [97].

$$\omega = 0.62198\frac{X_w}{1-X_w} \qquad (v)$$

The thermal conductivity is given by mixing that of air and water vapour according to the humidity. The same equation is used for the Prandtl number. Equation w, for this mixing is taken from [97].

$$P_{x,m} = \frac{P_{air}}{1+G_{aw}\frac{X_w}{X_a}} + \frac{P_{water}}{1+G_{wa}\frac{X_a}{X_w}} \qquad (w)$$

Where P is the property concerned

G is given by equations x & y

$$G_{wa} = 0.277609[1+1.12605(\frac{\mu_w}{\mu_a})^{0.5}]^2 \qquad (x)$$

$$G_{aw} = 0.2189366[1+0.8880306(\frac{\mu_a}{\mu_w})^{0.5}]^2 \qquad (y)$$

X is the molar concentrations of dry air X_a and water vapour X_w

$$X_a = \frac{1}{1+1.607793\omega} \qquad (z)$$

$$X_w = \frac{\omega}{0.62197058+\omega} \qquad (aa)$$

Thermal conductivities were taken at 20°C as 0.0257W/mK for air and 0.6W/mK for water. The Prandtl number is calculated from equation ab:

$$\Pr = \frac{\mu C_p}{k} \qquad (ab)$$

Where μ is the viscosity
C_p is the specific heat capacity

The specific heat capacity of humid air is given by the rate of change of enthalpy with temperature.

$$h = h_a + \omega h_w \qquad (ac)$$

Where

$$h_a = C_{pa} t \qquad (ad)$$

C_{pa} is the specific heat capacity of dry air, 1006J/Kg/K

$$h_w = C_{pw} t + h_{we} \qquad (ae)$$

C_{pw} is the specific heat capacity of water vapour, 1840J/Kg/K
h_{we} is the evaporation energy

Thus

$$\frac{dh}{dt} = C_{pa} + \omega C_{pw} \tag{af}$$

The Nusselt number is calculated from equation ag.

$$Nu = \frac{(f/8)(\mathrm{Re}_D - 1000)\,\mathrm{Pr}}{1 + 12.7(f/8)^{\frac{1}{2}}(\mathrm{Pr}^{\frac{2}{3}} - 1)} \tag{ag}$$

Where f is the friction factor given by

$$f = 0.184\,\mathrm{Re}_D^{-0.2} \qquad \text{for } 4\text{x}10^4 < \mathrm{Re}_D < 10^6 \tag{ah}$$

The Reynolds number is given by equation ai.

$$\mathrm{Re}_D = \frac{\rho u D_h}{\mu} \tag{ai}$$

Where u is the airflow velocity

The density of the mixture, ρ, is given by equation aj from [98].

$$\rho = \frac{(p/R^a T)(1+\omega)}{(1+\omega R^w / R^a)} \tag{aj}$$

Where R^w and R^a are the individual gas constants for water vapour and air.

The heat transfer coefficient was calculated for airflow velocities from 0.1 to 20m/s and humidities from 0 to 100%.

Table 22: Convective heat transfer coefficients

U (m/s)	0.1 m/s	5 m/s	10 m/s	15 m/s	20 m/s
h 100%	0.3	14.4	25.1	34.7	43.9
h 80%	0.3	14.4	25.0	34.7	43.8
h 60%	0.3	14.3	25.0	34.6	43.7
h 40%	0.3	14.3	24.9	34.5	43.6
h 20%	0.3	14.3	24.8	34.4	43.5
h 0%	0.3	14.3	24.8	34.3	43.3

The change in convective heat transfer coefficient in table 22 from dry to saturated air is a factor of 1.008 to 1.012 depending on flow velocity. Results from the equations developed here are compared to an experimental study for NASA [99] in figures 122 & 123.

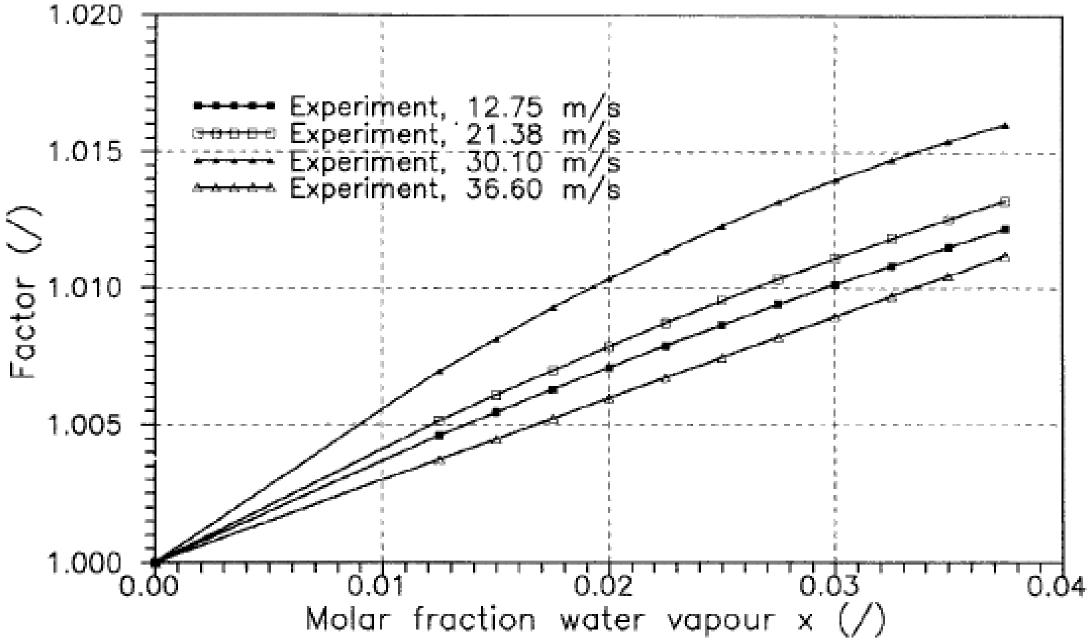

Figure 122: Ratio of dry heat transfer coefficient to moist heat transfer coefficient at 30°C from Richards *et Al* [99]

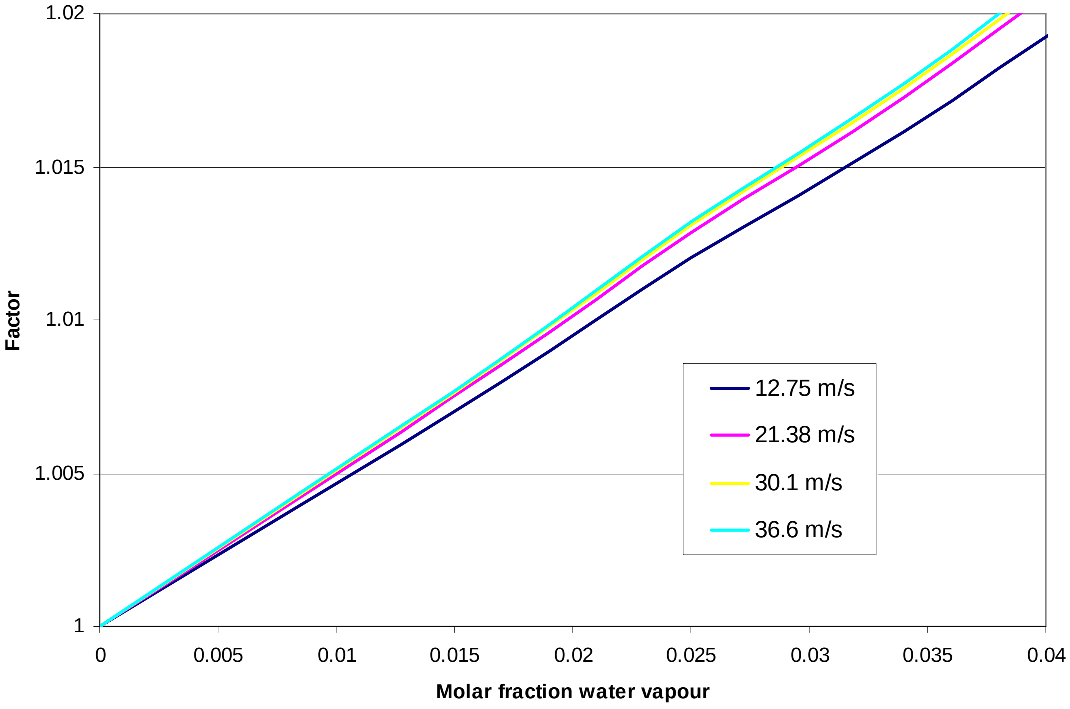

Figure 123: Ratio of dry heat transfer coefficient to moist heat transfer coefficient at 30°C

The water vapour present in the air will should not significantly alter the cooling of a generator in an OWC.

iv. MOTORCAD MODEL OF 18.5kW INDUCTION GENERATOR

Radial Cross Section

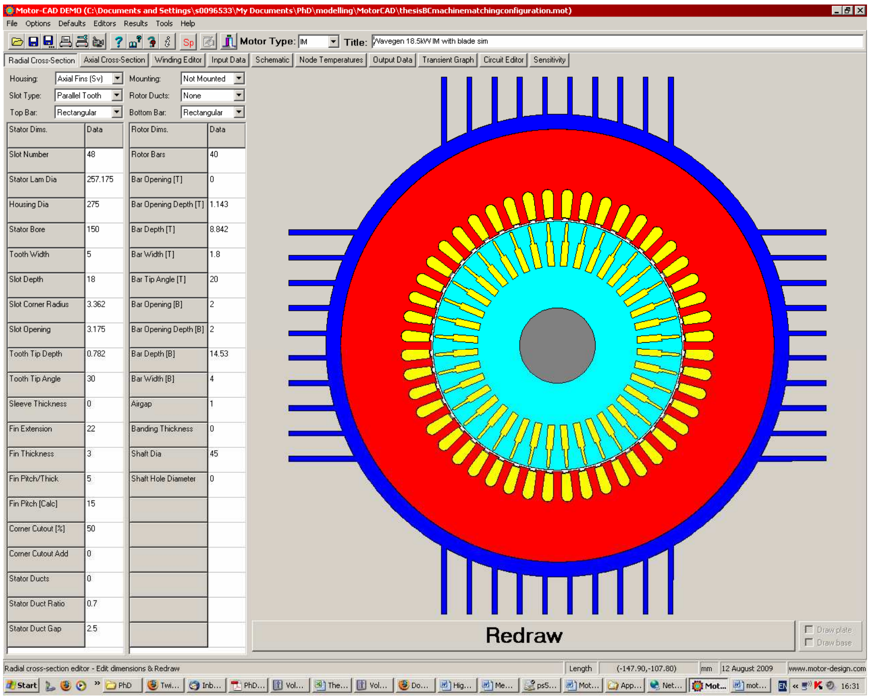

Motor-CAD DEMO (C:\Documents and Settings\s0096533\My Documents\PhD\modelling\MotorCAD\thesisBCmachinematchingconfiguration.mot)

Motor Type: IM
Title: Wavegen 18.5kW IM with blade sim

Housing: Axial Fins (Sv)
Slot Type: Parallel Tooth
Top Bar: Rectangular
Mounting: Not Mounted
Rotor Ducts: None
Bottom Bar: Rectangular

Stator Dims.	Data	Rotor Dims.	Data
Slot Number	48	Rotor Bars	40
Stator Lam Dia	257.175	Bar Opening [T]	0
Housing Dia	275	Bar Opening Depth [T]	1.143
Stator Bore	150	Bar Depth [T]	8.842
Tooth Width	5	Bar Width [T]	1.8
Slot Depth	18	Bar Tip Angle [T]	20
Slot Corner Radius	3.362	Bar Opening [B]	2
Slot Opening	3.175	Bar Opening Depth [B]	2
Tooth Tip Depth	0.782	Bar Depth [B]	14.53
Tooth Tip Angle	30	Bar Width [B]	4
Sleeve Thickness	0	Airgap	1
Fin Extension	22	Banding Thickness	0
Fin Thickness	3	Shaft Dia	45
Fin Pitch/Thick	5	Shaft Hole Diameter	0
Fin Pitch [Calc]	15		
Corner Cutout [%]	50		
Corner Cutout Add	0		
Stator Ducts	0		
Stator Duct Ratio	0.7		
Stator Duct Gap	2.5		

Radial cross-section editor - Edit dimensions & Redraw | Length | (-147.90,-107.80) | mm | 12 August 2009 | www.motor-design.com

Radial Cross Section

Dimension		Unit
Slot Number	48	
Stator Lam Dia.	257.175	mm
Housing Dia.	275	mm
Stator Bore	150	mm
Tooth Width	5	mm
Slot Depth	18	mm
Slot Corner Radius	3.362	mm
Slot Opening	3.175	mm
Tooth Tip Depth	0.782	mm
Tooth Tip Angle	30	Degrees
Sleeve Thickness	0	mm
Fin Extension	22	mm
Fin Thickness	3	mm
Fin Pitch/Thickness	5	
Fin Pitch	15	
Corner Cutout	50	%
Corner Cutout-Add	0	
Stator Ducts	0	
Stator Duct Ratio	0.7	

Stator Duct Gap	2.5	
Rotor Bars	40	
Bar Opening	0	mm
Bar Opening Depth	1.143	mm
Bar Depth	8.842	mm
Bar Width	1.8	mm
Bar Tip Angle	20	Degrees
Bar Opening	2	mm
Bar Opening Depth	2	mm
Bar Depth	14.53	mm
Bar Width	4	mm
Airgap	1	mm
Banding Thickness	0	mm
Shaft Diameter	45	mm
Shaft Hole Diameter	0	mm

Axial Cross Section

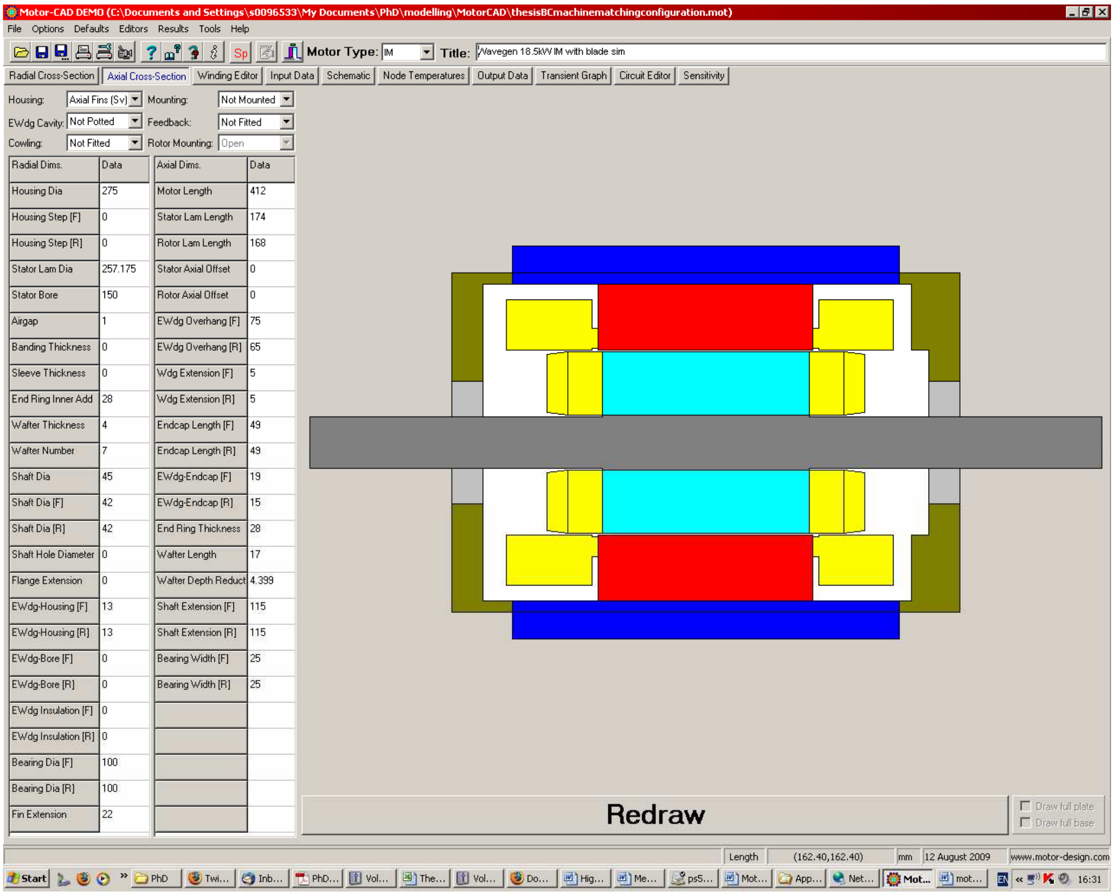

Motor-CAD DEMO (C:\Documents and Settings\s0096533\My Documents\PhD\modelling\MotorCAD\thesisBCmachinematchingconfiguration.mot)

Motor Type: IM
Title: Wavegen 18.5kW IM with blade sim

Housing: Axial Fins (Sv)
Mounting: Not Mounted
EWdg Cavity: Not Potted
Feedback: Not Fitted
Cowling: Not Fitted
Rotor Mounting: Open

Radial Dims.	Data	Axial Dims.	Data
Housing Dia	275	Motor Length	412
Housing Step [F]	0	Stator Lam Length	174
Housing Step [R]	0	Rotor Lam Length	168
Stator Lam Dia	257.175	Stator Axial Offset	0
Stator Bore	150	Rotor Axial Offset	0
Airgap	1	EWdg Overhang [F]	75
Banding Thickness	0	EWdg Overhang [R]	65
Sleeve Thickness	0	Wdg Extension [F]	5
End Ring Inner Add	28	Wdg Extension [R]	5
Wafter Thickness	4	Endcap Length [F]	49
Wafter Number	7	Endcap Length [R]	49
Shaft Dia	45	EWdg-Endcap [F]	19
Shaft Dia [F]	42	EWdg-Endcap [R]	15
Shaft Dia [R]	42	End Ring Thickness	28
Shaft Hole Diameter	0	Wafter Length	17
Flange Extension	0	Wafter Depth Reduct	4.399
EWdg-Housing [F]	13	Shaft Extension [F]	115
EWdg-Housing [R]	13	Shaft Extension [R]	115
EWdg-Bore [F]	0	Bearing Width [F]	25
EWdg-Bore [R]	0	Bearing Width [R]	25
EWdg Insulation [F]	0		
EWdg Insulation [R]	0		
Bearing Dia [F]	100		
Bearing Dia [R]	100		
Fin Extension	22		

☐ Draw full plate
☐ Draw full base

Length (162.40,162.40) mm 12 August 2009 www.motor-design.com

Axial Cross Section

Axial Cross Section

Housing Diameter	275	mm
Housing Step [F]	0	mm
Housing Step [R]	0	mm
Stator Lam Dia	257.175	mm
Stator Bore	150	mm
Airgap	1	mm
Banding thickness	0	mm
Sleeve Thickness	0	mm
End Ring Inner Add	28	mm
Wafter Thickness	4	mm
Wafter Number	7	
Shaft Dia	45	mm
F	42	mm
R	42	mm
Flange Exension	0	mm

Ewdg-Housing [f]	13	mm
Ewdg-Housing [r]	13	mm
Ewdg-Bore[F]	0	mm
EWdg-Bore[R]	0	mm
Ewdg-Insulation [F]	0	mm
Ewdg-Insulation [R]	0	mm
Bearing Dia [F]	100	mm
Bearing Dia [R]	100	mm
Motor Length	412	mm
Stator Lam Length	174	mm
Rotor Lam Length	168	mm
Stator Axial Offset	0	mm
Rotor Axial Offset	0	mm
Ewdg Overhang [F]	75	mm
Ewdg Overhang [R]	65	mm
Wdg Extension [F]	5	mm
Wdg Extension [R]	5	mm
Endcap Length [F]	49	mm
Endcap Length [R]	49	mm
Ewdg-Endcap [F]	19	mm
Ewdg-Endcap [R]	15	mm
End Ring Thickness	28	mm
Wafter Length	17	mm
Wafter Depth Reduction	4.399	mm
Shaft Extension [F]	115	mm
Shaft Extension [R]	115	mm
Bearing Width [F]	25	mm
Bearing Width [R]	25	mm

Winding Editor

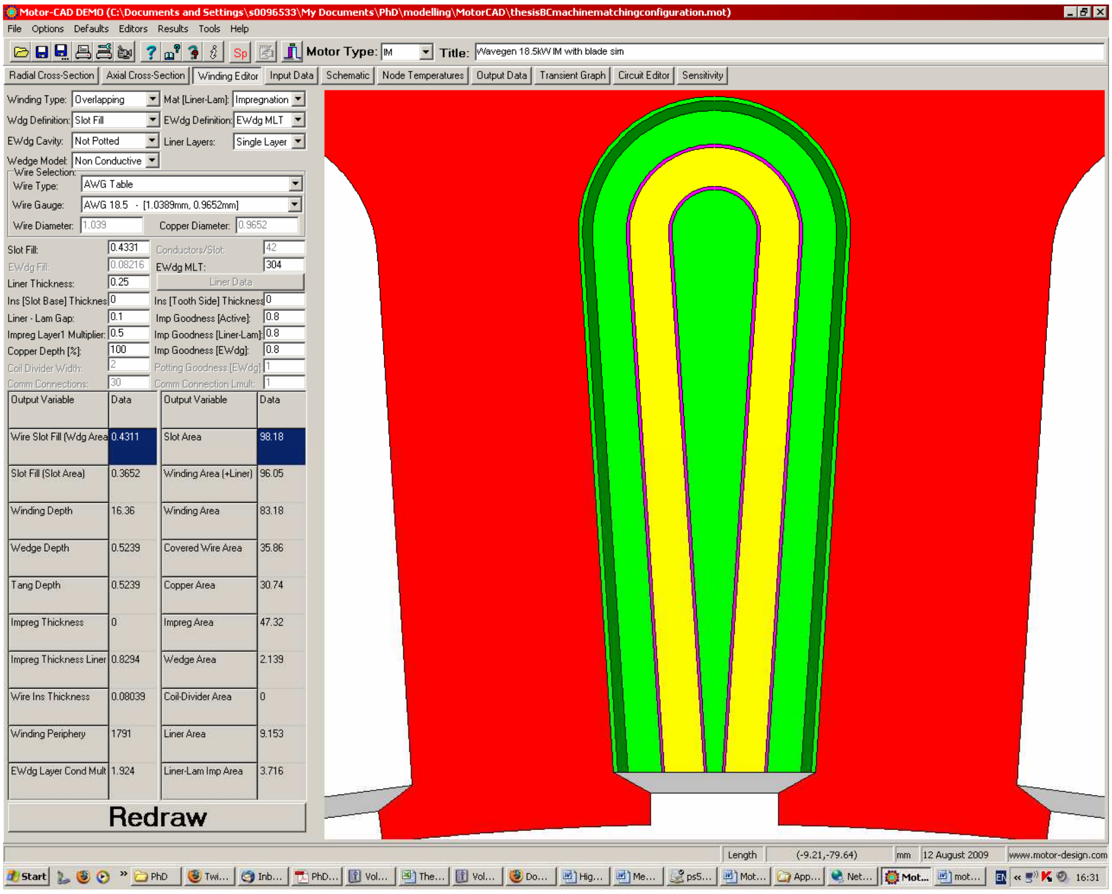

Motor Type: IM
Title: Wavegen 18.5kW IM with blade sim

Winding Type: Overlapping
Mat [Liner-Lam]: Impregnation
Wdg Definition: Slot Fill
EWdg Definition: EWdg MLT
EWdg Cavity: Not Potted
Liner Layers: Single Layer
Wedge Model: Non Conductive

Wire Selection:
Wire Type: AWG Table
Wire Gauge: AWG 18.5 - [1.0389mm, 0.9652mm]
Wire Diameter: 1.039
Copper Diameter: 0.9652

Slot Fill: 0.4331
Conductors/Slot: 42
EWdg Fill: 0.08216
EWdg MLT: 304
Liner Thickness: 0.25
Liner Data
Ins [Slot Base] Thicknes 0
Ins [Tooth Side] Thickness 0
Liner - Lam Gap: 0.1
Imp Goodness [Active]: 0.8
Impreg Layer1 Multiplier: 0.5
Imp Goodness [Liner-Lam]: 0.8
Copper Depth [%]: 100
Imp Goodness [EWdg]: 0.8
Coil Divider Width: 2
Potting Goodness [EWdg]: 1
Comm Connections: 30
Comm Connection Lmult: 1

Output Variable	Data	Output Variable	Data
Wire Slot Fill (Wdg Area	0.4311	Slot Area	98.18
Slot Fill (Slot Area)	0.3652	Winding Area (+Liner)	96.05
Winding Depth	16.36	Winding Area	83.18
Wedge Depth	0.5239	Covered Wire Area	35.86
Tang Depth	0.5239	Copper Area	30.74
Impreg Thickness	0	Impreg Area	47.32
Impreg Thickness Liner	0.8294	Wedge Area	2.139
Wire Ins Thickness	0.08039	Coil-Divider Area	0
Winding Periphery	1791	Liner Area	9.153
EWdg Layer Cond Mult	1.924	Liner-Lam Imp Area	3.716

Length (-9.21,-79.64) mm 12 August 2009 www.motor-design.com

Winding Editor

Winding Type	Overlapping	
Mat [Liner-Lam[	Impregnation	
Wdg Definition	Slot Fill	
Ewdg Definitiion	Ewdg MLT	
Ewdg Cavity	Not Potted	
Liner Layers	Single Layer	
Wedge Model	Nonconductive	
Wire type	AWG	
Wire Gauge	18.5	AWG
Wire Diameter	1.039	mm
Copper Diameter	0.9652	mm
Slot Fill	0.4331	
Ewdg MLT	304	
Liner Thickness	0.25	mm
Ins [Slot Base] Thickness	0	mm
Ins [Tooth Side] Thickness	0	mm
Liner-Lam Gap	0.1	mm
Impreg Layer1 Multiplier	0.5	mm

Imp Goodness [Active]	0.8	
Imp Goodness [Liner-Lam]	0.8	
Imp Goodness [EWdg]	0.8	
Impre Layer1 Multiplier	0.8	
Copper Depth [%]	100	%

Cooling Options

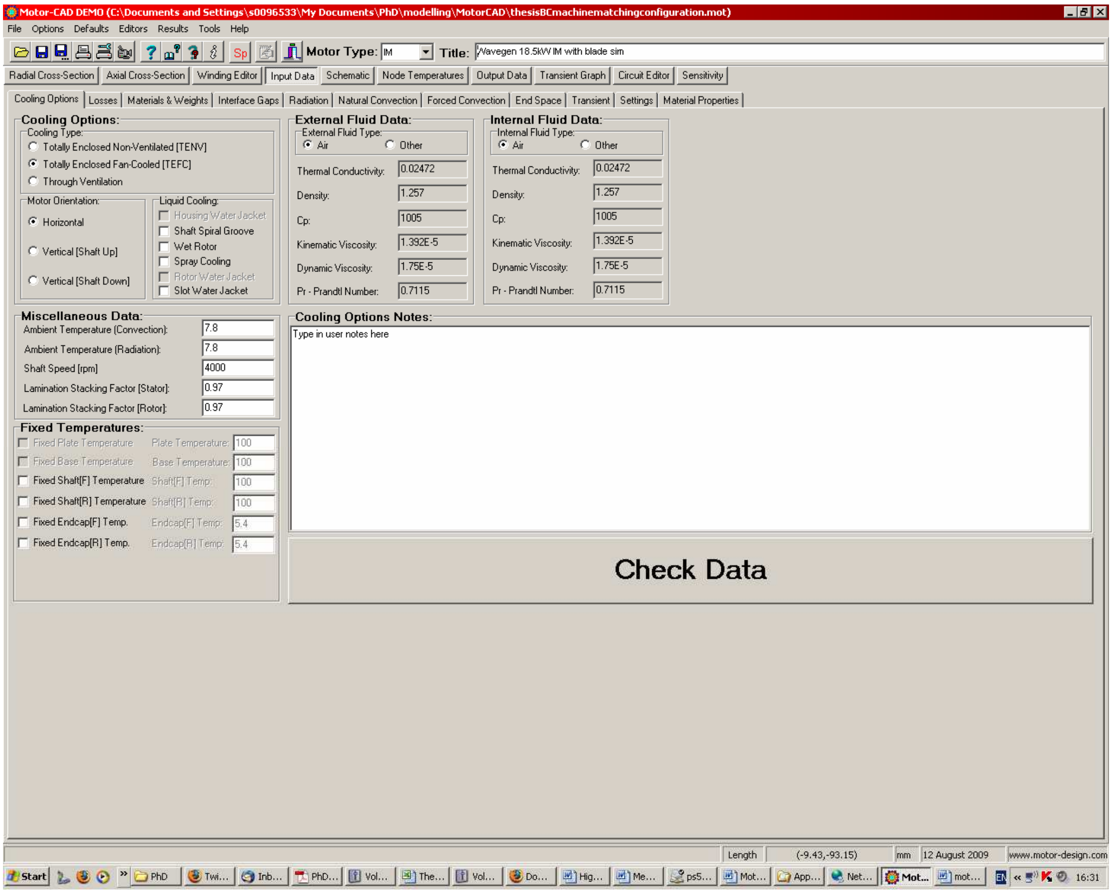

Motor-CAD DEMO (C:\Documents and Settings\s0096533\My Documents\PhD\modelling\MotorCAD\thesisBCmachinematchingconfiguration.mot)

Motor Type: IM **Title:** Wavegen 18.5kW IM with blade sim

Cooling Options:

Cooling Type:
○ Totally Enclosed Non-Ventilated [TENV]
● Totally Enclosed Fan-Cooled [TEFC]
○ Through Ventilation

Motor Orientation:
● Horizontal
○ Vertical [Shaft Up]
○ Vertical [Shaft Down]

Liquid Cooling:
☐ Housing Water Jacket
☐ Shaft Spiral Groove
☐ Wet Rotor
☐ Spray Cooling
☐ Rotor Water Jacket
☐ Slot Water Jacket

External Fluid Data:

External Fluid Type: ● Air ○ Other

Thermal Conductivity:	0.02472
Density:	1.257
Cp:	1005
Kinematic Viscosity:	1.392E-5
Dynamic Viscosity:	1.75E-5
Pr - Prandtl Number:	0.7115

Internal Fluid Data:

Internal Fluid Type: ● Air ○ Other

Thermal Conductivity:	0.02472
Density:	1.257
Cp:	1005
Kinematic Viscosity:	1.392E-5
Dynamic Viscosity:	1.75E-5
Pr - Prandtl Number:	0.7115

Miscellaneous Data:

Ambient Temperature (Convection):	7.8
Ambient Temperature (Radiation):	7.8
Shaft Speed [rpm]	4000
Lamination Stacking Factor [Stator]:	0.97
Lamination Stacking Factor [Rotor]:	0.97

Fixed Temperatures:

☐ Fixed Plate Temperature	Plate Temperature:	100
☐ Fixed Base Temperature	Base Temperature:	100
☐ Fixed Shaft[F] Temperature	Shaft[F] Temp:	100
☐ Fixed Shaft[R] Temperature	Shaft[R] Temp:	100
☐ Fixed Endcap[F] Temp.	Endcap[F] Temp:	5.4
☐ Fixed Endcap[R] Temp.	Endcap[R] Temp:	5.4

Cooling Options Notes:

Type in user notes here

Length (-9.43,-93.15) mm 12 August 2009 www.motor-design.com

Cooling Options

Cooling type	Totally Enclosed Fan-Cooled	
Horizontal	Horizontal	
Ambient Temp (Conv)	7.8	C
Ambient Temp (Rad)	7.8	C
Shaft Speed	4000	RPM
Lamination Stacking Factor [Stator]	0.97	
Lamination Stacking Factor [Rotor]	0.97	
External Fluid	Air	
Internal Fluid	Air	

v. Sensitivity of thermal model result to errors in loss measurement & modelling

Causes of error

The numerical errors in loss measurement stem from measurement error and from the simplified equations used to model the variation of loss with load and rotor speed. These errors can be found from analysing the equipment and equations used in making the measurement. The trends derived can be compared to the data and the modelling error measured.

The location of the loss is an input into the thermal model, MotorCAD allows the core & stray loads to be allocated to different parts of the generator in different proportions. Hence there is the possibility for an error in the location of the losses. Section 6.6.1 goes into some detail of how the location error for each loss is calculated. This appendix concerns how the effect is calculated.

Stator Copper loss

The stator copper loss is calculated using equation 70 from chapter 6, repeated here:

$$P_s = 1.5 I^2 R \tag{70}$$

Where I has an absolute error of 0.1A
R has an absolute error of 0.00144Ω

The relative error (henceforth RE) due to these instrumentation errors is given by equation l:

$$R.E._{Ps} = 200\left(\frac{0.1}{I}\right) + \left(\frac{0.00144}{R_{stator}}\right) \tag{l}$$

For full load at 3000rpm, a relative error of 0.6% is found for the stator copper loss.

Friction & Windage, iron loss

The fixed losses are separated by extrapolating no-load power data for changing terminal voltage to a zero voltage point. The power found at this point is the friction and windage power. The friction and windage power can be subtracted from the data at rated voltage to give the core loss at this point (equation m). Errors will arise in measurement of the core loss and copper loss, affecting both core and friction and windage losses.

$$P_{fe} = P_{in} - P_s \tag{m}$$

At no load, P_{in} has 0.1A and 1.4V instrumentation errors. The error in power input is therefore given by equation n:

$$R.E._{Pin} = 100\left[\left(\frac{0.1}{I}\right) + \left(\frac{1.4}{V}\right)\right] \tag{n}$$

This gives an error of 1.93%. The relative errors are combined with measured values in equation d to give an error of 3.4%.

$$R.E._{pfe} = 100\frac{\lfloor R.E_{pin}P_{in} + R.E_{ps}P_s \rfloor}{P_{fe}} \tag{m}$$

Rotor Copper loss

The rotor copper loss is found from equation (73) in chapter 6, repeated here:

$$P_r = (P_{in} - P_s - P_{fe})S \tag{73}$$

The relative errors for Pin, Ps can be calculated from equations a and c. The error in core loss is known and constant. The main source of error for the rotor copper loss is the inaccuracy in slip measurement. The instrument recording speed is accurate to 1 rpm, translating to 0.017Hz and the instrument recording frequency is accurate to 0.05Hz. The slip frequency at the measurement point is 1.25Hz. Using these values, a relative error of 5.4% is found using equation e.

$$R.E._{\mathrm{Pr}} = 100\left(\frac{R.E._{Pin} + R.E._{Ps} + R.E_{pfe}}{P_{in}} + \frac{0.05 + 0.017}{f_{slip}}\right) \tag{o}$$

Stray loss

The stray load loss is found from the measured remaining loss after all other forms of loss have been subtracted. Consequently it is prone to errors in every other loss condition, as can be seen in equation f:

$$R.E._{Pstray} = 100\frac{\left(R.E._{Pfw}P_{fw} + R.E._{Ps}P_{s} + R.E_{pfe}P_{fe} + R.E._{\mathrm{Pr}}P_{r} + 0.002P_{in}\frac{\eta}{100}\right)}{P_{stray}} \qquad \text{(p)}$$

Where η is the generator efficiency at that power input

This results in a relative error of 14%.

Modelling

These errors will lead to uncertainty in the thermal model, however the connection between the error in a given loss and the resulting error in stator endwinding temperature is complex. Hence the errors are found by using the MotorCAD thermal model in appendix V (with the parameters detailed in the preceding appendix) the maximum and minimum value of each loss is put into the model at loads from 25 to 125% and the change in the stator endwinding temperature noted. This is the percentage change reported in chapter 6 of this thesis.

vi. A Review of Electrical Power Take Off Technology for Oscillating Water Column Wave Energy Devices

N. Hodgins, M. Mueller

World Renewable Energy Congress, Florence, Italy, 2006

vii. Measurement and Modelling of Induction Generator Performance in an Oscillating Water Column Wave Energy Converter

N. Hodgins, M. Mueller, K. Tease, D. Staton

IET Power Electronics Machines and Drives conference, York 2008

viii. Integrated Design of Electrical Generators for Wave and Tidal Current Energy Converters

M. Mueller, A .McDonald, N. Hodgins, R. Crozier

2nd International Conference on Ocean Energy (ICOE 2008), Brest, France, 2008